HAL
open science

Modeling of damping in elastohydrodynamic lubricated contacts : Application to gear dynamics

Mouhamad Ankouni

To cite this version:

Mouhamad Ankouni. Modeling of damping in elastohydrodynamic lubricated contacts : Application to gear dynamics. Mechanics [physics.med-ph]. Université de Lyon, 2016. English. NNT : 2016LYSEI089 . tel-02005648

HAL Id: tel-02005648

https://theses.hal.science/tel-02005648v1

Submitted on 4 Feb 2019

HAL is a multi-disciplinary open access archive for the deposit and dissemination of scientific research documents, whether they are published or not. The documents may come from teaching and research institutions in France or abroad, or from public or private research centers.

L'archive ouverte pluridisciplinaire **HAL**, est destinée au dépôt et à la diffusion de documents scientifiques de niveau recherche, publiés ou non, émanant des établissements d'enseignement et de recherche français ou étrangers, des laboratoires publics ou privés.

N°d'ordre: NNT : 2016LYSEI089

THESE de DOCTORAT DE L'UNIVERSITE DE LYON

opérée au sein de

L'INSTITUT NATIONAL DES SCIENCES APPLIQUEES DE LYON

Ecole Doctorale ED162

Mécanique, Energétique, Génie Civil, Acoustique

Spécialité de doctorat:
Génie Mécanique

Soutenue publiquement le 28/09/2016, par:

Mouhamad ANKOUNI
(Ingénieur de l'Université Libanaise – Liban)

Modeling of damping in elastohydrodynamic lubricated contacts. Application to gear dynamics.

Devant le jury composé de :

JACQUET-RICHARDET, Georges	Professeur (INSA de Lyon)	Examinateur
EVANS, Pwt	Professeur (Cardiff University)	Rapporteur
THEODOSSIADES, Stephanos	Professeur (Loughborough University)	Rapporteur
LUBRECHT, Ton	Professeur (INSA de Lyon)	Invité
VELEX, Philippe	Professeur (INSA de Lyon)	Directeur de thèse

Cette thèse est accessible à l'adresse : http://theses.insa-lyon.fr/publication/2016LYSEI089/these.pdf
© [M. Ankouni], [2016], INSA Lyon, tous droits réservés

Cette thèse est accessible à l'adresse : http://theses.insa-lyon.fr/publication/2016LYSEI089/these.pdf
© [M. Ankouni], [2016], INSA Lyon, tous droits réservés

Département FEDORA – INSA Lyon - Ecoles Doctorales – Quinquennal 2016-2020

SIGLE	ECOLE DOCTORALE	NOM ET COORDONNEES DU RESPONSABLE
CHIMIE	CHIMIE DE LYON http://www.edchimie-lyon.fr Sec : Renée EL MELHEM Bat Blaise Pascal 3e etage secretariat@edchimie-lyon.fr Insa : R. GOURDON	M. Stéphane DANIELE Institut de Recherches sur la Catalyse et l'Environnement de Lyon IRCELYON-UMR 5256 Équipe CDFA 2 avenue Albert Einstein 69626 Villeurbanne cedex directeur@edchimie-lyon.fr
E.E.A.	ELECTRONIQUE, ELECTROTECHNIQUE, AUTOMATIQUE http://edeea.ec-lyon.fr Sec : M.C. HAVGOUDOUKIAN Ecole-Doctorale.eea@ec-lyon.fr	M. Gérard SCORLETTI Ecole Centrale de Lyon 36 avenue Guy de Collongue 69134 ECULLY Tél : 04.72.18 60.97 Fax : 04 78 43 37 17 Gerard.scorletti@ec-lyon.fr
E2M2	EVOLUTION, ECOSYSTEME, MICROBIOLOGIE, MODELISATION http://e2m2.universite-lyon.fr Sec : Safia AIT CHALAL Bat Darwin - UCB Lyon 1 04.72.43.28.91 Insa : H. CHARLES Safia.ait-chalal@univ-lyon1.fr	Mme Gudrun BORNETTE CNRS UMR 5023 LEHNA Université Claude Bernard Lyon 1 Bât Forel 43 bd du 11 novembre 1918 69622 VILLEURBANNE Cédex Tél : 06.07.53.89.13 e2m2@ univ-lyon1.fr
EDISS	INTERDISCIPLINAIRE SCIENCES-SANTE http://www.ediss-lyon.fr Sec : Safia AIT CHALAL Hôpital Louis Pradel - Bron 04 72 68 49 09 Insa : M. LAGARDE Safia.ait-chalal@univ-lyon1.fr	Mme Emmanuelle CANET-SOULAS INSERM U1060, CarMeN lab, Univ. Lyon 1 Bâtiment IMBL 11 avenue Jean Capelle INSA de Lyon 696621 Villeurbanne Tél : 04.72.68.49.09 Fax :04 72 68 49 16 Emmanuelle.canet@univ-lyon1.fr
INFOMATHS	INFORMATIQUE ET MATHEMATIQUES http://infomaths.univ-lyon1.fr Sec :Renée EL MELHEM Bat Blaise Pascal 3e etage infomaths@univ-lyon1.fr	Mme Sylvie CALABRETTO LIRIS – INSA de Lyon Bat Blaise Pascal 7 avenue Jean Capelle 69622 VILLEURBANNE Cedex Tél : 04.72. 43. 80. 46 Fax 04 72 43 16 87 Sylvie.calabretto@insa-lyon.fr
Matériaux	MATERIAUX DE LYON http://ed34.universite-lyon.fr Sec : M. LABOUNE PM : 71.70 –Fax : 87.12 Bat. Saint Exupéry Ed.materiaux@insa-lyon.fr	M. Jean-Yves BUFFIERE INSA de Lyon MATEIS Bâtiment Saint Exupéry 7 avenue Jean Capelle 69621 VILLEURBANNE Cedex Tél : 04.72.43 71.70 Fax 04 72 43 85 28 Ed.materiaux@insa-lyon.fr
MEGA	MECANIQUE, ENERGETIQUE, GENIE CIVIL, ACOUSTIQUE http://mega.universite-lyon.fr Sec : M. LABOUNE PM : 71.70 –Fax : 87.12 Bat. Saint Exupéry mega@insa-lyon.fr	M. Philippe BOISSE INSA de Lyon Laboratoire LAMCOS Bâtiment Jacquard 25 bis avenue Jean Capelle 69621 VILLEURBANNE Cedex Tél : 04.72 .43.71.70 Fax : 04 72 43 72 37 Philippe.boisse@insa-lyon.fr
ScSo	ScSo* http://recherche.univ-lyon2.fr/scso/ Sec : Viviane POLSINELLI Brigitte DUBOIS Insa : J.Y. TOUSSAINT viviane.polsinelli@univ-lyon2.fr	Mme Isabelle VON BUELTZINGLOEWEN Université Lyon 2 86 rue Pasteur 69365 LYON Cedex 07 Tél : 04.78.77.23.86 Fax :04.37.28.04.48

*ScSo : Histoire, Géographie, Aménagement, Urbanisme, Archéologie, Science politique, Sociologie, Anthropologie

Cette thèse est accessible à l'adresse : http://theses.insa-lyon.fr/publication/2016LYSEI089/these.pdf
© [M. Ankouni], [2016], INSA Lyon, tous droits réservés

Cette thèse est accessible à l'adresse : http://theses.insa-lyon.fr/publication/2016LYSEI089/these.pdf
© [M. Ankouni], [2016], INSA Lyon, tous droits réservés

Résumé

Les principaux mécanismes d'amortissement présents dans les transmissions par engrenages sont étudiés, en se basant sur une analyse transitoire du problème de lubrification élasto-hydrodynamique dans les contacts linéiques. Plusieurs modèles linéaires sont proposés suite à de nombreuses simulations numériques, permettant de prédire l'amortissement du lubrifiant dans les différentes conditions de contact, y compris les situations des pertes de contact momentanées suivies d'impact. Un modèle dynamique d'engrenage à un seul degré de liberté est présenté qui combine les contributions diverses du lubrifiant à l'amortissement structurel représentatif de la dissipation interne des engrenages. Un certain nombre de comparaisons avec des résultats expérimentaux est présenté pour une gamme de conditions de fonctionnement et de géométries d'engrenages, qui prouve la capacité du modèle à reproduire proprement le comportement dynamique des engrenages droits. On montre que l'amortissement associé au lubrifiant contribue essentiellement lors des pertes de contact et des chocs entre dentures se produisant au voisinage des vitesses critiques. Le cas des engrenages hélicoïdaux est analysé différemment du fait de l'absence de perte de contact pour ce type d'engrenage. Un modèle tridimensionnel simple est ainsi développé qui prend en compte la dissipation des différents éléments de la transmission. Un nombre de résultats est présenté qui, d'abord, confirme la contribution majeure de l'engrènement à l'amortissement global des engrenages droits, et, dans un second lieu, montre que les paliers constituent la principale source d'amortissement dans les transmissions par engrenages hélicoïdaux.

Mots clés: Amortissement, dynamique des engrenages, lubrification elasto-hydrodynamique, contacts linéiques, multigrilles, vibration et bruit, paliers.

Cette thèse est accessible à l'adresse : http://theses.insa-lyon.fr/publication/2016LYSEI089/these.pdf
© [M. Ankouni], [2016], INSA Lyon, tous droits réservés

Cette thèse est accessible à l'adresse : http://theses.insa-lyon.fr/publication/2016LYSEI089/these.pdf
© [M. Ankouni], [2016], INSA Lyon, tous droits réservés

Abstract

The primary damping mechanisms present in geared systems are investigated based on a transient analysis of the elasto-hydrodynamic lubrication problem for line contacts. Several linear models are derived from extensive numerical simulations, which make it possible to simulate the damping caused by the lubricant squeezing by the teeth with and without momentary contact losses and impacts. A one-degree-of-freedom gear dynamic model is set up which combines these lubricant damping sources along with structural damping that reproduces the internal dissipation in gear elements. A number of comparisons with benchmark experimental evidence are presented for a range of operating conditions and gear geometries, which prove that the proposed approach is sound in the case of spur gears. It is shown that the damping associated with lubricant squeezing contributes for the most part when contact losses and shocks between the teeth occur at critical speeds. The case of helical gears is analyzed differently since no contact loss occurs for such gears. A simple three-dimensional model is thus developed which accounts for the dissipation in the mechanical parts surrounding the gears. A number of results are presented which, first, confirm the primary contribution of the gear mesh to the overall damping in spur gears, and second, show that bearings constitute the main source of damping in helical gears transmissions.

Keywords: Damping, gear dynamics, elasto-hydrodynamic lubrication, line contacts, multigrid, vibration and noise, bearings.

Cette thèse est accessible à l'adresse : http://theses.insa-lyon.fr/publication/2016LYSEI089/these.pdf
© [M. Ankouni], [2016], INSA Lyon, tous droits réservés

Cette thèse est accessible à l'adresse : http://theses.insa-lyon.fr/publication/2016LYSEI089/these.pdf
© [M. Ankouni], [2016], INSA Lyon, tous droits réservés

Contents

Résumé i

Abstract iii

List of figures ix

List of tables xv

Notation xvii

General introduction 1

1 State of the art 3

1.1 ElastoHydrodynamic Lubrication 3

1.1.1 Description of the EHL problem 3

1.1.2 A brief historical overview 5

1.1.3 EHL contact dynamics 5

1.2 Multigrid and Multi-integration techniques 6

1.2.1 Full Approximation Scheme 7

1.2.2 Intergrid transfers 9

a. Restriction 9

b. Interpolation 9

1.2.3 Full Multigrid algorithms 10

1.2.4 Multilevel multi-integration 12

1.3 Gear Dynamics 13

1.3.1 Noise and vibration in geared transmission 13

a. Mesh stiffness variation 13

b. Tooth shape errors and mounting errors 17

c. Gear transmission error 19

Cette thèse est accessible à l'adresse : http://theses.insa-lyon.fr/publication/2016LYSEI089/these.pdf
© [M. Ankouni], [2016], INSA Lyon, tous droits réservés

1.3.2 Advances in gear dynamics study 22
1.3.3 The problem of damping 24
1.4 Conclusion 25
2 Modeling of damping in lubricated line contacts 27
2.1 Permanent lubricated line contacts 27
2.1.1 Permanent contact model 27
2.1.2 Discrete equations 29
2.1.3 Numerical results 31
2.2 Forced lubricated impact 39
2.2.1 EHL Model 39
2.2.1 Numerical results 40
2.3 Conclusion 44
3 Application to gear dynamics: Torsional model 45
3.1 Sources of damping 45
3.1.1 Lubricant normal viscous damping 45
3.1.2 Lubricant tangential viscous damping 46
3.1.3 Structural/Internal damping 47
3.2 Torsional dynamic model 48
3.3 Results 53
3.3.1 Spur gears 53
3.3.2 Helical gears 60
3.4 Conclusion 63
4 Application to gear dynamics: Three dimensional model 65
4.1 3D Lumped parameter model 65
4.1.1 Gear-Pinion Pair 66
a. Mass and Stiffness 66

Cette thèse est accessible à l'adresse : http://theses.insa-lyon.fr/publication/2016LYSEI089/these.pdf
© [M. Ankouni], [2016], INSA Lyon, tous droits réservés

b. Mesh damping 69
4.1.2 Shafts 72
a. Mass and Stiffness 72
b. Damping 74
4.1.3 Bearings 75
a. Journal bearings 75
b. Rolling element bearings 78
4.2 Results 78
4.2.1 Identical spur gears 78
4.2.2 Comparisons with experimental evidence 82
4.2.3 Identical helical gears 87
4.2.4 Modal analysis of the damped system 94
4.2.5 Further investigations 96
a. Spur gears 96
b. Helical gears 97
4.2.6 Non identical helical gears 98
4.3 Conclusion 105
General conclusion 107
References 109
A Damping under multi-frequency excitation 123
B A note on the influence of roughness on damping 125

Cette thèse est accessible à l'adresse : http://theses.insa-lyon.fr/publication/2016LYSEI089/these.pdf
© [M. Ankouni], [2016], INSA Lyon, tous droits réservés

Cette thèse est accessible à l'adresse : http://theses.insa-lyon.fr/publication/2016LYSEI089/these.pdf
© [M. Ankouni], [2016], INSA Lyon, tous droits réservés

List of figures

Figure 1.1: EHL line contact equivalent geometry. 4

Figure 1.2: Fine grid with mesh size $\boldsymbol{hx}$ and coarse grid with mesh size $\boldsymbol{Hx = 2hx}$ for a one dimensional problem. 7

Figure 1.3: Restriction from fine grid by full weighting for a one dimensional problem. 9

Figure 1.4: Linear interpolation from coarse to fine grid for a one dimensional problem. 10

Figure 1.5: An example of a Multi-Level Cycle ($\boldsymbol{\gamma = 1}$). $\boldsymbol{V\nu 1, \nu 2}$ cycle. 11

Figure 1.6: A FMG algorithm with one $\boldsymbol{V}$ cycle. 12

Figure 1.7: Parameters for Weber's formulae. 15

Figure 1.8: Examples of time-varying gear mesh stiffness. 16

Figure 1.9: Tooth profile error [75]. 17

Figure 1.10: Single pitch error [75]. 18

Figure 1.11: Examples of lead error traces on the base plane [78]. 18

Figure 1.12: Shaft misalignments [79]. 19

Figure 1.13: Transmission error definition [83]. 20

Figure 1.14: Quasi-static transmission errors. (a) experiments, (b) simulations [92]. 21

Figure 2.1: Discrete computational domain. 29

Figure 2.2: Examples of pressure distribution and film thickness in an EHL contact under periodic load. 32

Figure 2.3: Mutual approach and load evolution versus time. 33

Figure 2.4: Mutual approach versus load (hysteresis loop). 34

Figure 2.5: Numerical values of the damping constant $\boldsymbol{Cl}$ as a function of the amplitude of the excitation $\boldsymbol{A}$. 35

Figure 2.6: Numerical values of the damping constant $\boldsymbol{Cl}$ as a function of the frequency of the excitation $\boldsymbol{fl}$. 36

Cette thèse est accessible à l'adresse : http://theses.insa-lyon.fr/publication/2016LYSEI089/these.pdf
© [M. Ankouni], [2016], INSA Lyon, tous droits réservés

Figure 2.7: Damping constant $\boldsymbol{Cl}$ as a function of the load parameter $\boldsymbol{M}$ and the material parameter $\boldsymbol{L}$. 37

Figure 2.8: Numerical values of the damping constant $\boldsymbol{Cl}$ as a function of $\boldsymbol{\beta}$. 38

Figure 2.9: Numerical values of $\boldsymbol{Cl}$ as a function of $\boldsymbol{\beta}$ (symbols) and its curve fitted equation (drawn line). 38

Figure 2.10: Pressure distribution and film thickness evolution during impact. 41

Figure 2.11: Pressure distribution and film thickness evolution during rebound. 42

Figure 2.12: Dimensionless damping constant versus parameter $\boldsymbol{\xi}$. 43

Figure 2.13: Correcting factor in terms of load $\boldsymbol{f}$ and parameter $\boldsymbol{\xi}$. 44

Figure 3.1: Gear pair dynamic model. 48

Figure 3.2: Gear geometry and external forces. 49

Figure 3.3: Process of numerical simulation of the torsional model. 52

Figure 3.4: Measured [88] and numerical RMS of *DTE* versus the gear meshing frequency $\boldsymbol{fm}$. Spur gears. 54

Figure 3.5: Mean damping ratio versus the gear meshing frequency $\boldsymbol{fm}$. Different loads. Spur gears. 54

Figure 3.6: Relative contribution of the lubricant to the global damping ratio for $\boldsymbol{T = 300\ Nm}$. Spur gears. 55

Figure 3.7: Evolution of damping ratio and mesh stiffness versus dimensionless time for $\boldsymbol{T = 300\ N}$, at $\boldsymbol{2500\ Hz}$. Spur gears. 55

Figure 3.8: Tangential damping ratio versus dimensionless time for $\boldsymbol{T = 300\ N}$ at $(\boldsymbol{a})$ $\boldsymbol{600\ Hz}$, $(\boldsymbol{b})$ $\boldsymbol{1200\ Hz}$ and $(\boldsymbol{c})$ $\boldsymbol{2000\ Hz}$. Spur gears. 56

Figure 3.9: Numerical RMS of *DTE* versus the gear meshing frequency $\boldsymbol{fm}$. Different lubricant temperatures. $\boldsymbol{T = 100\ Nm}$. Spur gears. 58

Figure 3.10: Mean damping ratio versus the gear meshing frequency $\boldsymbol{fm}$. Different lubricant temperatures. $\boldsymbol{T = 100\ Nm}$. Spur gears. 58

Figure 3.11: Measured [102] and calculated RMS of *DTE* versus $\boldsymbol{fm/fn}$ for unmodified gears for $\boldsymbol{T = 340\ Nm}$. Spur gears. 59

Cette thèse est accessible à l'adresse : http://theses.insa-lyon.fr/publication/2016LYSEI089/these.pdf
© [M. Ankouni], [2016], INSA Lyon, tous droits réservés

Figure 3.12: Measured [103] and calculated RMS of *DTE* versus $\boldsymbol{fm/fn}$ for $\boldsymbol{T = 340\ Nm}$. Spur gears. 60

Figure 3.13: Measured [141] and calculated RMS of *DTE* versus input speed for 61

Figure 3.14: Tangential damping ratio versus input speed for $\boldsymbol{T = 250\ Nm}$. Helical gears. . 62

Figure 3.15: Measured [141] and calculated RMS of *DTE* versus input speed for $\boldsymbol{T = 250\ Nm}$. Various damping ratios. Helical gears. 62

Figure 4.1: Lumped parameter model. 65

Figure 4.2: Pinion-Gear Pair and base plane. 68

Figure 4.3: Line of action and bases definition. 69

Figure 4.4: Degrees of freedom for shaft elements. 73

Figure 4.5: Frame definition for the computation of the journal bearing dynamic coefficients. 76

Figure 4.6: Dynamic response curves. Comparison between structural damping and mesh damping. Spur gears. 80

Figure 4.7: Dynamic response curves. Comparison between mesh damping and REB damping. Spur gears. 80

Figure 4.8: Dynamic response curves. Comparison between mesh damping and journal bearing damping. Spur gears. 81

Figure 4.9: Dynamic response curves. Comparisons between various journal geometries. Spur gears. 81

Figure 4.10: Mean journal bearing radial damping variation for different geometries as a function of the gear mesh frequency. Spur gears. 82

Figure 4.11: Numerical RMS of *DTE* versus the gear meshing frequency. Comparison between rolling elements bearings and journal bearings. NASA GRC's test gearbox. 84

Figure 4.12: Mean journal bearing radial damping variation as a function of the gear mesh frequency. 85

Figure 4.13: $\boldsymbol{1 \times GMF}$ component of the *DTE*. 85

Figure 4.14: $\boldsymbol{2 \times GMF}$ component of the *DTE*. 86

Cette thèse est accessible à l'adresse : http://theses.insa-lyon.fr/publication/2016LYSEI089/these.pdf
© [M. Ankouni], [2016], INSA Lyon, tous droits réservés

Figure 4.15: Maximum radial displacement of the center of the bearing located at the loaded end of the input shaft. 86

Figure 4.16: Dynamic response curves. Comparison between internal damping and mesh damping. Helical gears. 88

Figure 4.17: Dynamic response curves. Comparison between mesh damping and rolling element bearing damping. Helical gears. 88

Figure 4.18: Dynamic response curves. Comparison between mesh damping and journal bearing damping. Helical gears. 89

Figure 4.19: Dynamic response curves. Comparison between different clearance values. Journal bearings. Helical gears. 90

Figure 4.20: Mean journal bearing radial damping variation. Comparison between different clearance values. Helical gears. 91

Figure 4.21: Dynamic response curves. Comparison between different lengths. Journal bearings. Helical gears. 91

Figure 4.22: Mean journal bearing radial damping variation. Comparison between different lengths. Helical gears. 92

Figure 4.23: Dynamic response curves. Comparison between different lubricant viscosities. Journal bearings. Helical gears. 92

Figure 4.24: Mean journal bearing radial damping variation. Comparison between different lubricant viscosities. Helical gears. 93

Figure 4.25: Dynamic response curves. Comparisons between various bearings damping (constant stiffness). Helical gears. 93

Figure 4.26: Dynamic response curves. Comparisons between rolling element and various journal bearings geometries. Spur gears. 97

Figure 4.27: Dynamic response curves. Comparisons between rolling element and various journal bearings geometries. Helical gears. 98

Figure 4.28: Dynamic response curves. Comparison between rolling element bearings and journal bearings. Non identical helical gears. 100

Figure 4.29: Dynamic response curves. Comparison between different clearance values ($\boldsymbol{L/D = 0.25, \mu 0 = 0.0178\ \mathrm{Pa.s}}$) . Journal bearings. Non identical helical gears. 100

Cette thèse est accessible à l'adresse : http://theses.insa-lyon.fr/publication/2016LYSEI089/these.pdf
© [M. Ankouni], [2016], INSA Lyon, tous droits réservés

Figure 4.30: Mean journal bearing radial damping variation. Comparison between different clearance values. Non identical helical gears. 101

Figure 4.31: Dynamic response curves. Comparison between different lengths ($\boldsymbol{R/C = 1000, \mu 0 = 0.0178\ \mathrm{Pa.s}}$). Journal bearings. Non identical helical gears..... 102

Figure 4.32: Mean journal bearing radial damping variation. Comparison between different lengths. Non identical helical gears..... 103

Figure 4.33: Dynamic response curves. Comparison between different lubricant viscosities ($\boldsymbol{L/D = 0.5, R/C = 1000}$). Journal bearings. Non identical helical gears..... 103

Figure 4.34: Mean journal bearing radial damping variation. Comparison between different lubricant viscosities. Non identical helical gears. 104

Cette thèse est accessible à l'adresse : http://theses.insa-lyon.fr/publication/2016LYSEI089/these.pdf
© [M. Ankouni], [2016], INSA Lyon, tous droits réservés

Cette thèse est accessible à l'adresse : http://theses.insa-lyon.fr/publication/2016LYSEI089/these.pdf
© [M. Ankouni], [2016], INSA Lyon, tous droits réservés

List of tables

Table 3.1: Test gear characteristics (*identical pinion and gear*). Spur gears. 53

Table 3.2: Lubricant basic properties. 53

Table 3.3: Test gear characteristics (*identical pinion and gear*). Helical gears. 61

Table 4.1: Test gears characteristics (*identical pinion and gear*). Spur gears. 79

Table 4.2: NASA GRC gearbox spur gear parameters. 83

Table 4.3: Test gears characteristics (*identical pinion and gear*). Helical gears. 87

Table 4.4: Natural frequencies and damping ratios. Journal bearings. 95

Table 4.5: Natural frequencies and damping ratios. Constant stiffness. 96

Table 4.6: Gear data. Non identical helical gears [98]. 99

Table 4.7: Shaft dimensions. 99

Table 4.8: Natural frequencies and damping ratios. 105

Cette thèse est accessible à l'adresse : http://theses.insa-lyon.fr/publication/2016LYSEI089/these.pdf
© [M. Ankouni], [2016], INSA Lyon, tous droits réservés

Cette thèse est accessible à l'adresse : http://theses.insa-lyon.fr/publication/2016LYSEI089/these.pdf
© [M. Ankouni], [2016], INSA Lyon, tous droits réservés

Notation

Chapter 1

^{h}	discrete form on grid h
DTE	dynamic transmission error $[m]$
f	general right hand side function
I_h^H	restriction operator from fine to coarse grid
I_H^h	interpolation operator from coarse to fine grid
k	number of grids/levels
K	continuous deformation kernel
$K^{h,h}$	discrete deformation kernel on grid h
L	differential operator
$NLTE$	no load transmission error $[m]$
r	residual
TEs	quasi-static transmission error $[m]$
u	continuous solution of the differential equation
$\bar{u}^h, \tilde{u}^h$	approximations to u^h
v^h	numerical error
γ	number of correction cycles
δ_b	tooth bending deformation $[m]$
δ_c	teeth contact deformation $[m]$
δ_{f_w}	gear body related deformation $[m]$
ν_0, ν_1, ν_2	number of relaxation sweeps on different levels
ω	deformation [m]

Chapter 2

a	amplitude of the imposed load $[N/m]$
A	dimensionless amplitude of the imposed load
b	Hertzian contact half width $[m]$
b^*	Hertzian contact half width $[m]$ (impact problem)

Cette thèse est accessible à l'adresse : http://theses.insa-lyon.fr/publication/2016LYSEI089/these.pdf
© [M. Ankouni], [2016], INSA Lyon, tous droits réservés

c_{im}	normal viscous damping during impact $[Ns/m]$
c_l	normal viscous damping during permanent contact $[Ns/m]$
C_l	dimensionless normal viscous damping
C_{im}	dimensionless normal viscous damping during impact
d	width of the line contact $[m]$
E	dissipated energy by the viscous forces
E'	reduced modulus of elasticity $[Pa]$
f	external load on the cylinder $[N/m]$ (impact problem)
f_l	frequency of excitation
F	dimensionless load on the cylinder (impact problem)
h	film thickness $[m]$
h_0	rigid body separation $[m]$
h_0	position of the cylinder $[m]$ (impact problem)
h_X	dimensionless grid mesh size
h_T	dimensionless time-step
H	dimensionless film thickness
H_0	dimensionless rigid body displacement
H_0	dimensionless position of the cylinder (impact problem)
L	dimensionless material parameter (Moes) $L = G\sqrt[4]{U}$
M	dimensionless load parameter (Moes) $M = W_1/\sqrt{U}$
p	pressure $[Pa]$
p_h	maximum Hertzian pressure $[Pa]$
p_h^*	maximum Hertzian pressure $[Pa]$ (impact problem)
P	dimensionless pressure $P = p/p_h$
R_x	reduced radius of curvature in x direction $[m]$
R_t	dimensionless reduced radius of curvature
t	time $[s]$
t_l	period of excitation $[s]$
T	dimensionless time
T_l	dimensionless period of excitation
u_m	mean surface velocity $u_m = (u_1 + u_2)/2$ $[m/s]$
U_{m_t}	dimensionless mean surface velocity
v	velocity of the cylinder $[m/s]$ (impact problem)

Cette thèse est accessible à l'adresse : http://theses.insa-lyon.fr/publication/2016LYSEI089/these.pdf
© [M. Ankouni], [2016], INSA Lyon, tous droits réservés

V	dimensionless velocity of the cylinder (impact problem)
w_t	load per unit length $[N/m]$
w^*	maximum load $[N/m]$ (impact problem)
W_t	dimensionless load
x	coordinate $[m]$
X	dimensionless coordinate $X = x/b$
α	pressure viscosity coefficient $[Pa^{-1}]$
$\bar{\alpha}$	dimensionless pressure viscosity index
β	dimensionless parameter $\beta = \sqrt{L}/M$
δ^*	maximum deformation $[m]$ (impact problem)
Δ	gear mesh displacement $[m]$
η	viscosity $[Pa\ s]$
η_0	viscosity at ambient pressure $[Pa\ s]$
$\bar{\eta}$	dimensionless viscosity
λ	dimensionless parameter
λ^*	dimensionless parameter (impact problem)
ρ	density $[kg/m^3]$
ρ_0	density at ambient pressure
$\bar{\rho}$	dimensionless density
χ	correction factor for impact damping
ω	frequency of the excitation
Ω	dimensionless frequency of the excitation $\Omega = 2\pi f_l$
ref	reference values (sub-script)

Chapter 3

$\dot{}$, $\ddot{}$	first and second derivative with respect to time
A_0	apparent contact area $[m]$ (friction law)
A_c	actual average contact area $[m]$ (friction law)
c_{im}	normal viscous damping during impact $[Ns/m]$
c_l	normal viscous damping during permanent contact $[Ns/m]$
c_n	equivalent normal damping $[Ns/m]$
c_{st}	structural damping $[Ns/m]$
c_t	friction induced damping $[Ns/m]$

Cette thèse est accessible à l'adresse : http://theses.insa-lyon.fr/publication/2016LYSEI089/these.pdf
© [M. Ankouni], [2016], INSA Lyon, tous droits réservés

C	equivalent damping $[Ns/m]$
d	gear face width $[m]$
DTE	dynamic transmission error $[m]$
f_m	gear meshing frequency $[Hz]$
f_n	gear natural frequency $[Hz]$
F_N	normal force on the line of action $[N]$
$\overrightarrow{F_{n_{1,2}}}$	normal contact forces
$\overrightarrow{F_{t_{1,2}}}$	tangential shear forces
F_e	excitation force $[N]$
h_c	central film thickness $[m]$
ICR	involute contact ratio
$J_{1,2}$	polar mass moments of inertia of gears 1 and 2, respectively
$k(M)$	mesh stiffness at point M $[N/m]$
K	equivalent stiffness $[N/m]$
m_0	average square value of the height of roughness (friction law) $[m^2]$
M_{eq}	equivalent mass $[kg]$
p_{moy}	average pressure on the contact $[Pa]$
$R_{1,2}$	contact radii of curvature of gears 1 and 2, respectively $[m]$
$R_{b_{1,2}}$	base radii of gears 1 and 2, respectively $[m]$
t_m	gear meshing period $[s]$
$T_{1,2}$	torque applied on gears 1 and 2, respectively $[N\ m]$
$T_{n_{1,2}}$	moments of the normal forces $[N\ m]$
$T_{t_{1,2}}$	moments of the tangential forces $[N\ m]$
$u_{1,2}$	tangential surface speeds of gears 1 and 2, respectively $[m/s]$
u_s	sliding velocity $[m/s]$
Δ	mesh deflection $\Delta = R_{b_1}\theta_1 + R_{b_2}\theta_2$ $[m]$
γ	starting roll angle [°]
ζ	damping factor
ζ_{fluid}	fluid traction $[Pa]$
ζ_{rough}	solid traction $[Pa]$
η	viscosity $[Pa\ s]$
$\theta_{1,2}$	rotational displacements of gears 1 and 2, respectively $[rad]$

Cette thèse est accessible à l'adresse : http://theses.insa-lyon.fr/publication/2016LYSEI089/these.pdf
© [M. Ankouni], [2016], INSA Lyon, tous droits réservés

μ_f	coefficient of friction
τ_L	limiting shear stress $[Pa]$
τ_N	shear stress $[Pa]$
ϕ	pressure angle [°]
ϕ_t	thermal correction factor (friction law)
$\Omega_{1,2}$	pinion, gear angular velocity $[rad/s]$

Chapter 4

$\dot{\ }$, $\ddot{\ }$	first and second derivative with respect to time
c_{im}	normal viscous damping during impact $[Ns/m]$
c_l	normal viscous damping during permanent contact $[Ns/m]$
c_n	equivalent normal damping $[Ns/m]$
c_{st}	structural damping $[Ns/m]$
c_t	friction induced damping $[Ns/m]$
C_f	maximum dynamic factor
DTE	dynamic transmission error $[m]$
$\overrightarrow{F_{n_{1,2}}}$	normal contact forces
$\overrightarrow{F_{t_{1,2}}}$	tangential shear forces
$k(M)$	mesh stiffness at point M $[N/m]$
k_{ϕ_p}	modal stiffness with mode P $[N/m]$
L/D	length to diameter ratio (journal bearing)
m_{ϕ_p}	mass associated with mode P $[kg]$
q	vector of the pinion-gear degrees of freedom
R/C	radius to clearance ratio (journal bearing)
$u_{1,2}$	small displacements along the axis $\vec{Z}$ of gears 1 and 2, respectively $[m]$
$U(M)$	structural vector at point M (shear forces)
$v_{1,2}$	small displacements along the axis $\vec{S}$ of gears 1 and 2, respectively $[m]$
$V(M)$	structural vector at point M (normal deflection)
$w_{1,2}$	small displacements along the axis $\vec{T}$ of gears 1 and 2, respectively $[m]$
X	total degrees of freedom vector.
$\delta_e(M)$	initial separation caused by tooth modifications or errors $[m]$

Cette thèse est accessible à l'adresse : http://theses.insa-lyon.fr/publication/2016LYSEI089/these.pdf
© [M. Ankouni], [2016], INSA Lyon, tous droits réservés

$\Delta(M)$	normal deflection $[m]$
ζ	damping factor
ζ_p	modal damping factor associated with mode P
$\theta_{1,2}$	small rotations around the axis $\vec{Z}$ of gears 1 and 2, respectively $[rad]$
$\upsilon_{1,2}$	tangential dynamic surface velocities of gear 1 and 2, respectively $[m/s]$
$\vec{\upsilon}_{1,2}$	vector of displacements of the centers of gears 1 and 2, respectively
μ_0	viscosity of the lubricant (journal bearing) $[Pa\ s]$
$\phi_{1,2}$	small rotations around the axis $\vec{S}$ of gears 1 and 2, respectively $[rad]$
Φ_p	eigenvector associated with mode P
$\psi_{1,2}$	small rotations around the axis $\vec{T}$ of gears 1 and 2, respectively $[rad]$
$\vec{\omega}_{1,2}$	vector of rotational displacements of gears 1 and 2, respectively
ω_p	eigenfrequency of the mode P $[Hz]$
$\Omega_{1,2}$	pinion, gear angular velocity $[rad/s]$
$[C]$	equivalent damping matrix
$[C_b]$	damping matrix related to bearings
$[C_m]$	damping matrix related to gear mesh
$[C_s]$	damping matrix related to shafts
$\left[C_{s_\phi}\right]$	modal damping matrix related to shafts
$[K]$	equivalent stiffness matrix
$[K_b]$	damping matrix related to bearings
$[K_m]$	damping matrix related to gear mesh
$[K_s]$	damping matrix related to shafts
$[M]$	equivalent mass matrix
$[M_G]$	mass matrix related to gears
$[M_s]$	mass matrix related to shafts

Cette thèse est accessible à l'adresse : http://theses.insa-lyon.fr/publication/2016LYSEI089/these.pdf
© [M. Ankouni], [2016], INSA Lyon, tous droits réservés

General introduction

Despite significant improvements in the analysis of gear dynamics over the last decades, the damping mechanisms remain major unknowns which, to a large extent, control gear vibrational responses. The main challenges in this research area are caused by i) the insufficient information on the dissipative properties of materials and ii) the diversity and complexity of the damping mechanisms in geared transmissions. In these conditions, the theoretical analyses to characterize and quantify gear damping are sparse and still challenging in view of the variety of operating conditions to be considered. Damping, however, is crucial in order to avoid detrimental vibrations and shocks and a better knowledge and control of the damping properties in gears is needed for successful designs and operations. It seems quite clear that one of the major contributions to gear damping comes from the lubricated contacts between the teeth and that the energy dissipated by the lubricant tends to limit dynamic tooth loads. It is therefore believed that an in-depth understanding of the lubrication dynamic properties in gears is required in order to set up realistic damping models. In this context, the main objective of this research work is to couple the analysis of gear lubrication with the dynamic study of gears in order to propose physics-based damping modeling which can be integrated in the numerical simulations of geared systems.

The outline of the memoir is as follows. The first chapter presents a survey of the literature related to EHL lubrication, gear dynamic modeling and multilevel methods. The second chapter introduces the theory used to study the dynamic characteristics of the lubricated contacts between gear teeth. Different contact models are considered which account for both permanent contact situations and contact loss/shock regimes mostly observed in spur gears. A set of numerical results is presented including curve-fitted equations derived from massive simulations which can be used to predict quickly the lubricant related damping for each situation. Then, in chapter 3, the damping formulations are introduced in a purely torsional gear model and validated via a number of comparisons with experimental evidence. Finally, a three dimensional dynamic model is considered in chapter 4 to extend the field of application of the proposed theory to different types of gears and incorporate the contributions of shafts and bearings. A number of numerical simulations have been performed for various gears, bearing technologies (rolling element and journal bearings) and the contribution of each source of

Cette thèse est accessible à l'adresse : http://theses.insa-lyon.fr/publication/2016LYSEI089/these.pdf
© [M. Ankouni], [2016], INSA Lyon, tous droits réservés

damping is analyzed. A general conclusion summarizes the major findings and presents possible further extensions of the proposed methodology.

Cette thèse est accessible à l'adresse : http://theses.insa-lyon.fr/publication/2016LYSEI089/these.pdf
© [M. Ankouni], [2016], INSA Lyon, tous droits réservés

Chapter 1

State of the art

The first chapter aims at presenting the basic notions and definitions related to the fields of elastohydrodynamic lubrication and gear dynamics. A brief overview of the progress in both fields is provided as well, going back to the first efforts made more than a century ago and ending with the latest improvements on which one can rely to elaborate any complex study. The basic routines employed when using the efficient multigrid and multi-integration techniques, are also highlighted.

1.1 ElastoHydrodynamic Lubrication

1.1.1 Description of the EHL problem

The so-called ElastoHydrodynamic Lubrication (EHL) is the kind of lubrication encountered in the contact between highly stressed machine elements in relative motions such as gears, rolling element bearings, cam tappets etc. This form of fluid film lubrication presents two essential characteristics:

- Large elastic deformations, i.e. the deformations of the contacting surfaces are generally much larger than the lubricant film thickness.
- Important piezo-viscous effects, i.e. the lubricant viscosity is far from being constant due to very high pressures in the contact (up to few GPa), viscosity is much larger than the atmospheric viscosity.

The basic EHL problem consists therefore of a system of equations that combine those different aspects to study the behavior of the lubricant inside the gap that separates the contacting bodies. The basic equation which describes the flow inside the contact, is the Reynolds equation [1]. It is derived from the Navier-Stokes equations assuming that inertia forces are neglected compared to viscous forces, a narrow gap assumption is also made. Hence the resulting equation, for a two dimensional problem, reads:

Cette thèse est accessible à l'adresse : http://theses.insa-lyon.fr/publication/2016LYSEI089/these.pdf
© [M. Ankouni], [2016], INSA Lyon, tous droits réservés

$$\underbrace{\frac{\partial}{\partial x}\left(\frac{\rho h^3}{12\eta}\frac{\partial p}{\partial x}\right)+\frac{\partial}{\partial y}\left(\frac{\rho h^3}{12\eta}\frac{\partial p}{\partial y}\right)}_{Poiseuille}-\underbrace{\frac{\partial(u_m\,\rho h)}{\partial x}}_{Couette}-\underbrace{\frac{\partial(\rho h)}{\partial t}}_{transient}=0 \tag{1.1}$$

A complementary cavitation condition is considered that guarantees a positive pressure inside the contact. The deformed geometry of the gap is described by the elastic deformation equation. A linear elastic deformation between two uniform and isotropic bodies is assumed, and the deformation can thus be approximated by:

$$\omega(x,y)=\frac{2}{\pi E'}\int_{-\infty}^{+\infty}\int_{-\infty}^{+\infty}\frac{p(x',y')dx'dy'}{\sqrt{(x-x')^2+(y-y')^2}} \tag{1.2}$$

The geometry of contacting bodies is generally rather complex and time-varying, such as the contact between two gear teeth. However, because the contact dimensions, i.e. the contact width and film thickness, are very small compared to the dimensions of the body, a parabolic approximation is used to model the contact geometry, i.e. the geometry is reduced to that of two parabolic bodies, each presenting a radius of curvature in each direction, and an equivalent contact geometry of a parabolic body with a plane is then considered as illustrated in Figure 1.1 (line contact). The viscosity increases enormously inside the contact, as stated earlier. The simplest form of the viscosity pressure dependence is exponential [2], generally the Roelands equation is used [3]. The density pressure relation is given by Dowson and Higginson [4]. Finally, the equilibrium of the applied load and the pressure generated inside the contact is checked through the force balance equation.

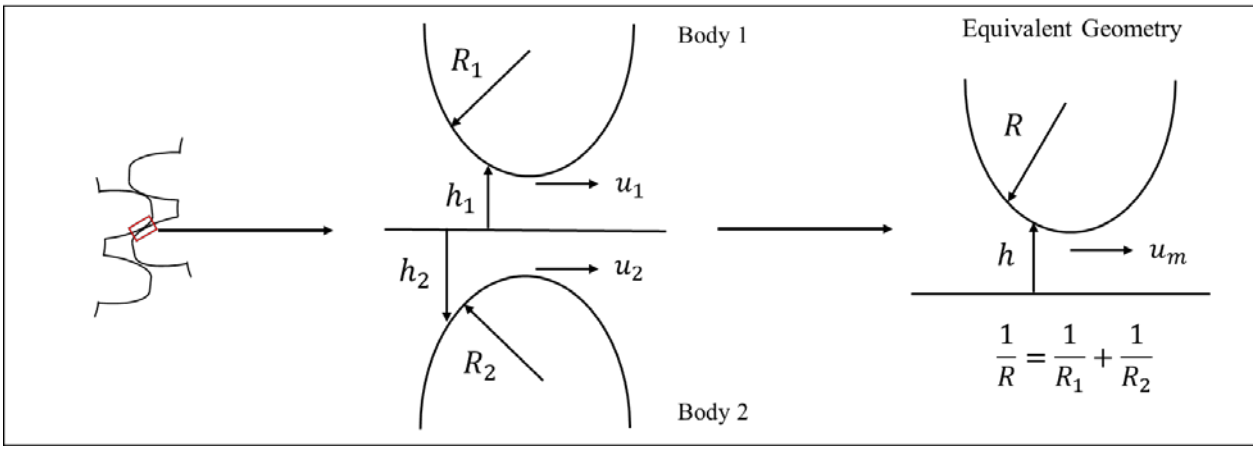

Figure 1.1: EHL line contact equivalent geometry.

Cette thèse est accessible à l'adresse : http://theses.insa-lyon.fr/publication/2016LYSEI089/these.pdf
© [M. Ankouni], [2016], INSA Lyon, tous droits réservés

1.1.2 A brief historical overview

The basics of ElastoHydrodynamic Lubrication were laid more than a century ago. Hertz [5] first described the elastic deformation of the contact between two solids. A few years later, Reynolds [1] established the basis of lubrication theory stimulated by the observations of Tower [6] of the pressure generation in journal bearings. Some of the first studies to couple the elastic deformation and lubrication were performed by Ertel [7] and Grubin [8] to predict the film thickness in line contacts. More detailed reviews of the history and fundamentals of elastohydrodynamic lubrication are proposed by Dowson [9] and Gohar [10]. Numerical solutions of the EHL problem were first proposed by Dowson and Higginson [11] for line contacts and, a decade later, by Hamrock and Dowson for point contacts [12,13]. Since then, the increased capacities of computers and the development of efficient numerical methods [14-15], enhanced the progress in numerical studies of the EHL problem. Various numerical work that considered several complex features affecting largely the lubrication behavior were performed. A few are mentioned in what follows as examples of the wide application of the EHL problem in varied fields. Generalized forms of the Reynolds equation were developed [16-18] to account basically for the non-Newtonian behavior of the lubricant. Thermal effects were also of a certain interest [19, 20]. The effect of surface roughness on lubrication under various conditions was extensively analyzed, the contributions of Venner and Lubrecht [21-24] and Evans et al. [25, 26] can be cited, among others. Some complex contact geometries were considered by Messé and Lubrecht [27] for the cam/tappet contact and more recently by Bouassida et al. [28] for the piston ring cylinder liner contact. Other work studied starved lubrication [29-31], along with friction forces in lubricated contacts [32-33]. The focus is placed on previous numerical work since a numerical study of the EHL problem is presently aimed. Otherwise, several experimental studies can be cited [34-37].

1.1.3 EHL contact dynamics

The dynamic behavior of lubricated contact is also of great interest, knowing that all machine elements are subjected to time varying operating conditions including dynamic loading and variable surface speeds and geometries. Wijnant et al. [38] analyzed the film thickness fluctuations due to structural vibrations in elastohydrodynamic lubrication (EHL) contacts and highlighted the limitation of steady state analyses. Later, the authors [39] investigated the accuracy of the simulated EHL responses to load fluctuations by comparing some of their previous results [40] with the experimental evidence of Sakamoto et al. [41]. Wang et al. [42]

Cette thèse est accessible à l'adresse : http://theses.insa-lyon.fr/publication/2016LYSEI089/these.pdf
© [M. Ankouni], [2016], INSA Lyon, tous droits réservés

solved the transient thermo-elastohydrodynamic lubrication problem of an involute spur gear using a simplified multi-grid method. Li and Kahraman [43] proposed a transient, non-Newtonian, mixed EHL model for involute spur gears and combined this model with a non-linear gear dynamic model [44] in order to predict the influence of dynamic tooth loads and contact losses on gear lubrication. Barbieri et al. [45] presented a model combining transient point contact EHL along with the dynamic behavior of spur gears and showed that neglecting dynamic loads and inertial effects would lead to unrealistic solutions. The lubricated impact problem was solved numerically as well [46-49]. Wang et al. [49], for instance, provided some predictions of the film thickness under pure impact for line contacts. They conducted a dimensionless analysis using modified Hertzian parameters and solved the problem using Multigrid techniques [50]. Most of the presented work focused on the influence of dynamic effects on film thickness and pressure inside the contact. Only few were dedicated to quantify the dynamic characteristics of EHL contact, i.e. stiffness and damping. For instance, Wijnant [51] proposed some fitted relations of the stiffness and damping in both circular and elliptical contacts in order to investigate the influence of the lubrication of the dynamic behavior of ball bearings [52]. Other contributions to this topic can as well be underlined as the work of Sarangi et al. [53, 54] and Hooke et al [55].

1.2 Multigrid and Multi-integration techniques

As stated earlier in this chapter, the simplest form of the EHL problem consists of a system of nonlinear integrodifferential equations, i.e. the Reynolds and deformation equations. Therefore, efficient numerical methods are needed to obtain fast and accurate solutions even when additional complex features are considered. Standard iterative methods such as Jacobi and Gauss-Seidel relaxation, converge slowly when applied to partial differential problems despite their good error smoothing properties [50]. The convergence is accelerated when the smooth error is solved on a coarser grid, which is the principle of multi-grid method. More details on the method and its principle are found in [50]. The method was first developed and proved to be efficient by Brandt [14, 56] in the mid 70's. Multi-grid was applied first to elastohydrodynamic lubrication by Lubrecht et al. [57-59] to calculate film thickness and pressure profiles in line and point contacts. Brandt and Lubrecht [60] developed later the multilevel multi-integration technique to reduce the complexity of the integration of the elastic deformation which dominated calculation times. Using the proposed technique, Venner [61] presented a stable algorithm for line and point contact problem of a much reduced complexity

Cette thèse est accessible à l'adresse : http://theses.insa-lyon.fr/publication/2016LYSEI089/these.pdf
© [M. Ankouni], [2016], INSA Lyon, tous droits réservés

compared to conventional algorithms. The emergence of those efficient numerical methods boosted the evolution of the numerical work in the EHL field as presented in the previous review. The basic principles of multi-grid and multi-integration methods are highlighted hereinafter.

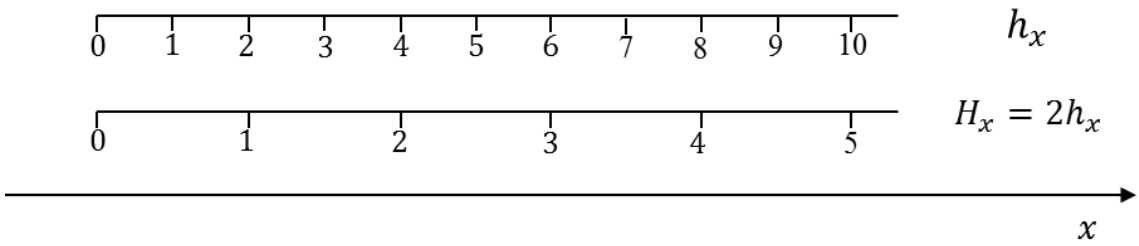

Figure 1.2: Fine grid with mesh size h_x and coarse grid with mesh size $H_x = 2h_x$ for a one dimensional problem.

The simplest form of a multigrid algorithm considers two grids, the target grid on which the problem is solved and an auxiliary grid coarser by a factor of 2 to solve the smooth error. Figure 1.2 shows a standard coarsening for a one dimensional problem, with two equidistant grid having a mesh size h_x (fine grid) and $H_x = 2h_x$ (coarse grid) respectively.

Therefore the equations are discretized on the grid points $x_I^{H_x} = x_{i=2I}^{h_x}$. Standard discretization and uniform grids are suitable for the EHL problem considered in the present work. However, for some problems of fluid dynamics, a different kind of discretization on the cells of the grid is used. Furthermore, a local grid refinement technique can be efficiently implemented into a multigrid algorithm [62] when some local effects are to be studied more precisely.

1.2.1 Full Approximation Scheme

There are two different ways of implementing a Multigrid process. The simplest scheme is the 'Correction Scheme' (CS) and is only applicable to linear equations. The 'Full Approximation Scheme' (FAS) is suited for both linear and non-linear equations, thus, compatible with the EHL problem. The FAS is described in this section. A differential equation generally reads:

$$L\langle u\rangle = f \tag{1.3}$$

with L a differential operator dependent on u and applied on u.

A discretized form of the equation is as follows:

$$L^h\langle u^h\rangle = f^h \tag{1.4}$$

Cette thèse est accessible à l'adresse : http://theses.insa-lyon.fr/publication/2016LYSEI089/these.pdf
© [M. Ankouni], [2016], INSA Lyon, tous droits réservés

Based on an approximate solution $\tilde{u}^h$ obtained after few relaxation on the finer grid, the residual of the equation is defined as:

$$r^h = f^h - L^h\langle\tilde{u}^h\rangle \tag{1.5}$$

Introducing the error vector $v^h = u^h - \tilde{u}^h$ in equation (1.5), one obtains:

$$r^h = f^h - L^h\langle u^h - v^h\rangle \tag{1.6}$$

For nonlinear equations, the error can't be treated separately from the solution. To approximate the error on the coarse grid, equation (1.5) as well as the definition of the error are substituted in equation (1.4):

$$L^h\langle\tilde{u}^h + v^h\rangle = L^h\langle\tilde{u}^h\rangle + r^h \tag{1.7}$$

The obtained approximate solution is then transferred to the coarser grid for correction. The coarse grid discrete problem is written as follows:

$$L^H\langle u^H\rangle \; = \; f^H \tag{1.8}$$

with:

$$u^H = I_h^H(\tilde{u}^h + v^h) = I_h^H\tilde{u}^h + v^H \tag{1.9}$$

and

$$f^H = L^H\langle I_h^H\tilde{u}^h\rangle + I_h^H r^h \tag{1.10}$$

where I_h^H is a restriction operator from the fine to the coarse grid.

A number of relaxations are performed on the coarse grid to obtain a good approximation of the coarse grid variable, then the approximate solution on the fine grid $\tilde{u}^h$ is corrected as follows:

$$\bar{u}^h = \tilde{u}^h + I_H^h(\tilde{u}^H - I_h^H\tilde{u}^h) \tag{1.11}$$

where I_H^h is an interpolation operator from coarser to finer grid.

Generally more than two grids are used and the fine grid solution is corrected using coarser grids, considering the above equations recursively.

Cette thèse est accessible à l'adresse : http://theses.insa-lyon.fr/publication/2016LYSEI089/these.pdf
© [M. Ankouni], [2016], INSA Lyon, tous droits réservés

1.2.2 Intergrid transfers

Some essential steps of the FAS scheme are the transfers between the fine and the coarse grid, i.e. the restriction of residuals from fine to coarse grid and the interpolation of the correction from the coarse to the fine grid. Both steps are highlighted.

a. Restriction

Restriction aims at representing residuals on coarser grid from the know residuals on fine grid (via operator I_h^H). The simplest way is to simply 'inject' the fine grid quantity to the coarse grid. This type of restriction is referred to as injection. The value in the coarse grid point is taken as the value of the coinciding fine grid point.

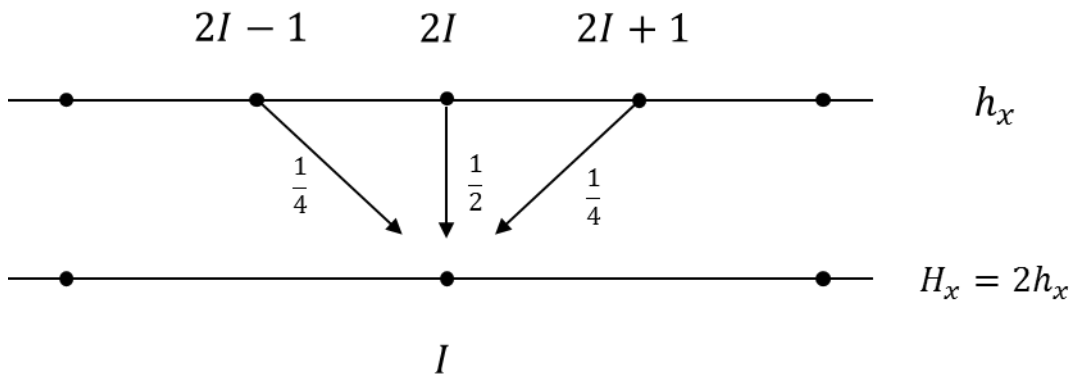

Figure 1.3: Restriction from fine grid by full weighting for a one dimensional problem.

A more sophisticated operation is used, that provide a more rich approximation of the smooth part of the fine grid function. This operation is known as full weighting. The value on the coarse grid is a weighted average of the value in the coinciding fine grid point and its two neighbors as in Figure 1.3 (one dimensional problem). Both types of restriction can be considered depending of the nature of the considered problem.

b. Interpolation

The interpolation is the operation that transfers the correction from the coarse to the fine grid (via operator I_H^h). Interpolation implies that the value of a fine grid point is determined by interpolation form from the values of a group of coarse grid points in its neighborhood. For a one dimensional problem, as in Figure 1.4, the representation of the correction on both grids are related as:

$$v_{2I}^h = v_I^H \quad 0 \leq I \leq n/2$$

Cette thèse est accessible à l'adresse : http://theses.insa-lyon.fr/publication/2016LYSEI089/these.pdf
© [M. Ankouni], [2016], INSA Lyon, tous droits réservés

$$v_{2I+1}^{h} = (v_I^H + v_{I+1}^H)/2 \quad 0 \leq I < n/2 \tag{1.12}$$

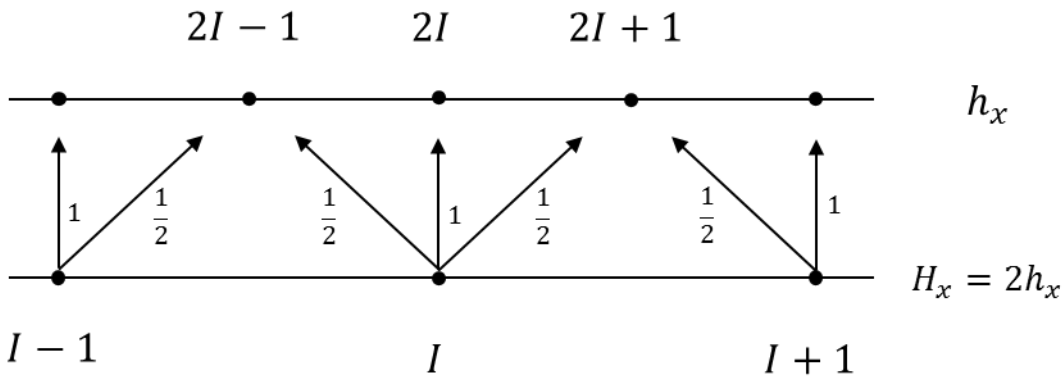

Figure 1.4: Linear interpolation from coarse to fine grid for a one dimensional problem.

1.2.3 Full Multigrid algorithms

Normally, a single coarse grid is not sufficient to approximate and reduce the smooth error of the solution on the fine grid, thus coarser grids are used and the procedure is repeated recursively to obtain the most efficient reduction of the error with the least number of relaxations. A Multi-Level Cycle (MLC) algorithm is thus considered, which consists in a coarse grid correction cycle with multiple grids. A recursive Multi-Level Cycle algorithm performed using k grids (levels) is presented as follows:

If $k > 1$

- ν_1 relaxations are performed on level k
- Restriction of the residual from level k to level $k-1$ (FAS, equations (1.9,1.10))
- γ Multi-Level Cycle using $k-1$ levels
- Interpolation of the correction from level $k-1$ to level k (FAS, equation (1.11))
- ν_2 relaxations are performed on level k

Else

- ν_0 relaxations are performed on the coarsest level

Cette thèse est accessible à l'adresse : http://theses.insa-lyon.fr/publication/2016LYSEI089/these.pdf
© [M. Ankouni], [2016], INSA Lyon, tous droits réservés

ν_0, ν_1, ν_2 represents the number of relaxations performed on each level and on the coarsest level. γ determines the number of correction cycles used on each level. A Multi-Level Cycle performed using 4 levels with $\gamma = 1$ is illustrated in Figure 1.5, each level is indicated by a circle with the number of relaxations inside. Due to its shape, it is known as a V-cycle. If more accuracy is needed, more work is performed on coarser grids and γ is set to 2, the obtained algorithm is referred to as a W-cycle.

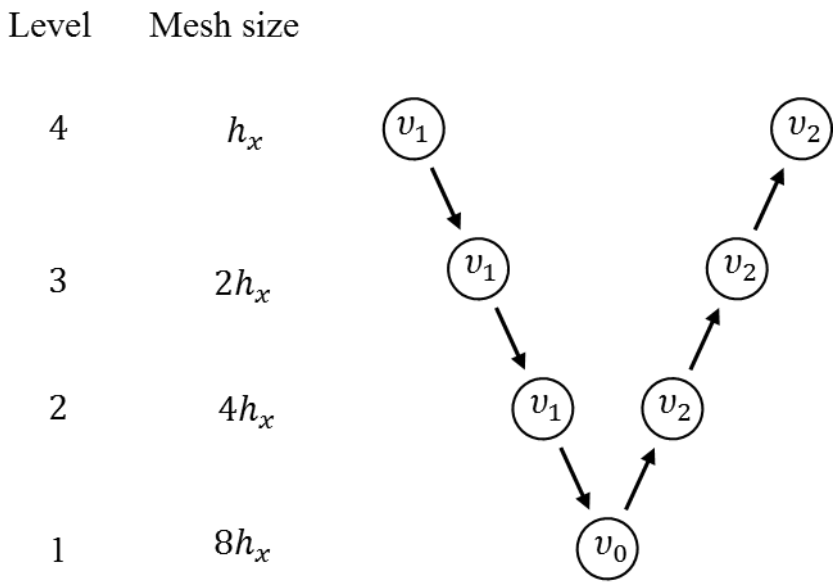

Figure 1.5: An example of a Multi-Level Cycle ($\gamma = 1$). $V(\nu_1, \nu_2)$ cycle.

The basic idea behind introducing the coarser grids is to accelerate the convergence of the solution, however coarse grid might serve to generate an accurate first approximation of the solution on the finest grid. The resulting process is the so-called Full Multi-Grid (FMG), which is an extended version of the recursive coarse grid correction cycle described as follows (k levels):

If $k > 1$

- Full Multi-Grid using $k - 1$ levels
- Interpolation of the approximation from level $k - 1$ to level k (operator I_{k-1}^{k})
- γ Multi-Level Cycle using k levels

Else

Cette thèse est accessible à l'adresse : http://theses.insa-lyon.fr/publication/2016LYSEI089/these.pdf
© [M. Ankouni], [2016], INSA Lyon, tous droits réservés

- ν_0 relaxations are performed on the coarsest level

Figure 1.6 illustrates a Full Multi-grid algorithm performed using 4 levels with one V-cycle. Double circles refer to the converged solution at the considered level.

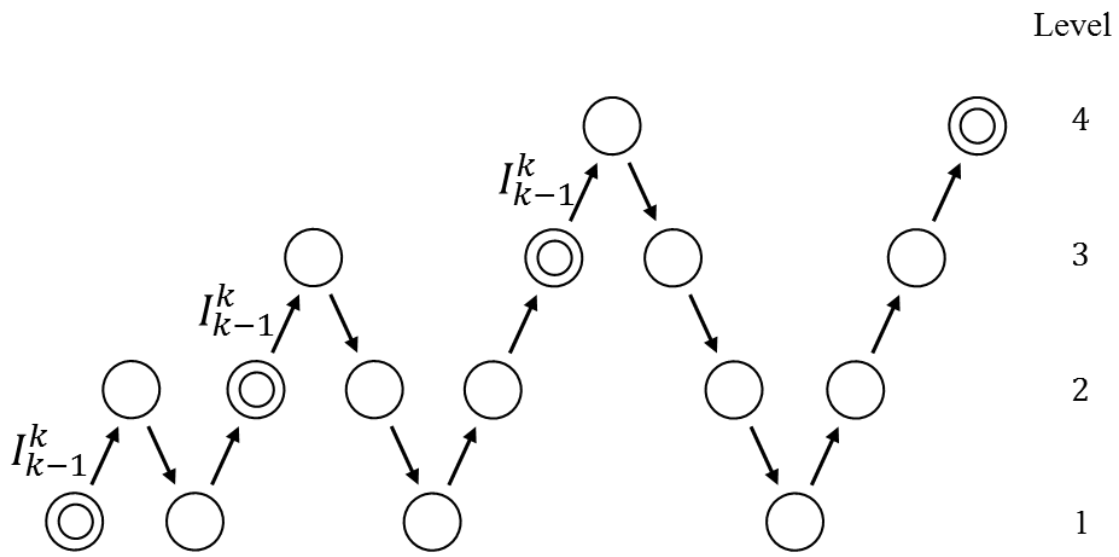

Figure 1.6: A FMG algorithm with one V cycle.

1.2.4 Multilevel multi-integration

The weak point of the Full Multi-Grid algorithm as presented here remains the time consuming calculation of the integral of the elastic deformation. The complexity of this task is reduced by mean of the multilevel multi-integration technique, presented briefly in this section. Multi-integration refers to the calculation of integral transforms (Multi-integral) as the following:

$$\omega(x) = \int_{\Omega} K(x,y)u(y)dy\,, \quad x \in \Omega \tag{1.13}$$

given the function u.

Discretized on a uniform grid of a mesh size h with n points, the integral reads:

$$\omega_i^h = h^n \sum_j K_{i,j}^{h,h} u_j^h \tag{1.14}$$

where $K_{i,j}^{h,h} = K(x_i, y_j)$, and the subscript i refers to each point of the grid.

Cette thèse est accessible à l'adresse : http://theses.insa-lyon.fr/publication/2016LYSEI089/these.pdf
© [M. Ankouni], [2016], INSA Lyon, tous droits réservés

Hence, one deals with an integral over all points i of the domain Ω, and to be calculated in all points of Ω, which would require a huge computational time ($O(n^2)$ operations) if evaluated on a single grid with classic summation. However, when calculated using multilevel multi-integration technique, it requires an optimal number of operations ($O(n \ln n)$) [50]. The basic idea of this technique is to benefit from the smoothness of the kernel K and to compute the value of the integral on the coarsest grid using less points and thus less computing time is needed. The solution (function u) is defined on the finest grid and transferred to coarser grid (anterpolation), then a coarse grid summation is performed followed by an interpolation of the calculated integral from coarser to finer grid. Additional attention is needed in case of singular kernels. All details on the development of the method and its implementation in the Full Multi-grid algorithm are found in [50].

1.3 Gear Dynamics

The main sources of noise and vibration in a geared transmission are highlighted in the current section along with the basic principles of gear dynamics. A brief overview of the progress in the study of gear dynamics is presented. A special focus is placed on the contributions to the problem of damping.

1.3.1 Noise and vibration in geared transmission

The various excitations found in geared transmissions are separated into internal and external excitations. Internal excitations are mainly related to the mating gear teeth via i) the mesh stiffness fluctuations, and ii) the diverse geometric imperfections and mounting errors. They result in a deviation of the transmitted load and the motion transfer between the two gears, commonly known as gear transmission error which represent a basic parameter used to judge the overall quality of a gear set. External excitations are basically related to the fluctuation in the input and output torque and equally the variation of the imposed speed of rotation. The emphasis is placed on internal sources of noise and vibration generally more complicated to analyze than external excitations.

a. Mesh stiffness variation

The stiffness of the pinion-gear link (mesh stiffness) is a key factor in the study of gear dynamics, it is actually representative of the gear teeth elasticity and its deformation when loaded. The computation of a mesh stiffness related to a teeth pair combines i) a local

Cette thèse est accessible à l'adresse : http://theses.insa-lyon.fr/publication/2016LYSEI089/these.pdf
© [M. Ankouni], [2016], INSA Lyon, tous droits réservés

contribution related to the contact between the teeth, and ii) a more global contribution associated to the tooth bending and its connection to the gear body. Some analytical formulations of the mesh stiffness are found in literature and are briefly exposed afterward. The local and global contributions are treated separately.

i. Contact stiffness

The classic way to compute the contact deformation assimilates the contact between the mating teeth to the contact between two semi-infinite plane subjected to a normal Hertzian pressure. A 2D formulation of the contact deformation is provided by Weber et al. [63, 64] as follows:

$$\delta_c = 4\frac{F}{b}\frac{1-\nu^2}{\pi E}\left[\ln\frac{2\sqrt{k_1 k_2}}{a} - \frac{\nu}{2(1-\nu)}\right] \tag{1.15}$$

with:

F/b : the force per unit face width

$k_{1,2}$: the distances between the point of contact and the tooth center line, on the pinion and gear respectively (Figure 1.7).

a: the half width of contact zone.

E, ν: the Young's modulus and the Poisson's ratio.

A more complete formulation of the contact deflection combine the analytical formula of Lundberg [65] with the approximate Hertzian approach originally used at Hamilton Standard [66] and the semi-empirical formula provided by Palmgren for rollers [67].

ii. Tooth bending stiffness

In order to compute the tooth bending deformations, the tooth is modeled as a cantilever of variable cross section. The strain energy of the tooth subjected to a concentrated load is then equated to the work of the corresponding imposed load. The most commonly used formula for bending displacements is provided by Weber and Banaschek [64] as follows:

$$\delta_b = \frac{F}{b}\frac{1}{E}\cos^2\alpha_u\left[10.92\int_0^{u_w}\frac{(u_w-y)^2}{d(y)^3}dy + 3.1(1+0.294\tan^2\alpha_u)\int_0^{u_w}\frac{1}{d(y)}dy\right] \tag{1.16}$$

with α_u the pressure angle and the other parameters are defined as in Figure 1.7.

Cette thèse est accessible à l'adresse : http://theses.insa-lyon.fr/publication/2016LYSEI089/these.pdf
© [M. Ankouni], [2016], INSA Lyon, tous droits réservés

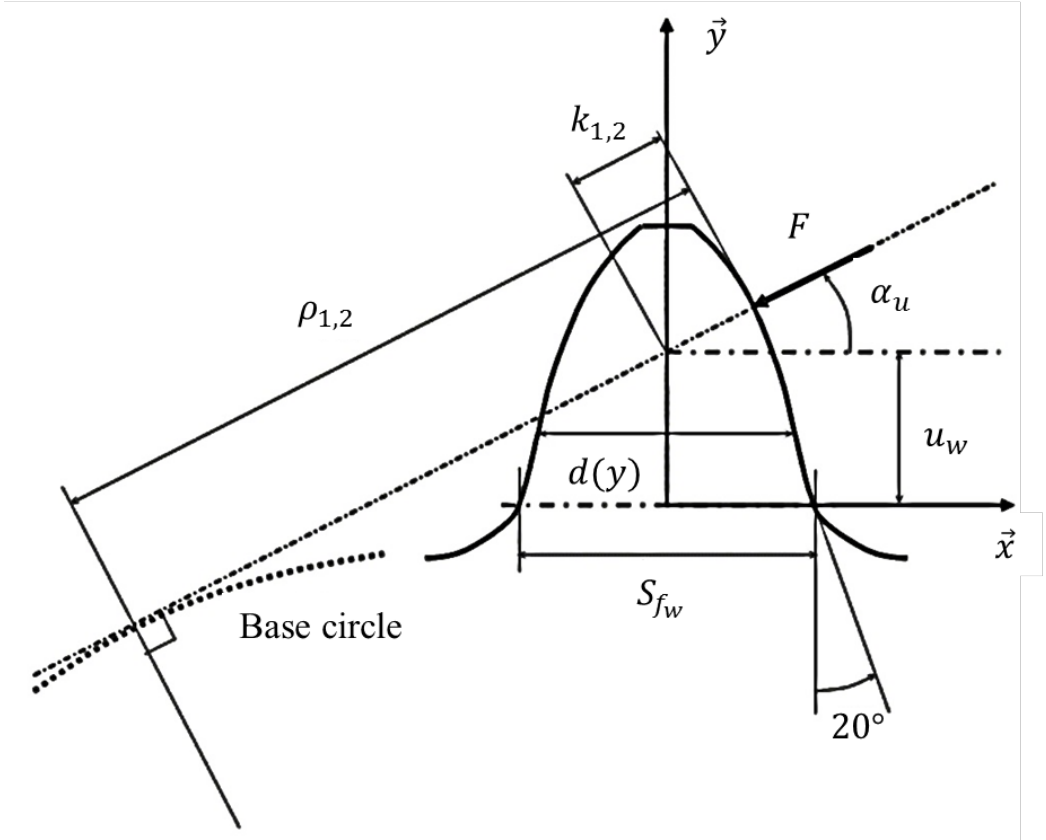

Figure 1.7: Parameters for Weber's formulae.

iii. Gear body contribution

The previous formulation considers a rigid connection between the tooth and the gear body. In order to take into account the gear body elasticity, the tooth is supposed to be rigid and the gear body is assimilated to a semi-infinite elastic plane subjected to normal and tangential forces as well as to bending moments. Assuming a linear distribution of normal stress and a constant shear stress at the tooth root, the displacement in the direction of the tooth load can be estimated under the form:

$$\delta_{f_w} = \frac{F}{b}\frac{1}{E}\cos^2\alpha_u\left[L\left(\frac{u_w}{S_{f_w}}\right)^2 + M\left(\frac{u_w}{S_{f_w}}\right) + P(1 + Q\tan^2\alpha_u)\right] \tag{1.17}$$

with:

S_{f_w}: the tooth thickness at the critical section (Figure 1.7).

L, M, P and Q: constants which differ depending on the authors [63, 66, 68].

Further developments of the previous formulations were brought by O'Donnell [69, 70], Attia [68] and Cornell [66]. Sainsot et al. [71] modeled the gear body as an elastic annulus instead of

Cette thèse est accessible à l'adresse : http://theses.insa-lyon.fr/publication/2016LYSEI089/these.pdf
© [M. Ankouni], [2016], INSA Lyon, tous droits réservés

a half-plane, and proposed a more accurate formulation of the base deflection. Numerical methods such as the finite element method, the boundary element method and finite differences have also been extensively used [72-74].

The above individual contributions are then superimposed in each point of contact and the total displacement is thus computed, resulting in a time-varying mesh stiffness that depends of the number of conjugate teeth pairs in contact during the convolute action (the contact length). Figure 1.8 shows two examples of mesh stiffness periodic evolution obtained using the aforementioned formulations for errorless spur and helical gear pairs.

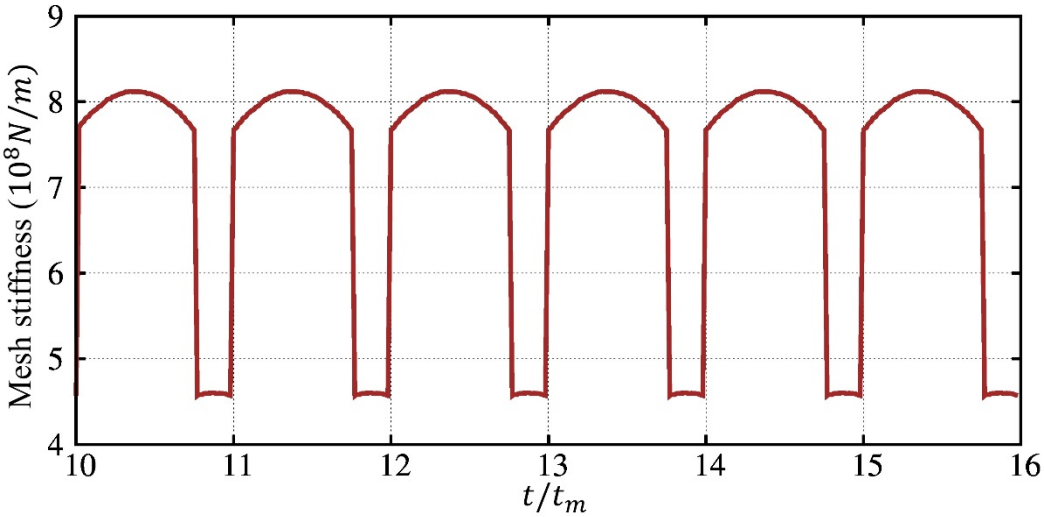

(a) Spur gear

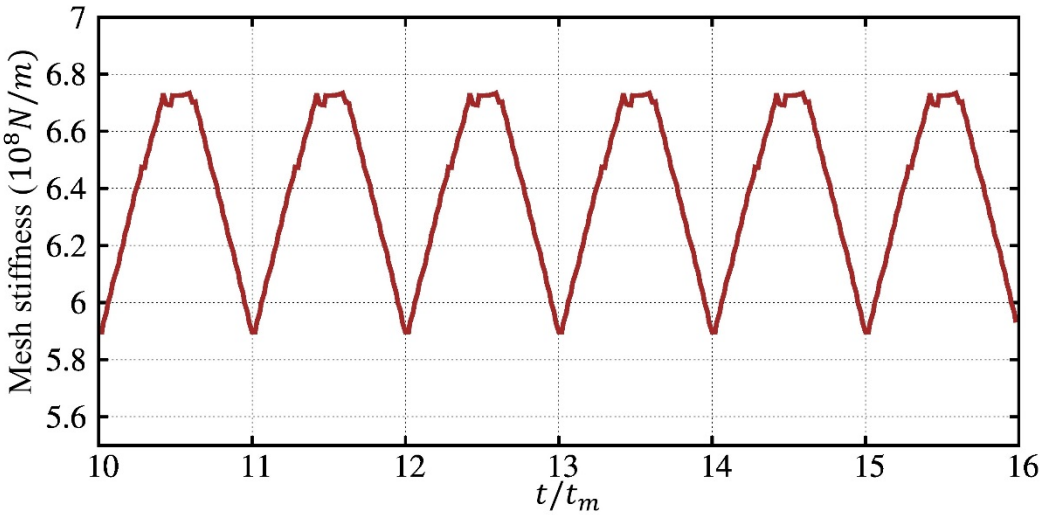

(b) Helical gear

Figure 1.8: Examples of time-varying gear mesh stiffness.

Cette thèse est accessible à l'adresse : http://theses.insa-lyon.fr/publication/2016LYSEI089/these.pdf
© [M. Ankouni], [2016], INSA Lyon, tous droits réservés

The figure illustrates the important effect of the gear type on the mesh stiffness variation, which tends to be smoother for helical gears. One can consequently state than even perfect gears can generate vibrations due to the elastic character of the mating gears resulting in these parametric excitations.

b. Tooth shape errors and mounting errors

The concept of perfect, errorless gears can hardly be representative of reality. Some unavoidable errors are indeed present to some extent in all gears. Tooth shape errors are basically due to the machining process including several inaccuracies, thermal distortions related to thermal treatment, etc. [75, 76]. The mounting errors are related to the assembly process of the different parts of the transmission. The presence of those imperfections and misalignments alters the motion transfer and may induce partial and total contact loss and thus gives rise to some undesirable vibrations.

Focusing on shape errors, on can separate i) pitch error, ii) tooth profile error and iii) lead error presented separately after.

i. Tooth profile errors

Tooth profile error basically illustrates the total deviation between the actual tooth profile and the theoretical involute curve, see Figure 1.9.

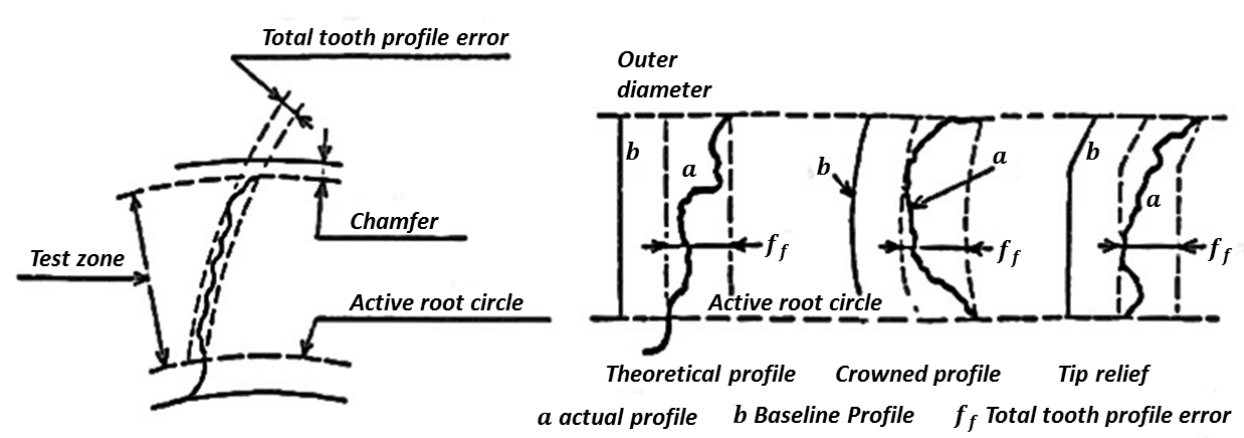

Figure 1.9: Tooth profile error [75].

ii. Pitch errors

Pitch error is defined as the difference between an actual measured pitch value and its theoretical value. One can distinguish i) individual pitch errors that illustrate the difference

Cette thèse est accessible à l'adresse : http://theses.insa-lyon.fr/publication/2016LYSEI089/these.pdf
© [M. Ankouni], [2016], INSA Lyon, tous droits réservés

between any adjacent tooth surfaces, ii) the pitch variation error that represents the actual pitch variation between two adjacent teeth and iii) the accumulated pitch error that cumulates the differences in pitch computed over any number of teeth.

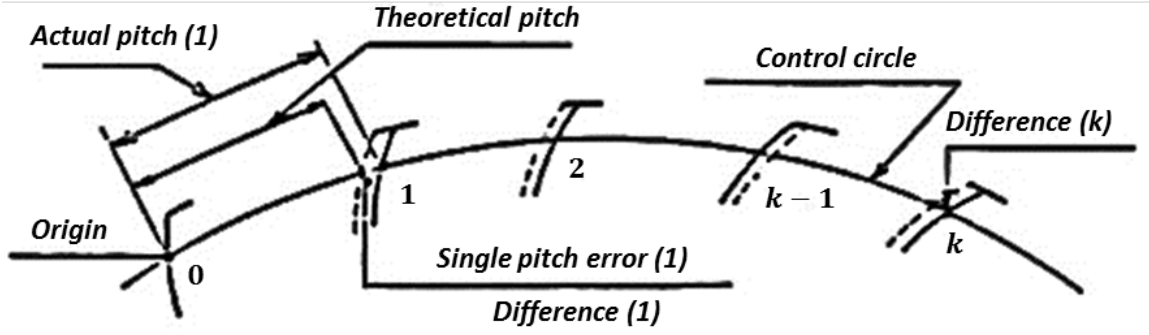

Figure 1.10: Single pitch error [75].

iii. Lead errors

Lead errors represent the deviations of the actual advance of the tooth profile from the ideal value or position, see Figure 1.11. Lead errors result in distorted flank traces on the base plane and are likely to deteriorate tooth contacts, particularly by concentrating contacts in certain areas. In addition to the previous shape errors, on can mention the effect of surface damage related generally to contact fatigue. This phenomenon results in superficial cracks and imperfections localized on some of the gear teeth and can thus affect the dynamic behavior of gears [77].

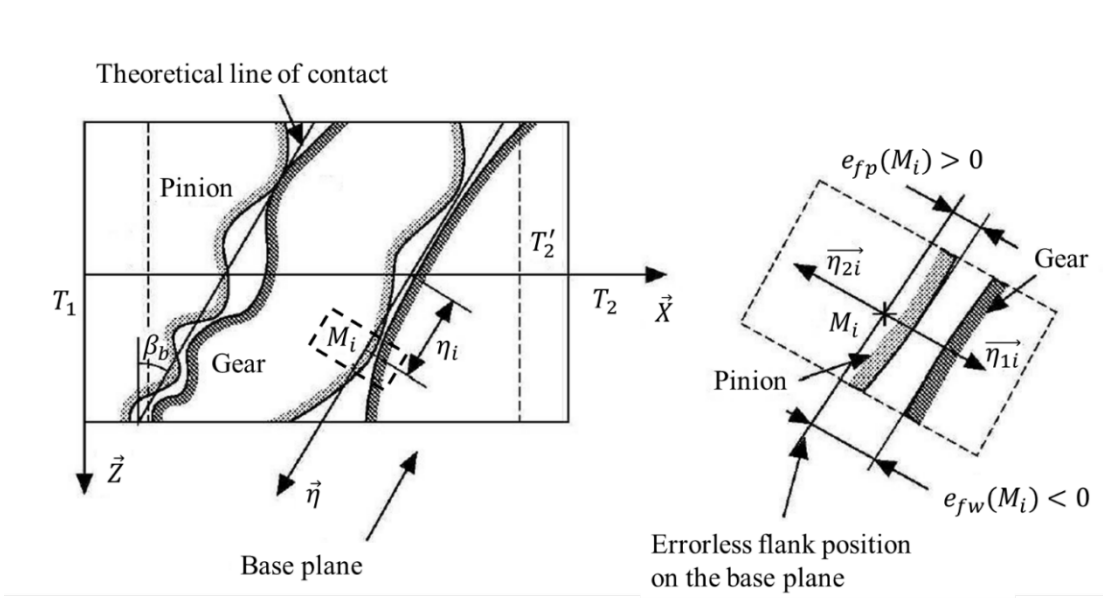

Figure 1.11: Examples of lead error traces on the base plane [78].

Cette thèse est accessible à l'adresse : http://theses.insa-lyon.fr/publication/2016LYSEI089/these.pdf
© [M. Ankouni], [2016], INSA Lyon, tous droits réservés

iv. Mounting errors

Mountings errors cannot always be avoided, and this can lead to i) misalignments, ii) run-out and iii) eccentricities. Misalignments illustrate the fact that the rotating shafts are not parallel, and can be produced during the assembly of the gears on the shafts or the assembly of the shafts itself on bearings. One can separate a) the shaft inclination that corresponds to a rotation of the shaft in the plane formed by the theoretical parallel shafts and b) the shaft deviation that corresponds to a rotation of the shaft in the normal plane to the plane formed by the two shafts (Figure 1.12).

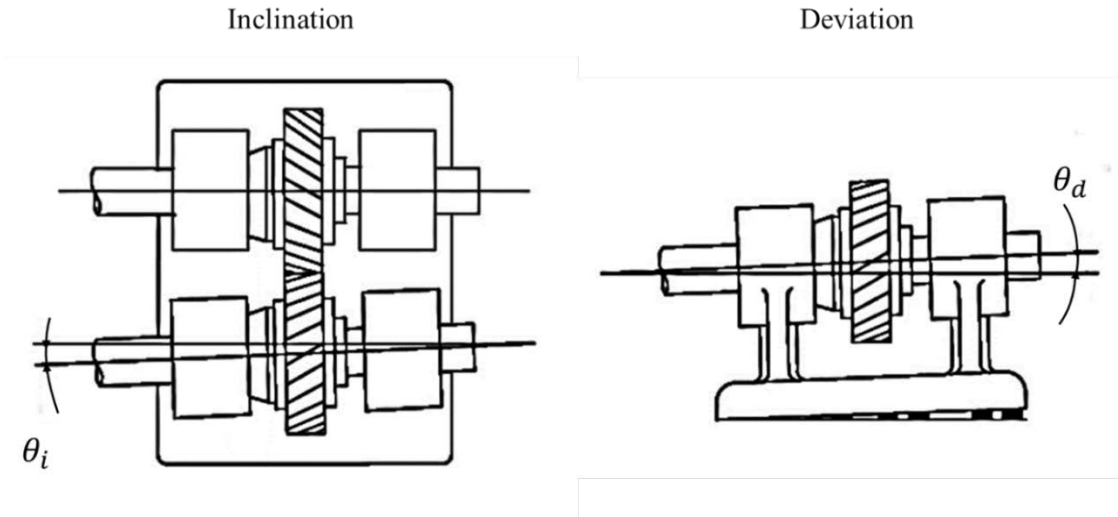

Figure 1.12: Shaft misalignments [79].

Umezawa et al. [79] studied, experimentally, the relation of misalignments with the dynamic behavior for different kinds of helical gears. The authors [79] underlined the clear effect of both types of misalignments on gear vibration. Run-out is the error in radial position of the teeth which can be measured by indicating the position of a pin or ball inserted in each tooth space around the gear and taking the largest difference. Eccentricities correspond to centers of rotation which do not coincide with the centers of the pinion and/or the gear. Eccentricities can therefore induce imbalance as presented by Sabot et al. [80].

c. Gear transmission error

Harris [81] introduced the concept of transmission error (*T.E.*) in relation to the study of gear dynamic tooth forces. Gear transmission error is defined as the deviation in the position of the driven gear (for any given position of the driving gear), relative to the position that the driven gear would occupy if both gears were geometrically perfect and rigid. *T.E.* is generally

Cette thèse est accessible à l'adresse : http://theses.insa-lyon.fr/publication/2016LYSEI089/these.pdf
© [M. Ankouni], [2016], INSA Lyon, tous droits réservés

expressed as an angular deviation computed on the driven gear nut also as a distance on the base plane [82].

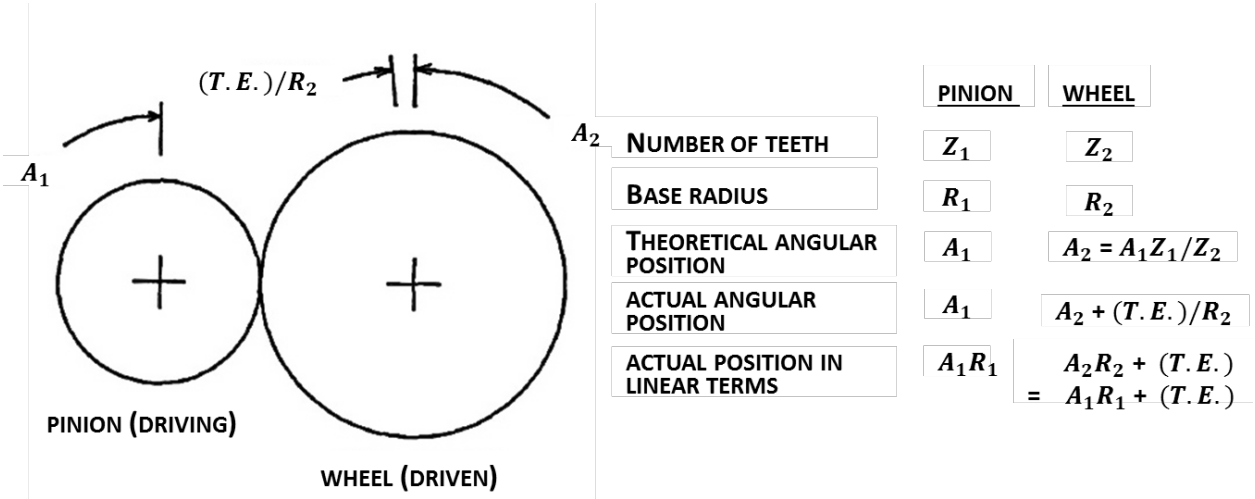

Figure 1.13: Transmission error definition [83].

Depending on operational conditions, one can separate i) the no-load transmission error (*NLTE*), ii) the quasi-static transmission error (*TEs*) and iii) the dynamic transmission error (*DTE*). The *NLTE* is measured on a gear pair rotating at low speed and transmitting zero load, it is actually representative of geometrical deviations related to machining defects and mounting errors. From a mathematical point of view, using the fact that the transmission error is null for perfect gears (no errors), the *NLTE* (projected on the base plane) reads [78]:

$$NLTE = -\frac{E_{max}(t)}{\cos\beta_b} \tag{1.18}$$

where $E_{max}(t)$ represents the maximum of the equivalent normal deviations superimposed on the gear and pinion, and β_b is the helix angle.

Based on the same concept, the *TEs* combines the *NLTE* and the elastic deflections that results from the transmitted load as follows:

$$TEs = x + NLTE \tag{1.19}$$

where x is the displacement in the base plane related to the teeth deformation along with shafts and bearings displacements.

TEs is widely used to study the effect of tooth shape deviations (error and shape modifications) [84,85], furthermore it can be used as an indicator of the excitations and noise level in a transmission, capturing most of the mesh excitation (linear behavior) as demonstrated by Velex

Cette thèse est accessible à l'adresse : http://theses.insa-lyon.fr/publication/2016LYSEI089/these.pdf
© [M. Ankouni], [2016], INSA Lyon, tous droits réservés

et al. [86]. *TEs* is introduced directly as a source of excitation as well in several models [82,87].The dynamic transmission error *DTE* includes as well the inertial effects and provide a better insight on the vibrational behavior of the transmission including some nonlinear phenomena as contact loss. Various experimental procedures are considered to measure the transmission error using i) accelerometers [88], ii) optical methods [89] or iii) interferometric systems [90, 91].

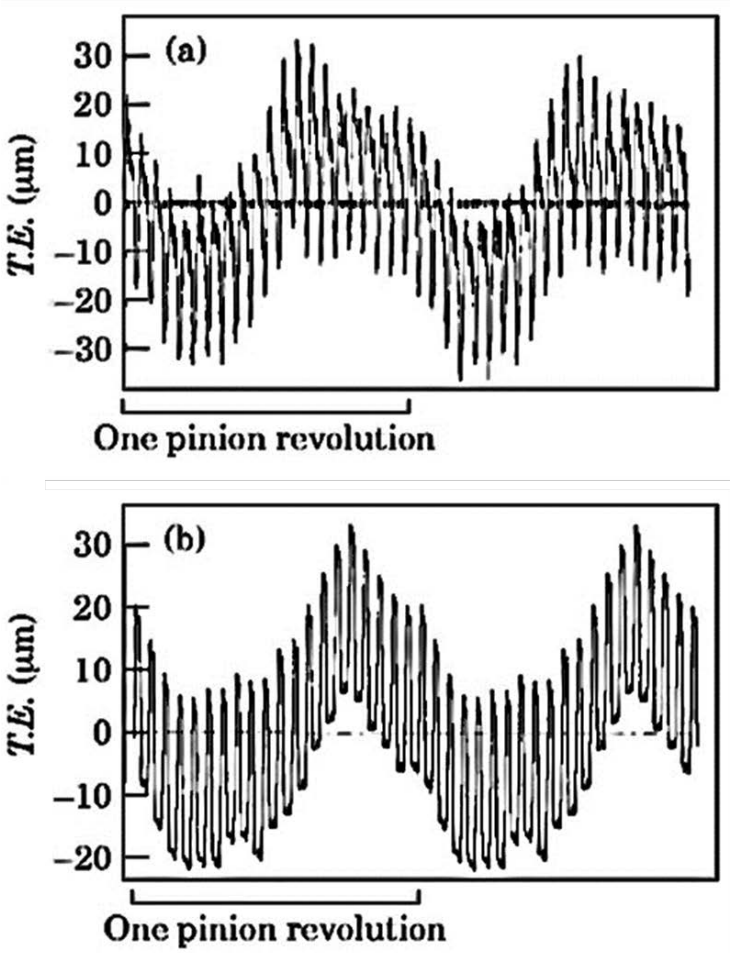

Figure 1.14: Quasi-static transmission errors. (a) experiments, (b) simulations [92].

Along with the transmission error, other parameters are used to illustrate the dynamic behavior of gears. The dynamic factor, for instance, is frequently used to describe the dynamic loading on gear teeth. It is defined as the ratio between the global dynamic transmitted load and the static load. The dynamic factor was initially computed through some empirical formulations [93, 94] considering spur gears without any contact loss. It was then investigated both experimentally and numerically by Houser and Seireg [95, 96] taking into account the mesh stiffness fluctuation, the inertial effects and geometric deviations for spur and helical gears. Moreover, Kubo [97] provided some valuable curves that serve as reference for models

Cette thèse est accessible à l'adresse : http://theses.insa-lyon.fr/publication/2016LYSEI089/these.pdf
© [M. Ankouni], [2016], INSA Lyon, tous droits réservés

validation. Furthermore, the notion of tooth root stress is also used to quantify the tooth loading [98]. This parameter is experimentally more easily reachable and can be computed using strain gauges placed at the root of several teeth and across the face width [98, 99].

1.3.2 Advances in gear dynamics study

The current section highlights the basic improvements in the study of geared transmissions in the last few decades from different viewpoint, i.e. experimental, analytical and numerical contributions. The first attempts date back more than half a century [81, 84, 93, 94], and aimed at understanding and quantifying the dynamic loading on gear teeth, mainly for spur gears. Since then, gear dynamics have been a major concern to respond to the increasingly complicated requirements and consequent constraints. This is illustrated by the vast literature extensively reviewed by Özgüven and Houser [82], Wang et al. [100] and Remond et al. [101] to name a few.

Several efforts were made to characterize experimentally the dynamic behavior of gears and thus provide a kind of reference for dynamic models developed later on. A large part of experimental work focused on spur gears [87, 90]. Measurements are made in terms of transmission errors, accelerations, tooth loads and tooth root stresses. Among others, Kahraman and Blankenship [88, 102, 103] performed benchmark measurements of dynamic transmission errors using a four-square test rig, and analyzed the effect of operating conditions and profile modifications on dynamic response for identical spur gear pairs. Umezawa et al. [79] studied the effect of misalignments and contact ratio on helical gears vibration. Moreover, Baud and Velex [99] investigated quasi-static and dynamic stresses at the root of spur and helical teeth on a geared rotor system. Multi-mesh geared transmissions were considered as well [104, 105]. Experimental data remain however rather sparse compared to theoretical and numerical developments.

A primary concern in the modeling of a geared transmission is the realistic description of the contact between the mating gears, i.e. the mesh stiffness fluctuation that presents one of the major sources of noise and vibration. From this point of view, one can distinguish i) models with constant mesh stiffness [87], ii) models with time-varying mesh stiffness [82] and iii) models with nonlinear mesh stiffness and more accurate description of the teeth contact [100]. The first type of models is basically suitable for modal analyses as in [106]. The mesh related excitations are introduced via the quasi-static transmission error. Though it provides exact solutions, this type of modeling lack a real description of the teeth contact problem. The first

Cette thèse est accessible à l'adresse : http://theses.insa-lyon.fr/publication/2016LYSEI089/these.pdf
© [M. Ankouni], [2016], INSA Lyon, tous droits réservés

models to consider time-varying stiffness were purely torsional [107]. Periodic mesh stiffness function that accounts for the variable number of teeth pairs in contact (step functions for spur gears and trapezoidal functions for helical gears) are basically introduced to illustrate the mesh. Such models served to analyze gears instability phenomenon [108], to study dynamic loading on gears for single [108] and multistage gear trains [109, 110] as well as planetary and epicyclic gears [111]. Nevertheless, the previous approaches are highly approximate omitting the great dependence of mesh stiffness on instantaneous contact conditions between active flanks along with possible contact losses and shocks encountered basically when using spur gears [112]. In this context, Velex and Maatar [92] proposed an original procedure which treats the equations of motions and the contact problem between mating flanks simultaneously. The problem is solved using a time-step numerical scheme [113] combined with a unilateral normal contact algorithm [114] which updates the mesh stiffness depending on contact conditions. Mesh stiffness is thus no more considered as an input of the problem, but a consequence of the instant behavior of the system. The transmission error is seen as a solution of the problem as well and not an imposed excitation as previously. The proposed method was then extended to deal with various types of gears and increasingly complex features. One can cite the work of Ajmi and Velex [115] which focused on wide-faced gears, Bettaïeb et al. [116] which proposed a hybrid approach that combines elastic foundations for tooth contact and substructures derived from three-dimensional finite element grids for thin-rimmed gears and their supporting shafts, Abousleiman and Velex [117] a hybrid model that accounts for ring-gear deflections to simulate quasi-static and dynamic behavior of planetary/epicyclic gear.

Furthermore, several models tempted to couple the gear elements with the surrounding elements, i.e. the supporting shafts and bearings that have essential effect on the dynamic performance of the transmission. Velex [107], for instance, attempted to model shaft elements using beam finite elements coupled with a spring-mass mesh model. Three dimensional finite elements were used as well to model shaft elements [118]. Focusing on bearings, Lahmar and Velex [119] proposed a model that treats simultaneously the contact conditions in gears and rolling element bearings. The bearings contribution is thus introduced as a time-varying, non-linear external force. They underlined the significant interaction between gears and bearing dynamic response. More recently, Abbes et al. [120] studied the effect of ball bearing waviness on the dynamic response of helical gears. Many models of varied complexity included journal bearings in geared transmission simulations. Kahraman et al. [121] combined a spring-damper configuration of the mesh with a bearing model using some classic dynamic coefficients. Later,

Cette thèse est accessible à l'adresse : http://theses.insa-lyon.fr/publication/2016LYSEI089/these.pdf
© [M. Ankouni], [2016], INSA Lyon, tous droits réservés

Theodossiades et al. [122] included a nonlinear short journal bearing model. Baud and Velex [98] worked somehow conversely, they coupled an accurate description of the gear teeth contact with a simple bearing configuration using dynamic coefficients. More recently, Baguet et al. [123, 124] proposed dynamic models that consider simultaneous solutions of the equations of motion, tooth contact conditions, and the isothermal Reynolds equation for short or finite length bearings. In the continuity of their work, Fargère and Velex [125-126] introduced a nonlinear modeling of gear mesh and journal bearings based on a direct solution of the Reynolds equation, including thermal effects and lubricant injection mode and circulation. They showed that bearing clearances and elastic coupling can largely influence static and dynamic tooth loading.

1.3.3 The problem of damping

In the conclusion of their seminal paper on gear dynamics, Gregory et al. [84] highlighted the paramount importance of damping on dynamic loading and the urgent need for further research into the mechanism of damping in mechanical transmissions. Damping does not only control the amplifications at critical speeds but has also a great influence on the transmission stability. Damping tends to eliminate or reduce the instability zones as proven by Velex [108], among others. More than 50 years later, and even if a large number of dynamic models have been proposed as shown earlier, the literature on the specific topic of gear damping mechanisms has remained sparse [127]. Most of the time, constant or time varying damping factors [128] are employed which can be estimated from experimental results but can hardly be generalized to any gear geometry and operating conditions. Considering a transmission model of N degree to freedom, the resulting equations of motions read:

$$[M]\ddot{X} + [C]\dot{X} + [K]X = F \tag{1.20}$$

Two classical procedures are most commonly employed when damping is assumed to be constant: i) damping is assumed to be proportional to the mass or/and the stiffness matrices (Rayleigh's damping [129]) which leads to the following damping matrix $[C] = a[M] + b[K]$, where a and b are two constants to be adjusted from experimental results, ii) a limited number of modal damping factors ζ_p is used, the damping matrix is supposed to be orthogonal with respect to the mode-shapes of the undamped system with averaged stiffness matrix which leads to a diagonal modal damping matrix $[C_\phi] = diag\left(2\zeta_p\sqrt{k_{\phi_p}m_{\phi_p}}\right), p = 1, N$, where k_{ϕ_p}, m_{ϕ_p} are respectively the modal stiffness and mass associated with mode P. The damping matrix $[C]$ is then deduced through i) a change of basis operation which implies that all the modes have

Cette thèse est accessible à l'adresse : http://theses.insa-lyon.fr/publication/2016LYSEI089/these.pdf
© [M. Ankouni], [2016], INSA Lyon, tous droits réservés

been calculated, or ii) by performing a truncated summation on a limited number of modes following Craig [130]. Here again, ζ_p is either estimated or measured to fit experimental evidence. Regardless of the method used, the proposed damping is unlikely to properly represent the dissipation mechanisms in a geared transmission.

In the last decade, some valuable contributions to the damping modeling in gears were published. [131-133] introduced the modeling of lubricant related damping in the analysis of gear rattle phenomena. Some analytical expressions of the hydrodynamic force acting on the tooth flanks were developed to account for the effect of the lubricant on the vibration, under isoviscous hydrodynamic conditions. More recently, Li and Kahraman [134] proposed a gear damping model by combining a mixed EHL model of a spur gear with a torsional dynamic model, thus accounting for a variety of contact conditions such as speed, load and lubricant temperature. Later, the authors extended their modeling strategy to study the combination of transverse and torsional degrees of freedom using a tribo-dynamic model [135]. Based on a similar approach, Guilbault et al. [136] considered a combination of simplified models to simulate the lubricant squeeze damping along with tooth hysteresis and the contributions of the elements surrounding the pinion-gear system. Finally, Liu et al. [137] recently characterized analytically damping and stiffness in lightly loaded gears for vibro-impact regimes at different speeds and lubricant temperatures. The previous efforts showed the interest and the feasibility of a realistic modeling of the damping mechanism in gears and thus inspired the present investigations.

1.4 Conclusion

Based on the previous survey, one can state that the fields of lubrication and gear dynamics have both evolved enormously, stimulated by the huge growth of computing capacities, the emergence of powerful numerical techniques and obviously the development of more accurate experimental devices. Furthermore, damping is proven to be a key factor in controlling the stability and the dynamic behavior of any geared system. Nevertheless, only few efforts were made to quantify the dissipation in such systems and to improve the modeling of the active sources of damping. This is mainly due to the diversity of the sources of dissipation in a complex system and to the lack in the information on dissipative properties of materials. In this context, the present work seeks to make a first constructive attempt to provide some realistic formulations of the damping found in geared transmissions, and more precisely due to

Cette thèse est accessible à l'adresse : http://theses.insa-lyon.fr/publication/2016LYSEI089/these.pdf
© [M. Ankouni], [2016], INSA Lyon, tous droits réservés

lubricated contacts, that could be generalized to different types of gears and transmissions, and bring a deeper understanding of the damping mechanisms in a geared transmissions.

Cette thèse est accessible à l'adresse : http://theses.insa-lyon.fr/publication/2016LYSEI089/these.pdf
© [M. Ankouni], [2016], INSA Lyon, tous droits réservés

Chapter 2

Modeling of damping in lubricated line contacts

The current research focuses on quantifying the damping related to the lubrication of rotating gears. The lubricant film separating the mating teeth can indeed dissipate energy by squeeze effect in the normal direction and in the tangential direction. In this chapter, emphasis is placed on the modeling of the normal contributions of the lubricant, i.e. acting in the direction of the line of action, to the total system damping. An EHL transient analysis is considered to study the dynamic behavior of lubricated line contacts. Both cases of permanent contact conditions and contact losses and shocks encountered in gears are studied separately.

2.1 Permanent lubricated line contacts

2.1.1 Permanent contact model

Following the approach of Wijnant for ball bearings [51], this section is aimed at analyzing line EHL contacts under time-varying loads in order to provide a viscous damping formulation for a wide range of operating conditions. Assuming isothermal, fully flooded lubrication between the teeth, the Reynolds equation for permanent line contacts reads:

$$\frac{\partial}{\partial x}\left(\frac{\rho h^3}{12\eta}\frac{\partial p}{\partial x}\right) - \frac{\partial(u_m\ \rho h)}{\partial x} - \frac{\partial(\rho h)}{\partial t} = 0 \tag{2.1}$$

Approximating the shape of the two contacting surfaces by parabolas, the corresponding film thickness separating the two surfaces is given by:

$$h(x) = h_0 + \frac{x^2}{2R_x} - \frac{2}{\pi E'}\int_{-\infty}^{+\infty} p(x')\, ln\left(\frac{x-x'}{x_0}\right)^2 dx' \tag{2.2}$$

where x_0 is a reference distance at which deflection is taken to be zero.

Equating the total pressure force and the external load w_t, the force balance equation leads to:

$$\int_{-\infty}^{+\infty} p(x)dx = w_t \tag{2.3}$$

Cette thèse est accessible à l'adresse : http://theses.insa-lyon.fr/publication/2016LYSEI089/these.pdf
© [M. Ankouni], [2016], INSA Lyon, tous droits réservés

The lubricant rheology is characterized by the Roelands equation [3] for viscosity-pressure dependency as

$$\eta(p) = \eta_0 \exp\left((ln(\eta_0) + 9.67)\left(-1 + \left(1 + \frac{p}{p_0}\right)^z\right)\right) \tag{2.4}$$

where z is the pressure viscosity index and p_0 a constant.

along with the formula of Dowson and Higginson [4] for the density-pressure relation, i.e.

$$\rho(p) = \rho_0 \frac{5.9.10^8 + 1.34p}{5.9.10^8 + p} \tag{2.5}$$

In order to simulate the dynamic loading conditions in gears, a time-varying excitation force is imposed under the form:

$$w_t = w_0 + \mathrm{a}\sin(\omega t) \tag{2.6}$$

The Hertzian contact parameters are used to obtain the dimensionless system of equations to be solved, i.e., the dry contact half width b and the maximum Hertzian pressure p_h. The time-varying parameters are normalized with respect to their values at a reference point.

The set of dimensionless variables are:

$$X = x/b\,;$$

$$P = p/p_h\,;$$

$$H = hR_x/b^2;$$

$$T = t\,u_{ref}/b\,;$$

$$\bar{\rho} = \rho/\rho_0;$$

$$\bar{\eta} = \eta/\eta_0;$$

$$W_t = w(t)/w_{ref}\,;$$

$$R_t = R(t)/R_{ref};$$

$$U_{mt} = u_m(t)/u_{ref}$$

and the resulting system of dimensionless equations reads:

Cette thèse est accessible à l'adresse : http://theses.insa-lyon.fr/publication/2016LYSEI089/these.pdf
© [M. Ankouni], [2016], INSA Lyon, tous droits réservés

$$\frac{\partial}{\partial X}\left(\xi\frac{\partial P}{\partial X}\right) - U_{mt}\frac{\partial(\bar{\rho}H)}{\partial X} - \frac{\partial\bar{\rho}H}{\partial T} = 0 \tag{2.7}$$

$$H(X) = H_0 + \frac{X^2}{2R_t} - \frac{1}{2\pi}\int_{-\infty}^{+\infty} P(X')\, ln(X - X')^2 dX' \tag{2.8}$$

$$\int_{-\infty}^{+\infty} P(X)dX = \frac{\pi}{2}W_t \tag{2.9}$$

$$W_t = 1 + A\sin(\Omega T) \tag{2.10}$$

where ξ is defined as :

$$\xi = \frac{\bar{\rho}H^3}{\bar{\eta}\lambda} \qquad \text{where} \quad \lambda = \frac{12u_{ref}\eta_0 R_x^2}{b^3 p_h}$$

2.1.2 Discrete equations

The governing equations are discretized on a uniform grid with mesh size h covering a computational domain Ω ($X_a \leq X \leq X_b$), see Figure 2.1. The discrete solution at time step k at any point X_i of the grid is denoted $P_{i,k}^h$. Using finite differences, equation (2.7) is approximated in each interior point of the grid.

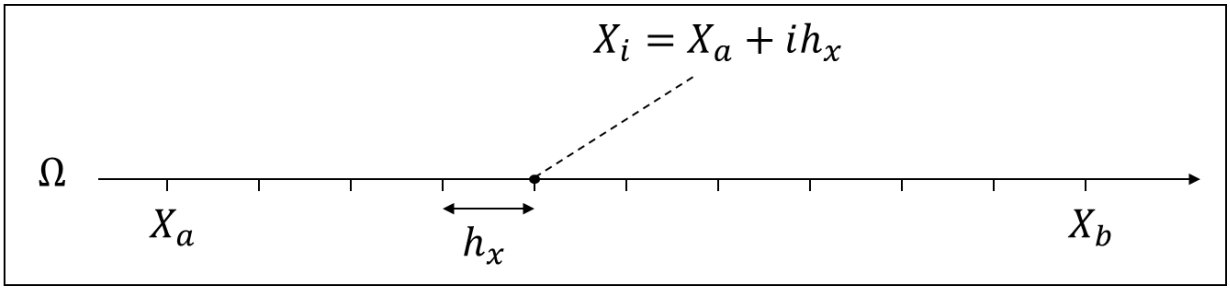

Figure 2.1: Discrete computational domain.

The outer differential $\partial/\partial X$ of the Poiseuille term is approximated using a short central second order discretization:

$$\left(\frac{\partial}{\partial X}\left(\xi\frac{\partial P}{\partial X}\right)\right)_{i,k} = \frac{\left(\xi\frac{\partial P}{\partial X}\right)_{i+1/2,k} - \left(\xi\frac{\partial P}{\partial X}\right)_{i-1/2,k}}{h_x} \tag{2.11}$$

Second, the inner derivatives are discretized as follows:

Cette thèse est accessible à l'adresse : http://theses.insa-lyon.fr/publication/2016LYSEI089/these.pdf
© [M. Ankouni], [2016], INSA Lyon, tous droits réservés

$$\left(\xi \frac{\partial P}{\partial X}\right)_{i+1/2,k} = \xi^h_{i+1/2,k} \frac{\left(P^h_{i+1,k} - P^h_{i,k}\right)}{h_x} \tag{2.12}$$

and

$$\left(\xi \frac{\partial P}{\partial X}\right)_{i-1/2,k} = \xi^h_{i-1/2,k} \frac{\left(P^h_{i,k} - P^h_{i-1,k}\right)}{h_x} \tag{2.13}$$

Combining these two steps, one obtains:

$$\left(\frac{\partial}{\partial X}\left(\xi \frac{\partial P}{\partial X}\right)\right)_{i,k} = \frac{\xi^h_{i-1/2,k} P^h_{i-1,k} - \left(\xi^h_{i+1/2,k} + \xi^h_{i-1/2,k}\right) P^h_{i,k} + \xi^h_{i+1/2,k} P^h_{i-1,k}}{h_x^2} \tag{2.14}$$

where $\xi^h_{i-1/2,k}$ and $\xi^h_{i+1/2,k}$ denote the parameter ξ at time-step k at some intermediate points $X_i - h_x/2$ and $X_i + h_x/2$ respectively, and are approximated as:

$$\xi^h_{i\pm1/2,k} = (\xi^h_{i,k} + \xi^h_{i\pm1,k})/2 \tag{2.15}$$

with

$$\xi^h_{i,k} = \frac{\bar{\rho}\left(P^h_{i,k}\right)\left(H^h_{i,k}\right)^3}{\bar{\eta}\left(P^h_{i,k}\right)\bar{\lambda}} \tag{2.16}$$

The wedge term and the squeeze term are approximated using a first order upstream discretization as follows:

$$\left(\frac{\partial(\bar{\rho}H)}{\partial X}\right)_{i,k} = \frac{\bar{\rho}^h_{i,k} H^h_{i,k} - \bar{\rho}^h_{i-1,k} H^h_{i-1,k}}{h_x} \tag{2.17}$$

$$\left(\frac{\partial(\bar{\rho}H)}{\partial T}\right)_{i,k} = \frac{\bar{\rho}^h_{i,k} H^h_{i,k} - \bar{\rho}^h_{i,k-1} H^h_{i,k-1}}{h_t} \tag{2.18}$$

leading to the discrete form of the equation (2.7):

$$\begin{aligned} &\frac{\xi^h_{i-1/2,k} P^h_{i-1,k} - \left(\xi^h_{i+1/2,k} + \xi^h_{i-1/2,k}\right) P^h_{i,k} + \xi^h_{i+1/2,k} P^h_{i-1,k}}{h_x^2} \\ &- U_{mt_k} \frac{\bar{\rho}^h_{i,k} H^h_{i,k} - \bar{\rho}^h_{i-1,k} H^h_{i-1,k}}{h_x} - \frac{\bar{\rho}^h_{i,k} H^h_{i,k} - \bar{\rho}^h_{i,k-1} H^h_{i,k-1}}{h_t} = 0 \end{aligned} \tag{2.19}$$

where $P^h_{i,k} = 0$ at the boundary, and $P^h_{i,k} \geq 0$ satisfying the cavitation condition at all points of the domain, the dimensionless time-step and the mesh size are chosen equal.

Cette thèse est accessible à l'adresse : http://theses.insa-lyon.fr/publication/2016LYSEI089/these.pdf
© [M. Ankouni], [2016], INSA Lyon, tous droits réservés

The film thickness equation (2.8) can be discretized as:

$$H_{i,k}^{h} = H_0 + \frac{X_i^2}{2R_{t_k}} - \frac{1}{\pi}\sum_j K_{i,j}^{hh} P_{i,k}^{h} \tag{2.20}$$

where the coefficients $K_{i,j}^{hh}$ can be computed as:

$$\begin{aligned} K_{i,j}^{hh} = &\left(X_i - X_j + \frac{h_x}{2}\right)\left(\ln\left|X_i - X_j + \frac{h_x}{2}\right| - 1\right) \\ &- \left(X_i - X_j - \frac{h_x}{2}\right)\left(\ln\left|X_i - X_j - \frac{h_x}{2}\right| - 1\right) \end{aligned} \tag{2.21}$$

Finally, the discrete force balance equation reads:

$$\sum_i P_{i,k}^{h} = \frac{\pi}{2} W_{t_k} \tag{2.22}$$

Because of the complexity of the Reynolds and deformation equations which are non-linear integro-differential equations, efficient numerical methods are needed. Multi-grid and multi-integration techniques briefly introduced in chapter 1 are used to solve the EHL problem and obtain fast and accurate solutions compatible with extensive parameter analyses.

2.1.3 Numerical results

Figure 2.2 shows some snapshots of the pressure and film thickness distributions at different time-steps during the simulation for a time-varying external load as defined in equation (2.10). In such conditions, the dimensionless load W_t and the rigid body displacement H_0 are re-calculated at every time-step. Figure 2.3(a) shows the corresponding evolution during the simulation. Though it is not easily observed, the solution is shifted in time compared with the imposed time-varying load; such a phase shift is caused by the viscous damping provided by the lubricant. This fact is more clearly illustrated in the magnified representation in Figure 2.3(b).

Simulating the lubricated normal contact as a linear viscous damper, one can write:

$$w_t = c_l \dot{h}_0 \tag{2.23}$$

where c_l is the damping constant, h_0 is the mutual approach and over-dots represent first order time derivatives.

Cette thèse est accessible à l'adresse : http://theses.insa-lyon.fr/publication/2016LYSEI089/these.pdf
© [M. Ankouni], [2016], INSA Lyon, tous droits réservés

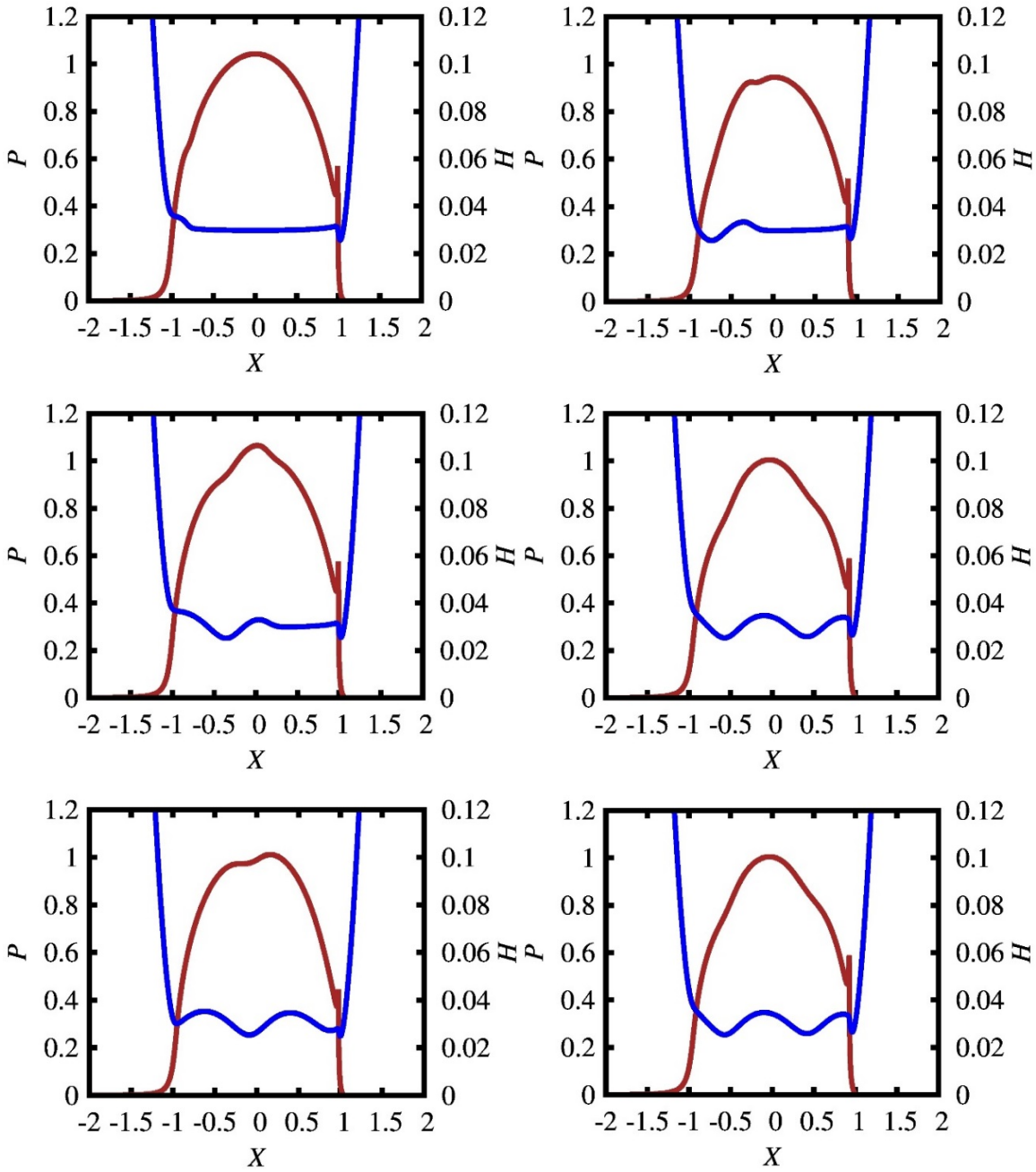

Figure 2.2: Examples of pressure distribution and film thickness in an EHL contact under periodic load.

Figure 2.4 shows an example of hysteresis loop obtained by plotting the mutual approach versus the dimensionless contact force. The trajectory is approximately elliptical, thus confirming that a linear damping model as in equation (2.23) can be employed.

The area enclosed by the ellipse equals the work done by the load, i.e. the energy dissipated by the viscous forces per period.

Cette thèse est accessible à l'adresse : http://theses.insa-lyon.fr/publication/2016LYSEI089/these.pdf
© [M. Ankouni], [2016], INSA Lyon, tous droits réservés

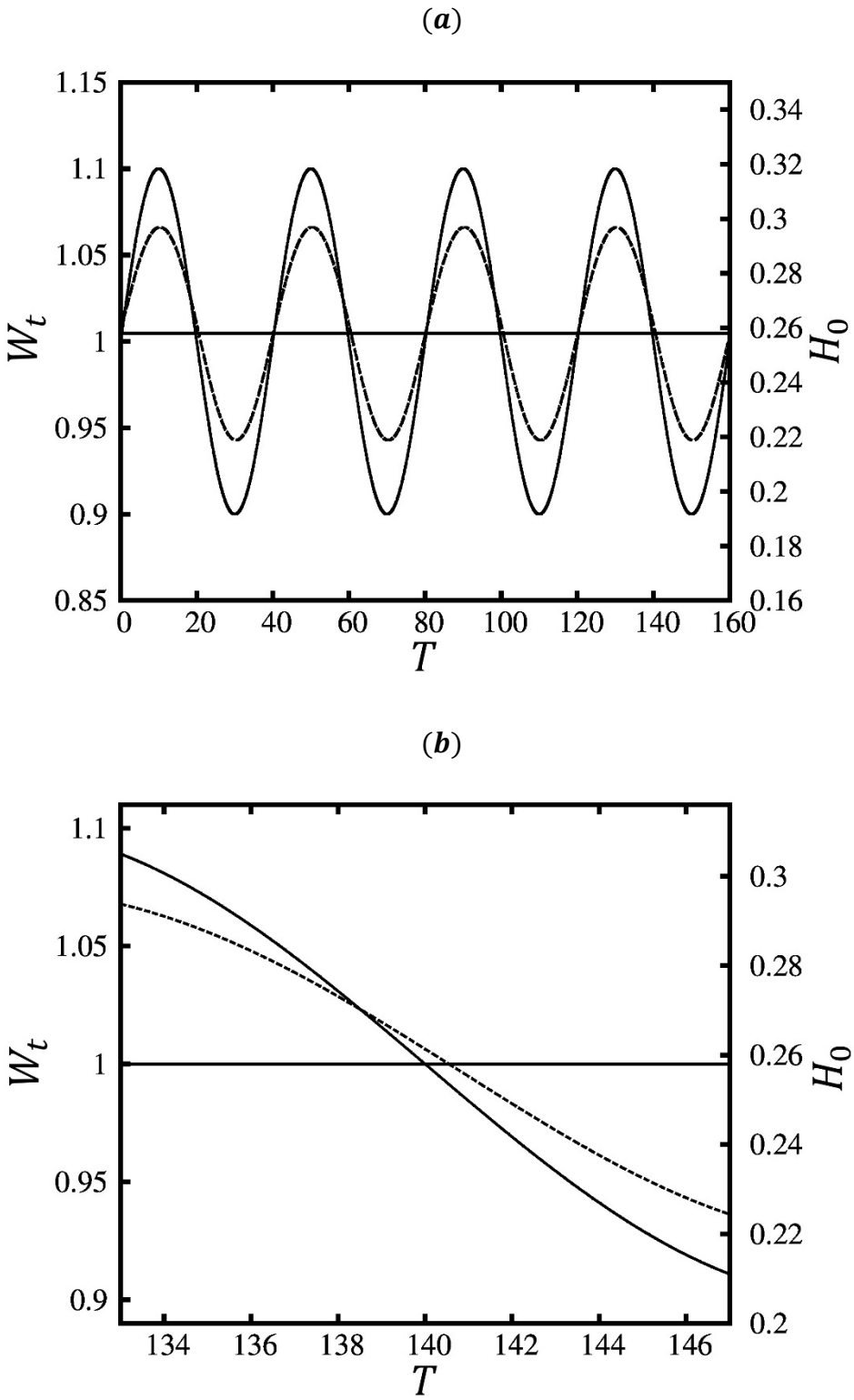

Figure 2.3: Mutual approach and load evolution versus time.

Introducing a dimensionless damping constant:

$$C_l = c_l \frac{u_m b}{w_0 R_x} \tag{2.24}$$

Cette thèse est accessible à l'adresse : http://theses.insa-lyon.fr/publication/2016LYSEI089/these.pdf
© [M. Ankouni], [2016], INSA Lyon, tous droits réservés

the dissipated energy for a sine excitation reads:

$$E = \pi C_l \Omega B^2 \tag{2.25}$$

where B represents the amplitude of the mutual approach H_0.

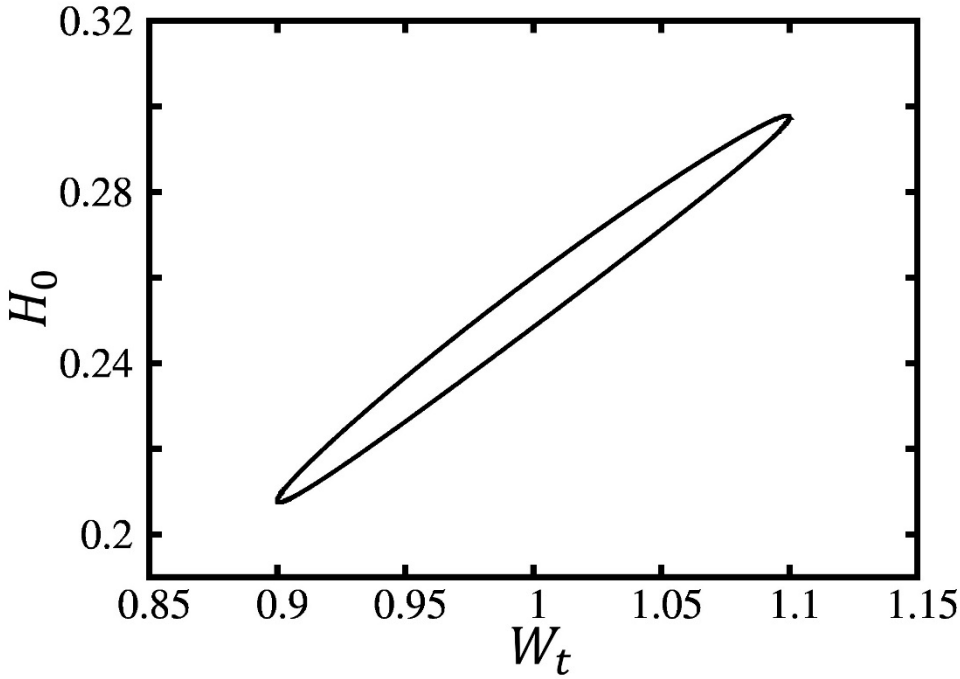

Figure 2.4: Mutual approach versus load (hysteresis loop).

The Moes parameters are normally sufficient to describe the behavior of an EHL contact considering either steady state or transient solutions. These parameters are defined as:

$$M = \pi \sqrt{\frac{3}{4\lambda}} \tag{2.26}$$

$$L = \bar{\alpha} \sqrt[4]{\frac{16\lambda}{3}} \tag{2.27}$$

In the present study, the frequency of the excitation f_l and its amplitude A need to be considered and further investigations are required in order to analyse their influence on the lubricated contact.

First, considering the excitation amplitude, calculations are performed for A varying from 0.1 to 0.9. With increasing amplitudes, a non-linearity appears which slightly alters the shape of the hysteresis loop (8% between the minimum and the maximum amplitude) but the linear

Cette thèse est accessible à l'adresse : http://theses.insa-lyon.fr/publication/2016LYSEI089/these.pdf
© [M. Ankouni], [2016], INSA Lyon, tous droits réservés

approximation still seems valid for estimating the equivalent damping C_l (Figure 2.5). Similar results have been obtained when sweeping over large ranges of M, L and f_l suggesting that the damping constant C_l can be considered as independent of the excitation amplitude A. The presented solutions have been obtained using a mesh with 4096 nodal points. The dimensionless time-step and the finest mesh grid size were equal $h_t = h_x = 0.0017$. The accuracy of the damping values was generally better than 1%. Considering the excitation frequency $f_l = \Omega/2\pi$, Figure 2.6 represents the resulting damping parameter C_l versus f_l, for $M = 100,\ L = 10,\ A = 0.1$. It can be noticed that C_l is constant for the lower frequencies and decreases for higher values of f_l. The results are confirmed through a large number of simulations considering wide ranges of M, L and A.

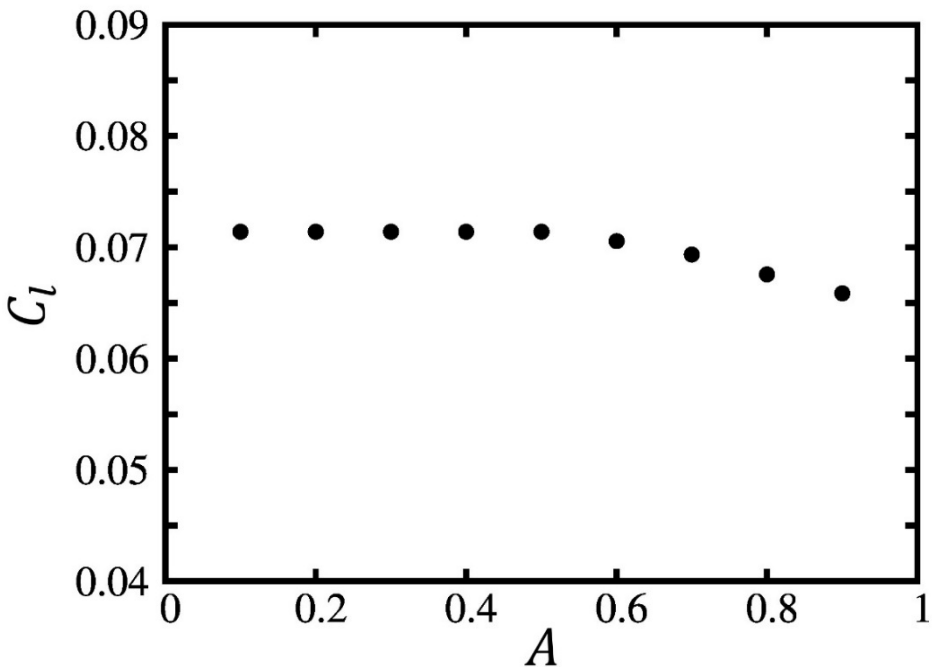

Figure 2.5: Numerical values of the damping constant C_l as a function of the amplitude of the excitation A.

A curve fitted equation (2.28) is proposed based on these results to describe the dependence of the damping constant C_l of the frequency of the imposed load f_l. The equation relates the values of the damping at high frequencies to the constant value at the lower ones.

$$f(T_l) = \frac{0.06\, T_l^{1.15}}{\sqrt[4]{1 + (0.06 T_l^{1.15})^4}} \tag{2.28}$$

where $T_l = t_l u_m / b$ is the dimensionless period $1/f_l$.

Cette thèse est accessible à l'adresse : http://theses.insa-lyon.fr/publication/2016LYSEI089/these.pdf
© [M. Ankouni], [2016], INSA Lyon, tous droits réservés

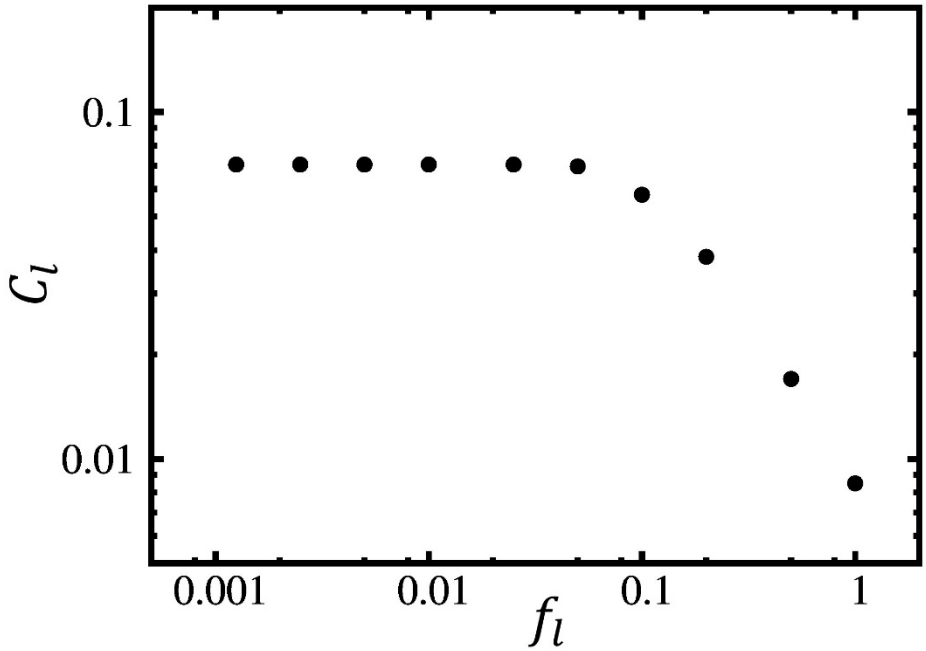

Figure 2.6: Numerical values of the damping constant C_l as a function of the frequency of the excitation f_l.

The sensitivity of the damping constant on the classic Moes parameters M and L is analyzed hereinafter. Considering first that the material parameter L is kept constant, the effect of the load parameter M is studied. Calculations were performed for $L = 10$ and M varying from 5 to 1000. As shown in Figure 2.7(a), the damping constant decreases with an increasing M, and since L is fixed, the variation of M is only due to load variations. Similar behavior has been observed for other values of L ($L = 1 \rightarrow 25$) and one can conclude that viscous damping becomes lower as load increases. Focusing on the material parameter L, Figure 2.7(b) shows that, for $M = 100$, damping increases with an increasing L parameter. Here again, similar trends have been found for a range of M parameters ($M = 5 \rightarrow 1000$). Based on these findings (only a few are shown), a single parameter combining M and L has been introduced under the form $\beta = \sqrt{L}/M$ which leads to a most satisfactory result in terms of damping constant C_l.

In Figure 2.8, the simulated values of C_l are plotted versus the new parameter β which show that damping increases with β. The best fit has been obtained by using the following expression:

$$C_l = \frac{2.5\,\beta^{1.2}}{\sqrt{1 + (3\beta^{0.85})^2}}\, f(T_l) \tag{2.29}$$

As illustrated in Figure 2.9 which shows that the numerical values and the results from (2.29) are in excellent agreement thus validating the proposed damping formula.

Cette thèse est accessible à l'adresse : http://theses.insa-lyon.fr/publication/2016LYSEI089/these.pdf
© [M. Ankouni], [2016], INSA Lyon, tous droits réservés

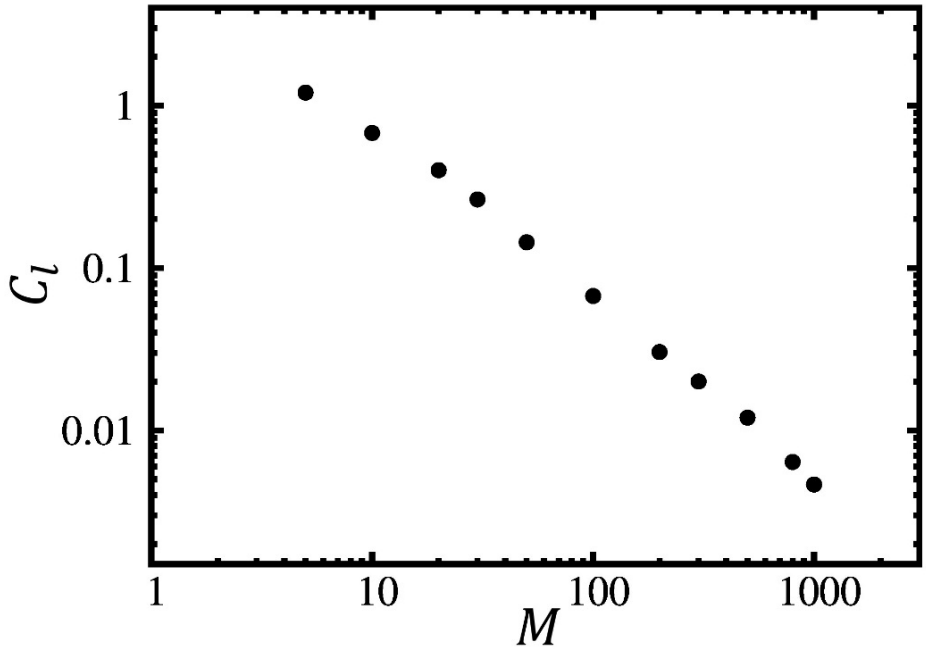

(a) $\boldsymbol{L = 10}$.

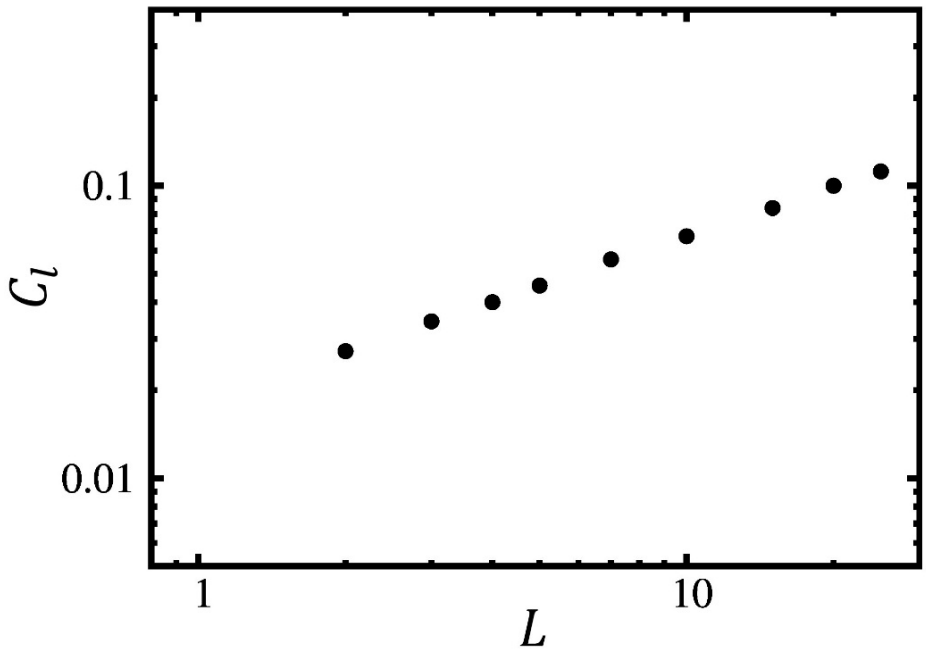

(b) $\boldsymbol{M = 100}$.

Figure 2.7: Damping constant C_l as a function of the load parameter M and the material parameter L.

Cette thèse est accessible à l'adresse : http://theses.insa-lyon.fr/publication/2016LYSEI089/these.pdf
© [M. Ankouni], [2016], INSA Lyon, tous droits réservés

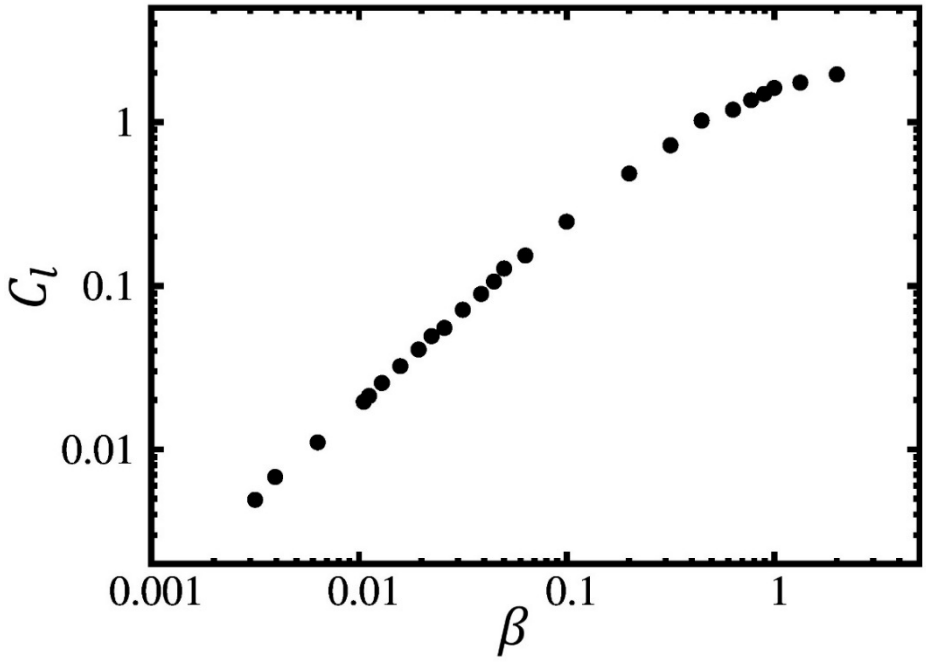

Figure 2.8: Numerical values of the damping constant C_l as a function of β.

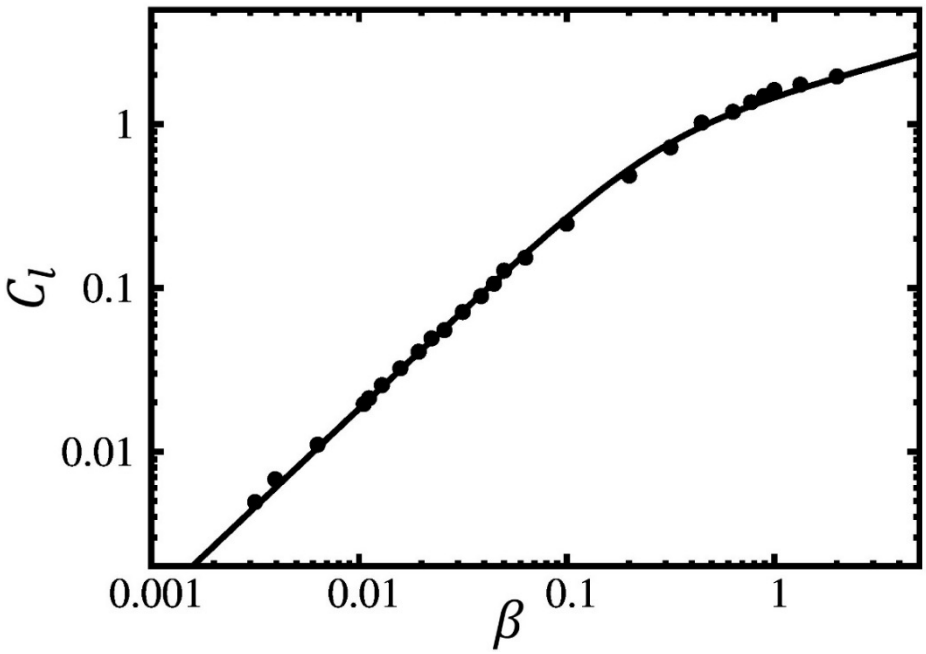

Figure 2.9: Numerical values of C_l as a function of β (symbols) and its curve fitted equation (drawn line).

Using the previous equation, a damping constant c_l for a line contact of width d is derived as:

$$c_l = C_l \frac{\omega_1 R_x}{u_m b} d \tag{2.30}$$

Cette thèse est accessible à l'adresse : http://theses.insa-lyon.fr/publication/2016LYSEI089/these.pdf
© [M. Ankouni], [2016], INSA Lyon, tous droits réservés

One must note that the range of values of M and L considered in the current study covers and even exceeds the range of operating conditions generally found in gears in terms of load, speed and temperature.

2.2 Forced lubricated impact

2.2.1 EHL Model

During the meshing course, the dynamic effects in spur gears can be large enough to momentarily unload the teeth and generate shocks at some critical speeds [84] which are detrimental in terms of tooth loading and gear noise (rattle noise). The corresponding dynamic tooth contact conditions can be assimilated to those for a forced impact problem between a cylinder and a lubricated plane. The problem of lubricated impact was studied both experimentally [34-36] and numerically [46-49]. In the current work, the pure impact for line contacts analyzed by Wang et al. [49] is extended accounting for additional external force imposed on the falling cylinder. Neglecting the entrainment velocity ($u_m = 0$), the Reynolds equation for line contacts is simplified as:

$$\frac{\partial}{\partial x}\left(\frac{\rho h^3}{12\eta}\frac{\partial p}{\partial x}\right) - \frac{\partial(\rho h)}{\partial t} = 0 \tag{2.31}$$

The film thickness function is still given by (2.2) but the static equilibrium equation (2.3) is replaced by the following dynamic equations:

$$\frac{\partial v}{\partial t} = \frac{1}{i}\left(\int_{-\infty}^{+\infty} p(x)dx - f\right) \tag{2.32}$$

$$\frac{\partial h_0}{\partial t} = v(t) \tag{2.33}$$

where i is the mass of the cylinder per unit width, f is the external load on the cylinder (corresponding to that generated by the torque on the pinion and the gear), v is the vertical velocity of the cylinder and h_0, its position.

The viscosity and density pressure relations in equations (2.4) and (2.5) are unchanged and a dimensionless analysis has been conducted for which the relevant dimensionless parameters can be found in [49]. The resulting system of dimensionless equations reads:

Cette thèse est accessible à l'adresse : http://theses.insa-lyon.fr/publication/2016LYSEI089/these.pdf
© [M. Ankouni], [2016], INSA Lyon, tous droits réservés

$$\frac{\partial}{\partial X}\left(\frac{\bar{\rho}H^3}{\lambda^*\bar{\eta}}\frac{\partial P}{\partial X}\right)-\frac{\partial(\bar{\rho}H)}{\partial T}=0 \tag{2.34}$$

$$H(X)=H_0+\frac{X^2}{2}-\frac{1}{2\pi}\int_{-\infty}^{+\infty}P(X')\,ln\left(\frac{X-X'}{X_0}\right)^2 dX' \tag{2.35}$$

$$\frac{\partial V}{\partial T}=\frac{1}{I}\left(\int_{-\infty}^{+\infty}P(X)dX-F\right) \tag{2.36}$$

$$\frac{\partial H_0}{\partial T}=V \tag{2.37}$$

where λ^* is a dimensionless parameter defined in [49] as:

$\lambda^*=(12\eta_0R_x^2)/(b^{*2}p_h^*t^*)$, $t^*=\delta^*/v_0$.

The problem is discretized and then iteratively solved using multilevel techniques. The first term in equation (2.34) is approximated using a second order central discretization, as for the squeeze term a second order backward discretization is used. Second order central discretization for the Poiseuille term and second order backward discretization for the squeeze term (equation (2.34)) are considered. Up to 9 levels with 2561 points are considered and an accuracy better than 5% is generally obtained.

2.2.1 Numerical results

Figure 2.10 and Figure 2.11 show examples of film thickness and pressure evolutions versus time during both impact and rebound respectively. As the cylinder falls, the pressure becomes higher until the lubricant ceases to flow and a bell-shape is formed at the center of the contact. During rebound, the film thickness evolution is approximately similar to that during impact but backwards. On the other hand, pressure decreases and lubricant flows out, symmetrical pressure spikes occur as well.

The pressure distribution, the cylinder position H_0 and velocity V are determined at each time-step and consequently the viscous force developed by the lubricant during impact can be computed. The lubricant being modelled as a linear viscous damper, the dimensionless viscous force that decelerates the falling cylinder is expressed as:

Cette thèse est accessible à l'adresse : http://theses.insa-lyon.fr/publication/2016LYSEI089/these.pdf
© [M. Ankouni], [2016], INSA Lyon, tous droits réservés

$$W_t = \int_{-\infty}^{+\infty} P(X)dX = C_{im}\frac{\partial H_0}{\partial T} \tag{2.38}$$

and the energy dissipation during impact is derived from the variation in kinetic energy as:

$$E = \frac{1}{2}I(V_0^2 - V_f^2) \tag{2.39}$$

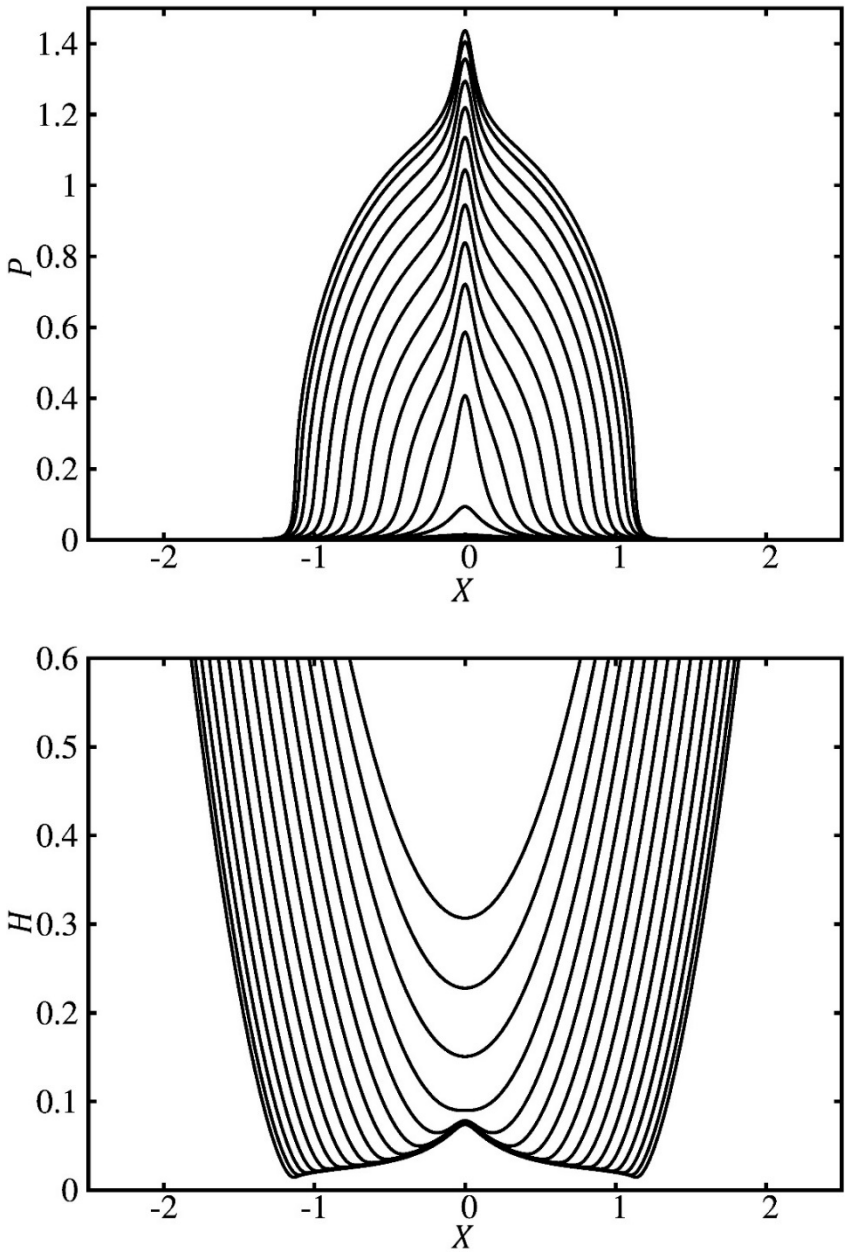

Figure 2.10: Pressure distribution and film thickness evolution during impact.

Equating E and the work produced by both the viscous force from the lubricant and the external force F, one obtains:

$$E = \int (W_t - F)dH_0 = \int C_{im}V^2 dT - F\int VdT \tag{2.40}$$

Cette thèse est accessible à l'adresse : http://theses.insa-lyon.fr/publication/2016LYSEI089/these.pdf
© [M. Ankouni], [2016], INSA Lyon, tous droits réservés

leading to the dimensionless equivalent damping constant C_{im}:

$$C_{im} = \frac{E + F\int V dT}{\int V^2 dT} \tag{2.41}$$

Based on dimensionless analysis, numerous numerical simulations have been performed and an approximate expression of the corresponding dimensionless damping constant C_{im} for impact conditions has been established for a wide range of operating conditions.

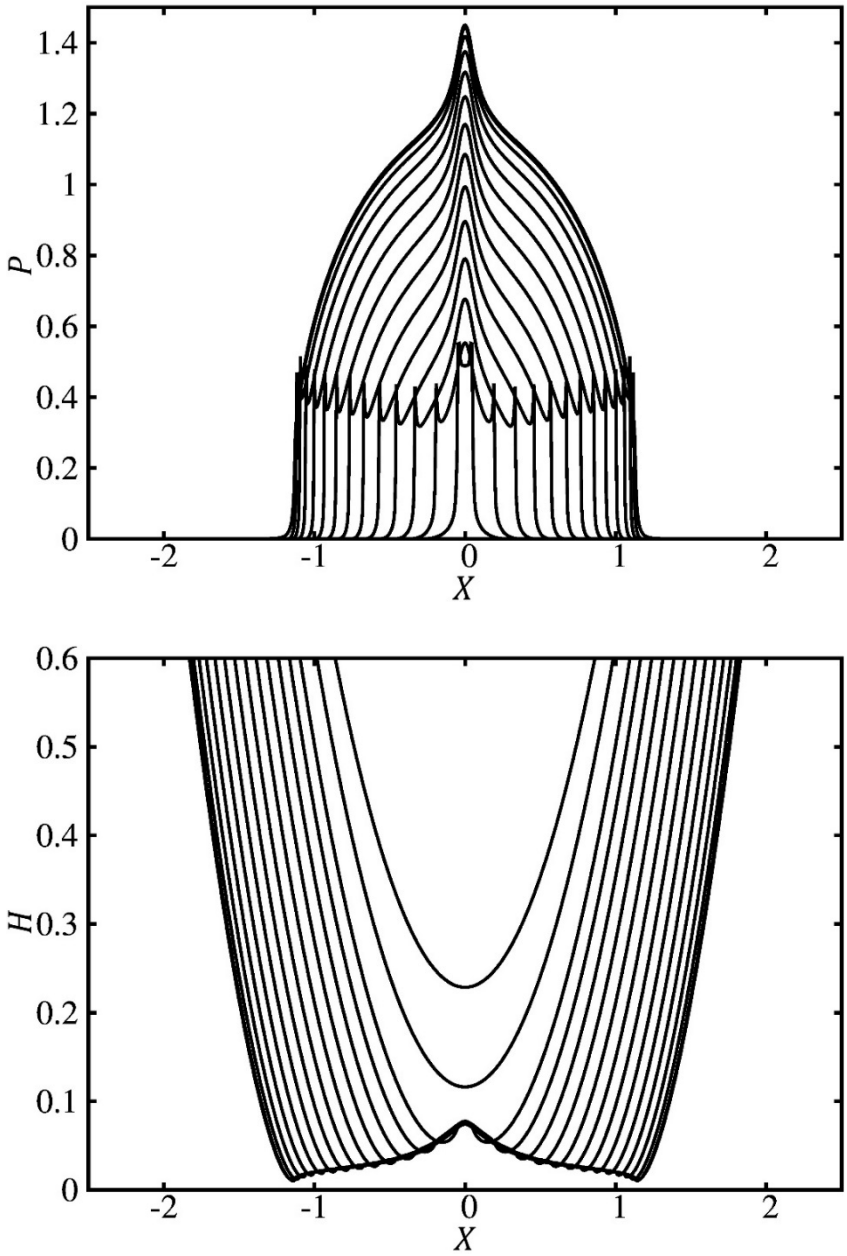

Figure 2.11: Pressure distribution and film thickness evolution during rebound.

Cette thèse est accessible à l'adresse : http://theses.insa-lyon.fr/publication/2016LYSEI089/these.pdf
© [M. Ankouni], [2016], INSA Lyon, tous droits réservés

As shown in Figure 2.12, the damping for pure impact conditions ($F = 0$) can be expressed in terms of parameter ξ only which is defined as:

$$\xi = \lambda^* \, \bar{\alpha}^{0.2} \tag{2.42}$$

and a curve fitted equation for C_{im} can be derived under the form:

$$C_{im} = \frac{1.2\xi + 0.025}{\xi + 0.45} \tag{2.43}$$

Considering the influence of a superimposed external load F, a correcting factor χ is introduced which, based on the results in Figure 2.13, can be expressed as:

$$\chi = \frac{1 + 0.1\left(\frac{f}{w^*}\xi^{-2}\right)^{0.75}}{1 + 0.055\left(\frac{f}{w^*}\xi^{-2}\right)^{0.75}} \tag{2.44}$$

and finally lead to the following damping constant c_{im} representative of the dissipation by impact in a line contact of width d:

$$c_{im} = \left(\frac{1}{4} + \frac{1}{2}\ln 2\right) C_{im}\, \chi \frac{w^*}{v_0} d \tag{2.45}$$

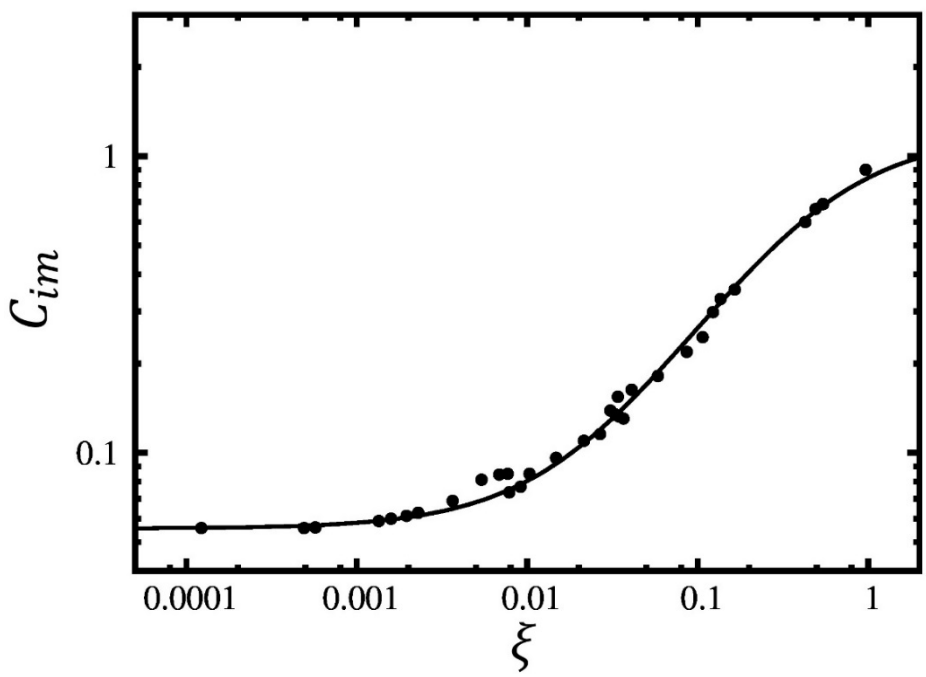

Figure 2.12: Dimensionless damping constant versus parameter ξ.

Cette thèse est accessible à l'adresse : http://theses.insa-lyon.fr/publication/2016LYSEI089/these.pdf
© [M. Ankouni], [2016], INSA Lyon, tous droits réservés

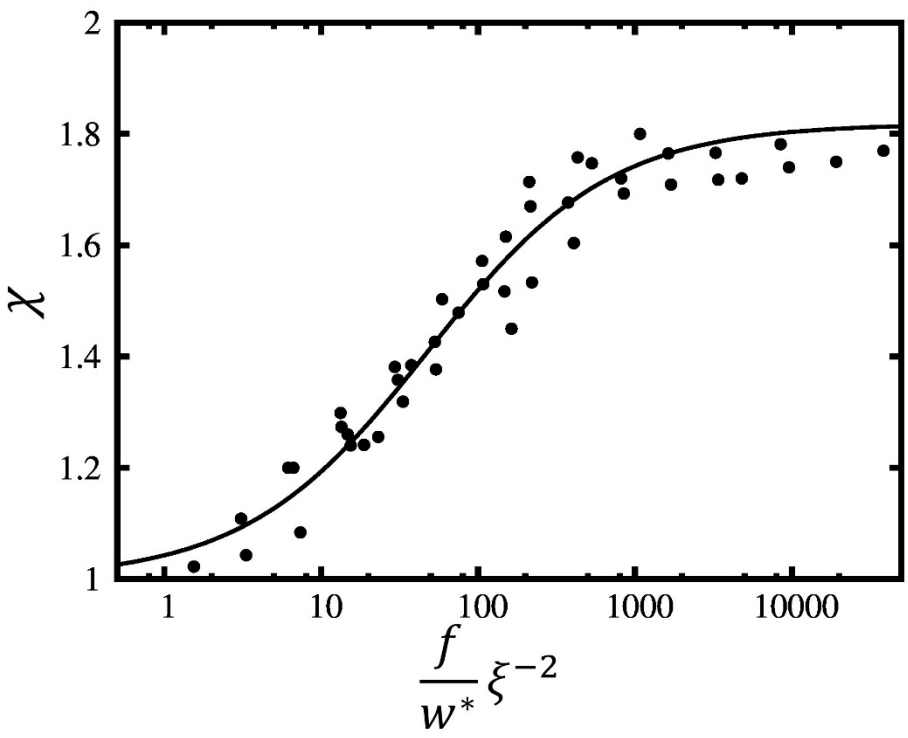

Figure 2.13: Correcting factor in terms of load f and parameter ξ.

2.3 Conclusion

A fully transient EHL model is proposed to precisely analyze the normal contact forces in dynamic conditions including the influence of momentary contact losses and shocks between the teeth. Following the approach of Wijnant et al. for rolling element bearings and Wang et al. for impact in lubricated contacts, the lubrication of line contacts is investigated from different perspectives. Several linear viscous damping formulations which are valid for a wide range of operating conditions are derived from extensive numerical EHL simulations. The proposed equations reproduce the lubricant damping capacities in both permanent contact conditions under an oscillating load and during the normal approach of two lubricated bodies. The obtained formulas are expected to provide substantial improvements to the damping modeling in gears and are therefore integrated in a gear dynamic model to be tested and validated in the following chapters.

Cette thèse est accessible à l'adresse : http://theses.insa-lyon.fr/publication/2016LYSEI089/these.pdf
© [M. Ankouni], [2016], INSA Lyon, tous droits réservés

Chapter 3

Application to gear dynamics: Torsional model

As a first attempt to validate the simple formulations of lubricant damping obtained in the previous chapter, a single degree of freedom gear model that accounts only for torsional displacements is considered. The model ignores the contributions of shafts, bearings, casings, and focuses basically on the gear mesh. Though such a torsional model is generally not appropriate for real applications, it represents an interesting first approach making it possible to illustrate and understand the damping mechanism in gears, particularly the lubricant contribution to the overall damping. The different sources of damping that can be introduced using the torsional model are first highlighted, the different formulations are then implemented and the simulation results are validated through comparison with experimental evidence.

3.1 Sources of damping

Focusing on a pinion-gear pair, it is generally accepted that, for medium speeds, damping mostly comes from i) the lubricated contacts between the teeth, and ii) the internal dissipation in the solid parts giving rise to structural (or internal) damping. The lubricant film separating the mating teeth can dissipate energy by squeeze effect in the normal direction and in the tangential direction (shear effect) whose contributions are successively analyzed as follows.

3.1.1 Lubricant normal viscous damping

The damping provided by the lubricant in the direction of the line of action is modelled using the simple formulations proposed in chapter 2, considering both permanent contact conditions and contact loss situation. The permanent contact damping coefficient, denoted c_l is computed using equations (2.28), (2.29) and (2.30) from the previous chapter. As for the damping model used when contact losses occur, it can be formulated based on the lubricate impact problem studied previously. Equations (2.43), (2.44) and (2.45) are combined to compute the corresponding damping coefficient c_{im}. The aforementioned components are introduced in the gear dynamic model as presented in the next section.

Cette thèse est accessible à l'adresse : http://theses.insa-lyon.fr/publication/2016LYSEI089/these.pdf
© [M. Ankouni], [2016], INSA Lyon, tous droits réservés

3.1.2 Lubricant tangential viscous damping

As said earlier, the lubricant contributes to the damping in the tangential direction to the contact through friction. A tangential damping coefficient is formulated in this section using some empirical traction law from literature [138].

The friction forces between mating teeth act perpendicular to the line of action and, for mixed lubrication regimes, they can be simulated by combining solid and fluid tractions [138] leading to the composite friction coefficient for one given contact line between two teeth:

$$\mu_f = \frac{1}{p_{moy}}\left(Sgn(u_s)\frac{A_c}{A_0}\zeta_{rough} + \left(1 - \frac{A_c}{A_0}\right)\zeta_{fluid}\right) \tag{3.1}$$

where p_{moy} is the average pressure on the contact, $Sgn(u_s)$ is +1 or -1 depending on the sign of the sliding speed u_s and the contact surface ratio A_c/A_0 is given by:

$$\frac{A_c}{A_0} = \frac{1}{2}\left(\frac{1}{2}\left(1 - erfc\left(\frac{\phi_T h_c}{\sqrt{2m_0}}\right)\right)\right) \tag{3.2}$$

Considering a classic Ree-Eyring model, the fluid traction can be expressed as:

$$\zeta_{fluid} = \tau_L \sinh^{-1}(\frac{\tau_N}{\tau_L}) \tag{3.3}$$

where

$$\tau_N = \frac{\eta \Delta u}{\phi_t h_c} \tag{3.4}$$

Introducing the instant tangential surface speeds of the pinion and gear as:

$$u_1 = \bar{u}_1 + \hat{u}_1, u_2 = \bar{u}_2 + \hat{u}_2 \tag{3.5}$$

where $\bar{u}_1$, $\bar{u}_2$ are the rigid-body speeds and $\hat{u}_1$, $\hat{u}_2$ represent the additional small perturbations due to the system vibrations,

Equation (3.3) is rewritten after separating the rigid-body and vibratory components as:

$$\tau_{fluid} = \tau_L \ln\left(\frac{\tau_N}{\tau_L} + \sqrt{1 + \left(\frac{\tau_N}{\tau_L}\right)^2}\right) = \tau_L \ln\left(2\frac{\tau_N}{\tau_L}\right)$$

Cette thèse est accessible à l'adresse : http://theses.insa-lyon.fr/publication/2016LYSEI089/these.pdf
© [M. Ankouni], [2016], INSA Lyon, tous droits réservés

$$= \tau_L(\ln 2 + \ln\left(\frac{\eta(\Delta\bar{u} + \Delta\hat{u})}{\phi_t h_c \tau_L}\right))$$

$$= \tau_L \ln\left(2\frac{\eta\Delta\bar{u}}{\phi_t h_c \tau_L}\right) + \tau_L \ln\left(1 + \frac{\Delta\hat{u}}{\Delta\bar{u}}\right)$$

$$= \tau_L \sinh^{-1}\left(\frac{\eta\Delta\bar{u}}{\phi_t h_c \tau_L}\right) + \frac{\tau_L}{\Delta\bar{u}}\Delta\hat{u} \tag{3.6}$$

thus leading to the following expression of the fluid friction force on one tooth

$$F_t = \mu F_N = \bar{F}_t + \frac{F_N}{p_{moy}}\left(1 - \frac{A_c}{A_0}\right)\frac{\tau_L}{\Delta\bar{u}}\Delta\hat{u} \tag{3.7}$$

from which, the equivalent tangential damping by the lubricant is deduced as:

$$c_t = \frac{F_N}{p_{moy}}\left(1 - \frac{A_c}{A_0}\right)\frac{\tau_L}{\Delta\bar{u}} \tag{3.8}$$

The influence of solid friction is accounted for as external forces on the pinion and the gear but its contribution to damping is discarded since ζ_{rough} does not vary with speed if a Coulomb's model is employed.

3.1.3 Structural/Internal damping

Internal damping results from the energy dissipation within the material due to various microscopic and macroscopic processes. Once deformed, energy is absorbed and dissipated by the material itself, due to the friction between the internal planes, which slip or slide as deformations take place. Structural damping accounts for the mechanical energy dissipation associated with the structural deflections of the different components in the system such as the teeth, gear bodies, shafts, etc. Several models are employed to represent both types of damping that are generally estimated from experimental results. In what follows, internal and structural damping mechanisms are not differentiated and an equivalent viscous damping factor is used to represent the related energy dissipations. The damping ratio is fixed around 0.5% based on results from the literature [139].

Cette thèse est accessible à l'adresse : http://theses.insa-lyon.fr/publication/2016LYSEI089/these.pdf
© [M. Ankouni], [2016], INSA Lyon, tous droits réservés

3.2 Torsional dynamic model

The damping components defined in the previous section are incorporated into the classic torsional gear dynamic model shown in Figure 3.1. The pinion and the gear are assimilated to two rigid cylinders connected by a non-linear, time-varying stiffness element $K(t)$ and a time-varying damping $C(t)$ determined by combining the elementary damping components presented in the previous section. The pinion is subjected to a torque T_1 and a resisting torque T_2 is applied to the gear. The polar moments of inertia of the pinion and the gear are J_1 and J_2 respectively. The contacts on tooth flanks are submitted to normal contact forces $\overrightarrow{F_{n_1}}$ and $\overrightarrow{F_{n_2}}$ in the line-of-action direction and tangential traction (friction) forces $\overrightarrow{F_{t_1}}$and $\overrightarrow{F_{t_2}}$ in the direction perpendicular to the line of action as illustrated in Figure 3.2. For errorless unmodified gears, the mesh deflection is given by:

$$\Delta = R_{b_1}\theta_1 + R_{b_2}\theta_2 \tag{3.9}$$

where θ_1 and θ_2 are the small perturbations caused by the mesh elasticity superimposed on rigid body displacements.

Considering the coordinate system in Figure 3.2, the normal contact forces $\overrightarrow{F_{n_1}}$ and $\overrightarrow{F_{n_2}}$ read:

$$\overrightarrow{F_{n_1}} = -\overrightarrow{F_{n_2}} = -\left(k\Delta + c_n\dot{\Delta}\right).\vec{x} \tag{3.10}$$

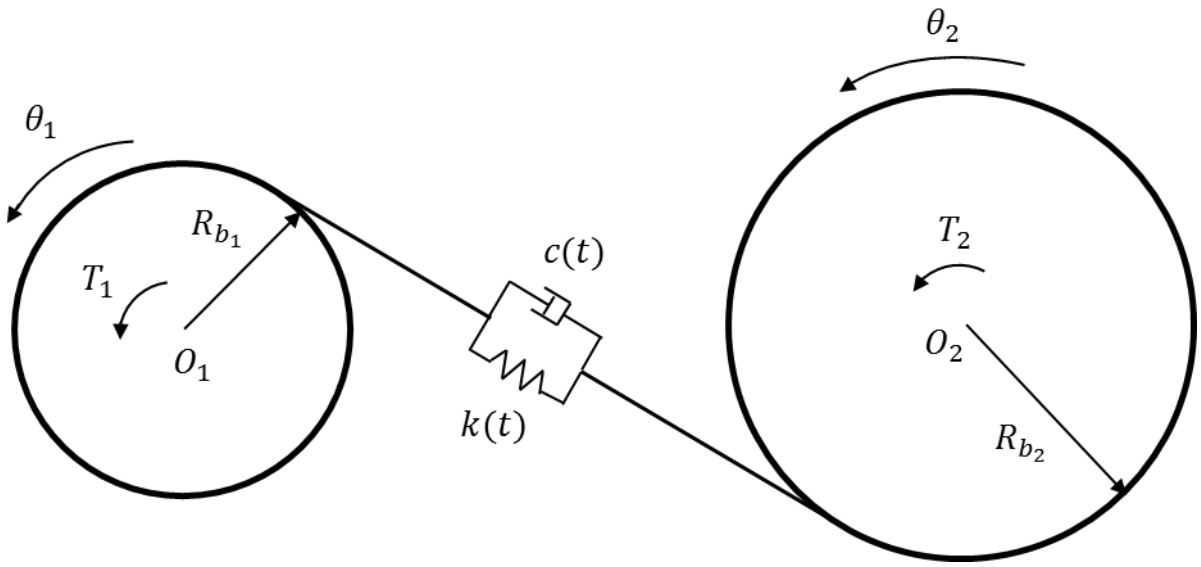

Figure 3.1: Gear pair dynamic model.

Cette thèse est accessible à l'adresse : http://theses.insa-lyon.fr/publication/2016LYSEI089/these.pdf
© [M. Ankouni], [2016], INSA Lyon, tous droits réservés

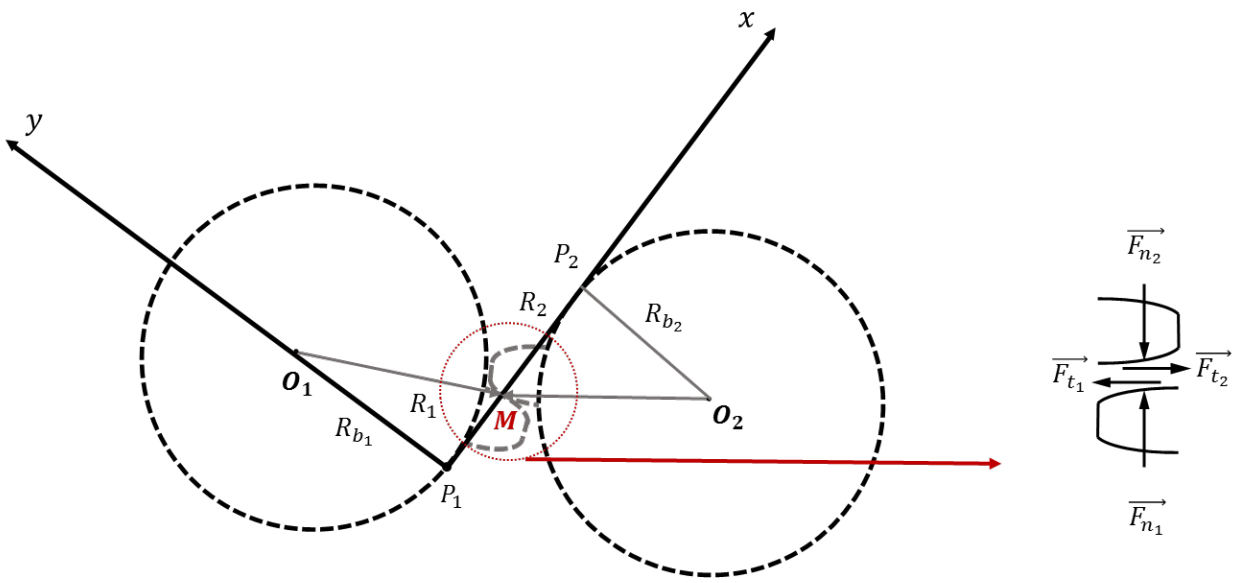

Figure 3.2: Gear geometry and external forces.

In equation (3.10), c_n is the normal damping coefficient which, depending on the contact conditions, is expressed as:

a) for permanent contacts,

$$c_n = \left(\frac{1}{c_{st}} + \frac{1}{c_l}\right)^{-1} \tag{3.11}$$

b) or, in case of contact losses and shocks,

$$c_n = c_{im} \tag{3.12}$$

where c_l refers to the equivalent viscous damping due to normal load, c_{st} is the structural damping (set to 0.5%) and c_{im} is the equivalent damping provided by the lubricant during contact regain.

It is to be noted that the structural damping and that associated with the normal effects on the lubricant film are in series and that, consequently, the smallest value will contribute most to the overall value of c_n. For the purely torsional gear dynamic model in Figure 3.1, the dynamic component $\Delta\hat{u}$ reduces to:

$$\Delta\hat{u} = R_1\dot{\theta}_1 + R_2\dot{\theta}_2 \tag{3.13}$$

which, according to Li and Kahraman [134] can be approximated by using the radii of curvature at pitch point as:

Cette thèse est accessible à l'adresse : http://theses.insa-lyon.fr/publication/2016LYSEI089/these.pdf
© [M. Ankouni], [2016], INSA Lyon, tous droits réservés

$$\Delta\hat{u} \cong tan(\phi)\left(R_{b1}\dot{\theta}_1 + R_{b2}\dot{\theta}_2\right) \cong tan(\phi)\,\dot{\Delta} \tag{3.14}$$

and, using (3.7) and (3.14), the tangential forces $\overrightarrow{F_{t_1}}$and $\overrightarrow{F_{t_2}}$ are expressed as:

$$\overrightarrow{F_{t_1}} = -\overrightarrow{F_{t_2}} = -\mu_f F_n \vec{y} \cong -(\overline{F_t} + c_t tan(\phi)\dot{\Delta}\,)\vec{y} \tag{3.15}$$

The dynamic moment equations for the pinion and the gear lead to:

$$J_1\ddot{\theta}_1(t) = T_{n_1} + T_{t_1} + T_1 \tag{3.16}$$

$$J_2\ddot{\theta}_2(t) = T_{n_2} + T_{t_2} + T_2 \tag{3.17}$$

where $T_{n_1}, T_{n_2}, T_{t_1}, T_{t_2}$ are respectively the moments of the normal and the tangential forces at the pinion and gear centers O_1, O_2 defined as:

$$T_{n_1} = \left(\overrightarrow{O_1M} \times \overrightarrow{F_{n1}}\right).\vec{z} \tag{3.18}$$

$$T_{n_2} = \left(\overrightarrow{O_2M} \times \overrightarrow{F_{n2}}\right).\vec{z} \tag{3.19}$$

$$T_{t_1} = \sum_{k=1}^{2}\left(\overrightarrow{O_1M_k} \times \overrightarrow{F_{t_{1k}}}\right).\vec{z} \tag{3.20}$$

$$T_{t_2} = \sum_{k=1}^{2}\left(\overrightarrow{O_2M_k} \times \overrightarrow{F_{t_{2k}}}\right).\vec{z} \tag{3.21}$$

Replacing the normal and tangential forces by their analytical expressions, the following differential system is obtained:

$$\begin{bmatrix} J_1 & 0 \\ 0 & J_2 \end{bmatrix}\begin{bmatrix} \ddot{\theta}_1 \\ \ddot{\theta}_2 \end{bmatrix} + \begin{bmatrix} C_{11} & C_{12} \\ C_{21} & C_{22} \end{bmatrix}\begin{bmatrix} \dot{\theta}_1 \\ \dot{\theta}_2 \end{bmatrix} + K(t,\Delta)\begin{bmatrix} {R_{b_1}}^2 & R_{b_1}R_{b_2} \\ R_{b_1}R_{b_2} & {R_{b_2}}^2 \end{bmatrix}\begin{bmatrix} \theta_1 \\ \theta_2 \end{bmatrix} = \begin{bmatrix} T_{tot_1} \\ T_{tot_2} \end{bmatrix} \tag{3.22}$$

where

$$C_{11} = c_n {R_{b_1}}^2 + R_{b_1}\sum_{1}^{2} R_{1_i}\tan(\phi)\,c_{t_i} \tag{3.23}$$

$$C_{12} = c_n R_{b_1}R_{b_2} + R_{b_2}\sum_{1}^{2} R_{1_i}\tan(\phi)\,c_{t_i} \tag{3.24}$$

Cette thèse est accessible à l'adresse : http://theses.insa-lyon.fr/publication/2016LYSEI089/these.pdf
© [M. Ankouni], [2016], INSA Lyon, tous droits réservés

$$C_{21} = c_n R_{b_1} R_{b_2} + R_{b_1} \sum_{1}^{2} R_{2_i} \tan(\phi)\, c_{t_i} \tag{3.25}$$

$$C_{22} = c_n {R_{b_2}}^2 + R_{b_2} \sum_{1}^{2} R_{2_i} \tan(\phi)\, c_{t_i} \tag{3.26}$$

$$T_{tot_1} = T_1 - \sum_{1}^{2} \overline{F_t} R_{1_i} \tag{3.27}$$

$$T_{tot_2} = T_2 - \sum_{1}^{2} \overline{F_t} R_{2_i} \tag{3.28}$$

After multiplying the first line by $R_{b_1} J_2$ and the second one by $R_{b_2} J_1$, adding and dividing all the terms by ${R_{b_2}}^2 J_1 + {R_{b_1}}^2 J_2$, the semi-definite system (3.22) is reduced to a single differential equation of the form:

$$M_{eq} \ddot{\Delta} + C(t) \dot{\Delta} + K(t, \Delta) \Delta = F_e \tag{3.29}$$

where

$$M_{eq} = \frac{J_1 J_2}{{R_{b_2}}^2 J_1 + {R_{b_1}}^2 J_2} \tag{3.30}$$

$$F_e = \frac{R_{b_1} J_2 T_{tot_1} + R_{b_2} J_1 T_{tot_2}}{{R_{b_2}}^2 J_1 + {R_{b_1}}^2 J_2} \tag{3.31}$$

$$C = c_n + \frac{c_{t_1} J_2 R_{b_1} + c_{t_2} J_1 R_{b_2}}{{R_{b_2}}^2 J_1 + {R_{b_1}}^2 J_2} \quad \text{(contact)}$$

$$= c_n \quad \text{(contact loss)} \tag{3.32}$$

$$c_{t_1} = \sum_{1}^{2} R_{1_i} \tan(\phi)\, c_{t_i} \tag{3.33}$$

$$c_{t_2} = \sum_{1}^{2} R_{2_i} \tan(\phi)\, c_{t_i} \tag{3.34}$$

The equation of motion is integrated step-by-step in time by using a Newmark's scheme coupled with a unilateral normal contact algorithm [140] which verifies that the contact forces

Cette thèse est accessible à l'adresse : http://theses.insa-lyon.fr/publication/2016LYSEI089/these.pdf
© [M. Ankouni], [2016], INSA Lyon, tous droits réservés

are positive, cancel the mesh stiffness when contact is lost and select the proper damping model depending on the dynamic contact conditions as illustrated in Figure 3.3.

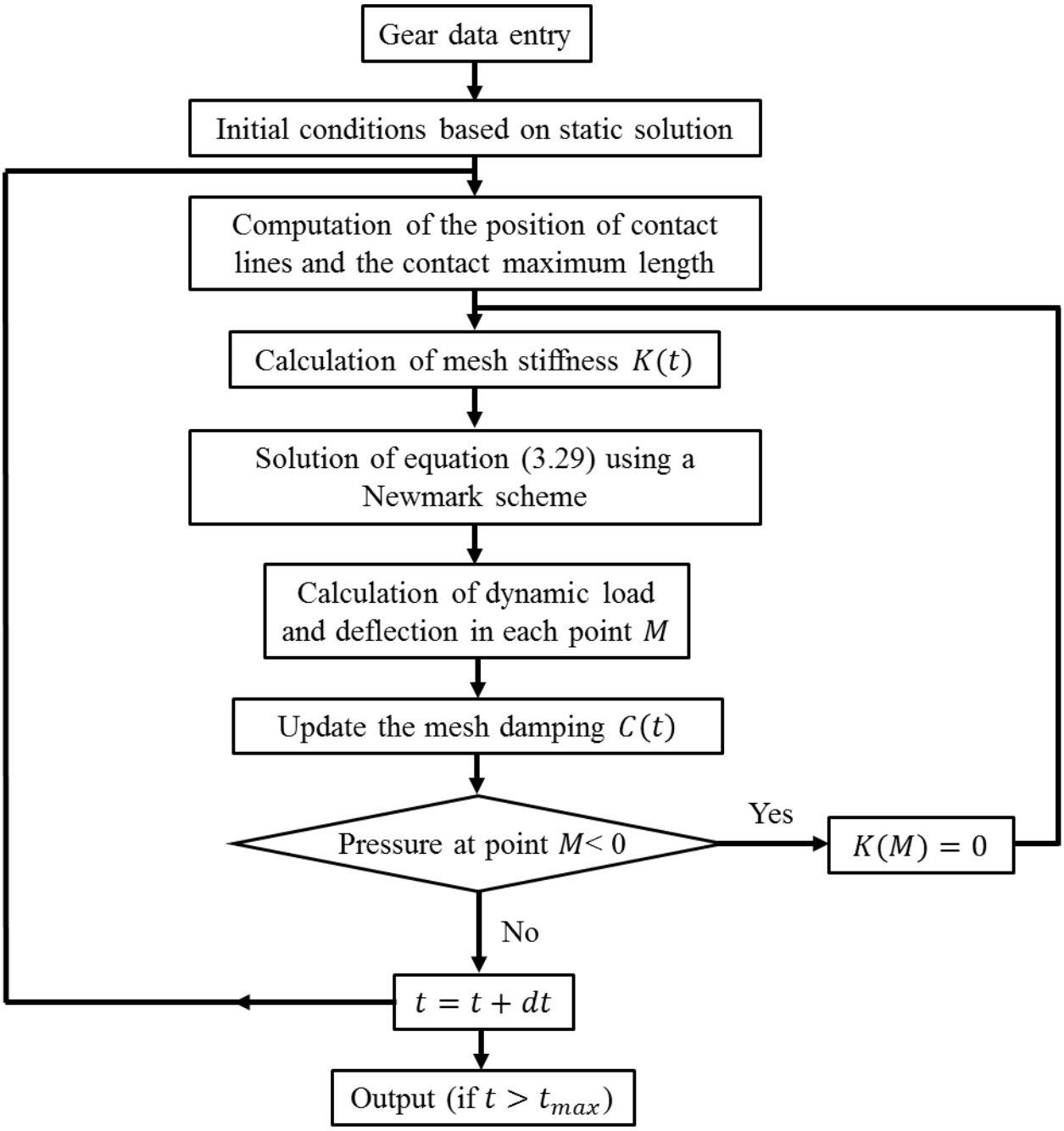

Figure 3.3: Process of numerical simulation of the torsional model.

Cette thèse est accessible à l'adresse : http://theses.insa-lyon.fr/publication/2016LYSEI089/these.pdf
© [M. Ankouni], [2016], INSA Lyon, tous droits réservés

3.3 Results

3.3.1 Spur gears

Using a four-square test rig, Kahraman and Blankenship [88, 102, 103] performed benchmark measurements of dynamic transmission errors (*DTE*) for several 1:1 spur gears (identical pinions and gears), operating conditions and profile modifications. For the unmodified gears defined in Table 3.1 and the lubricant properties in Table 3.2, Figure 3.4 shows a series of experimental *DTE* speed-sweep curves versus gear mesh frequency f_m at three different load levels. The dynamic responses are dominated by amplitude jumps at the major and secondary tooth critical speeds typical of contact losses and shocks between the teeth. The numerical curves obtained by solving (3.29) have been superimposed and it can be noticed that the *DTE* variations are correctly reproduced in terms of peak positions and amplifications thus proving that the damping modeling is sound. A temperature of 55°C is considered for the considered simulations.

Number of teeth	50
Module	3 mm
Pressure angle	20°
Face width	20 mm
Outside diameter	156 mm
Pitch diameter	150 mm
Base circle diameter	140.95 mm
Involute contact ratio (ICR)	1.75

Table 3.1: Test gear characteristics (*identical pinion and gear*). Spur gears.

Density ρ $(\mathrm{kg/m^3})$	859
Viscosity at 40°C $(\mathrm{Pa.s})$	0.043
Pressure viscosity coefficient $\alpha(\mathrm{GPa^{-1}})$	19.8

Table 3.2: Lubricant basic properties.

Cette thèse est accessible à l'adresse : http://theses.insa-lyon.fr/publication/2016LYSEI089/these.pdf
© [M. Ankouni], [2016], INSA Lyon, tous droits réservés

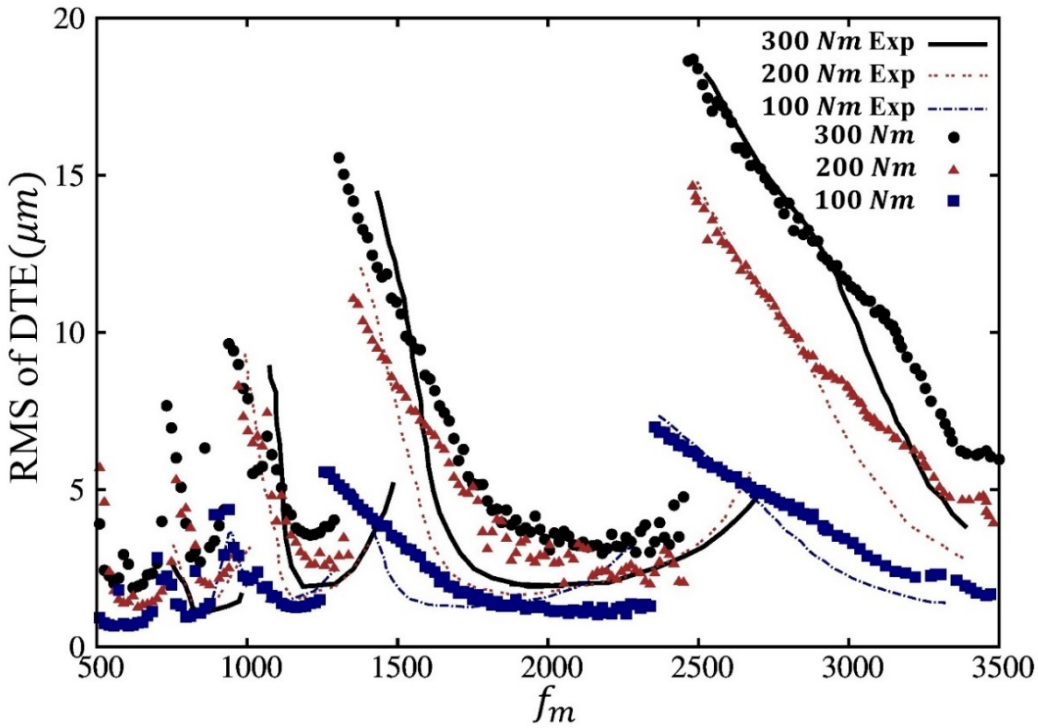

Figure 3.4: Measured [88] and numerical RMS of *DTE* versus the gear meshing frequency f_m. Spur gears.

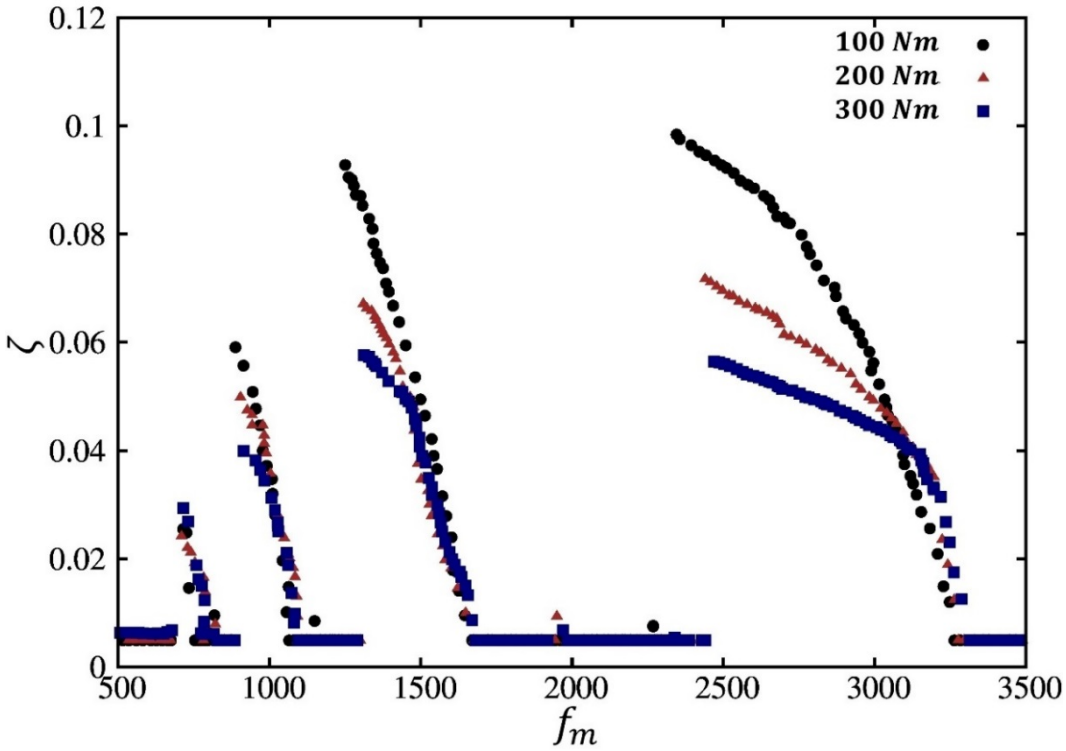

Figure 3.5: Mean damping ratio versus the gear meshing frequency f_m. Different loads. Spur gears.

Cette thèse est accessible à l'adresse : http://theses.insa-lyon.fr/publication/2016LYSEI089/these.pdf
© [M. Ankouni], [2016], INSA Lyon, tous droits réservés

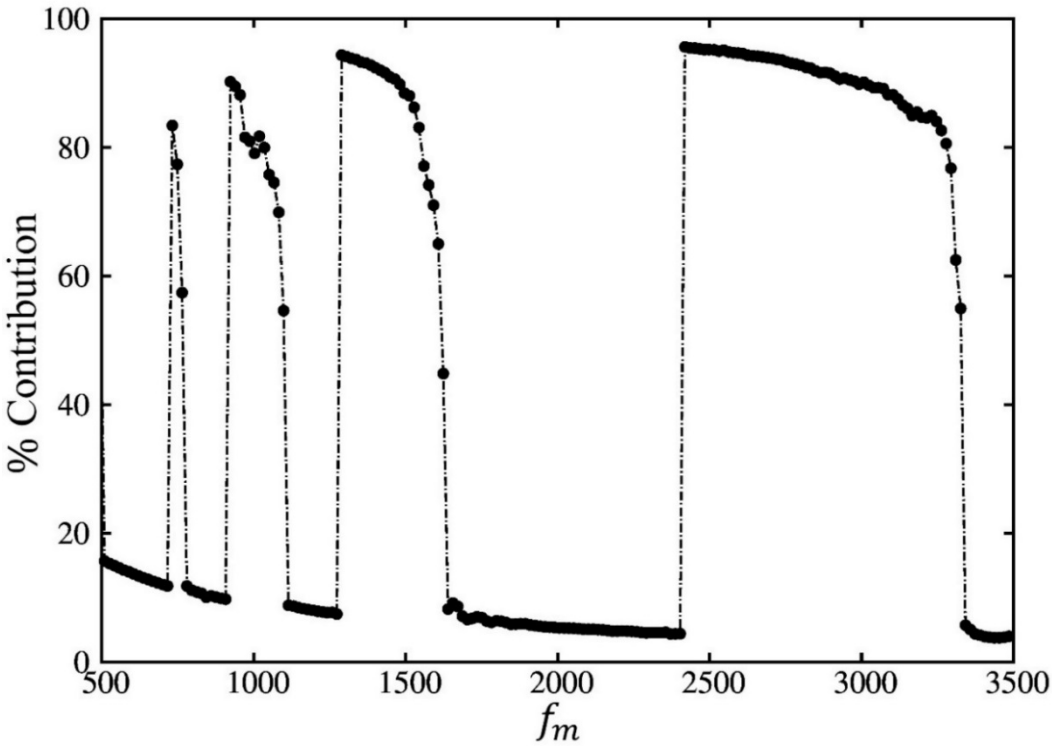

Figure 3.6: Relative contribution of the lubricant to the global damping ratio for $T = 300\ Nm$. Spur gears.

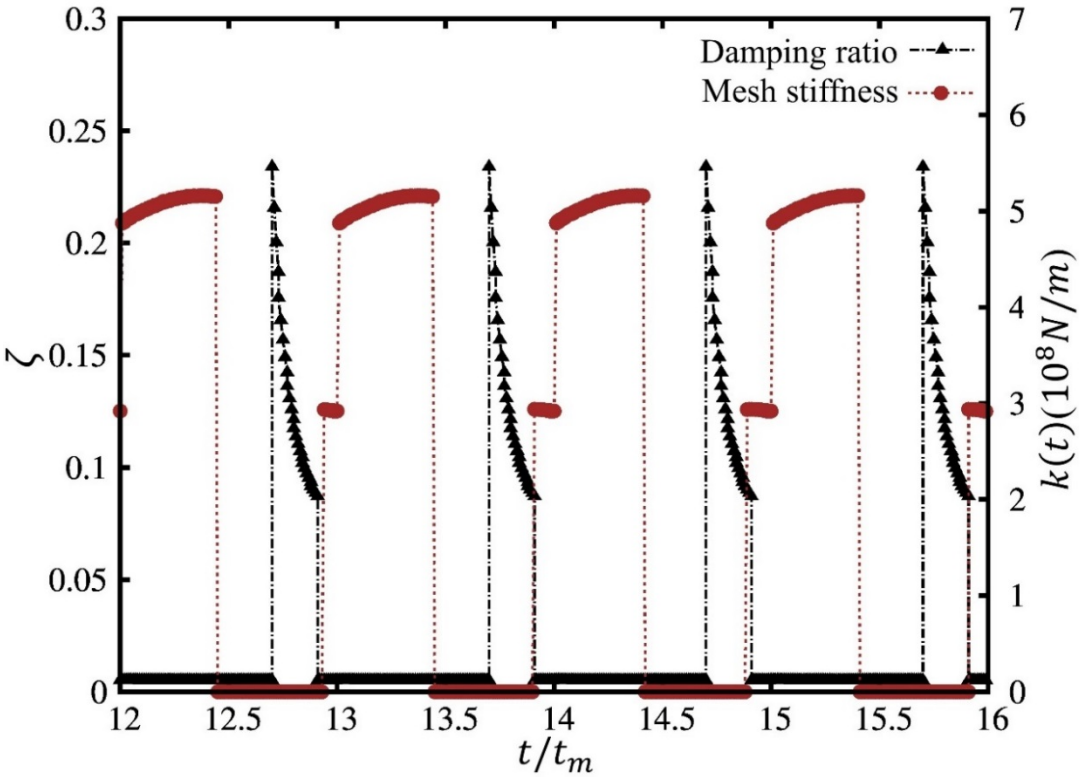

Figure 3.7: Evolution of damping ratio and mesh stiffness versus dimensionless time for $T = 300\ N$, at $2500\ Hz$. Spur gears.

Cette thèse est accessible à l'adresse : http://theses.insa-lyon.fr/publication/2016LYSEI089/these.pdf
© [M. Ankouni], [2016], INSA Lyon, tous droits réservés

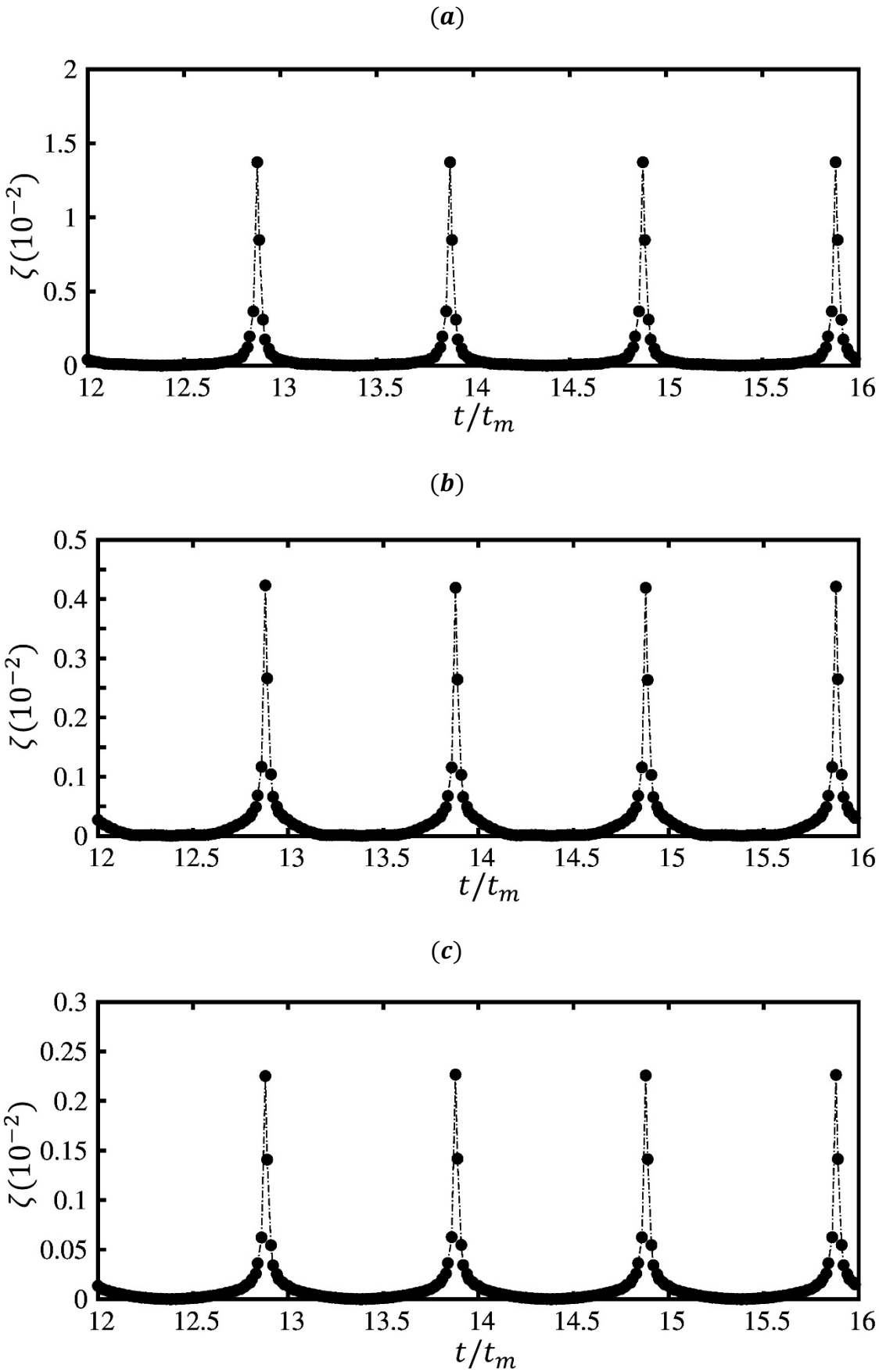

Figure 3.8: Tangential damping ratio versus dimensionless time for $T = 300\ N$ at (a) $600\ Hz$, (b) $1200\ Hz$ and (c) $2000\ Hz$. Spur gears.

Cette thèse est accessible à l'adresse : http://theses.insa-lyon.fr/publication/2016LYSEI089/these.pdf
© [M. Ankouni], [2016], INSA Lyon, tous droits réservés

The average damping factor calculated over a mesh period is plotted in Figure 3.5 versus mesh frequency and shows that i) the lubricant contributes significantly when contact is lost whereas, ii) structural damping seems prominent for permanent contact conditions. It is also noticed that the amount of damping decreases with load. These trends are confirmed in Figure 3.6 which shows that the percentage of damping from the lubricant can reach 80% at the critical speeds in the presence of impacts while its contribution hardly exceeds 20% in the rest of the speed range.

The previous investigations provide some global information on the damping variation for a range of operating speeds. To better understand the damping mechanism during contact losses, Figure 3.7 reproduces the evolution of the time-variant damping and mesh stiffness functions at the main critical speed $2500\,Hz$ $(3000\,RPM)$ for $T = 300\,Nm$. The mesh stiffness fluctuates depending on the length of contact, i.e. due to the variation of the number of teeth in contact, and becomes null when contact loss occurs (the unilateral normal contact algorithm). When the gear teeth are in contact, the damping is approximately constant and is dominated by the structural contribution. During the phase of contact regain, the squeezing film becomes active and introduces a significant amount of damping which plays a major role in limiting the magnitude of the tooth dynamic loading. Moreover, no clear information is provided by Figure 3.5 regarding the tangential contribution of the lubricant to the overall damping, which is mainly active during permanent contact situations. Therefore, to get a better insight on this contribution, the time evolution of the tangential component of the damping is computed for different speeds at which permanent contact conditions prevail. Figure 3.8 shows that some local high damping compared to the rest of the mesh period are found, with a clear decrease of the damping for higher speeds. However, the amount of the damping related to lubricant shear is generally very low compared to the other contributions, with the higher values hardly exceeding the constant structural damping (0.5%) and mainly for low speeds.

The precedent statements on the different contributions to the damping are thus reinforced, it is the lubricant squeeze effect during teeth separation that contributes most to the overall damping with a limited contribution of the lubricant shear effect. The internal dissipation is the main active source of damping otherwise. The previous simulations considered a given temperature and lower loads are found to yield higher damping. However, temperature can change depending on operating conditions, the effect of the temperature on damping is actually analyzed considering, for a given load, three different lubricant temperatures. The obtained responses are presented in Figure 3.9. Higher temperatures lead clearly to higher amplitudes at critical speeds, this is explained in Figure 3.10 that shows the evolution of the mean damping

Cette thèse est accessible à l'adresse : http://theses.insa-lyon.fr/publication/2016LYSEI089/these.pdf
© [M. Ankouni], [2016], INSA Lyon, tous droits réservés

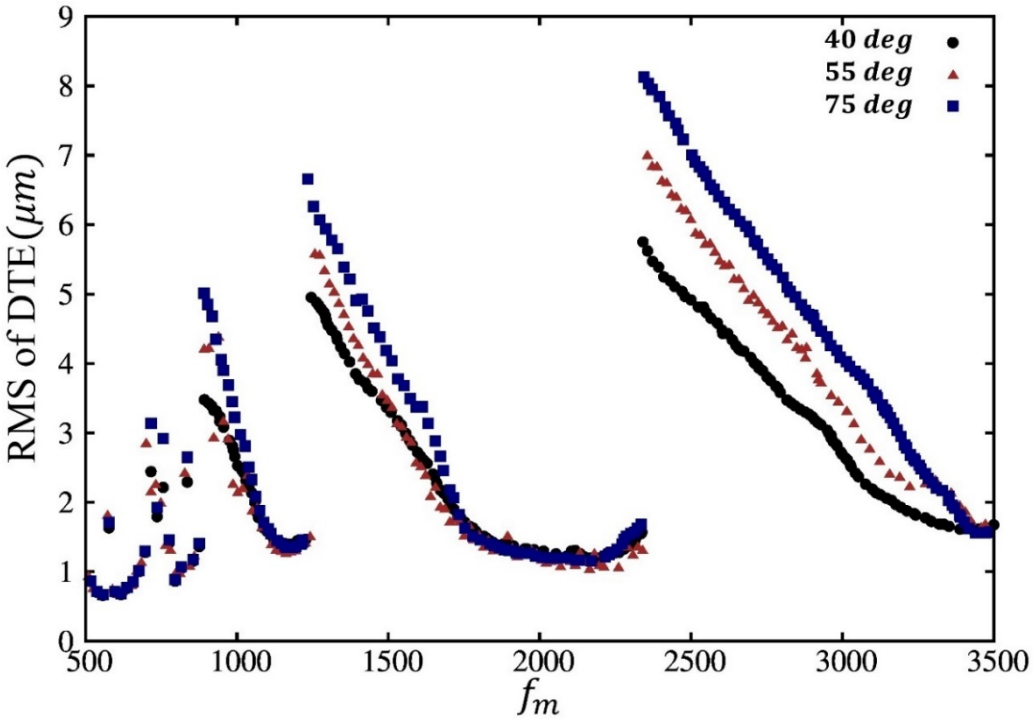

Figure 3.9: Numerical RMS of *DTE* versus the gear meshing frequency f_m . Different lubricant temperatures. $T = 100\ Nm$. Spur gears.

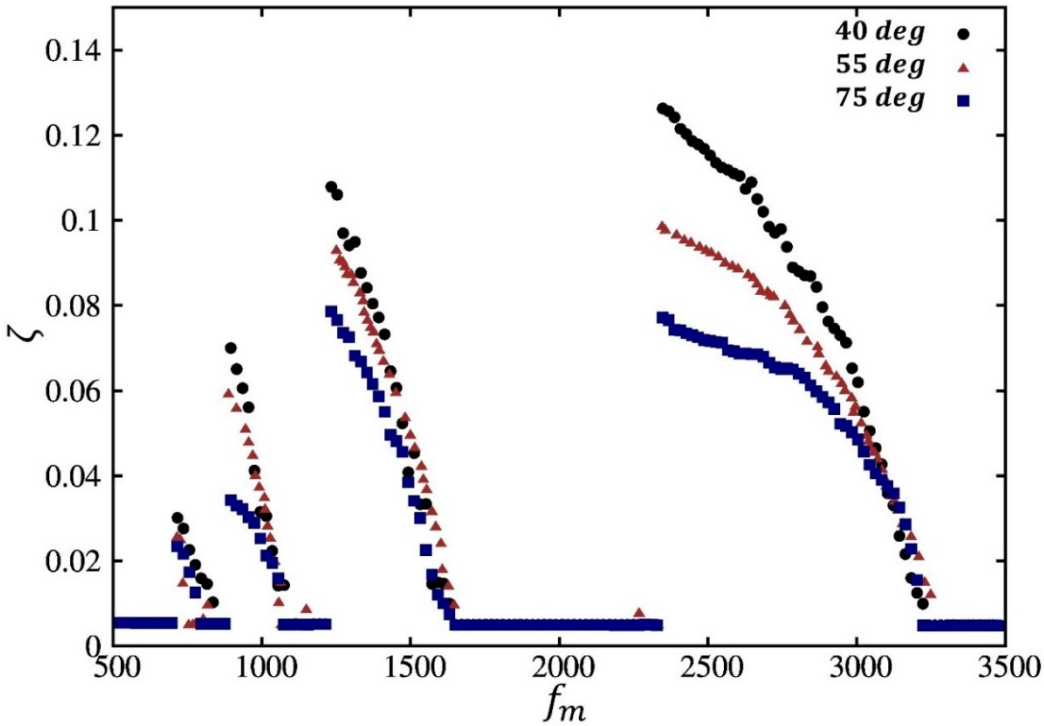

Figure 3.10: Mean damping ratio versus the gear meshing frequency f_m. Different lubricant temperatures. $T = 100\ Nm$. Spur gears.

Cette thèse est accessible à l'adresse : http://theses.insa-lyon.fr/publication/2016LYSEI089/these.pdf
© [M. Ankouni], [2016], INSA Lyon, tous droits réservés

ratio for a range of operating speeds. In fact, the higher is the temperature, the lower is the damping provided by the lubricant which is caused basically by the decrease of the lubricant viscosity.

Further comparisons are displayed in Figure 3.11 which illustrate the influence of gear geometry on dynamic *DTE* response curves. Three different profile (or involute) contact ratios (ICR) have been tested which were obtained by changing the gear outside diameter re the gear data in Table 3.1. The tooth profiles were still unmodified and a slight symmetrical lead crown of amplitude 0-5μm was added to make sure that the load distribution was reasonably centered on the face width and avoid edge contacts. Figure 3.11 represents the RMS of *DTE* versus the mesh frequency normalized with respect to the measured system natural frequency f_n so that the three gear geometries can be directly compared. It can be observed that the simulated results compare well with the experimental findings both in terms of amplitudes and frequencies. It is also confirmed that gears with ICR close to 2 exhibit very limited dynamic response. Finally, the influence of profile modifications is examined in Figure 3.12 by considering the response curves obtained for a pinion and a gear both modified by a constant tip relief of amplitude $10\ \mu m$ and two different extents of modification (starting roll angle α of 20.9° and 24.8°). Here again, the predicted numerical response curves agree well with the measurements and confirm the versatility of the proposed damping model.

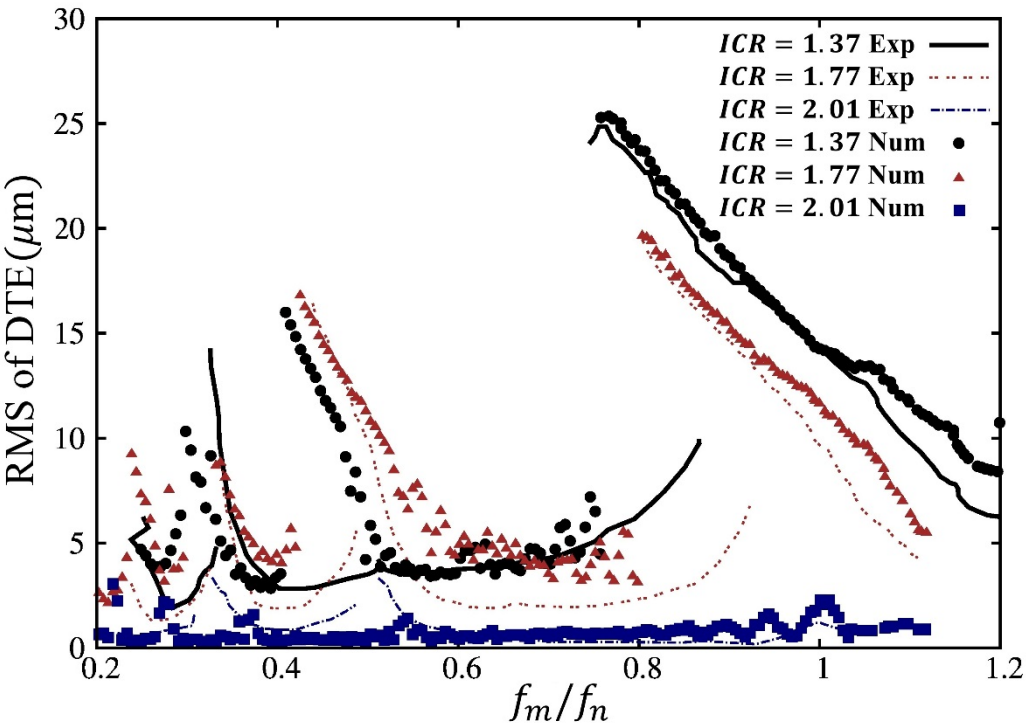

Figure 3.11: Measured [102] and calculated RMS of *DTE* versus f_m/f_n for unmodified gears for $T = 340\ Nm$. Spur gears.

Cette thèse est accessible à l'adresse : http://theses.insa-lyon.fr/publication/2016LYSEI089/these.pdf
© [M. Ankouni], [2016], INSA Lyon, tous droits réservés

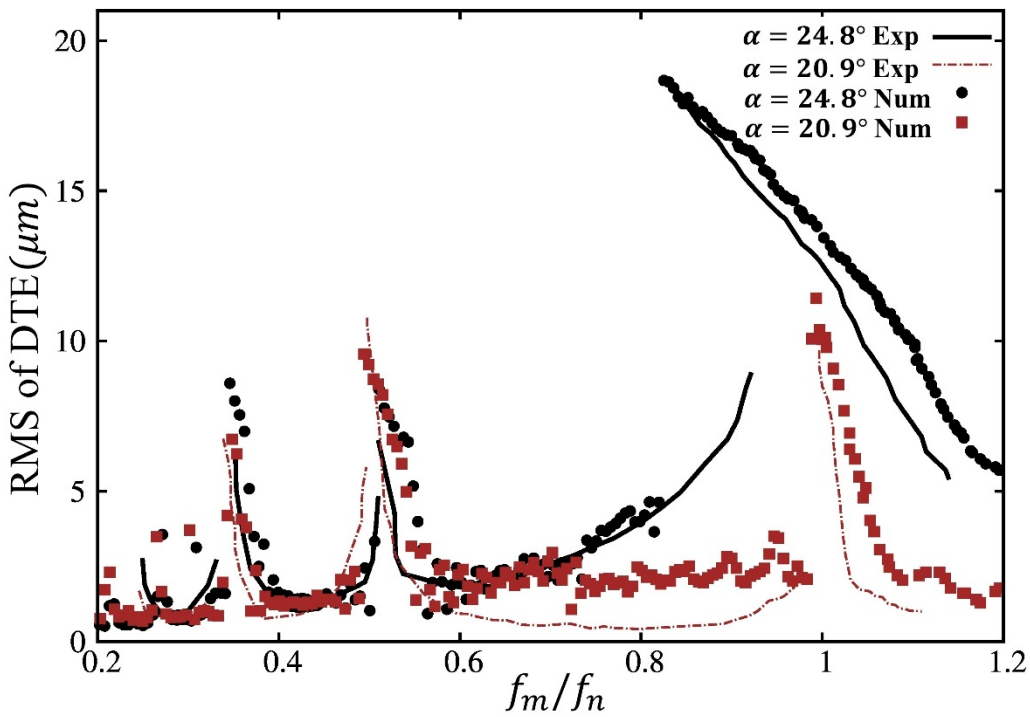

Figure 3.12: Measured [103] and calculated RMS of *DTE* versus f_m/f_n for $T = 340\ Nm$. Spur gears.

3.3.2 Helical gears

The proposed modeling of damping is shown to be suitable for spur gear simulations. Helical gears, however, present some different behavior compared with spur gears and contact losses at critical speeds do not generally occur. Therefore, the major active source of damping for spur gears is missing when helical gears are considered. Some measurements made on a pair of identical helical gears (Table 3.3) are performed by Kubur et al. [141]. The obtained response curves are used to test the relevance of the proposed model for helical gears simulations.

Number of teeth	50
Module	2.714 mm
Pressure angle	18.224°
Face width	20 mm
Outside diameter	155.4 mm
Pitch diameter	150 mm
Base circle diameter	140.95 mm

Cette thèse est accessible à l'adresse : http://theses.insa-lyon.fr/publication/2016LYSEI089/these.pdf
© [M. Ankouni], [2016], INSA Lyon, tous droits réservés

Helix angle	25.232°
Involute contact ratio (ICR)	1.6

Table 3.3: Test gear characteristics (*identical pinion and gear*). Helical gears.

Figure 3.13 presents the RMS of *DTE* versus the operational speed, the numerical curve is compared to the experimental curve obtained by [141]. A slightly damped response curve is observed and the simulated maximum amplitude at the critical speed is shown to be largely higher than the measured amplitude.

The lubricant contribution in this case is highlighted through the computation of the tangential component of the lubricant damping. The related mean damping ratio is plotted in Figure 3.14. A damping ratio lower than 0.5 % for the lower speeds and much lower for higher speeds can be observed. Thus one can state the tangential contribution of the lubricant to the damping in helical gears is relatively limited and contributes very little to the reduction in vibration amplitudes.

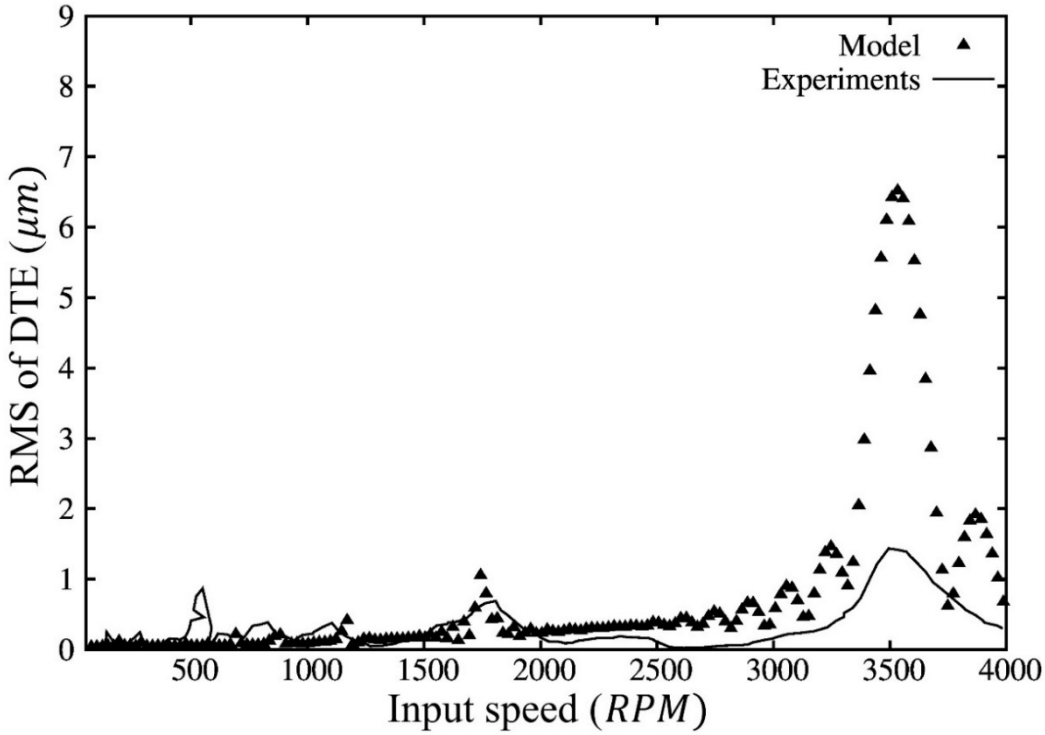

Figure 3.13: Measured [141] and calculated RMS of *DTE* versus input speed for $T = 250\ Nm$. Helical gears.

Cette thèse est accessible à l'adresse : http://theses.insa-lyon.fr/publication/2016LYSEI089/these.pdf
© [M. Ankouni], [2016], INSA Lyon, tous droits réservés

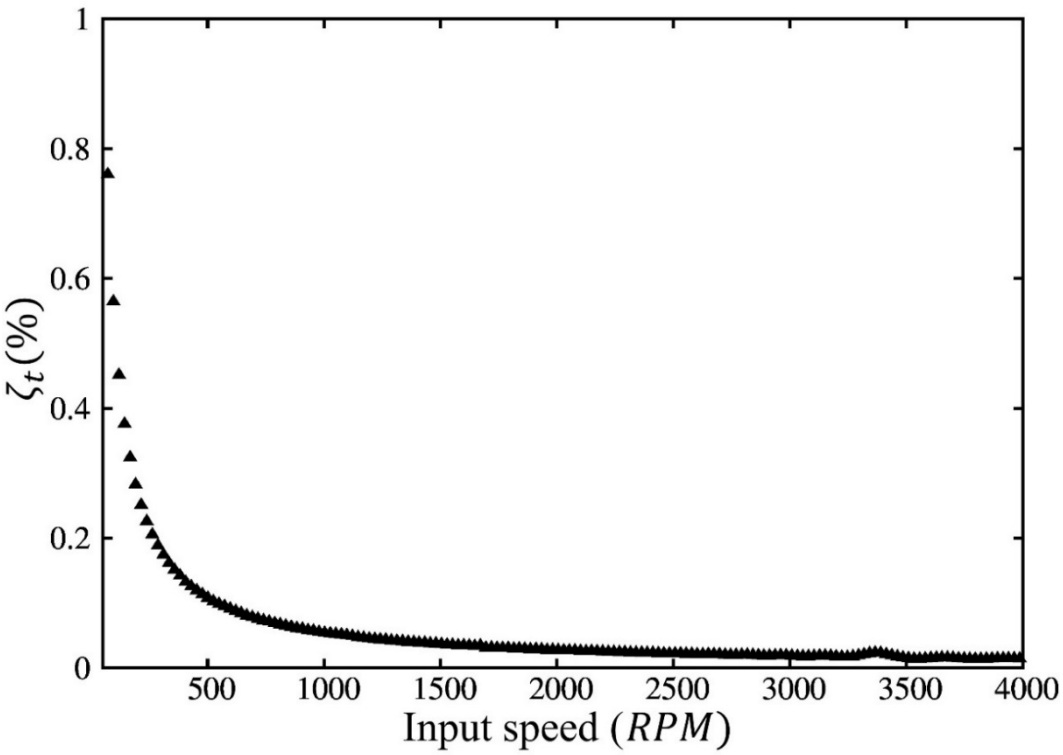

Figure 3.14: Tangential damping ratio versus input speed for $T = 250\ Nm$. Helical gears.

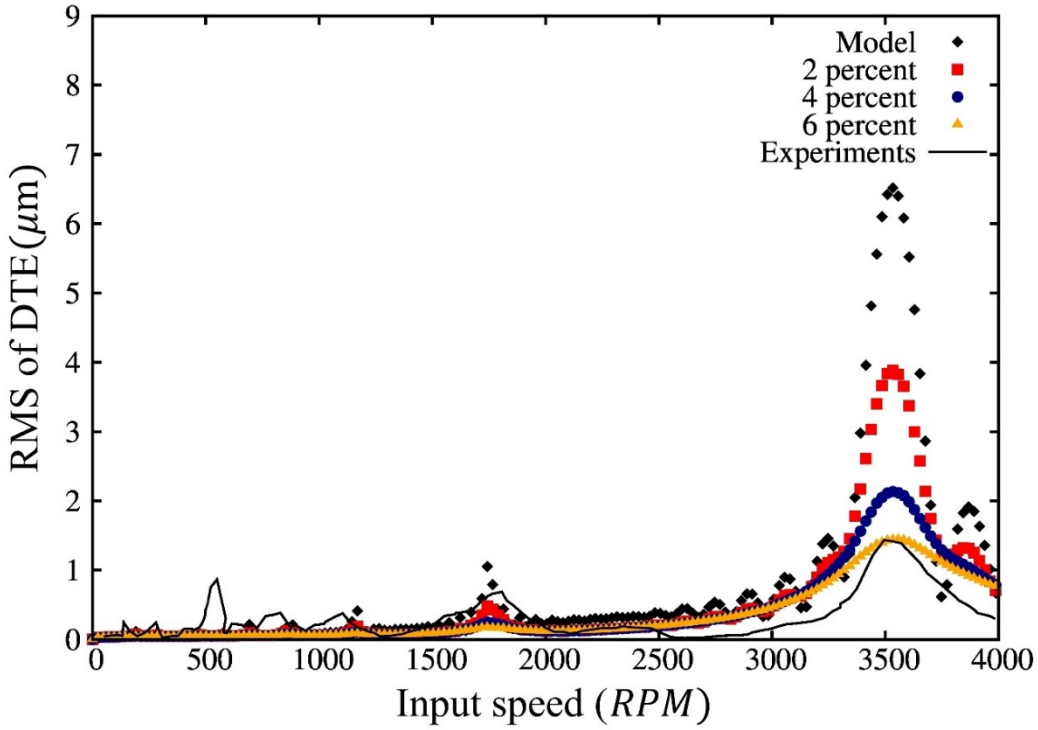

Figure 3.15: Measured [141] and calculated RMS of *DTE* versus input speed for $T = 250\ Nm$. Various damping ratios. Helical gears.

Cette thèse est accessible à l'adresse : http://theses.insa-lyon.fr/publication/2016LYSEI089/these.pdf
© [M. Ankouni], [2016], INSA Lyon, tous droits réservés

Much higher damping is indeed needed to obtain amplitudes that are comparable to the measurements as illustrated in Figure 3.15. Figure 3.15 compares the numerical results using the present model with the results corresponding to higher constant damping. A damping ratio higher than 6 % is required to properly reproduce the amplitude of the DTE at the main critical speed. The limitation of the present approach in analyzing the dynamic behavior for helical gears is thus underlined. The gear mesh barely contributes to the amplitude reduction at critical speeds and quite different damping sources from the surrounding elements are to be investigated comprising mainly the supporting shafts and bearings.

3.4 Conclusion

The various contributions of the lubricant to the damping mechanisms in spur and helical gears have been investigated mostly based on transient EHL analyses for line contacts. Both normal and tangential effects have been considered and characterized via equivalent linearized damping elements derived from extensive numerical simulations. Internal (structural) damping has also been taken into account and added in series with the lubricant normal damping whereas the contributions of friction have been superimposed in parallel. Two different normal damping models have been employed depending on the dynamic contact conditions, i.e. when contact between the teeth is established or when tooth contact is momentarily lost and a regime characterized by impacts arises (spur gears). These damping elements have been inserted into a classic one-degree-of-freedom gear dynamic model and the corresponding numerical predictions have been compared with benchmark experimental results from the literature. Focusing on spur gears, it has been shown that the simulated dynamic transmission errors compare well with the measurements for a variety of gears and operating conditions thus proving that the damping models are sound. Based on these results, it has been observed that the lubricant seems to contribute mostly to the damping mechanism in the presence of shocks whereas internal damping is prevalent for the other regimes. These findings are in line with the theoretical and measurement results obtained by Dareing and Johnson [142] for rolling contact vibrations and suggest that damping should depend on load and be sensitive to temperature via the lubricant properties. The case of helical gears, however, needs to be analyzed from a rather different perspective since contact losses at critical speeds do not generally occur and consequently rather different damping mechanisms should be expected.

Cette thèse est accessible à l'adresse : http://theses.insa-lyon.fr/publication/2016LYSEI089/these.pdf
© [M. Ankouni], [2016], INSA Lyon, tous droits réservés

Cette thèse est accessible à l'adresse : http://theses.insa-lyon.fr/publication/2016LYSEI089/these.pdf
© [M. Ankouni], [2016], INSA Lyon, tous droits réservés

Chapter 4

Application to gear dynamics: Three dimensional model

Based on the results in chapter 3, extended gear models need to be employed in order to simulate the damping mechanisms in helical gears and more specifically the couplings between the mesh and shaft-bearing dissipative properties. To this end, a three-dimensional model is set up which accounts for torsional, bending, axial displacements and makes it possible to consider shafts and bearings of different natures.

4.1 3D Lumped parameter model

The model comprises 6 nodes with 6 degrees of freedom each, in order to simulate simple geared transmissions with one pinion-gear pair supported by two parallel shafts with bearings at the ends of each shaft as illustrated in Figure 4.1.

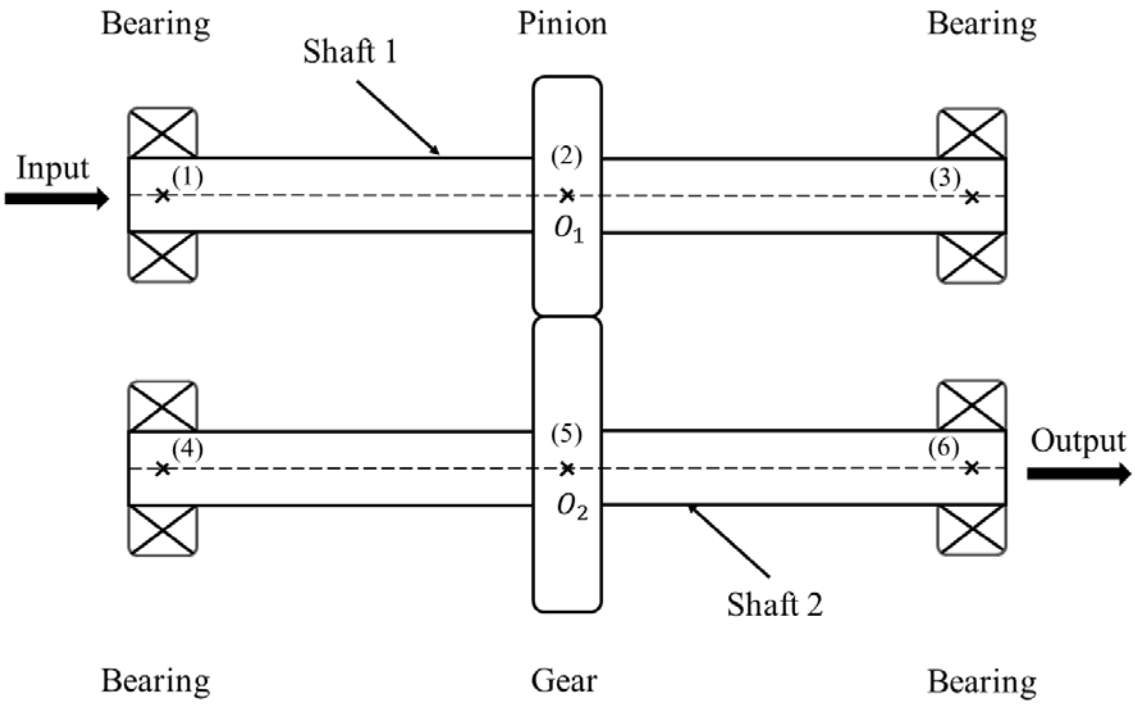

Figure 4.1: Lumped parameter model.

Cette thèse est accessible à l'adresse : http://theses.insa-lyon.fr/publication/2016LYSEI089/these.pdf
© [M. Ankouni], [2016], INSA Lyon, tous droits réservés

The state equations associated with this model are of the form:

$$[M]\ddot{X} + [C(t,X)]\dot{X} + [K(t,X)]X = F_0 + F_\delta(t,\delta_e) + F_{\dot{\delta}}\left(t,\dot{\delta_e}\right) + F_t(t,\dot{X}) \tag{4.1}$$

where

X represents the total degrees of freedom vector.

$[M],[C(t,X)]$ and $[K(t,X)]$ are the mass, damping and stiffness matrices. Damping and stiffness matrices are generally nonlinear and time-varying.

F_0 , constant applied torques.

$F_\delta(t,\delta_e)$ introduces the contribution of shape deviations.

$F_{\dot{\delta}}(t,\dot{\delta_e})$ results from the mesh normal contribution to the damping mechanism.

$F_t(t,\dot{X})$ results from the lubricant shear contribution to the damping mechanism.

The mass, stiffness and damping matrices are derived subsequently as the sum of the different matrices related to gears, shafts and bearings. A classic approach is used regarding the mass and stiffness whereas the overall damping matrix is original and constructed by considering the various damping sources in the transmission including the mesh contribution.

4.1.1 Gear-Pinion Pair

a. Mass and Stiffness

The pinion and gear are assimilated to two rigid cylinders with 6 degrees of freedom each as in Figure 4.2. The corresponding 12 degrees of freedom are:

6 translations: u_1, v_1, w_1 (pinion) and u_2, v_2, w_2 (gear)

6 rotations: ϕ_1, ψ_1, θ_1 (pinion) and ϕ_2, ψ_2, θ_2 (gear)

O_1, O_2 are the pinion and gear centers respectively.

The axial and radial displacements of the gear and pinion centers are expressed as follows:

$$\vec{v}_1(O_1) = v_1\vec{s} + w_1\vec{t} + u_1\vec{z} \tag{4.2}$$

$$\vec{v}_2(O_2) = v_2\vec{s} + w_2\vec{t} + u_2\vec{z} \tag{4.3}$$

The rotational displacements read:

Cette thèse est accessible à l'adresse : http://theses.insa-lyon.fr/publication/2016LYSEI089/these.pdf
© [M. Ankouni], [2016], INSA Lyon, tous droits réservés

$$\vec{\omega}_1 = \phi_1 \vec{s} + \psi_1 \vec{t} + \theta_1 \vec{z} \tag{4.4}$$

$$\vec{\omega}_2 = \phi_2 \vec{s} + \psi_2 \vec{t} + \theta_2 \vec{z} \tag{4.5}$$

The inertial effects of the gear-pinon pair are introduced through a diagonal matrix $[M_G]$ that includes the mass of each gear and the moments of inertia with respect to each axis of the $(\vec{S}, \vec{T}, \vec{Z})$ coordinate system (Figure 4.2) as:

$$[M_G] = \begin{bmatrix} m_1 & 0 & 0 & 0 & 0 & 0 & \cdots & \cdots & \cdots & \cdots & \cdots & 0 \\ & m_1 & 0 & 0 & 0 & 0 & & & & & & \vdots \\ & & m_1 & 0 & 0 & 0 & & & & & & \vdots \\ & & & I_1 & 0 & 0 & & & & & & \vdots \\ & & & & I_1 & 0 & & & & & & \vdots \\ & & & & & I_{02} & & & & & & \vdots \\ & & & & & & m_2 & & & & & \vdots \\ & & & & & & & m_2 & & & & \vdots \\ & & & sym & & & & & m_2 & & & \vdots \\ & & & & & & & & & I_2 & & \vdots \\ & & & & & & & & & & I_2 & \vdots \\ & & & & & & & & & & & I_{02} \end{bmatrix} \tag{4.6}$$

where m_1, m_2 denotes the mass of the pinion and gear respectively, and I_1, I_2, I_{01}, I_{02} represents their moments of inertia re the three axes $(\vec{S}, \vec{T}, \vec{Z})$.

The corresponding stiffness matrix is obtained by considering the elastic component of the elemental force at point of contact M transmitted between the pinion and the gear (see Figure 4.3):

$$d\vec{F}(M) = k(M)\Delta(M)dM.\vec{n} \tag{4.7}$$

where $k(M)$ represents the time-varying mesh stiffness and $\vec{n}$ the unit normal vector to the tooth flanks at point M.

The normal deflection $\Delta(M)$ can be expressed as:

$$\Delta(M) = \vec{v}_1(M).\vec{n} - \vec{v}_2(M).\vec{n} - \delta_e(M) \tag{4.8}$$

$$\Delta(M) = V(M)^T q - \delta_e(M) \tag{4.9}$$

Cette thèse est accessible à l'adresse : http://theses.insa-lyon.fr/publication/2016LYSEI089/these.pdf
© [M. Ankouni], [2016], INSA Lyon, tous droits réservés

where $V(M) = \begin{bmatrix} \vec{n} \\ \overrightarrow{O_1M} \times \vec{n} \\ -\vec{n} \\ -\overrightarrow{O_2M} \times \vec{n} \end{bmatrix}$, $\delta_e(M)$ represents the initial separation caused by tooth modifications or errors.

Integrating the elemental force $d\vec{F}$ and developing the force wrench between the pinion and gear lead to the time-varying mesh stiffness matrix $[K_m(t,X)]$ and the excitation vector related to shape deviations $F_\delta(t,\delta e)$ under the form:

$$[K_m(t,X)] = \int k(M)V(M)V(M)^T dM \tag{4.10}$$

$$F_\delta(t,\delta e) = \int k(M)\delta e(M)V(M)dM \tag{4.11}$$

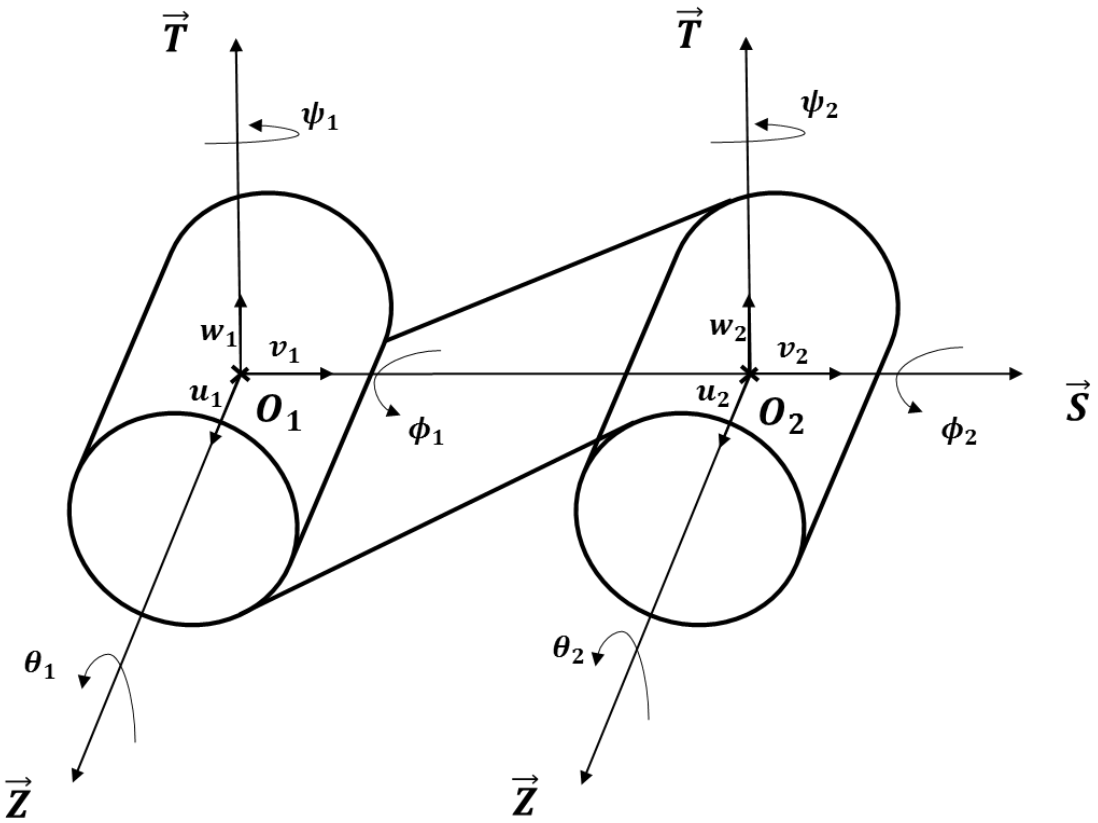

Figure 4.2: Pinion-Gear Pair and base plane.

Cette thèse est accessible à l'adresse : http://theses.insa-lyon.fr/publication/2016LYSEI089/these.pdf
© [M. Ankouni], [2016], INSA Lyon, tous droits réservés

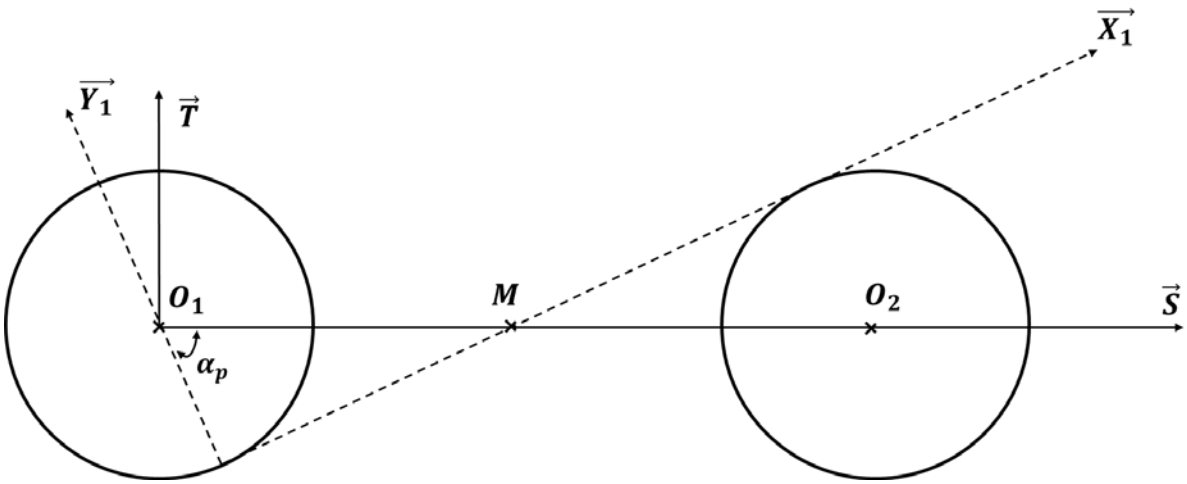

Figure 4.3: Line of action and bases definition.

b. Mesh damping

A gear mesh damping matrix is developed as the combination of the tangential and the normal contributions to the damping related to the gear teeth and the lubricant separating the mating surfaces. Both contributions are developed subsequently.

As considered for the torsional model, friction forces between the mating teeth contribute to the overall damping mechanism and their contribution is introduced using the model proposed by Diab et al. [138]. Considering the lumped parameter model for the gear-pinion pair as in Figure 4.2, the velocity of any potential point of contact on the base plane M, reads:

$$\vec{V}(M_1) = \Omega_1 \vec{z} \times \overrightarrow{O_1M_1} + \dot{\vec{v}}_1(O_1) + \dot{\vec{\omega}}_1 \times \overrightarrow{O_1M_1} \tag{4.12}$$

$$\vec{V}(M_2) = \Omega_2 \vec{z} \times \overrightarrow{O_2M_2} + \dot{\vec{v}}_2(O_2) + \dot{\vec{\omega}}_2 \times \overrightarrow{O_2M_2} \tag{4.13}$$

The tangential dynamic surface velocities in the off line of action direction of the gears are as follows:

$$\upsilon_1 = \bar{\upsilon}_1 + \tilde{\upsilon}_1 = X(M_1)\Omega_1 + \dot{\vec{v}}_1(O_1) \cdot \vec{Y} + \dot{\vec{\omega}}_1 \cdot (\overrightarrow{O_1M_1} \times \vec{Y}) \tag{4.14}$$

$$\upsilon_2 = \bar{\upsilon}_2 + \tilde{\upsilon}_2 = -X(M_2)\Omega_2 + \dot{\vec{v}}_2(O_2) \cdot \vec{Y} + \dot{\vec{\omega}}_2 \cdot (\overrightarrow{O_2M_2} \times \vec{Y}) \tag{4.15}$$

The dynamic component $\Delta\hat{\upsilon}$ reads:

$$\begin{aligned} \Delta\hat{\upsilon} = &(X(M_2)\Omega_2 + X(M_1)\Omega_1) - \dot{\vec{v}}_2(O_2) \cdot \vec{Y} + \dot{\vec{v}}_1(O_1) \cdot \vec{Y} \\ &-\dot{\vec{\omega}}_2 \cdot \left(\overrightarrow{O_2M_2} \times \vec{Y}\right) + \dot{\vec{\omega}}_1 \cdot \left(\overrightarrow{O_1M_1} \times \vec{Y}\right) \\ &= \bar{\upsilon}_1 - \bar{\upsilon}_2 + U^T \dot{q} \end{aligned} \tag{4.16}$$

Cette thèse est accessible à l'adresse : http://theses.insa-lyon.fr/publication/2016LYSEI089/these.pdf
© [M. Ankouni], [2016], INSA Lyon, tous droits réservés

where

$$U = \begin{bmatrix} \vec{Y} \\ \overrightarrow{O_1M_1} \times \vec{Y} \\ -\vec{Y} \\ -\overrightarrow{O_2M_2} \times \vec{Y} \end{bmatrix} \text{ and } q = \begin{bmatrix} v_1 \\ w_1 \\ u_1 \\ \phi_1 \\ \psi_1 \\ \theta_1 \\ v_2 \\ w_2 \\ u_2 \\ \phi_2 \\ \psi_2 \\ \theta_2 \end{bmatrix}$$

thus leading to the following expression of the fluid friction force on one tooth

$$F_t = \mu_f F_N = \bar{F}_t + \frac{F_N}{p_{moy}}\left(1 - \frac{A_c}{A_0}\right)\frac{\tau_L}{\Delta\bar{v}} U^T \dot{q} \tag{4.17}$$

From which, the equivalent tangential damping by the lubricant is deduced as:

$$c_t = \frac{F_N}{p_{moy}}\left(1 - \frac{A_c}{A_0}\right)\frac{\tau_L}{\Delta\bar{v}} \tag{4.18}$$

The tangential forces $\overrightarrow{F_{t_1}}$ and $\overrightarrow{F_{t_2}}$ are expressed as:

$$F_{t_1} = \bar{F}_{t_1} + U^T \dot{q} \iint \frac{\eta(x)}{h(x)} ds = \bar{F}_{t_1} + c_t U^T \dot{q} \tag{4.19}$$

$$F_{t_2} = \bar{F}_{t_2} + U^T \dot{q} \iint \frac{\eta(x)}{h(x)} ds = \bar{F}_{t_2} + c_t U^T \dot{q} \tag{4.20}$$

$$\overrightarrow{F_{t_1}} = -F_{t_1}\vec{Y} \tag{4.21}$$

$$\overrightarrow{F_{t_2}} = F_{t_2}\vec{Y} \tag{4.22}$$

A compact form of the resulting viscous shear forces wrench is finally obtained as:

$$\begin{cases} -F_{t_1}\vec{Y} \\ -\overrightarrow{O_1M_1} \times F_{t_1}\vec{Y} \\ F_{t_2}\vec{Y} \\ \overrightarrow{O_2M_2} \times F_{t_2}\vec{Y} \end{cases} = -c_t U U^T \dot{q} + c_t U^T \dot{q} = -[C_t(t)]\dot{q} + F_t(t, \dot{X}) \tag{4.23}$$

where $[C_t(t)]$ is a time-varying gear mesh viscous damping matrix generated by tooth friction.

Cette thèse est accessible à l'adresse : http://theses.insa-lyon.fr/publication/2016LYSEI089/these.pdf
© [M. Ankouni], [2016], INSA Lyon, tous droits réservés

Furthermore, the normal viscous elemental force at the point of contact M of the gears reads:

$$d\overrightarrow{F_n}(M) = c_n(M)\dot{\Delta}(M)dM.\vec{n} \tag{4.24}$$

The normal deflection $\Delta(M)$ reads:

$$\Delta(M) = \vec{u}_1(M).\vec{n} - \vec{u}_2(M).\vec{n} - \delta_e(M) \tag{4.25}$$

$$\Delta(M) = V(M)^T q - \delta_e(M) \tag{4.26}$$

where $V(M)$ and $\delta_e(M)$ are defined as previously.

The resulting normal viscous forces read:

$$F_{n_1} = \int c_n(M)\dot{\Delta}(M)dM = \int (c_n(M)V(M)^T\dot{q} - c_n(M)\dot{\delta}_e(M))dM \tag{4.27}$$

$$F_{n_2} = \int c_n(M)\dot{\Delta}(M)dM = \int \left(c_n(M)V(M)^T\dot{q} - c_n(M)\dot{\delta}_e(M)\right)dM \tag{4.28}$$

$$\overrightarrow{F_{n_1}} = -F_{n_1}\vec{n} \tag{4.29}$$

$$\overrightarrow{F_{n_2}} = F_{n_2}\vec{n} \tag{4.30}$$

The resulting viscous normal forces and moments on gear and pinion:

$$\begin{cases} -F_{n_1}\vec{n} \\ -\overrightarrow{O_1M} \times F_{n_1}\vec{n} \\ F_{n_2}\vec{n} \\ \overrightarrow{O_2M} \times F_{n_2}\vec{n} \end{cases} = -\int c_n(M)V(M)V(M)^T dM\dot{q} + \int c_n(M)\dot{\delta}_e V(M)dM$$

$$= -\int c_n(M)VV^T\dot{q} + \int c_n(M)\dot{\delta}_e V$$

$$= -[C_n(t)]\dot{q} + F_{\dot{\delta}}(t, \dot{\delta}_e) \tag{4.31}$$

where c_n is the time-varying normal damping coefficient which, depending on the contact conditions, is expressed as :

for permanent contacts,

$$c_n = \left(\frac{1}{c_{st}} + \frac{1}{c_l}\right)^{-1}$$

b) or, in case of contact losses and shocks,

Cette thèse est accessible à l'adresse : http://theses.insa-lyon.fr/publication/2016LYSEI089/these.pdf
© [M. Ankouni], [2016], INSA Lyon, tous droits réservés

$$c_n = c_{im}$$

where c_l refers to the equivalent viscous damping due to normal loading, c_{st} is the structural damping (set to 0.5-1%) and c_{im} is the equivalent damping provided by the lubricant during impact.

The resulting normal viscous damping matrix $[C_n(t)]$ can be written as follows:

$$[C_n(t)] = \begin{pmatrix} [C_{n_{1,1}}] & [C_{n_{1,2}}] \\ [C_{n_{2,1}}] & [C_{n_{2,2}}] \end{pmatrix} \Bigg\} 12DoF \tag{4.32}$$

As well as for the tangential viscous damping matrix $[C_t(t)]$:

$$[C_t(t)] = \begin{pmatrix} [C_{t_{1,1}}] & [C_{t_{1,2}}] \\ [C_{t_{2,1}}] & [C_{t_{2,2}}] \end{pmatrix} \Bigg\} 12DoF \tag{4.33}$$

Resulting in a mesh damping matrix that can be introduced into the overall damping matrix of the complete system as follows:

$$[C_m(t,X)] = \begin{pmatrix} 0 & & & & \\ & [C_{n_{1,1}}] + [C_{t_{1,1}}] & \cdots & [C_{n_{1,2}}] + [C_{t_{1,2}}] & \\ & \vdots & \ddots \; 0 & \vdots & \\ & [C_{n_{2,1}}] + [C_{t_{2,1}}] & \cdots & [C_{n_{2,2}}] + [C_{t_{2,2}}] & \\ & & & & 0 \end{pmatrix} \Bigg\} 36DoF \tag{4.34}$$

4.1.2 Shafts

a. Mass and Stiffness

Some classic mass and stiffness matrix are used to account for all the possible motions of the shaft elements. Uniform cylindrical segments with two nodes and 6 degree of freedom per node are considered as in Figure 4.4.

Cette thèse est accessible à l'adresse : http://theses.insa-lyon.fr/publication/2016LYSEI089/these.pdf
© [M. Ankouni], [2016], INSA Lyon, tous droits réservés

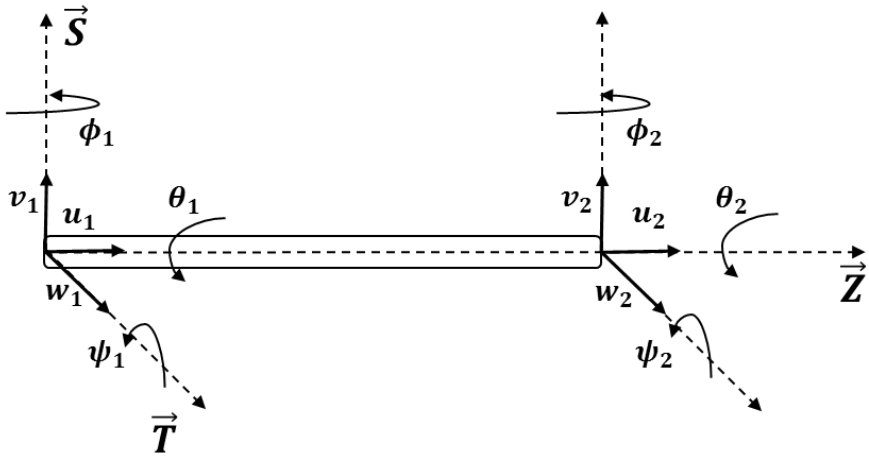

Figure 4.4: Degrees of freedom for shaft elements.

The total mass and stiffness matrices are expressed as the sum of some individual matrices associated with traction, bending and torsion:

$$[M_s] = [M_{ax}] + [M_{be_S}] + [M_{be_T}] + [M_{to}] \tag{4.35}$$

$$[K_s] = [K_{ax}] + [K_{be_S}] + [K_{be_T}] + [K_{to}] \tag{4.36}$$

where

$[M_{ax}]$ and $[K_{ax}]$ represent the mass and stiffness matrices related to axial displacements:

$$[M_{ax}] = \frac{\rho SL}{6}\begin{bmatrix} 2 & 1 \\ 1 & 2 \end{bmatrix} \rightarrow \begin{Bmatrix} u_1 \\ u_2 \end{Bmatrix} \tag{4.37}$$

$$[K_{ax}] = \frac{ES}{L}\begin{bmatrix} 1 & -1 \\ -1 & 1 \end{bmatrix} \rightarrow \begin{Bmatrix} u_1 \\ u_2 \end{Bmatrix} \tag{4.38}$$

$[M_{be_S}]$, $[M_{be_T}]$, $[K_{be_S}]$ and $[K_{be_T}]$ represent respectively the mass and stiffness matrices related to bending in two perpendicular radial directions:

$$[M_{be_S}] = \frac{\rho SL}{420}\begin{bmatrix} 156 & -22L & 54 & 13L \\ & 4L^2 & 13L & -3L^2 \\ & & 156 & 22L \\ Sym. & & & 4L^2 \end{bmatrix} \rightarrow \begin{Bmatrix} v_1 \\ \psi_1 \\ v_2 \\ \psi_2 \end{Bmatrix} \tag{4.39}$$

$$[M_{be_T}] = \frac{\rho SL}{420}\begin{bmatrix} 156 & -22L & 54 & 13L \\ & 4L^2 & 13L & -3L^2 \\ & & 156 & 22L \\ Sym. & & & 4L^2 \end{bmatrix} \rightarrow \begin{Bmatrix} w_1 \\ \phi_1 \\ w_2 \\ \phi_2 \end{Bmatrix} \tag{4.40}$$

Cette thèse est accessible à l'adresse : http://theses.insa-lyon.fr/publication/2016LYSEI089/these.pdf
© [M. Ankouni], [2016], INSA Lyon, tous droits réservés

$$[K_{be_S}] = \frac{E\ I_x}{(1+a)L^3}\begin{bmatrix} 12 & 6L & -12 & 6L \\ & (4+a)L^2 & -6L & (2-a)L^2 \\ & & 12 & -6L \\ Sym. & & & (4+a)L^2 \end{bmatrix} \rightarrow \begin{Bmatrix} v_1 \\ \psi_1 \\ v_2 \\ \psi_2 \end{Bmatrix} \tag{4.41}$$

$$[K_{be_T}] = \frac{E\ I_x}{(1+a)L^3}\begin{bmatrix} 12 & -6L & -12 & -6L \\ & (4+a)L^2 & 6L & (2-a)L^2 \\ & & 12 & 6L \\ Sym. & & & (4+a)L^2 \end{bmatrix} \rightarrow \begin{Bmatrix} w_1 \\ \phi_1 \\ w_2 \\ \phi_2 \end{Bmatrix} \tag{4.42}$$

$[M_{to}]$ and $[K_{to}]$ represent the mass and stiffness matrices related to torsion:

$$[M_{to}] = \frac{I_0 L}{6}\begin{bmatrix} 2 & 1 \\ 1 & 2 \end{bmatrix} \rightarrow \begin{Bmatrix} \theta_1 \\ \theta_2 \end{Bmatrix} \tag{4.43}$$

$$[K_{to}] = \frac{G\ J}{L}\begin{bmatrix} 1 & -1 \\ -1 & 1 \end{bmatrix} \rightarrow \begin{Bmatrix} \theta_1 \\ \theta_2 \end{Bmatrix} \tag{4.44}$$

Where

$$a = \frac{12EI_x}{GL^2S}, I_x = \frac{\pi R^4}{4}, J = \frac{\pi R^4}{2}, I_0 = \rho J$$

L: Length of the shaft element

S: surface area of cross section

E: Young's Modulus

G: Shear modulus

ρ: density

b. Damping

A damping matrix that accounts for the internal dissipation in the shaft elements is introduced based on a modal analysis of the system.

For low to moderate modal densities, modal damping matrices $[C_{s_\phi}]$ can be supposed to be orthogonal with respect to the modes and can be expressed as:

Cette thèse est accessible à l'adresse : http://theses.insa-lyon.fr/publication/2016LYSEI089/these.pdf
© [M. Ankouni], [2016], INSA Lyon, tous droits réservés

$$\left[C_{s_\phi}\right] = diag\left(2\zeta_p\sqrt{k_{\phi_p} m_{\phi_p}}\right), p = 1, N_{mod} \tag{4.45}$$

with: ζ_p: modal damping factor associated with mode P (later set to 0.5-1% for internal damping).

k_{ϕ_p}, m_{ϕ_p}: modal stiffness and mass associated with mode P.

To uncouple the different sources of damping and only account for the contribution of the internal damping of the shafts, a limited number of modes is considered, i.e., the modes with zero or negligible amount of strain energy stored in the bearings and gears (for which the major contribution comes from the shafts). Following Craig [130], a physical internal damping matrix can be determined by a truncated summation over a limited number of modes as:

$$[C_s] = \sum_{p=1}^{N_r} \frac{2\zeta_p\omega_p}{m_{\phi_p}}\left([M]\Phi_p\right)\left([M]\Phi_p\right]^T) \tag{4.46}$$

with: N_r: the number of modes related to shaft elements.

$\omega_p = \sqrt{k_{\phi_p}/m_{\phi_p}}$.

Φ_p: the eigenvector associated with mode P.

4.1.3 Bearings

It is commonly accepted that bearings are likely to play a determinant role in vibration transfer. They are generally characterized by a nonlinear behavior which is dependent on operational conditions and different types of defects so that bearings can also, to a certain extent, be regarded as possible sources of excitation. This memoir being centered on gears, a linearized bearing model is used leading to lumped stiffness and damping parameters deduced from radial displacements (v, w) assuming that the contributions of axial displacements and infinitesimal rotations can be neglected. Both journal bearings and rolling element bearings are considered and successively analyzed in what follows.

a. Journal bearings

Journal bearings are generally suited for high speed applications and are characterized by their low friction and relatively high damping levels. Hydrodynamic lubrication normally prevails in

Cette thèse est accessible à l'adresse : http://theses.insa-lyon.fr/publication/2016LYSEI089/these.pdf
© [M. Ankouni], [2016], INSA Lyon, tous droits réservés

journal bearings and the shaft and bushing are fully separated by a pressurized thin lubricant film. The dynamic behavior of journal bearings is usually investigated based on a numerical solution of the Reynolds equation while surface deflections are neglected. In this section, the basic developments used to derive the so-called dynamic coefficients of journal bearings are briefly presented. A more detailed formulation of the problem along with the numerical values of the bearing stiffness and damping introduced later in the proposed model can be found for various geometries and operating conditions in [143].

The force applied at the bearing generally oscillates around a mean value that corresponds to the static loading F_0. Assuming that both displacements and velocities induced by the dynamic loading in the vicinity of the static position remain small, the relation between the dynamic bearing force denoted F_b and the displacement and velocities can be linearized around the static position $A_1(x_0, y_0)$ (Figure 4.5) as follows:

$$F_b(\{x,y\}^t) = F_0(\{x_0,y_0\}^t) - \left[\frac{\partial F_b}{\partial u}\right](\{x,y\}^t - \{x_0,y_0\}^t) - \left[\frac{\partial F_b}{\partial \dot{u}}\right]\{\dot{x},\dot{y}\}^t \tag{4.47}$$

where x and y represent the displacements around the static position, $\dot{x}$ and $\dot{y}$ are the components of the velocity of the center of the shaft, $[\partial F_b/\partial u]$ and $[\partial F_b/\partial \dot{u}\,]$ denotes respectively the tangent stiffness and damping matrices of the bearing.

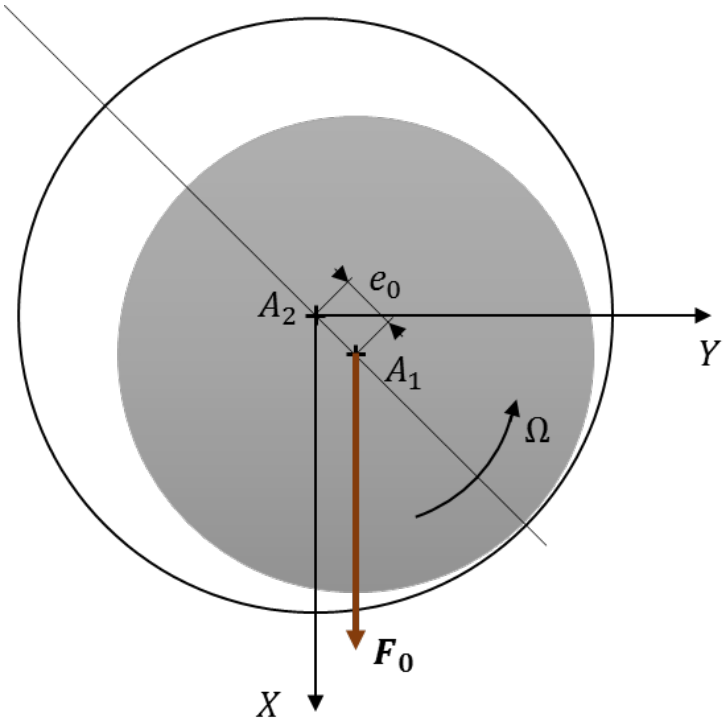

Figure 4.5: Frame definition for the computation of the journal bearing dynamic coefficients.

Cette thèse est accessible à l'adresse : http://theses.insa-lyon.fr/publication/2016LYSEI089/these.pdf
© [M. Ankouni], [2016], INSA Lyon, tous droits réservés

The stiffness and damping matrices are written as:

$$\left[\frac{\partial F_b}{\partial u}\right] = \begin{bmatrix} K_{b_{xx}} & K_{b_{xy}} \\ K_{b_{yx}} & K_{b_{yy}} \end{bmatrix}, \left[\frac{\partial F_b}{\partial \dot{u}}\right] = \begin{bmatrix} C_{b_{xx}} & C_{b_{xy}} \\ C_{b_{yx}} & C_{b_{yy}} \end{bmatrix} \tag{4.48}$$

The eight coefficients presented in equation (4.48) are computed using Reynolds equation that describes the flow of the lubricant withstanding the dynamic loading. For cylindrical coordinates, Reynolds equation for hydrodynamic lubrication reads:

$$\frac{1}{R^2}\frac{\partial}{\partial \theta}\left(\frac{h^3}{\mu}\frac{\partial p}{\partial \theta}\right) + \frac{\partial}{\partial z}\left(\frac{h^3}{\mu}\frac{\partial p}{\partial z}\right) = 6\Omega\frac{\partial h}{\partial \theta} + 12(\dot{x}cos\theta + \dot{y}sin\theta) \tag{4.49}$$

The problem can be normalized, i.e. the force components are divided by the static load and the displacements and velocities are made dimensionless with respect to the clearance and the angular velocity. The various dynamic coefficients are determined by imposing small perturbations in displacement and speed to the center of the shaft A_1 in both X and Y directions and computing the resulting additional dynamic forces, see [143]. One must note that the obtained values are expressed in the frame (A_2, X, Y) as in Figure 4.5, where the X direction is considered parallel to the static bearing force F_0. A change of basis is thus needed to obtain the stiffness and damping coefficients in the frame (A_2, S, T, Z) employed in the gear dynamic model see Figure 4.2. The resulting stiffness and damping matrices corresponding to each bearing are as follows:

$$\left.\begin{matrix} [K_{b_i}] = \begin{bmatrix} K_{b_{iv,v}} & K_{b_{iv,w}} & \cdots \\ K_{b_{iw,v}} & K_{b_{iw,w}} & \cdots \\ \vdots & & \ddots \end{bmatrix}_{S,T,Z}, [C_{b_i}] = \begin{bmatrix} C_{b_{iv,v}} & C_{b_{iv,w}} & \cdots \\ C_{b_{iw,v}} & C_{b_{iw,w}} & \cdots \\ \vdots & & \ddots \end{bmatrix}_{S,T,Z} \end{matrix}\right\} 6DoF \tag{4.50}$$

where $i = 1,3,4,6$ denotes the number of the bearing (node) considered.

After assembly of the individual matrices, the overall bearing damping matrix takes a form similar to that of the stiffness matrix, i.e.,

$$[C_b] = \left.\begin{pmatrix} [C_{b_1}] & \cdots & \cdots & \cdots & \cdots & \cdots & \cdots \\ & \ddots & & & & & \vdots \\ & & [C_{b_3}] & & & & \vdots \\ & sym & & [C_{b_4}] & & & \vdots \\ & & & & \ddots & & \vdots \\ & & & & & & [C_{b_6}] \end{pmatrix}\right\} 36DoF \tag{4.51}$$

Cette thèse est accessible à l'adresse : http://theses.insa-lyon.fr/publication/2016LYSEI089/these.pdf
© [M. Ankouni], [2016], INSA Lyon, tous droits réservés

b. Rolling element bearings

Rolling element bearings are appropriate for low to moderate speeds. Various types of bearings are used depending on the application (ball bearing, roller bearings, etc.). The dynamic behavior of rolling bearings is far from being simple [144-146], however a detailed analysis of its nonlinear behavior is beyond the scope of our study. Hence some simple configuration of a rolling element bearing is considered. Diagonal matrices that include representative values of stiffness and damping related to the rolling bearings are introduced.

Based on the previous analysis the overall mass, stiffness and damping matrices (equation (4.1)) respectively read:

$$[M] = [M_s] + [M_G] \tag{4.52}$$

$$[K(t,X)] = [K_s] + [K_m(t,X)] + [K_b] \tag{4.53}$$

$$[\boldsymbol{C}(\boldsymbol{t},\boldsymbol{X})] = [\boldsymbol{C_s}] + [\boldsymbol{C_m}(\boldsymbol{t},\boldsymbol{X})] + [\boldsymbol{C_b}] \tag{4.54}$$

4.2 Results

Several simulations are performed for both spur and helical gears. The trends found with the single degree of freedom model are questioned and the couplings between the mesh force and the bearing damping properties are investigated.

4.2.1 Identical spur gears

The contribution of each of the previously mentioned sources of damping is analyzed considering first a spur gear transmission. A pair of identical gears is considered (Table 4.1) which are mounted on identical shafts of 320 mm length with two uniform segments of 90 mm diameter each. A 300 Nm torque is imposed on the pinion shaft.

Number of teeth	50
Module	3 mm
Pressure angle	20°
Face width	20 mm
Outer diameter	156 mm
Pitch diameter	150 mm
Base diameter	140.95 mm

Cette thèse est accessible à l'adresse : http://theses.insa-lyon.fr/publication/2016LYSEI089/these.pdf
© [M. Ankouni], [2016], INSA Lyon, tous droits réservés

Involute contact ratio (ICR)	1.75

Table 4.1: Test gears characteristics (*identical pinion and gear*). Spur gears.

First, the contributions of the shafts and the gear mesh to the damping mechanism are inspected. The dynamic response of the gear-pinion pair is computed with and without the mesh damping matrix and the corresponding maximum dynamic factor C_f versus mesh frequency is shown in Figure 4.6. The dynamic factor is defined as the maximum dynamic mesh force to the static mesh force ratio. The response curves in Figure 4.6 underline the limited effect of the internal damping of the shafts on the dynamic behavior of the gear pair since it only slightly affects the response amplitude at the main critical speed. On the other hand, it can be observed that mesh damping, which is here dominated by the lubricant contribution when contact is lost, leads to a significant reduction in amplitudes close to the tooth critical speeds. The effect is however limited for other speeds, i.e. for permanent contact conditions where the structural deflections of the teeth appears as the major source of damping. These observations are in line with the results obtained previously using the torsional model.

Considering bearings at both ends of the shafts, they are expected to contribute to the overall damping of the system and their influence on dynamic mesh forces is highlighted hereinafter. Starting with a bearing model representative of rolling element bearings, i.e. with relatively low damping, constant stiffness and damping coefficients of $5.10^5 N/mm$ and $5\ N.s/mm$ respectively are introduced in the simulations. The dynamic factor curves in Figure 4.7 show that the amplifications at the major tooth critical speeds are unchanged whereas some secondary peaks are smoothened by bearing damping in spite of their relatively small contributions. Under these conditions, mesh damping related to impacts still dominates the overall damping.

A second series of results have been obtained considering journal bearings whose characteristics are $L/D = 0.25, R/C = 1000, \mu_0 = 0.0178$ Pa. s. Journal bearings are known to generate larger damping levels compared to rolling element bearings of comparable stiffness but their introduction in the dynamic model mainly leads to a shift of the response peaks while the response amplitudes remain more or less unchanged as illustrated in Figure 4.8.

This particular behavior has been investigated further by changing the journal bearing dimensions. The corresponding response curves are plotted in Figure 4.9 and the respective damping values versus speed are presented in Figure 4.10. As shown in Figure 4.9, three different bearings with different damping levels (Figure 4.10) lead to approximately the same response curve with negligible differences at some operational speeds.

Cette thèse est accessible à l'adresse : http://theses.insa-lyon.fr/publication/2016LYSEI089/these.pdf
© [M. Ankouni], [2016], INSA Lyon, tous droits réservés

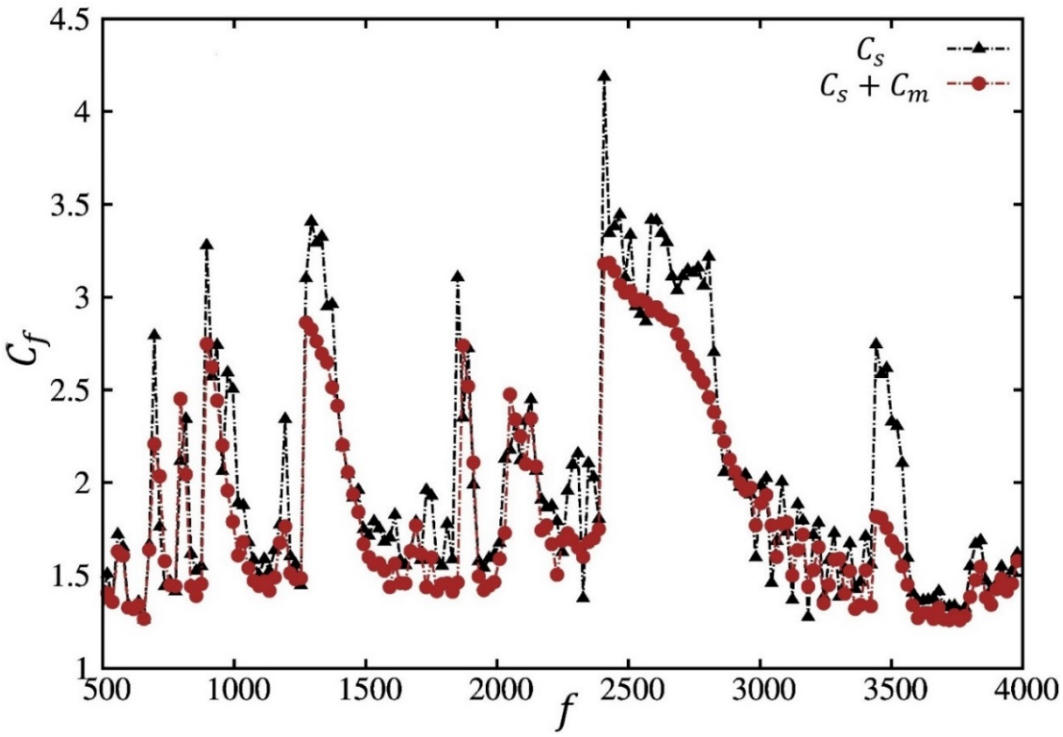

Figure 4.6: Dynamic response curves. Comparison between structural damping and mesh damping. Spur gears.

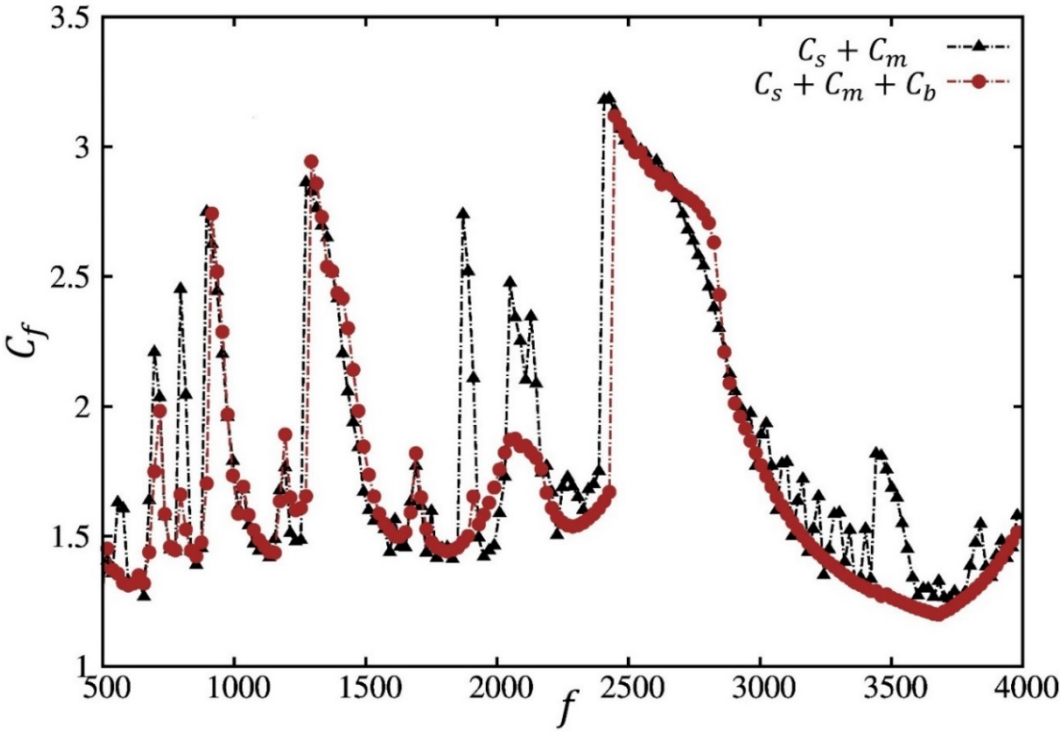

Figure 4.7: Dynamic response curves. Comparison between mesh damping and REB damping. Spur gears.

Cette thèse est accessible à l'adresse : http://theses.insa-lyon.fr/publication/2016LYSEI089/these.pdf
© [M. Ankouni], [2016], INSA Lyon, tous droits réservés

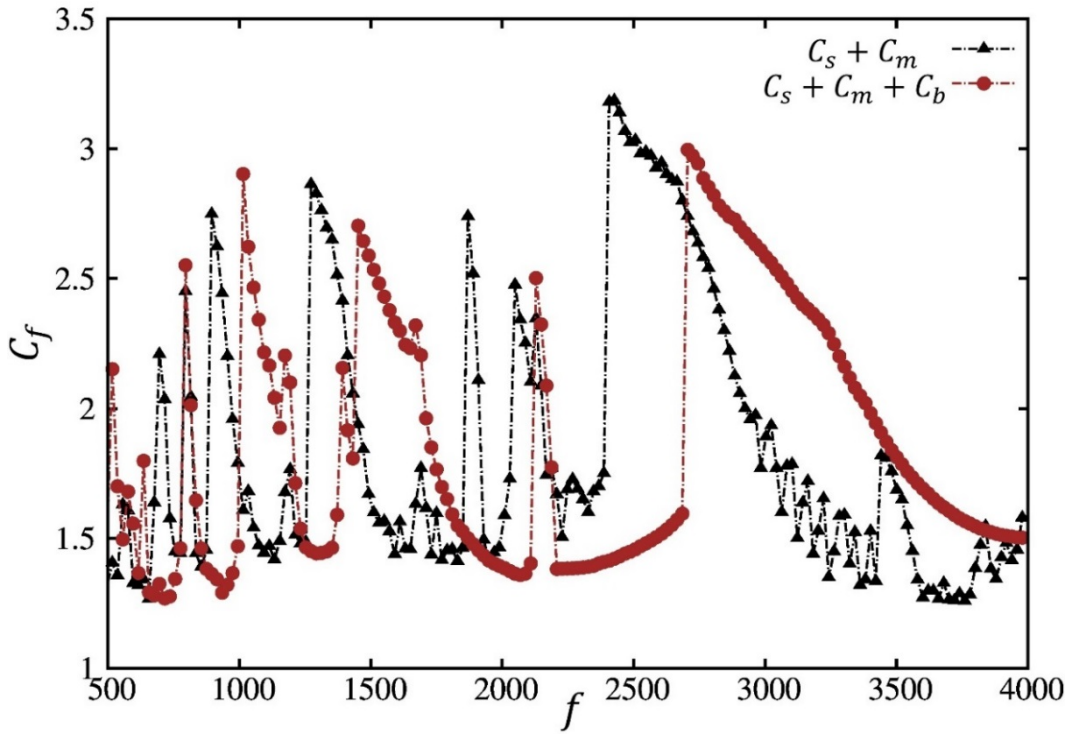

Figure 4.8: Dynamic response curves. Comparison between mesh damping and journal bearing damping. Spur gears.

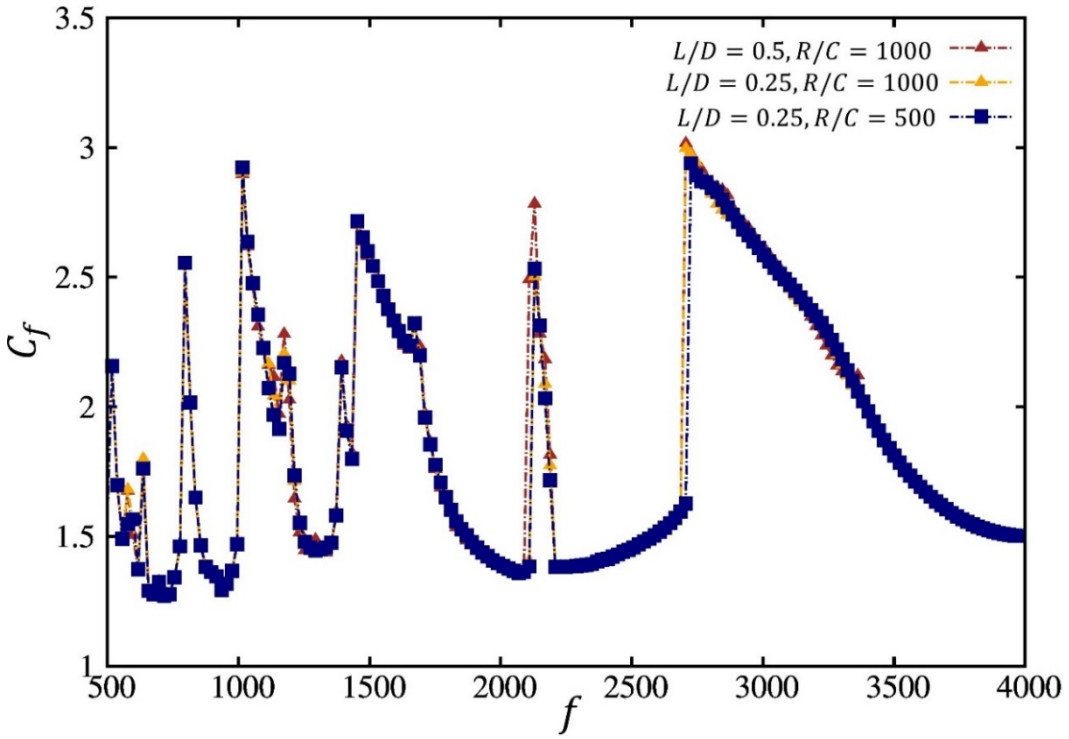

Figure 4.9: Dynamic response curves. Comparisons between various journal geometries. Spur gears.

Cette thèse est accessible à l'adresse : http://theses.insa-lyon.fr/publication/2016LYSEI089/these.pdf
© [M. Ankouni], [2016], INSA Lyon, tous droits réservés

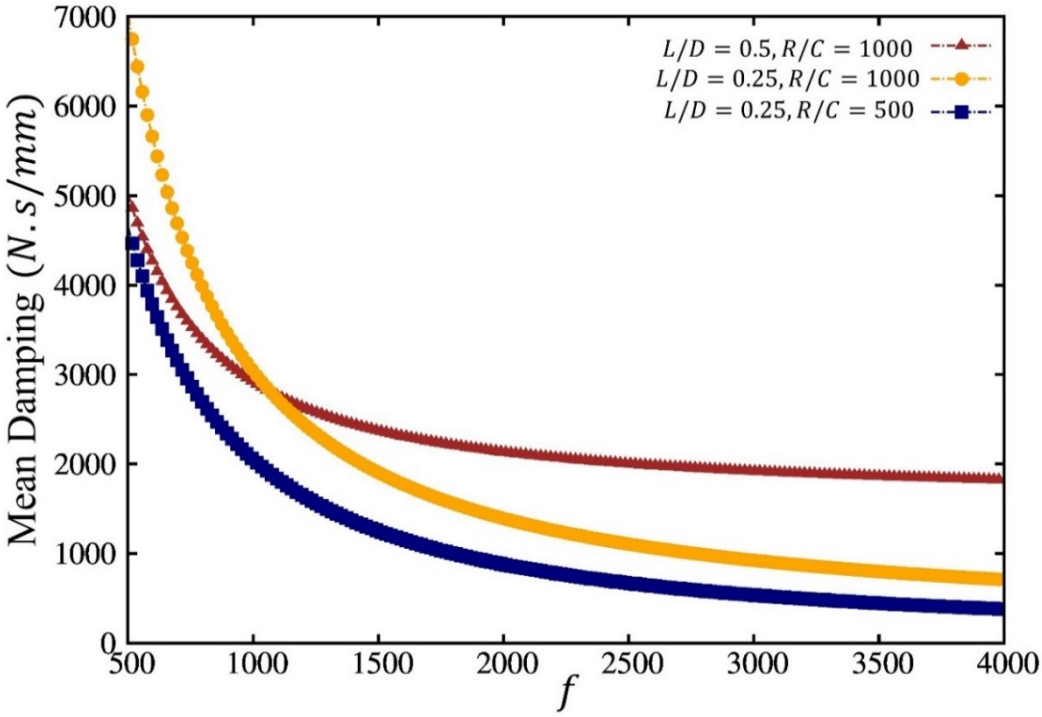

Figure 4.10: Mean journal bearing radial damping variation for different geometries as a function of the gear mesh frequency. Spur gears.

Based on these findings, one can state that i) mesh damping is the major source of damping at the main amplifications, ii) bearing generally provide a smoother behavior with shifted speeds in the case of journal bearings, and finally iii) no clear difference between rolling element bearings and journal bearings is found with regard to dynamic amplitudes, in spite of large differences in damping levels. These observations agree with the conclusions derived by Hambric et al. [147] who studied both numerically and experimentally the benefit of replacing rolling element bearings by journal bearings in a simple test gearbox which is simulated in the next section.

4.2.2 Comparisons with experimental evidence

Hambric et al. [147] stated that no clear benefits were found by replacing the rolling element bearings with journal bearings in the NASA GRC's test gearbox. This conclusion was drawn after several measurements and simulations of the vibration and sound at gear mesh frequency (*GMF*) tones for several operational speeds considering both types of bearings. The authors showed that for $2 \times GMF$ tones, the gearbox is quieter at all considered speeds when journal bearings are used, however no clear conclusion was made on the noise reduction for $1 \times GMF$ tones. The NASA GRC's test gearbox dimensions are reproduced and the three dimensional dynamic model is used to study the dynamic behavior using different bearings. The considered

Cette thèse est accessible à l'adresse : http://theses.insa-lyon.fr/publication/2016LYSEI089/these.pdf
© [M. Ankouni], [2016], INSA Lyon, tous droits réservés

gearbox comprises a pair of identical gears as in Table 4.2, supported on identical shafts of 256 mm with two uniform segments of about 35 mm each. Ball bearings support the shafts at their loaded ends and roller bearings are used at the free ends. Identical journal bearings are employed to replace the rolling element bearings otherwise ($L/D = 0.62,\ \ R/C = 1065,\ \mu_0 = 0.0294\ \mathrm{Pa.s}$).

Number of teeth	50
Module	3.175 mm
Pressure angle	20°
Face width	6.35 mm
Outer diameter	95.3 mm
Pitch diameter	88.9 mm
Root diameter	79.73 mm
Linear tip relief on both flanks	18 μm starting at 24 deg

Table 4.2: **NASA GRC gearbox spur gear parameters.**

Gear dynamic transmission error (*DTE*) variations are analyzed to illustrate the vibration reduction in the gearbox as it is accepted that *DTE* time-variations are representative of gear noise Therefore, the RMS of *DTE* were computed over a wide range of operational speeds for both bearing configurations, and the variations of *DTE* are plotted versus the gear meshing frequency in Figure 4.11.

Information on the stiffness and damping values used for rolling elements bearings can be found in [147]. Figure 4.12 shows the evolution of the mean damping associated with the journal bearings versus gear mesh frequency. Figure 4.11 shows that replacing the rolling elements bearings by journal bearings introduce mainly a shift of the response peaks towards the higher speeds whereas the corresponding amplitudes remain similar. This confirms the trends previously shown by the authors as well as the conclusions of Hambric et al. [147].

In order to appraise the noise level at different GMF, the amplitudes of the $1 \times GMF$ and $2 \times GMF$ components of *DTE* are extracted for a range of operational speeds and plotted in Figure 4.13 and Figure 4.14 respectively with respect to the gear mesh frequency (Hz) and the corresponding operational speeds (rpm). For $1 \times GMF$, contrasted results are observed as journal bearings lead to higher amplitudes at some speeds and lower amplitude at some others. As for $2 \times GMF$, the amplitudes using journal bearings are lower for a range of operational speeds, considered by [147] in their analysis, however, for higher speeds, rolling elements

Cette thèse est accessible à l'adresse : http://theses.insa-lyon.fr/publication/2016LYSEI089/these.pdf
© [M. Ankouni], [2016], INSA Lyon, tous droits réservés

bearing become quieter. Here again, the results confirm the previous observations. The maximum displacement of the shaft center at the bearing locations on the input shaft has been computed for rolling element and journal bearings (Figure 4.15). It is shown that, as expected, displacements are smaller in the case of journal bearings thus showing that, even if there is some degree of coupling between the gear mesh and shaft dynamic behavior, they react differently to bearing damping depending on the frequency range of interest.

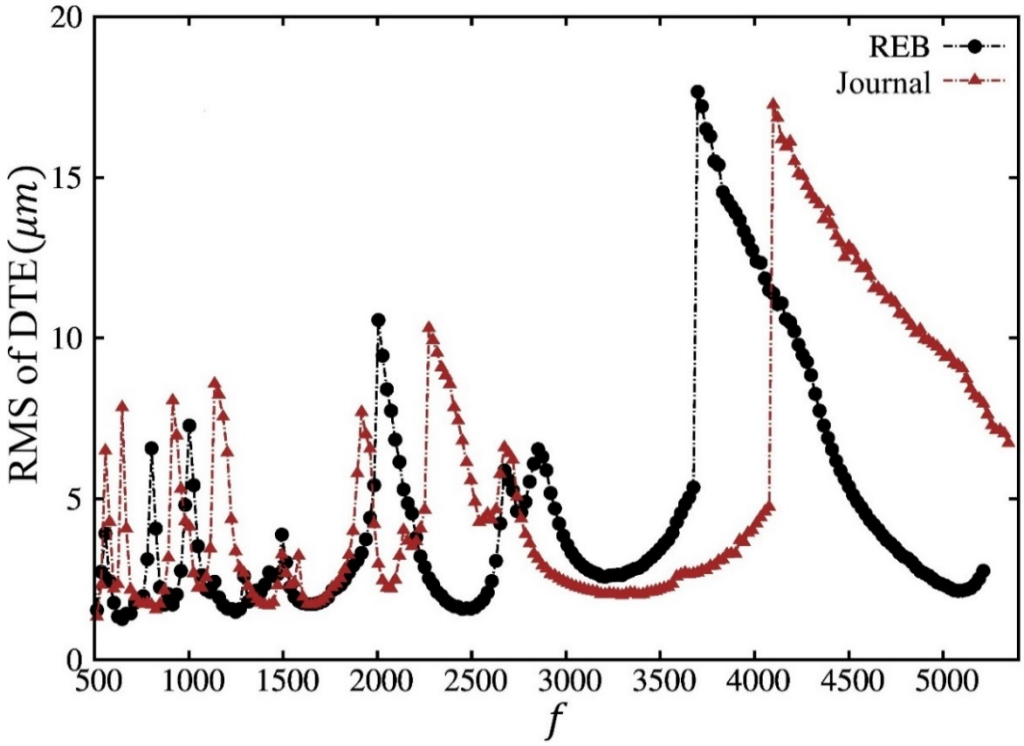

Figure 4.11: Numerical RMS of *DTE* versus the gear meshing frequency. Comparison between rolling elements bearings and journal bearings. NASA GRC's test gearbox.

Cette thèse est accessible à l'adresse : http://theses.insa-lyon.fr/publication/2016LYSEI089/these.pdf
© [M. Ankouni], [2016], INSA Lyon, tous droits réservés

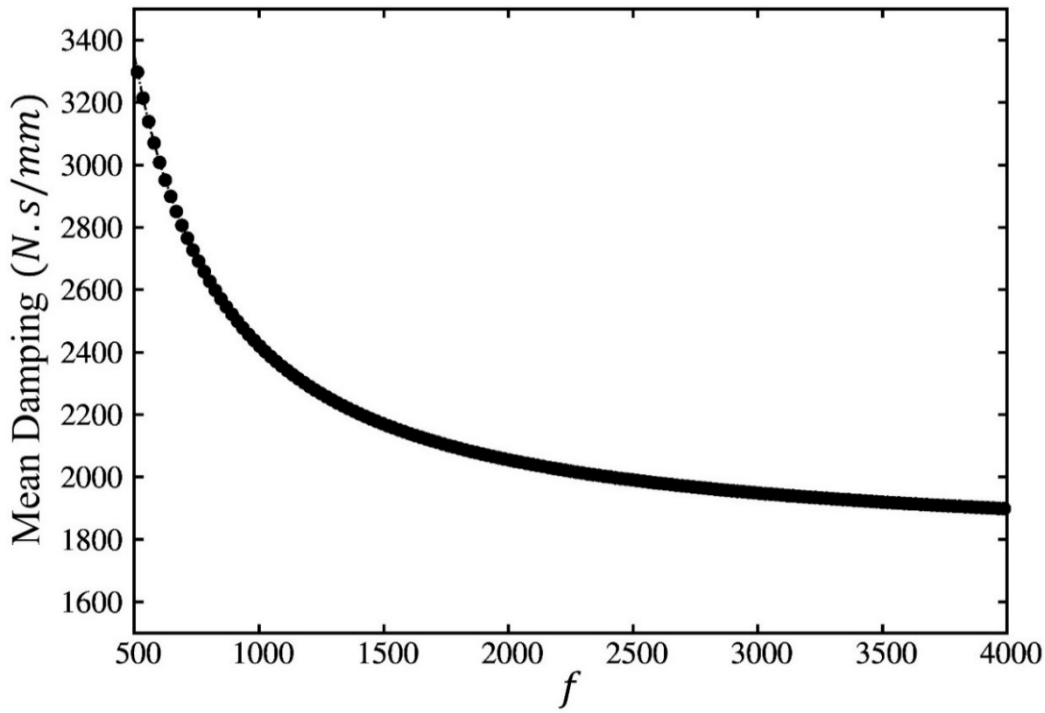

Figure 4.12: Mean journal bearing radial damping variation as a function of the gear mesh frequency.

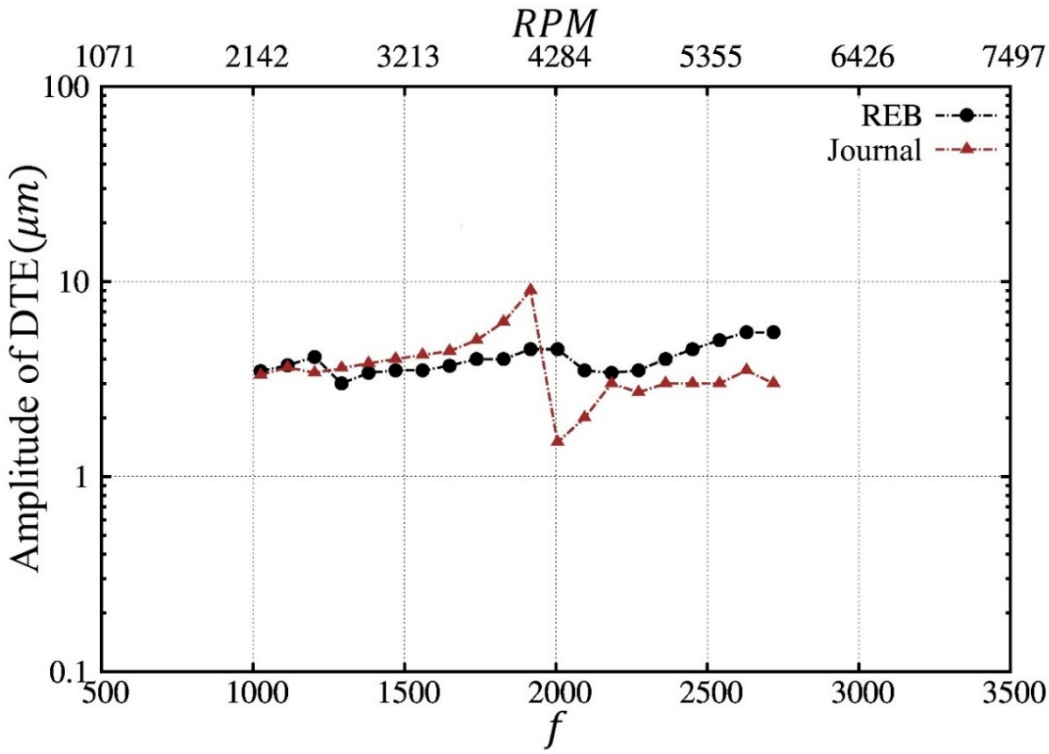

Figure 4.13: $1 \times GMF$ component of the DTE.

Cette thèse est accessible à l'adresse : http://theses.insa-lyon.fr/publication/2016LYSEI089/these.pdf
© [M. Ankouni], [2016], INSA Lyon, tous droits réservés

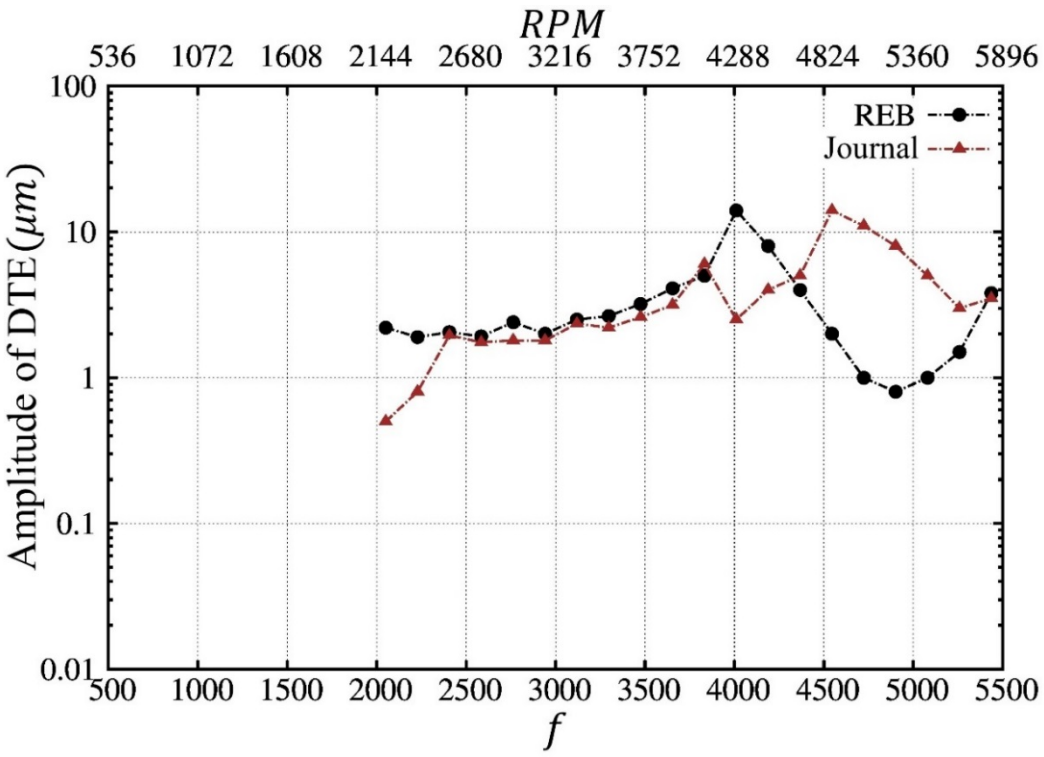

Figure 4.14: $2 \times GMF$ component of the DTE.

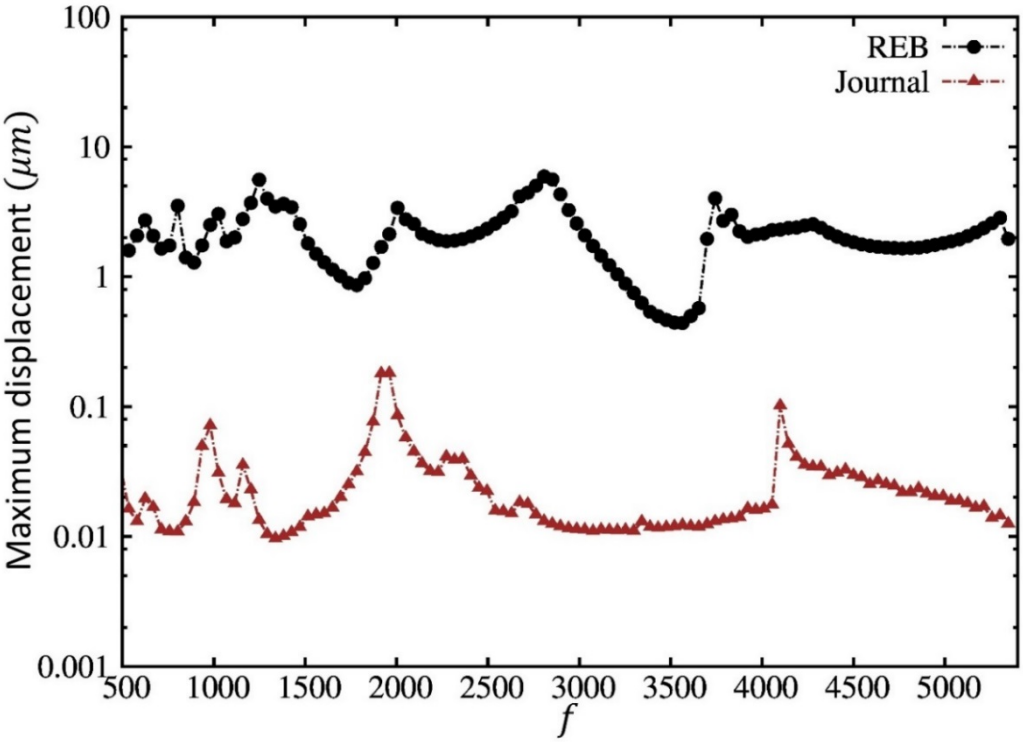

Figure 4.15: Maximum radial displacement of the center of the bearing located at the loaded end of the input shaft.

Cette thèse est accessible à l'adresse : http://theses.insa-lyon.fr/publication/2016LYSEI089/these.pdf
© [M. Ankouni], [2016], INSA Lyon, tous droits réservés

4.2.3 Identical helical gears

Compared with spur gears, helical gear mesh excitations are generally lower leading to smoother dynamic behavior suggesting that the damping mechanisms might be rather different since contact losses and shocks are unlikely. In this context, it is believed that the other sources of damping can become prevalent and need to be investigated on a model that accounts for translational degree-of-freedoms and not just for torsional displacements.

Number of teeth	50
Normal module	2.714 mm
Pressure angle	18.224°
Helix angle	25.232°
Face width	20 mm
Outside diameter	156 mm
Pitch diameter	150 mm
Base circle diameter	140.954 mm
Involute contact ratio (ICR)	1.6

Table 4.3: Test gears characteristics (*identical pinion and gear*). Helical gears.

A pair of identical gears is considered (Table 4.3) which are supported on identical shafts of 320 mm length with two uniform segments of 90 mm diameter each (same as for the spur gears case). An external torque of $250\ Nm$ is imposed. As for helical gears, it can be noticed that the internal damping of shafts barely contributes to amplitude reduction as shown in Figure 4.16. The dynamic response obtained when adding mesh damping also indicates that it has limited effect on the dynamic behavior. In a next phase, emphasis is placed on bearing contributions to damping. Rolling element bearings are considered first, a constant damping of $5\ N.s/mm$ is introduced at the ends of the shafts in both radial directions. The corresponding response curve is presented in Figure 4.17 that shows a significant reduction of the higher amplitudes along with smoother dynamic responses at all speeds. Considering journal bearings ($L/D = 0.25, R/C = 500, \mu_0 = 0.0178\ \mathrm{Pa.s}$), the results in Figure 4.18 clearly reveal that they strongly contribute to the overall damping since the response peaks are all flattened. It can also be observed that the major tooth critical speed is shifted towards the higher speeds.

Cette thèse est accessible à l'adresse : http://theses.insa-lyon.fr/publication/2016LYSEI089/these.pdf
© [M. Ankouni], [2016], INSA Lyon, tous droits réservés

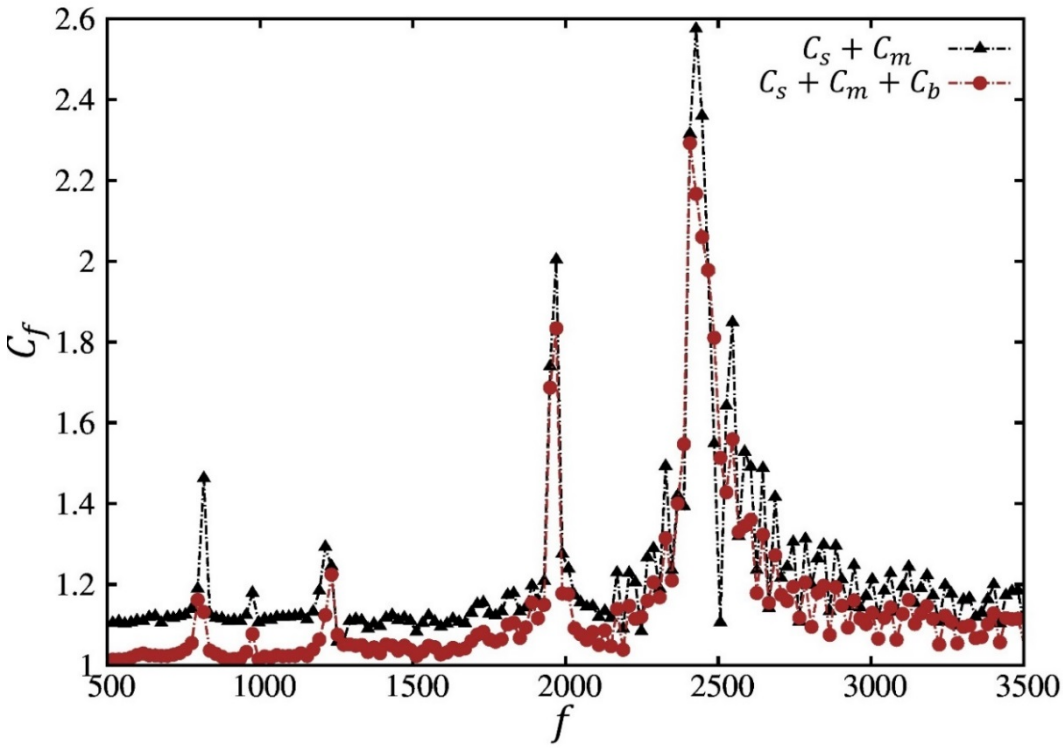

Figure 4.16: Dynamic response curves. Comparison between internal damping and mesh damping. Helical gears.

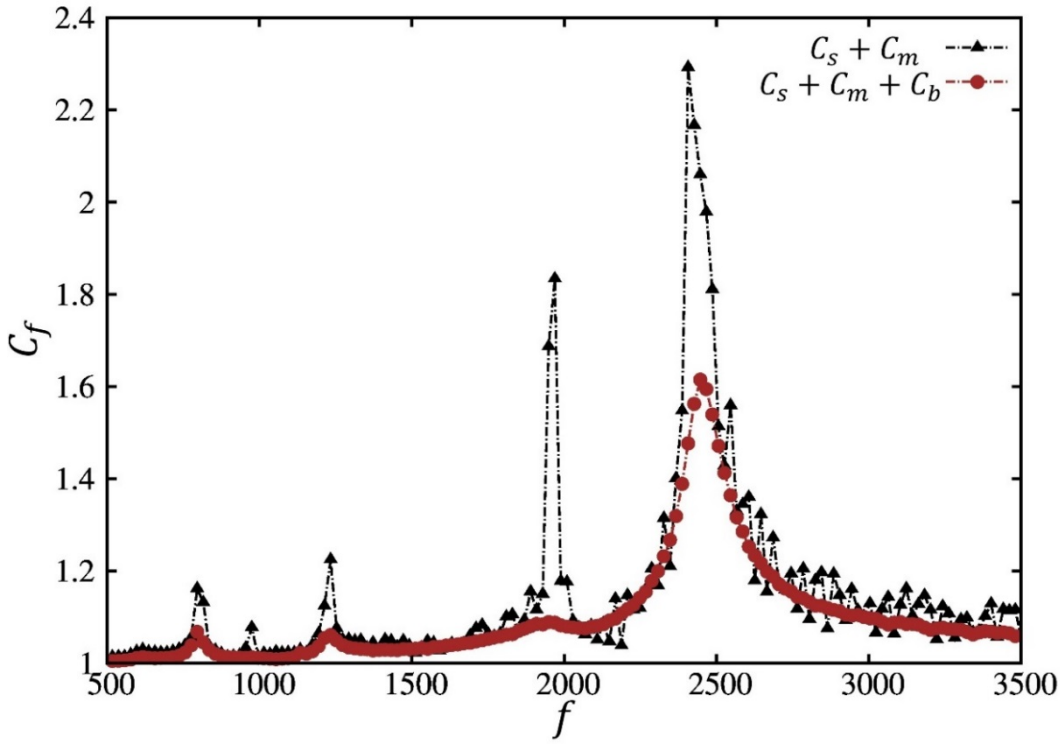

Figure 4.17: Dynamic response curves. Comparison between mesh damping and rolling element bearing damping. Helical gears.

Based on these results, the following provisional conclusions can be drawn: bearings contribute significantly to the overall damping mechanism in helical gear transmissions and, b) journal

Cette thèse est accessible à l'adresse : http://theses.insa-lyon.fr/publication/2016LYSEI089/these.pdf
© [M. Ankouni], [2016], INSA Lyon, tous droits réservés

bearings seem to provide more damping than rolling element bearings (contrary to what was reported for spur gears).

The damping coefficients for journal bearings are known to strongly depend on a number of geometrical and lubricant parameters (length L, clearance C and lubricant viscosity μ_0) and it is certainly interesting to examine their contribution to damping. The clearance effect is analyzed by varying the ratio R/C ($L/D = 0.25$, $\mu_0 = 0.0178$ Pa. s). Three different values are considered, and the corresponding dynamic tooth load curves are plotted in Figure 4.19, showing that a larger clearance leads to a more damped response. The evolution of the respective bearing damping versus speed is presented in Figure 4.20 which shows that, unexpectedly, higher damping in the bearings can result in stronger dynamic mesh force amplifications. This somewhat singular behavior will be investigated further in the following section.

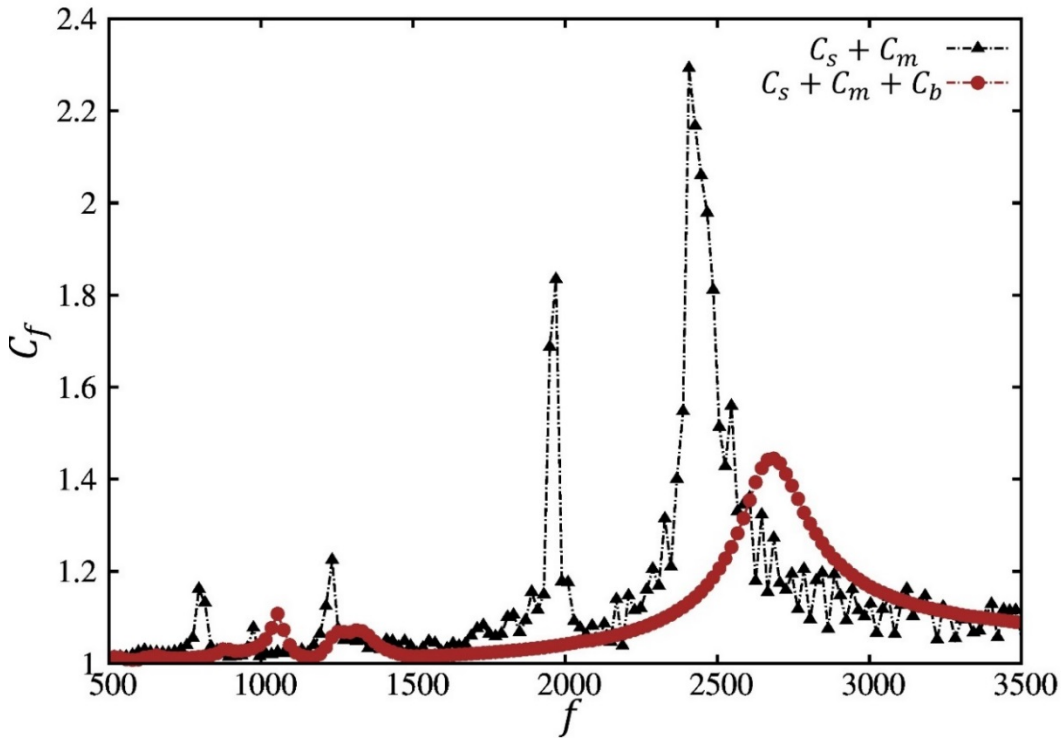

Figure 4.18: Dynamic response curves. Comparison between mesh damping and journal bearing damping. Helical gears.

Considering the influence of bearing length, Figure 4.21 shows that a shorter bearing ($R/C = 1000$, $\mu_0 = 0.0178$ Pa. s) is more effective in terms of dynamic tooth load amplifications although the damping provided in this case is lower than that produced by longer bearings as presented in Figure 4.22 confirming the unexpected behavior previously exposed. Finally, the effect of the lubricant is studied ($L/D = 0.5$, $R/C = 500$) and the results in Figure 4.23

Cette thèse est accessible à l'adresse : http://theses.insa-lyon.fr/publication/2016LYSEI089/these.pdf
© [M. Ankouni], [2016], INSA Lyon, tous droits réservés

indicate that a lower viscosity reduce dynamic response at the mesh whereas, here too, bearing damping evolves the opposite way (Figure 4.24).

At this stage, further investigations are therefore needed to explain the apparently contradictory results which show that increasing bearing damping is not necessarily beneficial for dynamic tooth loading. In order to separate the effect of bearing stiffness and damping on the behavior of the system, and understand more deeply the effect of the variation in damping levels on the amplifications of dynamic tooth load, a constant stiffness value is imposed while damping is varied over a wide range going from the lower values of rolling elements bearings ($\sim 5\ N.s/mm$) to the higher levels associated with journal bearings ($\sim 1000\ N.s/mm$). The different dynamic responses are compared in Figure 4.25 which reveals two opposite behaviors: a) starting with the lowest damping values, a logical evolution of the maximum amplitude with the increase in damping is observed, b) after a certain threshold, however, the tendency is inversed and larger response amplitudes are obtained when damping is increased, along with a shift of the response peaks.

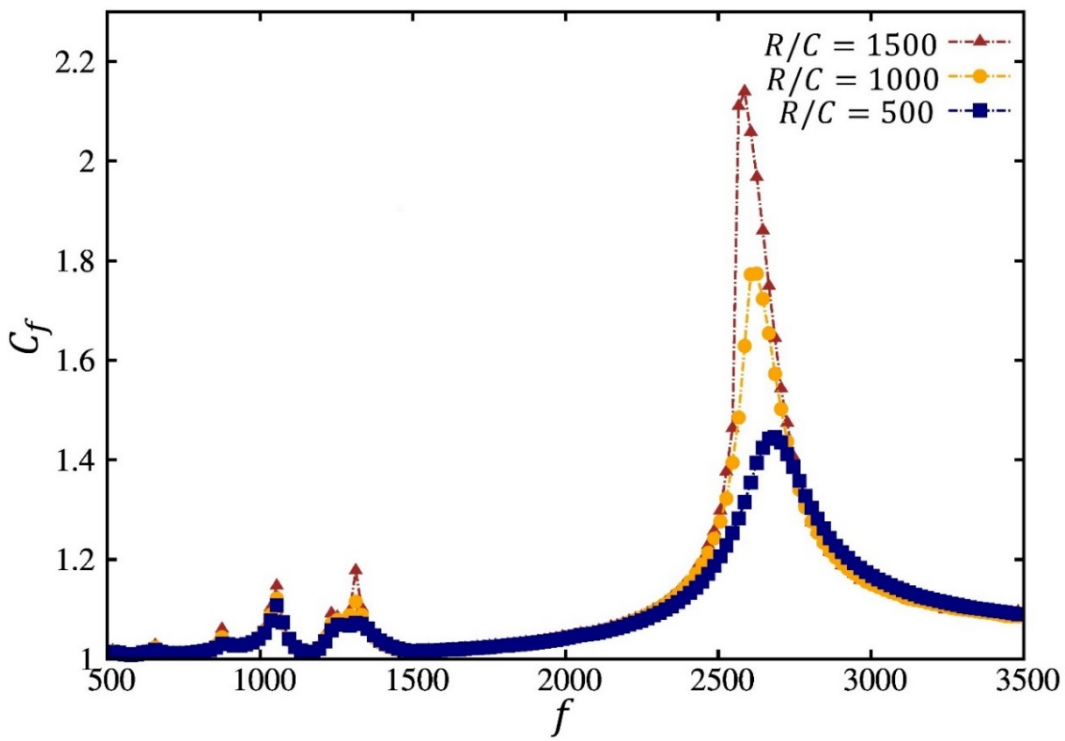

Figure 4.19: Dynamic response curves. Comparison between different clearance values. Journal bearings. Helical gears.

Cette thèse est accessible à l'adresse : http://theses.insa-lyon.fr/publication/2016LYSEI089/these.pdf
© [M. Ankouni], [2016], INSA Lyon, tous droits réservés

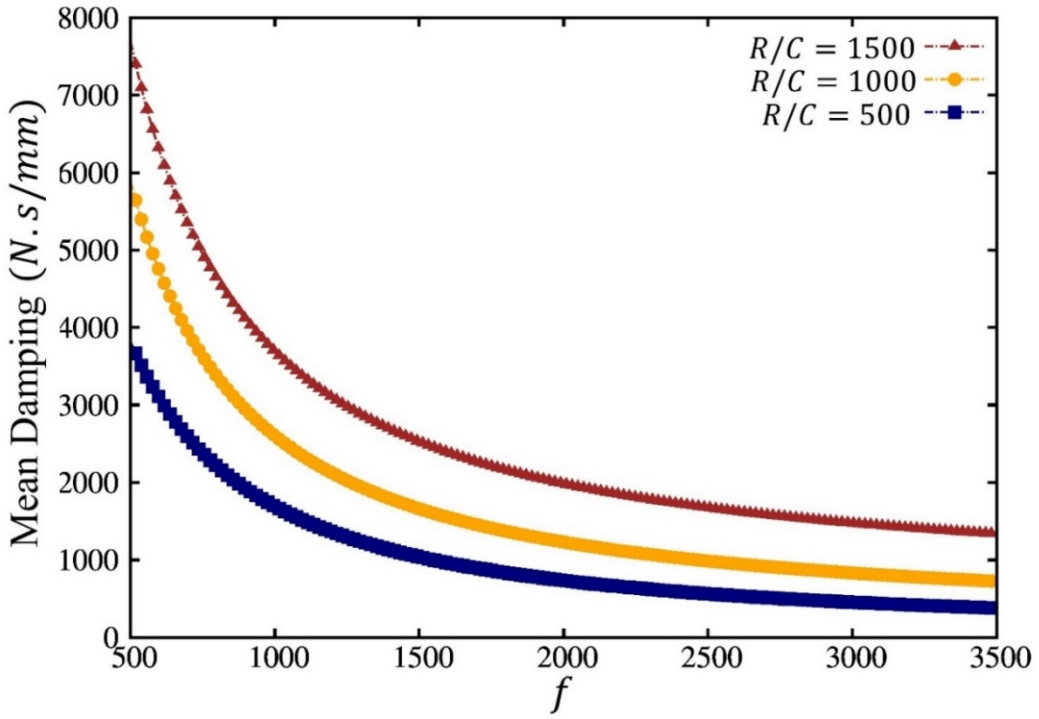

Figure 4.20: Mean journal bearing radial damping variation. Comparison between different clearance values. Helical gears.

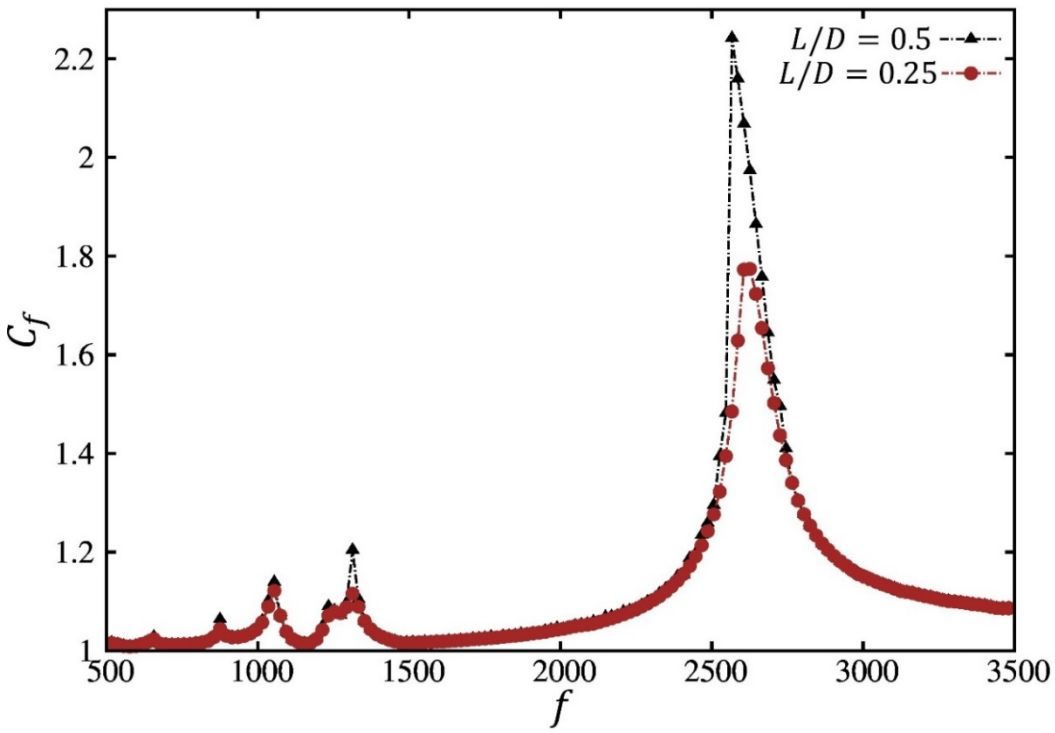

Figure 4.21: Dynamic response curves. Comparison between different lengths. Journal bearings. Helical gears.

Cette thèse est accessible à l'adresse : http://theses.insa-lyon.fr/publication/2016LYSEI089/these.pdf
© [M. Ankouni], [2016], INSA Lyon, tous droits réservés

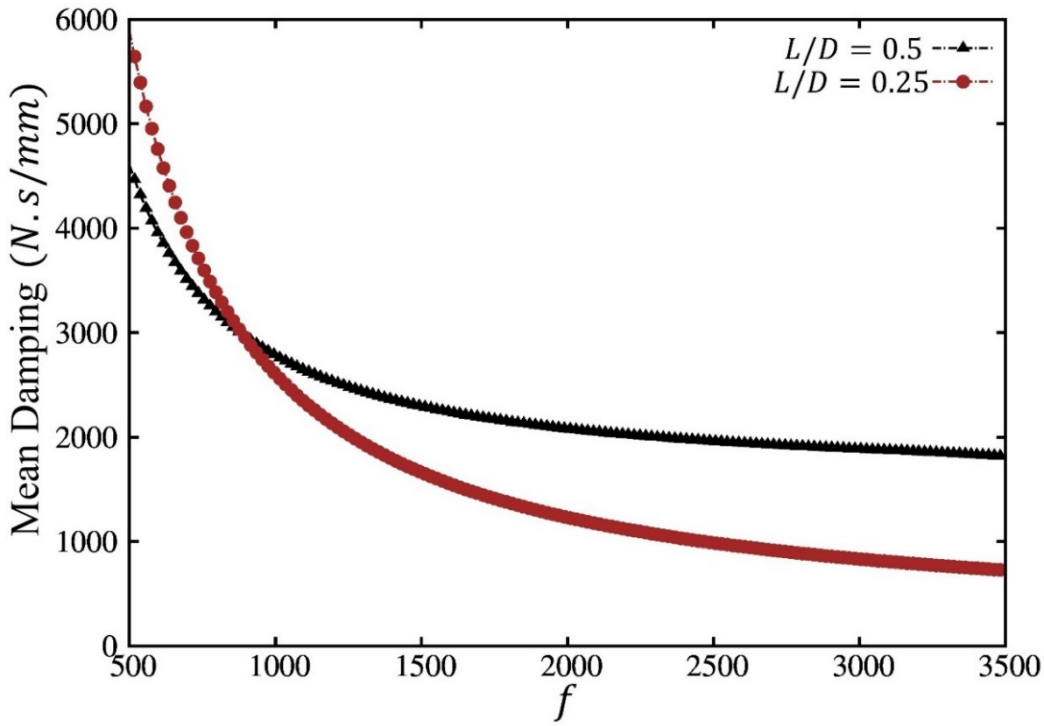

Figure 4.22: Mean journal bearing radial damping variation. Comparison between different lengths. Helical gears.

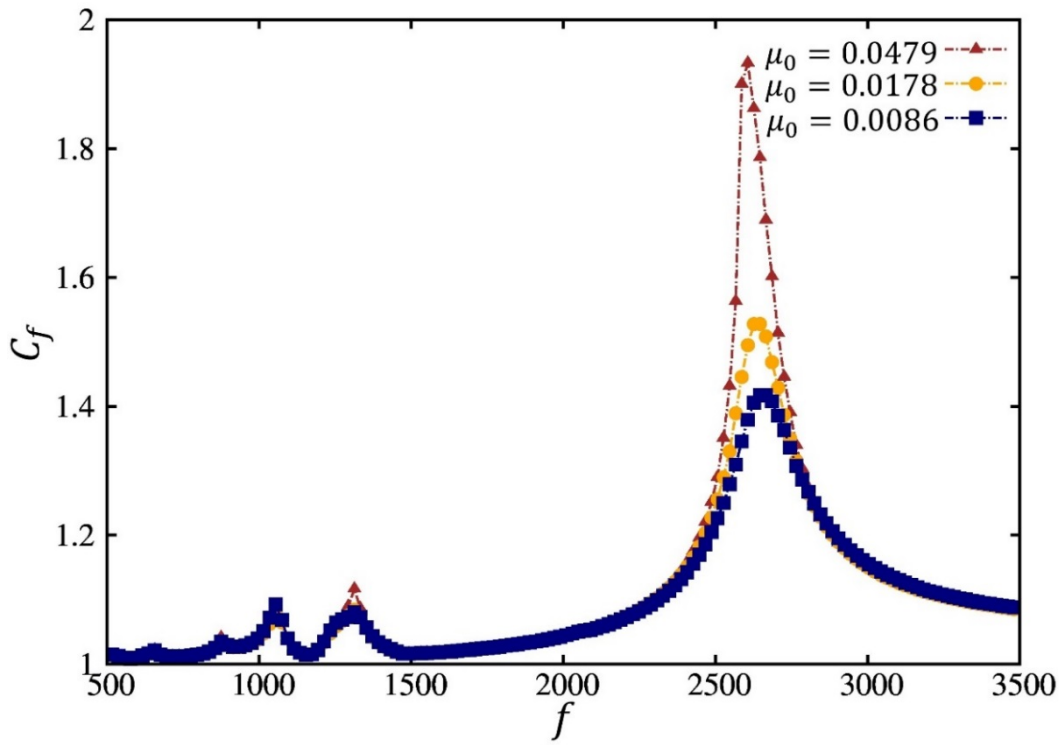

Figure 4.23: Dynamic response curves. Comparison between different lubricant viscosities. Journal bearings. Helical gears.

Cette thèse est accessible à l'adresse : http://theses.insa-lyon.fr/publication/2016LYSEI089/these.pdf
© [M. Ankouni], [2016], INSA Lyon, tous droits réservés

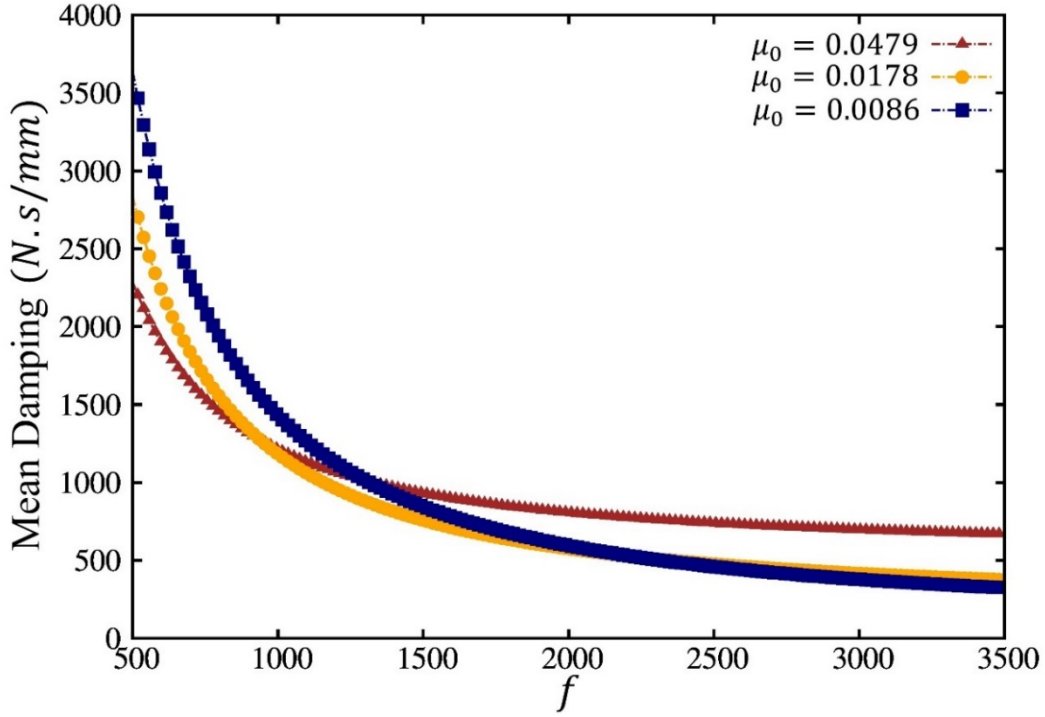

Figure 4.24: Mean journal bearing radial damping variation. Comparison between different lubricant viscosities. Helical gears.

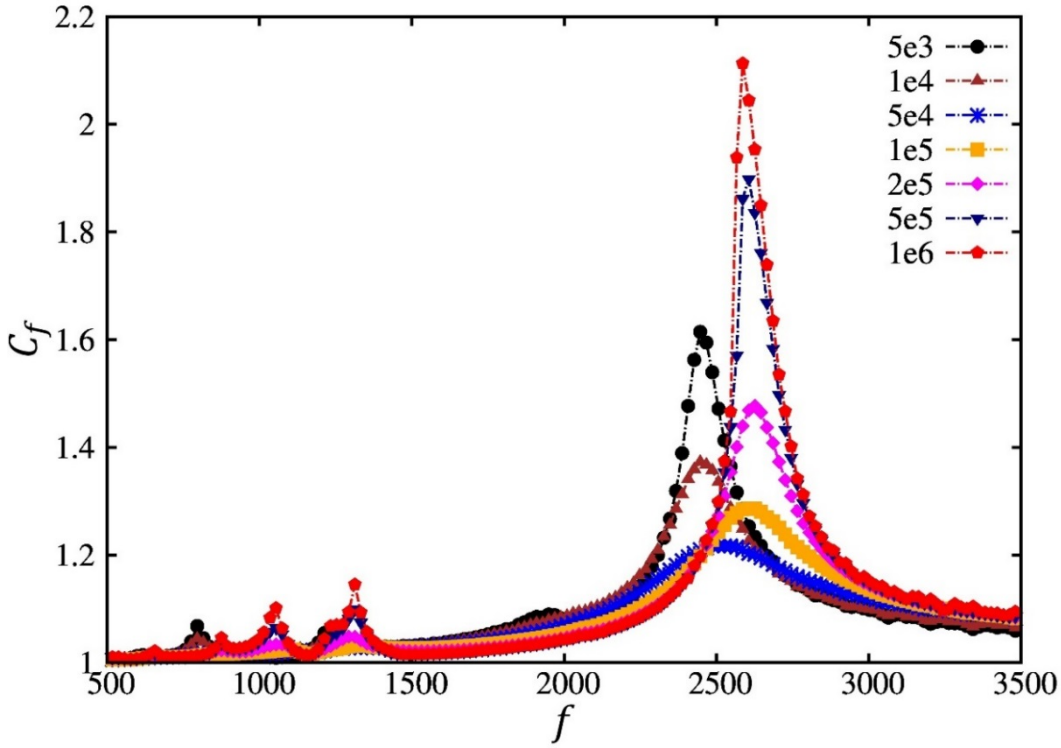

Figure 4.25: Dynamic response curves. Comparisons between various bearings damping (constant stiffness). Helical gears.

Cette thèse est accessible à l'adresse : http://theses.insa-lyon.fr/publication/2016LYSEI089/these.pdf
© [M. Ankouni], [2016], INSA Lyon, tous droits réservés

This set of simulations, though simplified re journal bearing modeling, actually reproduces the system behavior well when more accurate journal bearing models are employed. This observation leads to the conclusion that the frequency shift is caused by damping and not by stiffness variations. Under such conditions, more refined modal analyses incorporating the influence of damping (often neglected at this stage) need to be performed.

4.2.4 Modal analysis of the damped system

In the majority of mechanical systems, the influence of damping on critical speeds can be ignored, i.e. the computation of the natural frequencies is performed considering the undamped system and solely based on the overall mass and the stiffness matrices. Basically this kind of analysis is suited for systems with moderate damping. However, when high damping is introduced in the system, a modified modal analysis is needed. Based on the previous results, it transpires that journal bearing damping cannot be discarded in the case of geared transmission as it appears as strongly influential on the position of the critical speeds.

Considering an N degree of freedom system with constant viscous damping and constant averaged stiffness matrices, the free-vibration system can be expressed as:

$$M\ddot{x} + C\dot{x} + Kx = 0 \tag{4.55}$$

Introducing $v = \dot{x}$, so that $\ddot{x} = \dot{v}$, the 2nd order differential equation is classically transformed into two sets of first order differential equations as follows:

$$\frac{d}{dt}\begin{Bmatrix} x \\ v \end{Bmatrix} = \begin{bmatrix} 0_{N\times N} & I_{N\times N} \\ -M^{-1}K & -M^{-1}C \end{bmatrix}\begin{Bmatrix} x \\ v \end{Bmatrix} \tag{4.56}$$

A general solution of the form $x = \bar{x}e^{\lambda t}$ is considered, hence $v = \lambda\bar{x}e^{\lambda t}$ which, after substituting x and v in the previous equation, gives:

$$\begin{bmatrix} 0_{N\times N} & I_{N\times N} \\ -M^{-1}K & -M^{-1}C \end{bmatrix}\begin{Bmatrix} \bar{x} \\ \lambda\bar{x} \end{Bmatrix} = \lambda\begin{Bmatrix} \bar{x} \\ \lambda\bar{x} \end{Bmatrix} \tag{4.57}$$

Leading to a standard Eigen-value problem, where the eigenvalues are:

$\lambda_p = -\zeta_p\omega_p + i\omega_p\sqrt{1-\zeta_p^2}$, (for the undamped case $\lambda_p = i\omega_p$).

Cette thèse est accessible à l'adresse : http://theses.insa-lyon.fr/publication/2016LYSEI089/these.pdf
© [M. Ankouni], [2016], INSA Lyon, tous droits réservés

where ω_p and ζ_p represent respectively the undamped natural frequency and the modal damping ratio corresponding to the mode P, $\omega_p = |\lambda_p|$, $\zeta_p = -Re(\lambda_p)/\omega_p$ [148].

Using the overall mass, stiffness and damping matrices of the helical gear system with journal bearings, the real natural frequencies of the system and the resulting damping ratio related to each natural mode have been determined as described above. The corresponding natural frequencies and damping factors are listed in Table 4.4 for each set of bearing parameters studied. The results show that the modal analysis indicates that the position of the major tooth critical frequency follows the same law of variation as the position with the maximum dynamic factor amplitude in figures 4.19, 4.21 and 4.23.

$\frac{L}{D}$	$\frac{R}{C}$	μ_0 $(Pa.s)$	f_p (Hz)	ζ_p (%)
0.25	500	0.0178	2679	4.15
0.25	1000	0.0178	2626	2.29
0.25	1500	0.0178	2583	1.27
0.5	500	0.0086	2665	4.33
0.5	500	0.0178	2643	3.36
0.5	500	0.0479	2600	1.86
0.5	1000	0.0178	2567	1.01

Table 4.4: Natural frequencies and damping ratios. Journal bearings.

Moreover, the amplitude evolution is directly correlated to the damping factors. For instance, as said earlier, a higher clearance (Figure 4.19) lead to a more damped response and the results in the table show that a higher clearance leads to a higher damping ratio (4.15% compared to 2.29% and 1.28%) even if the locally imposed damping values are lower than those in the other cases. Similar analysis is conducted to clarify the tendencies shown in Figure 4.25. Once again, both the shift in critical speeds and the different amplitude levels can be explained by the modal analysis when damping is taken into account.

Cette thèse est accessible à l'adresse : http://theses.insa-lyon.fr/publication/2016LYSEI089/these.pdf
© [M. Ankouni], [2016], INSA Lyon, tous droits réservés

$C_{b_{i_{v,v}}}\left(C_{b_{i_{w,w}}}\right)$ $(N.s/mm)$	f_p (Hz)	ζ_p (%)
5	2435	2.45
10	2442	4.38
50	2486	8.85
100	2606	6.34
200	2608	3.56
500	2599	1.95
1000	2586	1.28

Table 4.5: Natural frequencies and damping ratios. Constant stiffness.

4.2.5 Further investigations

In this section, further results are presented in order to study the effect of geometry (inter-bearing distance, shaft length) on the dynamic response of gears with the objective of consolidating the previous conclusions and gain more information on bearing-gear dynamic interactions. Spur and helical gear simulations are presented separately.

a. Spur gears

The spur gear geometry is described in Table 4.1, the shaft diameter is kept the same and the distance between the bearings is reduced to 250 mm. Three different configurations of journal bearing are compared with the results obtained with a rolling element bearing configuration (same as in section 4.2.1) as illustrated in Figure 4.26. The viscosity of the lubricant is the same for the three journal bearing configurations ($\mu_0 = 0.0178$ Pa. s).

The results confirm the trends highlighted earlier, e.g. both types of bearing (journal /rolling element) provide comparable dynamic load amplitudes at critical speeds thus neither of them appear as superior with regard to dynamic tooth loads. Moreover, despite the significant difference in damping for the three journal bearing cases (Figure 4.10), the variation of the

Cette thèse est accessible à l'adresse : http://theses.insa-lyon.fr/publication/2016LYSEI089/these.pdf
© [M. Ankouni], [2016], INSA Lyon, tous droits réservés

amplitude at the main critical speed is limited. Once again, the complementary contribution of bearings is underlined compared to the major contribution of the gear mesh to damping in spur gears. A number of simulations have been performed considering shorter/longer shafts with different diameters which all led to similar conclusions.

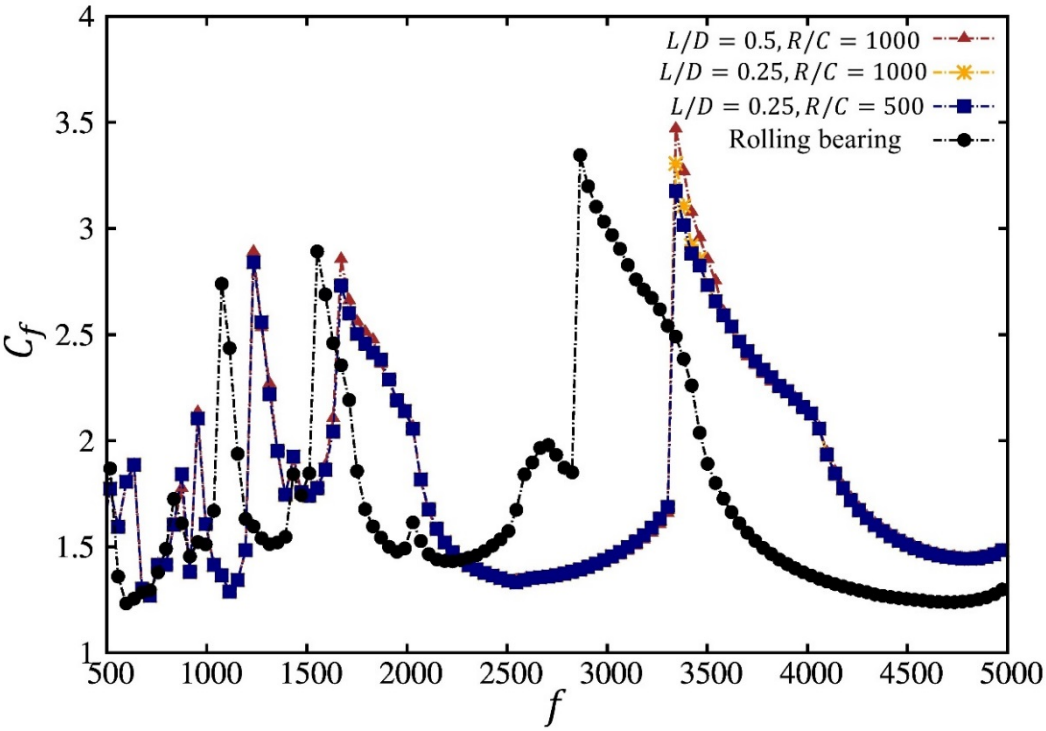

Figure 4.26: Dynamic response curves. Comparisons between rolling element and various journal bearings geometries. Spur gears.

b. Helical gears

The helical gear dimensions of Table 4.3 are used and the distance between the bearings is reduced to 200 mm. The same bearing configurations as for spur gears (see above) are considered. As shown in Figure 4.27, journal bearings of different dimensions lead to a more damped tooth load curves compared to rolling element bearings which indicates that either types of bearing can be chosen to lower dynamic tooth loads depending on operational speeds and system compliance. Furthermore, the inversed trend noticed for high damping levels is confirmed, i.e. beyond a certain limit of bearing damping, the natural frequencies of the system are modified and larger tooth load amplifications are found. The same behavior has been repeatedly observed with various shafts dimensions.

Cette thèse est accessible à l'adresse : http://theses.insa-lyon.fr/publication/2016LYSEI089/these.pdf
© [M. Ankouni], [2016], INSA Lyon, tous droits réservés

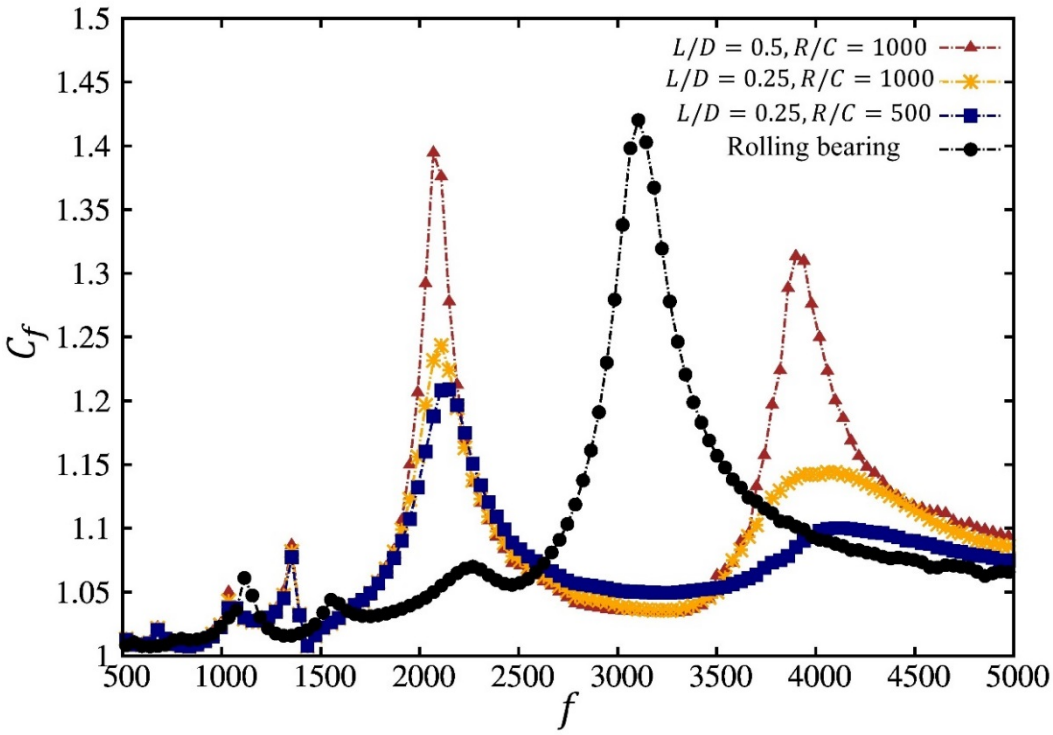

Figure 4.27: Dynamic response curves. Comparisons between rolling element and various journal bearings geometries. Helical gears.

4.2.6 Non identical helical gears

Only identical gear pairs and shafts were considered in the previous sections. The present section focuses on the behavior of systems with one pinion and one gear (Table 4.6) of different dimensions (as is the case in most industrial applications) supported by shafts whose dimensions are given in Table 4.7. The results obtained using rolling element bearings ($C_{b_{v,v}} = C_{b_{w,w}} = 1\ N.s/mm$) and journal bearings ($L/D = 0.25,\ R/C = 1000,\ \mu_0 = 0.0178$ Pa. s) are confronted in Figure 4.28 where it can clearly be seen that lower amplitudes of the maximum dynamic factor are obtained using the rolling elements bearings. Moreover, it is found that the natural frequency positions are mainly affected by the type of bearing. For instance, journal bearings eliminate one of the modes near 3000 Hz and move the major and secondary critical speeds towards the lower speed range, mostly because of the high value of damping as pointed out earlier in this chapter. The analysis is extended by considering several journal bearing configurations with a variety of parameters controlling their dynamic properties such as bearing length, radial clearance and lubricant viscosity. Figure 4.29 to 4.34 illustrate the various response curves obtained by sweeping over the range of parameters described above along with the corresponding mean damping on the input and output bearings. Based on these results, it is

Cette thèse est accessible à l'adresse : http://theses.insa-lyon.fr/publication/2016LYSEI089/these.pdf
© [M. Ankouni], [2016], INSA Lyon, tous droits réservés

confirmed that larger journal bearing damping can lead to higher vibrations thus suggesting that bearing design re dynamic tooth loads requires special attention. Finally, Table 4.8 synthetizes the critical speed positions and related damping factors for each of the configuration treated.

	Pinion	**Gear**
Number of teeth	26	157
Normal module	4 mm	
Pressure angle	20°	
Helix angle	12.5°	
Face width	50 mm	40 mm
Addendum coefficient	1.4	
Dedendum coefficient	1.0	
Pitch diameter	106.5 mm	643.2 mm
Center distance	375 mm	
Linear tip relief on both flanks	13 μm on 20% of the active profile length	

Table 4.6: Gear data. Non identical helical gears [98].

	Input shaft (pinion)	**Output shaft (gear)**
External diameter	70 mm	90 mm
Internal diameter	30 mm	30 mm
Bearings distance	320 mm	

Table 4.7: Shaft dimensions.

Cette thèse est accessible à l'adresse : http://theses.insa-lyon.fr/publication/2016LYSEI089/these.pdf
© [M. Ankouni], [2016], INSA Lyon, tous droits réservés

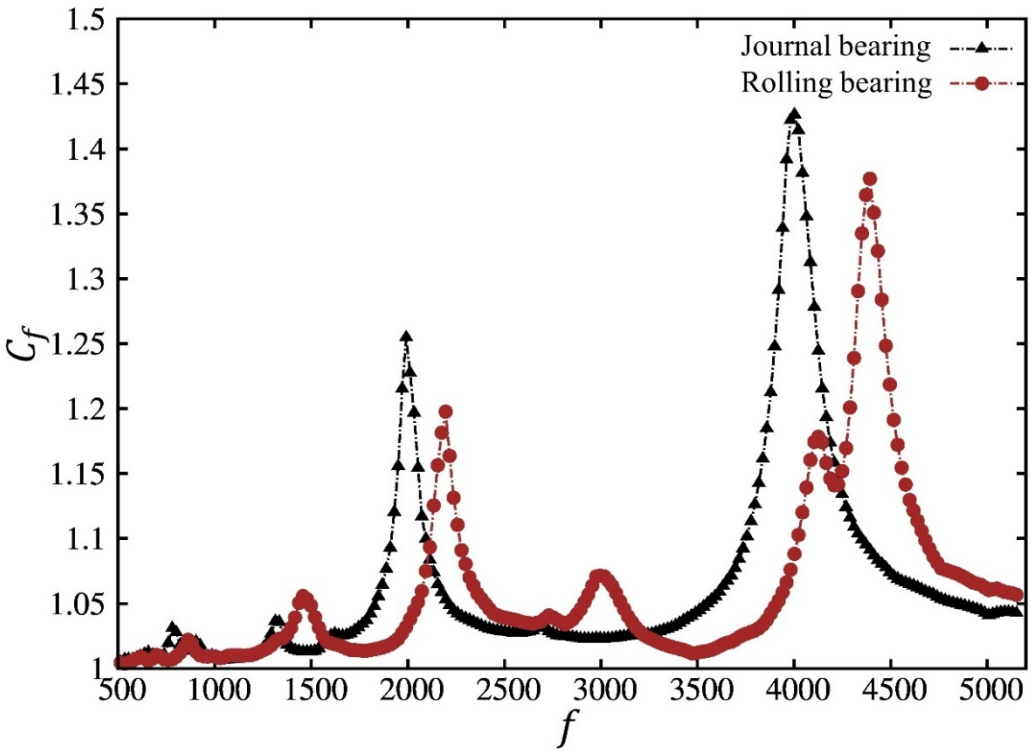

Figure 4.28: Dynamic response curves. Comparison between rolling element bearings and journal bearings. Non identical helical gears.

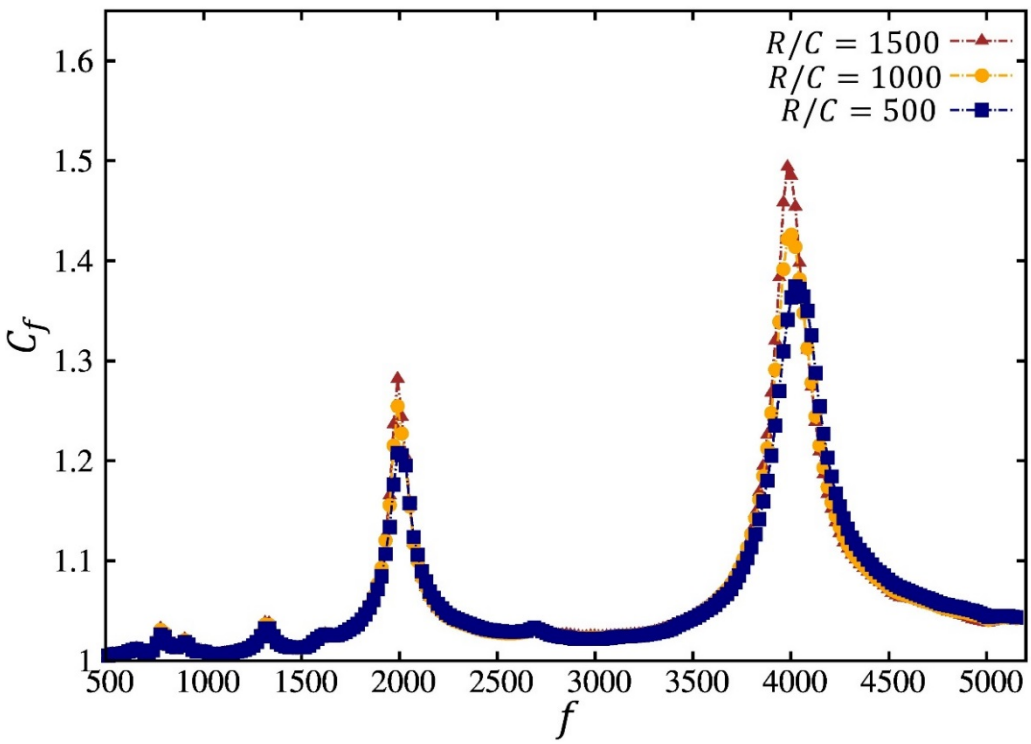

Figure 4.29: Dynamic response curves. Comparison between different clearance values ($L/D = 0.25, \mu_0 = 0.0178$ Pa. s) . Journal bearings. Non identical helical gears.

Cette thèse est accessible à l'adresse : http://theses.insa-lyon.fr/publication/2016LYSEI089/these.pdf
© [M. Ankouni], [2016], INSA Lyon, tous droits réservés

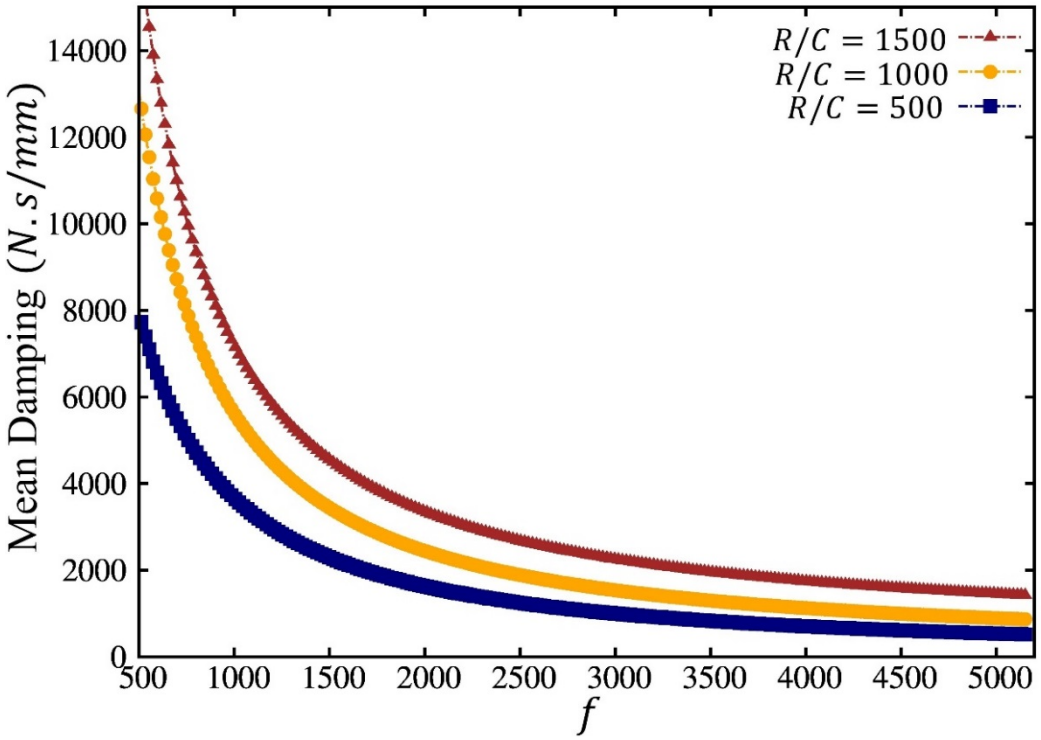

(a) Bearing 1 (input)

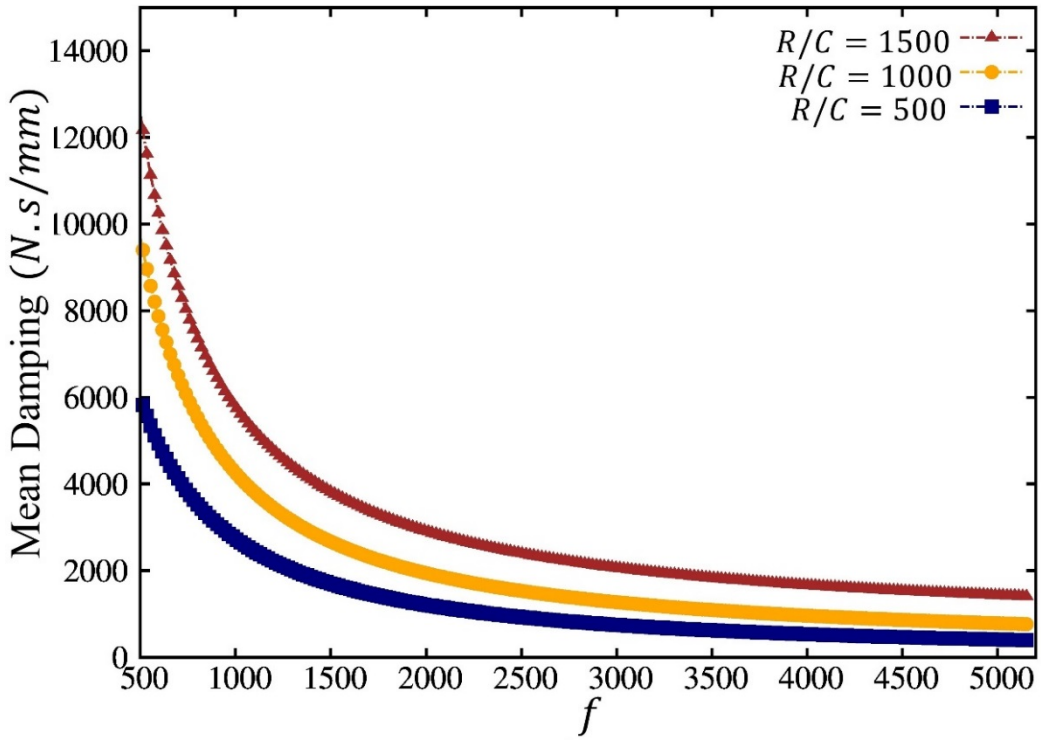

(b) Bearing 6 (output)

Figure 4.30: Mean journal bearing radial damping variation. Comparison between different clearance values. Non identical helical gears.

Cette thèse est accessible à l'adresse : http://theses.insa-lyon.fr/publication/2016LYSEI089/these.pdf
© [M. Ankouni], [2016], INSA Lyon, tous droits réservés

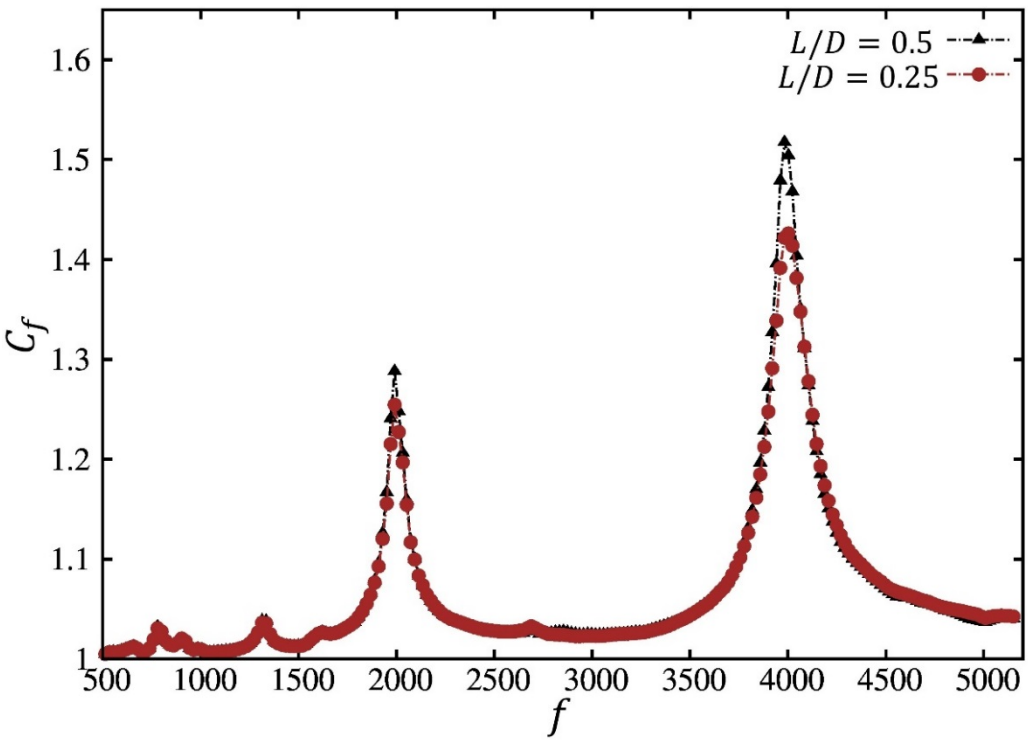

Figure 4.31: Dynamic response curves. Comparison between different lengths ($R/C = 1000, \mu_0 = 0.0178$ Pa.s). Journal bearings. Non identical helical gears.

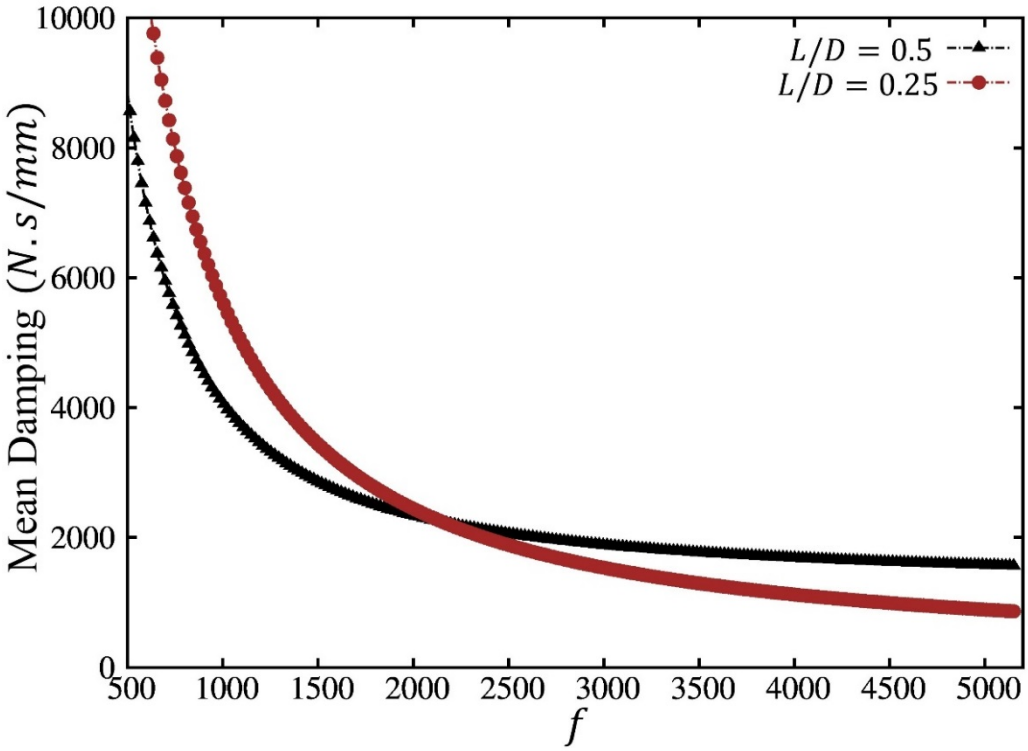

(a) Bearing 1 (input)

Cette thèse est accessible à l'adresse : http://theses.insa-lyon.fr/publication/2016LYSEI089/these.pdf
© [M. Ankouni], [2016], INSA Lyon, tous droits réservés

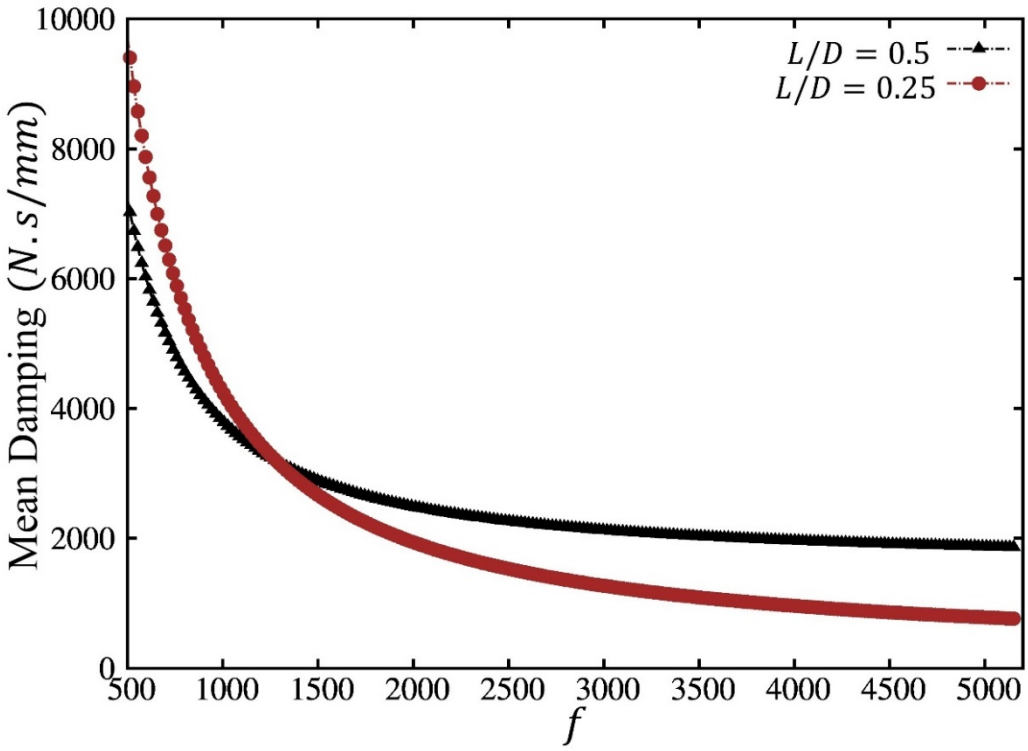

(b) Bearing 6 (output)

Figure 4.32: Mean journal bearing radial damping variation. Comparison between different lengths. Non identical helical gears.

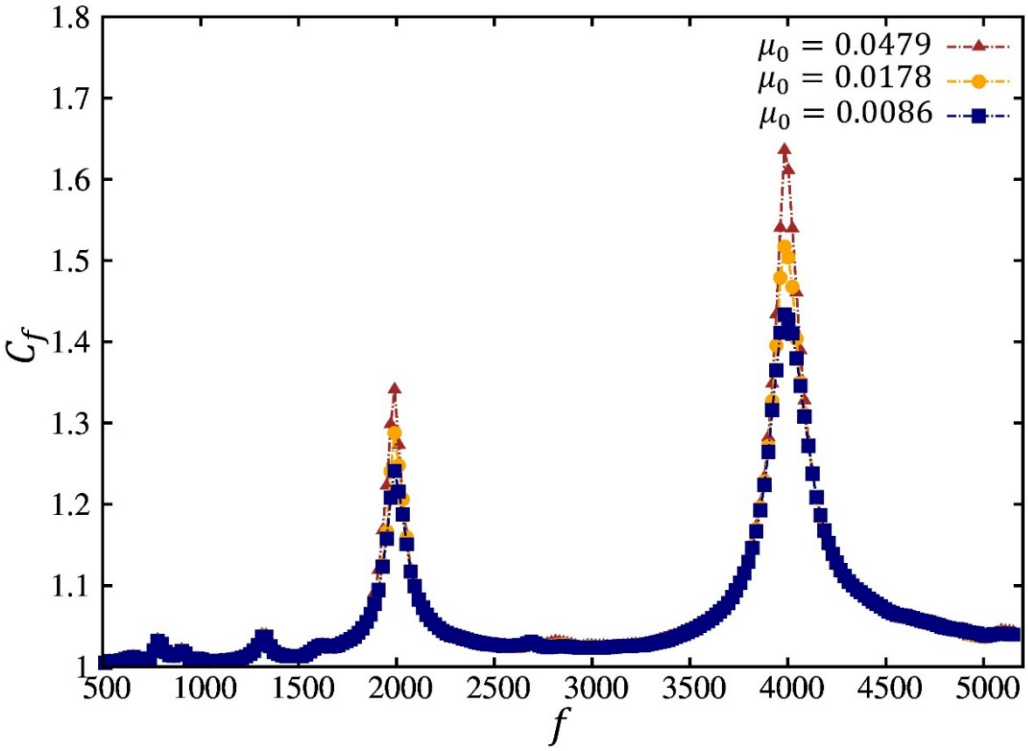

Figure 4.33: Dynamic response curves. Comparison between different lubricant viscosities ($L/D = 0.5, R/C = 1000$). Journal bearings. Non identical helical gears.

Cette thèse est accessible à l'adresse : http://theses.insa-lyon.fr/publication/2016LYSEI089/these.pdf
© [M. Ankouni], [2016], INSA Lyon, tous droits réservés

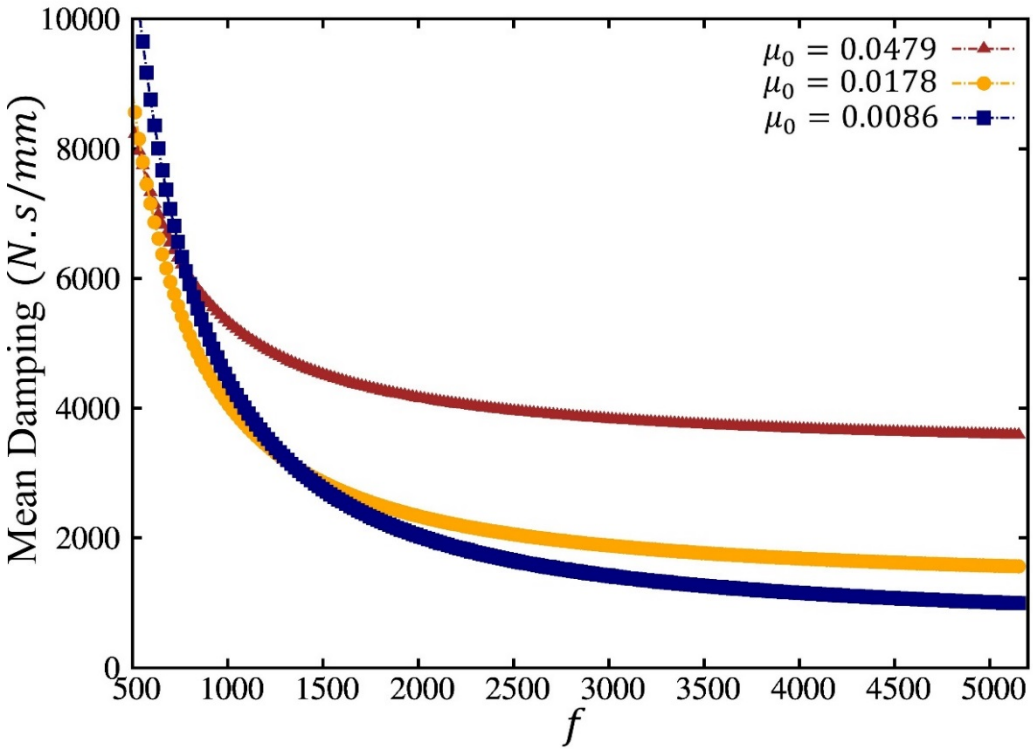

(a) Bearing 1 (input)

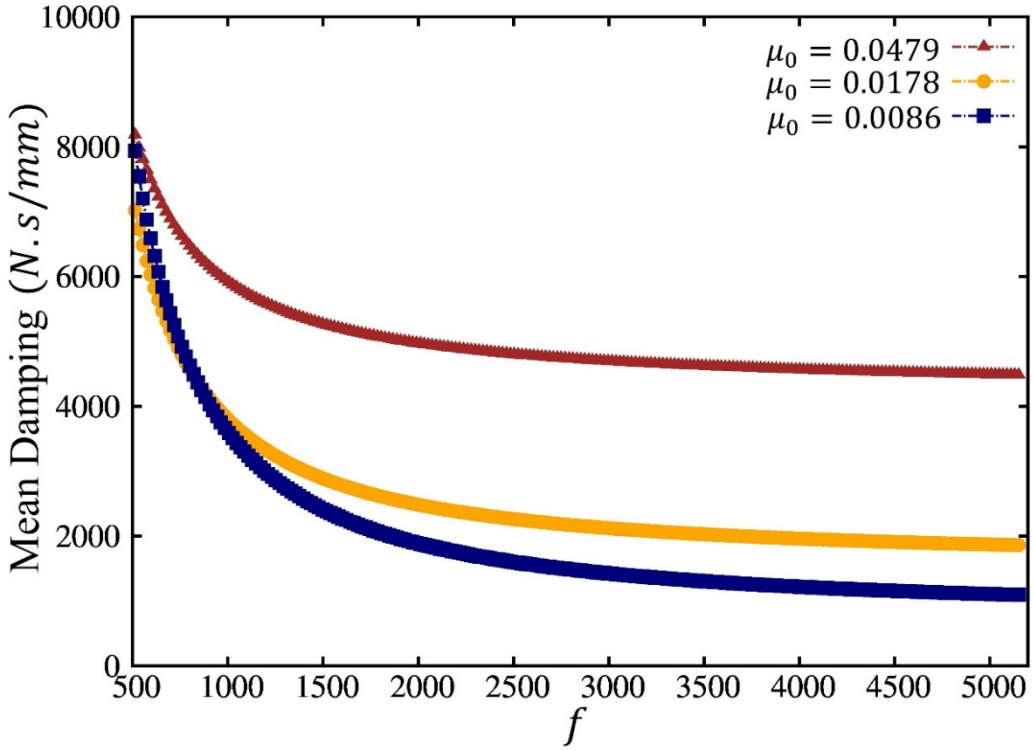

(b) Bearing 6 (output)

Figure 4.34: Mean journal bearing radial damping variation. Comparison between different lubricant viscosities. Non identical helical gears.

Cette thèse est accessible à l'adresse : http://theses.insa-lyon.fr/publication/2016LYSEI089/these.pdf
© [M. Ankouni], [2016], INSA Lyon, tous droits réservés

$\frac{L}{D}$	$\frac{R}{C}$	μ_0 $(Pa.s)$	f_p (Hz)	ζ_p (%)
0.25	500	0.0178	4021	2.82
0.25	1000	0.0178	4005	2.15
0.25	1500	0.0178	3982	1.75
0.5	1000	0.0086	3982	1.81
0.5	1000	0.0178	3982	1.68
0.5	1000	0.0479	3982	1.46
REB $(1\ N.s/mm)$			4392	2.7

Table 4.8: Natural frequencies and damping ratios.

4.3 Conclusion

A variety of damping sources has been investigated for both spur and helical gears based on a three dimensional lumped parameter dynamic model from which contrasted conclusions have been drawn depending on the type of gear (spur or helical).

As for spur gears, mesh damping, i.e. lubricant and tooth contributions, plays a major role in the damping mechanism mainly when contact losses occur. Concerning the role of bearings, their complementary contribution has been pointed out as they lead to smoother responses at all operational speeds. The amplitude at critical speeds are, however, hardly affected but a major influence on the positions of critical speeds has been put forward. In line with experimental evidence from the literature, no clear interest on dynamic tooth loads has been found on using either rolling element or journal bearings.

Focusing on helical gears, other damping sources become predominant. Mesh damping and the internal damping of the supporting shafts barely contribute to vibration reduction. The main active source of damping in helical gears is actually the bearings at both ends of the shafts. Both

Cette thèse est accessible à l'adresse : http://theses.insa-lyon.fr/publication/2016LYSEI089/these.pdf
© [M. Ankouni], [2016], INSA Lyon, tous droits réservés

rolling element and journal bearings are shown to have a prominent contribution to the vibration reduction. An unexpected behavior has been highlighted when journal bearings are used as it has been found that, for high levels of bearing damping, any increase in damping results in higher amplifications of the dynamic tooth loading. Based on modal analyses, it has been demonstrated that high damping introduced locally at some points of the system modifies largely the natural frequencies of the system but do not necessarily have the expected effect at other points of the system, at the gear nodes for instance. Special attention must therefore be paid to restrict damping within a certain favorable range of values when dealing with gears supported by journal bearings.

Cette thèse est accessible à l'adresse : http://theses.insa-lyon.fr/publication/2016LYSEI089/these.pdf
© [M. Ankouni], [2016], INSA Lyon, tous droits réservés

General conclusion

The present work can be viewed as an approach to understanding and quantifying the damping mechanisms in geared systems. Having placed emphasis on the damping related to the lubricant entrapped between the gear teeth and regarded as a primary source of dissipation, a transient EHL analysis has been conducted and different contact models have been developed which reproduce the dynamic contact conditions found in gears: i) a permanent contact model that describes the contact behavior under oscillating loads and, ii) a forced impact model that illustrates the contact loss situations followed by shocks found mainly in spur gears. Both problems have been solved using efficient multigrid techniques making it possible to run massive parameter analyses and sweep over wide ranges of operating conditions. The resulting numerical values have been fitted and simple linearized formulas have been derived to predict the damping related to tooth lubrication. The introduction of these approximate damping formulae in any gear dynamic model is straightforward.

Considering first a classic one-degree-of-freedom torsional gear dynamic model, realistic damping models based on the simplified outcomes of EHL analyses are assessed which comprise the normal and tangential contributions of the lubricant along with the internal damping in the gear material. Several comparisons with benchmark measurements from the literature show that this model can realistically reproduce the damping mechanisms in spur gears but is less efficient for helical gears. The main information on damping provided by the torsional model are summarized as follows: i) the lubricant mainly prevents the high tooth load amplifications when shocks between the teeth occur, ii) structural damping prevails for permanent contact regimes, iii) lubricant shear and tooth friction contributions can be influential but generally of secondary importance and finally, iv) mesh damping associated with lubricated tooth contacts has a minor effect on dynamic loads in helical gears.

The study is then extended to investigate the contributions to the overall damping of the mechanical parts surrounding the gears. To this end, a simple three-dimensional model is developed which accounts for the dissipation in gears, shafts and bearings. Focusing on spur gears, the major influence of mesh damping on dynamic tooth loads is confirmed whereas bearings play a complementary role since they only slightly reduce amplitudes at critical speeds, regardless of their damping level. As for helical gears, the following conclusions can be drawn: i) mesh damping only has a limited effect on dynamic loading (in contrast with spur spears), ii)

Cette thèse est accessible à l'adresse : http://theses.insa-lyon.fr/publication/2016LYSEI089/these.pdf
© [M. Ankouni], [2016], INSA Lyon, tous droits réservés

bearings constitute the main source of damping in such transmissions, iii) no general conclusion can be made concerning more favorable bearing architecture regarding dynamic tooth loading, journal bearings can lead to smoother dynamic responses but can also induce high amplifications despite their large damping.

It is believed that the present work presents some useful quantitative and qualitative pieces of information concerning damping in geared transmissions. Nevertheless, further improvements are certainly needed to provide a more complete analysis of the different features related to gear damping. In particular, the influence of tooth surface roughness would deserve attention as it can significantly modify the normal and tangential damping elements. The friction (tangential) damping ratio depends on the actual contact area hence on roughness morphology (via parameter m_0 in (3.2)). At the same time, the lubricant film and pressure distribution can be strongly affected by surface roughness with high pressure zones where the lubricant viscosity can be large enough so that their contribution to the normal damping can be highly altered in both permanent contact and impact conditions. A deep analysis of the nonlinear behavior of the contact that arises when pronounced surface roughness is considered (see appendix B) is indeed necessary. Furthermore, the realistic description of the contact between the mating gears, in terms of rigidity and damping must be combined with a more accurate modeling of the bearings dynamic behavior including the related nonlinearities for each type of bearing as in [119] for rolling element bearings and [126] for journal bearings.

Cette thèse est accessible à l'adresse : http://theses.insa-lyon.fr/publication/2016LYSEI089/these.pdf
© [M. Ankouni], [2016], INSA Lyon, tous droits réservés

References

[1] Reynolds, O., 1886, “On the theory of lubrication and its application to Mr. Beauchamp tower’s experiments, including an experimental determination of the viscosity of olive oil”, *Philosophical Transactions of the Royal Society*, **177**, 157-234.

[2] Barus, C., 1893, “Isothermals, isopiestics and isometrics relative to viscosity”, *American journal of science*, **45(3),** 87-96.

[3] Roelands, C.J.A., 1966, “Correlational Aspects of the Viscosity-Temperature-Pressure Relationship of Lubricating Oils”, Phd Thesis, Technical University Delft, Delft, The Netherlands.

[4] Dowson, D. and Higginson, G.R., 1966, “Elastohydrodynamic Lubrication, The Fundamentals of Roller and Gear Lubrication”, Pergamon, Oxford, Great Britain.

[5] Hertz, H., 1881, “On the Contact of Elastic Solids”, *Journal für die reine und angewandte Mathematik*, **92**, 292-302.

[6] Tower, B., 1885, “Second report on friction experiments (experiments on the oil pressure in a bearing)”, *Proceedings of the Institution of Mechanical Engineers*, 58-70.

[7] Ertel, A.M., 1939, “Hydrodynamic Lubrication Based on New Principles”, *Akad. Nauj SSSR Prikadnaya Mathematica i Mekhanika*, **3(2)**, 41-52.

[8] Grubin, A.N., 1949, “Fundamentals of the Hydrodynamic Theory of Lubrication of Heavily Loaded Cylindrical Surfaces”, Central Scientific Research Institute for Technology and Mechanical Engineering, **30**, Moscow, D.S.I.R. translation, 115-166.

[9] Downson, D., 1998, “History of Tribology”, 2nd edition, Professional Engineering publishing ltd, London, Burry St Edmunds, UK, ISBN -86058-070-X.

[10] Gohar, R., 2001, “Elastohydrodynamics”, World Scientific.

[11] Dowson, D. and Higginson, G.R., 1959, “A Numerical Solution to the Elastohydrodynamic Problem”, *Proceedings of the Institution of Mechanical Engineers, Part C: Journal of Mechanical Engineering Science*, **1(1)**, 6-15.

Cette thèse est accessible à l'adresse : http://theses.insa-lyon.fr/publication/2016LYSEI089/these.pdf
© [M. Ankouni], [2016], INSA Lyon, tous droits réservés

[12] Hamrock, B.J. and Dowson, D., 1976, “Isothermal Elastohydrodynamic Lubrication of Point Contacts, part I-Theoretical Formulation”, *ASME Journal of Tribology*, **98**, 223-229.

[13] Hamrock, B.J. and Dowson, D., 1977, “Isothermal Elastohydrodynamic Lubrication of Point Contacts, part III, Fully Flooded Results”, *ASME Journal of Tribology*, **99**, 264-276.

[14] Brandt, A., 1973, “Multi-level adaptive technique (MLAT) for fast numerical solution to boundary value problems”, *Proceedings of the Third International Conference on Numerical Methods in Fluid Mechanics*, 82-89. Springer Berlin Heidelberg.

[15] Evans, H.P. and Snidle, R.W., 1981, “Inverse solution of Reynolds’ equation of lubrication under point-contact elastohydrodynamic conditions”, *Journal of Lubrication Technology*, **103(4)**, 539-546.

[16] Dowson, D., 1962, “A generalized Reynolds equation for fluid-film lubrication”, *International Journal of Mechanical Sciences*, **4(2)**, 159-170.

[17] Peiran, Y. and Shizhu W., 1990, “A generalized Reynolds equation for non-Newtonian thermal elastohydrodynamic lubrication”, *ASME Journal of Tribology*, **112(4)**, 631-636.

[18] Holt, C. A., Evans, H.P., Snidle, R.W., 1996, “Solution of the non-Newtonian elastohydrodynamic problem for circular contacts based on a flow continuity method”, *Proceedings of the Institution of Mechanical Engineers, Part J: Journal of Engineering Tribology*, **210(4)**, 247-258.

[19] Sadeghi, F. and Sui, P.C., 1990, “Thermal elastohydrodynamic lubrication of rolling/sliding contacts”, *ASME Journal of Tribology*, **112(2)**, 189-195.

[20] Sui, P.C. and Sadeghi, F., 1991, “Non-Newtonian thermal elastohydrodynamic lubrication”, *ASME Journal of Tribology*, **113(2)**, 390-396.

[21] Venner, C.H. and Lubrecht, A.A., 1994, “Numerical Simulation of Transverse Ridge in a Circular EHL Contact Under Rolling/Sliding”, *ASME Journal of Tribology*, **116**, 751-761.

[22] Venner, C.H. and Lubrecht A.A., 1994, “Transient analysis of surface features in an EHL line contact in the case of sliding”, *ASME Journal of Tribology*, **116(2)**, 186-193.

Cette thèse est accessible à l'adresse : http://theses.insa-lyon.fr/publication/2016LYSEI089/these.pdf
© [M. Ankouni], [2016], INSA Lyon, tous droits réservés

[23] Venner, C.H. and Lubrecht, A.A., 1995, “Numerical Analysis of Influence of Waviness on the Film Thickness of a Circular EHL Contact”, *ASME Journal of Tribology*, **118**, 153-161.

[24] Venner, C.H. and Lubrecht, A.A., 1999, “Amplitude reduction of non-isotropic harmonic patterns in circular EHL contacts, under pure rolling”, *Tribology Series*, **36**, 151-162.

[25] Kweh, C.C., Evans H.P., Snidle R.W., 1989, “Micro-elastohydrodynamic lubrication of an elliptical contact with transverse and three-dimensional sinusoidal roughness”, *ASME Journal of Tribology*, **111(4)**, 577-584.

[26] Evans H. P, Snidle R.W., Sharif K.J., 2009, “Deterministic mixed lubrication modelling using roughness measurements in gear applications”, *Tribology International*, **42(10)**, 1406-1417 ISSN 0301-679X.

[27] Messe, S. and Lubrecht, A.A., 2000, “Transient elastohydrodynamic analysis of an overhead cam/tappet contact”, *Proceedings of the Institution of Mechanical Engineers, Part J: Journal of Engineering Tribology*, **214(5)**, 415-425.

[28] Bouassida, H., Biboulet, N., Sainsot, P., Lubrecht, A.A., 2014, “Piston ring load carrying capacity: Influence of cross-hatching parameters”, *Proceedings of the Institution of Mechanical Engineers, Part J: Journal of Engineering Tribology*, 1350650114522779.

[29] Chevalier F.F., Lubrecht A.A., Cann P.E., Colin F.F., 1998, “Film thickness in starved EHL point contacts”, *ASME Journal of Tribology*, **120(1)**, 126-133.

[30] Noutary, M.P. and Lubrecht, A.A., 2003, “Starved lubrication of isoviscous rigid circular contacts”, *Tribology Series*, **41**, 713-718.

[31] Biboulet, N., Colin, F., Lubrecht, A.A., 2013, “Friction in starved hydrodynamically lubricated line contacts”, *Tribology International*, **58**, 1-6.

[32] Biboulet, N. and Houpert, L., 2010, “Hydrodynamic force and moment in pure rolling lubricated contacts. Part 2: point contacts”, *Proceedings of the Institution of Mechanical Engineers, Part J: Journal of Engineering Tribology*, **224(8)**, 777-787.

[33] Stahl K., Höhn BR., Michaelis K., Hinterstoisser M., Mayer J., 2013, “Influence of Surface Texture and Coating on the Coefficient of Friction in EHL Contacts”. *VDI. International Conference on Gears.* Munich.

Cette thèse est accessible à l'adresse : http://theses.insa-lyon.fr/publication/2016LYSEI089/these.pdf
© [M. Ankouni], [2016], INSA Lyon, tous droits réservés

[34] Britton, R.D., Elcoate, C.D., Alanou, M.P., Evans, H.P., Snidle, R.W., 2000, “Effect of surface finish on gear tooth friction”, *Journal of tribology*, **122(1)**, 354-360.

[35] Guo, F., Kaneta, M., Wang, J., Nishikawa, H., Yang, P., 2006, “Occurrence of a noncentral dimple in squeezing EHL contacts”, *Journal of tribology*, **128(3)**, 632-640.

[36] Kaneta, M., Ozaki, S., Nishikawa, H., Guo, F., 2007, “Effects of impact loads on point contact elastohydrodynamic lubrication films”, *Proceedings of the Institution of Mechanical Engineers, Part J: Journal of Engineering Tribology*, **221(3)**, 271-278.

[37] Nishikawa, H., Miyazaki, H., Kaneta, M., Guo, F., 2008, “Effects of two-stage impact load on point contact elastohydrodynamic lubrication films”, *Proceedings of the Institution of Mechanical Engineers, Part J: Journal of Engineering Tribology*, **222(7)**, 807-814.

[38] Wijnant, Y. H., Venner, C. H., Larsson, R., Eriksson, P., 1999, “Effects of structural vibrations on the film thickness in an EHL circular contact”, *ASME Journal of Tribology*, **121(2)**, 259-264.

[39] Venner, C.H. and Wijnant, Y.H., 2005, “Validation of EHL contact predictions under time varying load”, *Proceedings of the Institution of Mechanical Engineers, Part J: Journal of engineering tribology*, **219**, 1-13.

[40] Wijnant, Y.H. and Venner, C.H., 1999, “Contact dynamics in starved elastohydrodynamic lubrication”, *Tribology Series*, **36**, 705-716.

[41] Sakamoto, M., Nishikawa, H., Kaneta, M., 2003, “Behaviour of point contact EHL films under pulsating loads”, *Tribology Series*, **43**, 391-399.

[42] Wang, Y., Li, H., Tong, J., Yang, P., 2004, “Transient thermo-elastohydrodynamic lubrication analysis of an involute spur gear”, *Tribology International*, **37(10)**, 773-782.

[43] Li, S. and Kahraman, A., 2010, “A Transient Mixed Elastohydrodynamic Lubrication Model for Spur Gear Pairs”, *ASME Journal of Tribology*, **132**,1-9.

[44] Li, S. and Kahraman, A., 2011, “Influence of dynamic behavior on elastohydrodynamic lubrication of spur gears”, *Proceedings of the Institution of Mechanical Engineers, Part J: Journal of Engineering Tribology*, **225**, 740-753.

[45] Barbieri, M., Lubrecht, A.A., Pellicano, F., 2013, “Behavior of lubricant fluid film in gears under dynamic conditions”, *Tribology International*, **62**, 37-48.

Cette thèse est accessible à l'adresse : http://theses.insa-lyon.fr/publication/2016LYSEI089/these.pdf
© [M. Ankouni], [2016], INSA Lyon, tous droits réservés

[46] Christensen, H., 1970, “Elastohydrodynamic theory of spherical bodies in normal approach”, *Journal of Lubrication Technology*, **92(1)**, 145-153.

[47] Larsson, R., and Höglund, E., 1995, “Numerical simulation of a ball impacting and rebounding a lubricated surface”, *ASME Journal of Tribology*, **117(1)**, 94-102.

[48] Dowson, D., and Wang, D., 1995, “Impact elastohydrodynamics”, *Tribology Series*, **30**, 565-582.

[49] Wang, J., Venner, C.H., Lubrecht, A.A., 2013, “Central film thickness prediction for line contacts under pure impact”, *Tribology International*, **66**, 203-207.

[50] Venner C.H. and Lubrecht A.A., 2000, “MultiLevel Methods in Lubrication”, Elsevier Tribology Series, **37**.

[51] Wijnant, Y.H., 1998, “Contact dynamics in the field of elastohydrodynamic lubrication”, Phd Thesis, Universiteit Twente. Netherlands.

[52] Wijnant, Y.H., Wensing, J. A., Nijen, G.C., 1999, “The influence of lubrication on the dynamic behaviour of ball bearings”, *Journal of Sound and Vibration*, **222(4)**, 579-596.

[53] Sarangi, M., Majumdar, B.C., Sekhar, A.S., 2004, “Stiffness and damping characteristics of lubricated ball bearings considering the surface roughness effect. Part 1: theoretical formulation”, *Proceedings of the Institution of Mechanical Engineers, Part J: Journal of Engineering Tribology*, **218(6)**, 529-538.

[54] Sarangi, M., Majumdar, B.C., Sekhar, A.S., 2004, “Stiffness and damping characteristics of lubricated ball bearings considering the surface roughness effect. Part 2: numerical results and application”, *Proceedings of the Institution of Mechanical Engineers, Part J: Journal of Engineering Tribology*, **218(6)**, 539-548.

[55] Hooke, C. J., and Morales-Espejel, G.E., 2016, “The Effects of Small Sinusoidal Load Variations in Elastohydrodynamic Line Contacts”, *ASME Journal of Tribology*, **138(3)**, 031501.

[56] Brandt, A., 1977, “Multi-level adaptive solutions to boundary-value problems”, *Mathematics of computation*, **31(138)**, 333-390.

[57] Lubrecht, A.A., 1987, “The numerical solution of the elastohydrodynamically lubricated line and point contact problem, using multigrid techniques”, Phd Thesis, Universiteit Twente. Netherlands.

Cette thèse est accessible à l'adresse : http://theses.insa-lyon.fr/publication/2016LYSEI089/these.pdf
© [M. Ankouni], [2016], INSA Lyon, tous droits réservés

[58] Lubrecht, A.A., Ten Napel, W.E., Bosma, R., 1986, “Multigrid, an alternative method for calculating film thickness and pressure profiles in elastohydrodynamically lubricated line contacts”, *ASME Journal of Tribology*, ***108*(4)**, 551-556.

[59] Lubrecht, A. A., Ten Napel, W.E., Bosma, R., 1987, “Multigrid, an alternative method of solution for two-dimensional elastohydrodynamically lubricated point contact calculations”, *ASME Journal of Tribology*, **109(3)**, 437-443.

[60] Brandt, A. and Lubrecht, A.A., 1990, “Multilevel matrix multiplication and fast solution of integral equations”, *Journal of Computational Physics*, **90(2)**, 348-370.

[61] Venner, C.H., 1991, “Multi-level solution of the elastohydrodynamic line and point contact problems”, Phd Thesis, Universiteit Twente. Netherlands.

[62] Bai, D. and Brandt, A., 1987, “Local mesh refinement multilevel techniques”, *SIAM Journal on Scientific and Statistical Computing*, **8(2)**, 109-134.

[63] Weber, C. and Banaschek, K., 1951, “The deformation of loaded gears and the effect on their load carrying capacity”, Department of Scientific and Industrial Research.

[64] Weber, C. and Banaschek, K., 1953, “Formänderung und Profilrücknahme bei Gerad- und Schrägverzahnten Antriebstechnik”, Vieweg, Braunschweig, **11**.

[65] Lundberg, G., 1939, “Elastische beruehrung zweier halbraeume”, *Forschung auf dem Gebiet des Ingenieurwesens A*, **10(5)**, 201-211.

[66] Cornell, R.W., 1981, “Compliance and stress sensitivity of spur gear teeth”, *Journal of Mechanical Design*, **103(2)**, 447-459.

[67] Palmgren, A., 1959, “Ball and Roller Bearing Engineering”, Philadelphia, Burbanks, third edition.

[68] Attia, A.Y., 1964, “Deflection of spur gear teeth cut in thin rims”, *ASME Journal of Engineering for Industry*, **86(4)**, 333-341.

[69] O’donnell, W.J., 1960, “The Additional Deflection of a Cantilever Due to the Elasticity of the Support”, *ASME, Journal of Applied Mechanics*, **27**, 461-464.

[70] O’donnel, W.J., 1963, “Stresses and Deflections in Built-In Beams”, *ASME Journal of Engineering for Industry*, **85**, 265-273.

Cette thèse est accessible à l'adresse : http://theses.insa-lyon.fr/publication/2016LYSEI089/these.pdf
© [M. Ankouni], [2016], INSA Lyon, tous droits réservés

[71] Sainsot, P., Velex, P., Duverger, O., 2004, “Contribution of gear body to tooth deflections- A new bidimensional analytical formula”, *ASME Journal of Mechanical Design*, **126(4)**, 748-752.

[72] Chabert G., Dang Tron, T., Mathis, R., 1974, “An Evaluation of Stresses and Deflection of Spur Gear Teeth under Strain”, *ASME Journal of Engineering for Industry*, **96**, 85-93.

[73] Wang K.L. and Cheng H.S., 1981, “A Numerical Solution to the Dynamic Load, Film Thickness, and Surface Temperatures in Spur Gears, Part I: Analysis”, *ASME Journal of Mechanical Design*, **103**, 177-187.

[74] Sainsot, A., 1989, “Analyse du Contact entre Dentures des Engrenages Cylindriques de Réducteurs”, Phd Thesis, INSA de Lyon.

[75] Henriot, G., 1978, “Traité théorique et pratique des engrenages, Tome II : Etude complète du matériel”, 4ème édition, Paris, Dunod Technique

[76] Henriot, G., 1979, “Traité théorique et pratique des engrenages, Tome I : Théorie et technologie”, 6ème édition, Paris, Dunod Technique

[77] Osman, T. and Velex, P., 2012, “A model for the simulation of the interactions between dynamic tooth loads and contact fatigue in spur gears”, *Tribology International*, **46**, 84-96.

[78] Velex, P., 2015, “Advanced Mechanical Transmissions”, Lecture Notes, INSA de Lyon.

[79] Umezawa, K., Suzuki, T., Houjoh, H., Bagiasna, K., 1986, “Influence of misalignment on vibration of helical gear”, *Bulletin of JSME*, **12(53)**, 85-91.

[80] Sabot, J., and Perret-Liaudet, J., 1992, “Excitation d’un carter de boîte de vitesses par l’erreur de transmission”, *3ème congrès mondial des engrenages et des transmissions*, Paris, 829-840.

[81] Harris, S.L., 1958, “Dynamic loads on the teeth of spur gears”, *Proceedings of the Institution of Mechanical Engineers*, **172**, 87-112.

[82] Nevzat Ozguven, H., and Houser, DR., 1988, “Mathematical models used in gear dynamics – a review”, *Journal of Sound and Vibration*, **121,** 383-411.

[83] Munro, R.G., 1989, "The D.C. component of gear transmission error", *Proc. 1989 International Power Transmission and gearing conference*, Chicago, 467-470.

Cette thèse est accessible à l'adresse : http://theses.insa-lyon.fr/publication/2016LYSEI089/these.pdf
© [M. Ankouni], [2016], INSA Lyon, tous droits réservés

[84] Gregory, R.W., Harris, S.L., Munro, R.G., 1963, “Dynamic behaviour of spur gears”. *Proceedings of the Institution of Mechanical Engineers*, **178**, 207–218.

[85] Lin, H.H., Townsend, D.P., Oswald, F.B., 1989, “Profile modification to minimize spur gear dynamic loading”, *Proceedings of the 5th ASME International Power Transmission and Gearing Conference*, Chicago, **1**, 455-465.

[86] Velex, P. and Ajmi, M, 2006, “On the modelling of excitations in geared systems by transmission errors”, *Journal of Sound and Vibration*, **290(3)**, 882-909.

[87] Munro, R.G., 1969-1970, “Effects of geometrical errors on the transmission of motion between gears”, *Proceedings of Institution of Mechanical Engineers*, **184(30)**, 79-83.

[88] Blankenship, G.W. and Kahraman, A., 1996, “Gear dynamics experiments, Part I: characterization of forced response”, *ASME Power Transmission Gearing Conference*, **88**, 373-380.

[89] Remond, D., 1991, “Contribution à l’étude et à l’analyse expérimentale du bruit d’engrènement. Développement et application de la transformée en ondelettes rapide”, Phd Thesis, INSA de Lyon.

[90] Gregory, R.W., Harris, S.L., Munro, R.G., 1963, “A method of measuring transmission error in spur gears of 1:1 ratio”, *Journal of Scientific Instruments*, **40(1)**, 5-9.

[91] Rosinski, J., Hoffman, D.A., Pennell, J.A., 1994, “Dynamic transmission error measurements in the time domain in high speed gears”, *Proceedings of International Gearing Conference*, University of Newcastle upon Tyne, 363-370.

[92] Velex, P. and Maatar, M., 1996, “A mathematical model for analyzing the influence of shape deviations and mounting errors on gear dynamic behaviour”, *Journal of Sound and Vibration*, **191(5)**, 629-660.

[93] Buckingham, E., 1931, “Dynamic loads on gear teeth”, *ASME Research Publication, New York*, **10**.

[94] Tuplin, W.A., 1953, “Dynamic loads on gear teeth”, *Machine Design*, **25(10)**, 203.

[95] Houser, D.R. and Seireg, A., 1970, “An experimental investigation of dynamic factors in spur and helical gears”, *Journal of Engineering for Industry*, **92(2)**, 495-503.

[96] Seireg, A. and Houser, D.R., 1970 "Evaluation of dynamic factors for spur and helical gears”, *Journal of Engineering for Industry*, **92(2)**, 504-514.

Cette thèse est accessible à l'adresse : http://theses.insa-lyon.fr/publication/2016LYSEI089/these.pdf
© [M. Ankouni], [2016], INSA Lyon, tous droits réservés

[97] Kubo, A., 1978, “Stress condition, vibrational exciting force, and contact pattern of helical gears with manufacturing and alignment error”, *Journal of Mechanical Design*, **100(1)**, 77-84.

[98] Baud, S., 1998, “Développement et validation sur banc d'essais de Modèles du comportement dynamique de réducteurs à engrenages à axes parallèles”, Phd Thesis, INSA de Lyon.

[99] Baud, S., and Velex, P., 2002, “Static and dynamic tooth loading in spur and helical geared systems-experiments and model validation”, *Journal of Mechanical Design*, **124(2)**, 334-346.

[100] Wang, J., Li, J., Peng, X., 2003, “Survey of nonlinear vibration of gear transmission systems”, *ASME Applied Mechanics Reviews*, **56**, 309-329.

[101] Remond, D., Velex, P., Sabot, J., 1993, “Comportement dynamique et acoustique des transmissions par engrenages : synthèse bibliographique”, *CETIM*, pp.127, 1993. <hal-00694869>

[102] Kahraman, A. and Blankenship, G.W., 1996, “Gear dynamics experiments: Part II: effect of involute contact ratio”, *ASME Power Transmission Gearing Conference*, **88**, 381–388.

[103] Kahraman, A. and Blankenship, G.W., 1996, “Gear dynamics experiments, Part III: effect of involute tip relief”, *ASME Power Transmission Gearing Conference*, **88**, 389–396.

[104] Hayashi, T., Li, X.Y., Hayashi, I., Endo, K., Watanbe, W., 1986, “Measurement and some discussions on dynamic load sharing in planetary gears”, *Bulletin of JSME*, **29(253)**, 2290-2297.

[105] Kahraman, A., 1999, “Static load sharing characteristics of transmission planetary gear sets: model and experiment”, No. 1999-01-1050. SAE Technical Paper.

[106] Kahraman, A., 1993, “Effect of axial vibrations on the dynamics of a helical gear pair”, *Journal of Vibration and Acoustics*, **115(1)**, 33-39.

[107] Gregory, R.W., Harris, S.L., Munro, R.G., 1963, “Torsional Motions of a Pair of Spur Gears”, *Proceedings of the Institution of Mechanical Engineers, Conference Proceedings*, **178(10)**, 166-173.

Cette thèse est accessible à l'adresse : http://theses.insa-lyon.fr/publication/2016LYSEI089/these.pdf
© [M. Ankouni], [2016], INSA Lyon, tous droits réservés

[108] Velex, P., 1988, “Contribution à l'analyse du comportement dynamique de réducteur à engrenages à axes parallèles”, Phd Thesis, INSA de Lyon.

[109] Velex, P. and Saada, A., 1991, “A model for the dynamic behavior of multi-stage geared systems”, *Proc of 8th Int Federation Theory Mach Mech World Congress*, 621-625.

[110] Velex, P. and Saada, A., 1991, “Modal analysis for the prediction of dynamic tooth loads in geared trains”, *Proceedings JSME International Conference Motion Power Transmissions*, *November*, 23-26.

[111] Saada, A., 1992, “Contribution à l'analyse du comportement dynamique de réducteurs à engrènements multiples. Applications aux trains double étage et épicycloïdaux”, Phd Thesis, INSA de Lyon.

[112] Azar, R.C. and Crossley, F.E., 1977, “Digital Simulation of Impact Phenomenon in Spur Gear Systems”, ASME. *J. Eng. Ind.*, **99(3)**, 792-798.

[113] Hilber, H.M., Hughes, T.J.R. and Taylor, R.L., 1977, “Improved numerical dissipation for time integration algorithms in structural dynamics”, *Earthquake Engineering and Structural Dynamics*, **5**, 283–292.

[114] Kalker, J.J., 1982, “Two algorithms for the contact problem in elastostatics”. Technische Hogeschool Delft. Onderafdeling der Wiskunde en Informatica.

[115] Ajmi, M. and Velex, P., 2005, “A model for simulating the quasi-static and dynamic behaviour of solid wide-faced spur and helical gears”, *Mechanism and Machine Theory*, **40(2)**, 173-190.

[116] Bettaïeb, M.N., Velex, P. and Ajmi, M., 2007, “A static and dynamic model of geared transmissions by combining substructures and elastic foundations—applications to thin-rimmed gears”, *Journal of Mechanical Design*, **129(2)**, 184-194.

[117] Abousleiman, V. and Velex, P., 2006, “A hybrid 3D finite element/lumped parameter model for quasi-static and dynamic analyses of planetary/epicyclic gear sets”, *Mechanism and Machine Theory*, **41(6)**, 725-748.

[118] Furukawa, T., 1991, “Vibration analysis of gear and shaft system by modal method”, *JSME International Conference on Motion and Power transmissions*, 123-127.

[119] Lahmar, F. and Velex, P., 2003, “Simulations of Gear-Rolling Element Bearing Interactions in Geared Transmissions”, *ASME 2003 International Design Engineering*

Cette thèse est accessible à l'adresse : http://theses.insa-lyon.fr/publication/2016LYSEI089/these.pdf
© [M. Ankouni], [2016], INSA Lyon, tous droits réservés

Technical Conferences and Computers and Information in Engineering Conference, 315-324.

[120] Abbes, M.S., Hentati, T., Maatar, M., Fakhfakh, T., Haddar, M., 2011, "Dynamic analysis of helical gears supported by rolling elements bearings", *Journal of Theoretical and Applied Mechanics*, **41(1)**, 33-50.

[121] Kahraman, A. and Singh, R., 1991, "Interactions between time-varying mesh stiffness and clearance non-linearities in a geared system", *Journal of Sound and Vibration*, ***146*(1)**, 135-156.

[122] Theodossiades, S. and Natsiavas, S., 2001, "On geared rotordynamic systems with oil journal bearings", *Journal of sound and vibration*, **243(4)**, 721-745.

[123] Baguet, S., and Velex, P., 2005, "Influence of the Nonlinear Dynamic Behavior of Journal Bearings on Gear-Bearing Assemblies," *Proceeding of the ASME Power Transmission Gearing International Conference*, **5**, 735-745.

[124] Baguet, S., and Jacquenot, G., 2010, "Nonlinear Couplings in a Gear–Shaft-Bearing System", *Mechanism and Machine Theory*, **45(12)**, 1777-1796.

[125] Fargère, R., and Velex, P., 2011, "Some Simulations of Gear–Journal Bearing Interactions", *ASME 2011 International Design Engineering Technical Conferences and Computers and Information in Engineering Conference*, 345-355.

[126] Fargère, R. and Velex, P., 2013, "Influence of Clearances and Thermal Effects on the Dynamic Behavior of Gear-Hydrodynamic Journal Bearing Systems", *Journal of Vibration and Acoustics*, **135(6)**, 061014-1-16.

[127] Velex, P., 2001, "Some problems in the modelling of gear dynamics", *Proceedings of the JSME international conference on motion and power transmission*, Japan, Fukuoka, **1**, 45-50.

[128] Amabili, M. and Rivola, A., 1997, "Dynamic analysis of spur gear pairs: steady-state response and stability of the SDOF model with time-varying meshing damping". *Mechanical System Signal Process*, **11**, 375–390.

[129] Lord Rayleigh, 1945, Theory of Sound, Dover.

[130] Craig, R.R., 1977, "Methods of component mode synthesis", *The Shock and Vibration Digest*, **9(11)**, 3-10.

Cette thèse est accessible à l'adresse : http://theses.insa-lyon.fr/publication/2016LYSEI089/these.pdf
© [M. Ankouni], [2016], INSA Lyon, tous droits réservés

[131] Brancati, R., Rocca, E., Russo, R., 2005, “A gear rattle model accounting for oil squeeze between the meshing gear teeth”, *Proceedings of the Institution of Mechanical Engineers, Part D: Journal of Automobile Engineering*, **219(9)**, 1075-1083.

[132] Theodossiades, S., Tangasawi, O., Rahnejat, H., 2007, “Gear teeth impacts in hydrodynamic conjunctions promoting idle gear rattle”, *Journal of sound and vibration*, **303(3)**, 632-658.

[133] Tangasawi, O., Theodossiades, S., Rahnejat, H, 2007, “Lightly loaded lubricated impacts: Idle gear rattle”, *Journal of Sound and Vibration*, **308(3)**, 418-430.

[134] Li, S. and Kahraman, A., 2011, “A spur gear mesh interface damping model based on elastohydrodynamic contact behaviour”, *International Journal of Powertrains*, **1**, 4-21.

[135] Li, S. and Kahraman, A., 2013, “A tribo-dynamic model of a spur gear pair”, *Journal of Sound and Vibration*, **332**, 4963-4978.

[136] Guilbault, R., Lalonde, S., Thomas, M., 2012, “Nonlinear damping calculation in cylindrical gear dynamic modeling”, *Journal of Sound and Vibration*, **331(9)**, 2110-2128.

[137] Liu, F.H., Theodossiades, S., Bergman, L.A., Vakakis, A.F., McFarland, D.M., 2015, “Analytical characterisation of damping in gear teeth dynamics under hydrodynamic conditions”. *Mechanism and Machine Theory*, **94**, 141-147.

[138] Diab, Y., Ville, F., Velex, P., 2006, “Prediction of power losses due to tooth friction in gears”, *Tribology transactions*, **49(2),** 260-270.

[139] De Silva, C.W., 2005, “Vibration and shock handbook”, CRC Press.

[140] Velex, P., Maatar, M., Raclot, J.P., 1997, “Some numerical methods for the simulation of geared transmission dynamic behavior formulation and assessment”, *Journal of Mechanical Design*, **119(2)**, 292-298.

[141] Kubur, M., Kahraman, A., Zini, D.M., Kienzle, K., 2004, “Dynamic analysis of a multi-shaft helical gear transmission by finite elements: model and experiment”, *Journal of vibration and acoustics*, **126(3)**, 398-406.

[142] Dareing, D.W. and Johnson, K.L., 1975, “Fluid film damping of rolling contact vibrations”, *Journal of Mechanical Engineering Science*, **17(4)**, 214-218.

Cette thèse est accessible à l'adresse : http://theses.insa-lyon.fr/publication/2016LYSEI089/these.pdf
© [M. Ankouni], [2016], INSA Lyon, tous droits réservés

[143] Frêne, J., 1995, “Butées et paliers hydrodynamiques”, Techniques de l'ingénieur. Génie mécanique, (B5320), B5320-1.

[144] Lim, T. C., and Singh, R., 1990, “Vibration Transmission through Rolling Element Bearings, Part I: Bearing Stiffness Formulation”, *Journal of sound and vibration*, **139(2)**, 179-199.

[145] Lim, T. C., and Singh, R., 1990). “Vibration transmission through rolling element bearings, part II: system studies”, *Journal of sound and vibration*, **139(2)**, 201-225.

[146] Lim, T. C., and Singh, R., 1991, “Vibration Transmission through Rolling Element Bearings, Part III: Geared Rotor Studies”, *Journal of sound and vibration*, **151(1)**, 31-54.

[147] Hambric, S.A., Shepherd, M.R., Campbell, R.L., Hanford, A.D., 2013, “Simulations and measurements of the vibroacoustic effects of replacing rolling element bearings with journal bearings in a simple gearbox”, *Journal of Vibration and Acoustics*, **135(3)**, 031012.

[148] Chang, C. J. and Mohraz, B., 1990, “Modal analysis of nonlinear systems with classical and non-classical damping”, *Computers & Structures*, **36(6)**, 1067-1080.

[149] Johnson, K.L., 1985, “Contact mechanics”, Cambridge University Press.

Cette thèse est accessible à l'adresse : http://theses.insa-lyon.fr/publication/2016LYSEI089/these.pdf
© [M. Ankouni], [2016], INSA Lyon, tous droits réservés

Cette thèse est accessible à l'adresse : http://theses.insa-lyon.fr/publication/2016LYSEI089/these.pdf
© [M. Ankouni], [2016], INSA Lyon, tous droits réservés

Appendix A

Damping under multi-frequency excitation

Gear teeth are generally subjected to multi-frequency periodic loading that can be decomposed into Fourier series as follows:

$$w_t = w_0 + \sum_{i=1}^{n} a_i \sin(\mathrm{i}\omega \mathrm{t} + \phi_i) \tag{A.1}$$

In order to compute the damping provided by the lubricated contact subjected to such loading, further numerical simulations are performed considering first a bi-frequency excitation as in equation (A.2) and then the general case of multi-frequency excitation. The main purpose is to relate the damping corresponding to each frequency with the overall damping that corresponds to the total load.

$$w_t = 1 + a_1 \sin(\omega t + \phi_1) + a_2 \sin(2\omega t + \phi_2) \tag{A.2}$$

Introducing the dimensionless parameters as in chapter 2, the load reads:

$$W_t = 1 + A_1 \sin(\Omega T + \Phi_1) + A_2 \sin(2\Omega T + \Phi_2) \tag{A.3}$$

The resulting rigid body displacement Δ is, thus:

$$\Delta = B_0 + B_1 \sin(\Omega T + \psi_1) + B_2 \sin(2\Omega T + \psi_2) \tag{A.4}$$

The total dissipated energy equals:

$$E = \int_0^{2\pi/\Omega} D_{eq} \dot{\Delta}^2 dT = \pi D_{eq} \Omega (\mathrm{B}_1^2 + 4B_2^2) \tag{A.5}$$

The equivalent damping D_{eq} along with the different amplitudes of the normal approach can be computed numerically, following the same strategy as in chapter 2.

Through several numerical simulations, it can be noticed that the energy dissipated by imposing a load as in equation (A.3) can be related to the energy dissipated if each component were taken separately as follows:

$$E = E_1 + 2E_2 \tag{A.6}$$

where $E_1 = \pi D_1 \Omega (B_{11}^2 + B_{12}^2)$ and $E_2 = 2\pi D_2 \Omega (B_{21}^2 + B_{22}^2)$.

Cette thèse est accessible à l'adresse : http://theses.insa-lyon.fr/publication/2016LYSEI089/these.pdf
© [M. Ankouni], [2016], INSA Lyon, tous droits réservés

Equating equations (A.5) and (A.6), the equivalent damping D_{eq} is computed as:

$$D_{eq} = \frac{D_1 B_1^2 + 4D_2 B_2^2}{B_1^2 + 4B_2^2} \tag{A.7}$$

with D_1 and D_2 that can be simply computed using the proposed formulation of the damping in equations (2.28) and (2.29).

The previous procedure can be extended to multi-frequency excitation as in equation (A.1). The corresponding dimensionless load and rigid body displacement read:

$$W_t = 1 + \sum_{i=1}^{n} A_i \sin(\mathrm{i}\Omega\mathrm{T} + \Phi_i) \tag{A.8}$$

$$\Delta = \Delta_0 + \sum_{i=1}^{n} B_i \sin(\mathrm{i}\Omega\mathrm{t} + \psi_i) \tag{A.9}$$

The total dissipated energy is developed by analogy as:

$$E = \int_0^{2\pi/\Omega} D_{eq} \dot{\Delta}^2 dT = \pi D_{eq} \Omega \sum_{i=1}^{n} i^2 B_i = \sum_{i}^{n} iE_i = \sum_{i}^{n} i^2 \pi D_i \Omega (B_i^2) \tag{A.10}$$

where E_i is the dissipated energy , and D_i the damping coefficient corresponding to each frequency $i\Omega$ separately.

Based on the previous analysis, the equivalent damping is computed as:

$$D_{eq} = \frac{\sum_{i=1}^{n} i^2 D_i B_i^2}{\sum_{i=1}^{n} i^2 B_i^2} \tag{A.11}$$

Cette thèse est accessible à l'adresse : http://theses.insa-lyon.fr/publication/2016LYSEI089/these.pdf
© [M. Ankouni], [2016], INSA Lyon, tous droits réservés

Appendix B

A note on the influence of roughness on damping

It is accepted that surface roughness influence greatly the performance and characteristics of lubricated contacts. Non-smooth surfaces can induce some local high pressure zones that can lead to a reduction of the damping capacity of the lubricant film caused by the largely increased values of the lubricant viscosity. Therefore, some few simulations are conducted to provide more precise information on the surface roughness influence. To do so, a one-sided waviness is introduced to the gap between the contacting surfaces and the transient EHL problem for permanent contacts presented in chapter 2 is reproduced. Accounting for surface features, the dimensionless film thickness equation reads:

$$H(X) = H_0 + \frac{X^2}{2} - \frac{1}{2\pi}\int_{-\infty}^{+\infty} P(X')\, ln\left(\frac{X - X'}{X_0}\right)^2 dX' - R(X) \tag{B.1}$$

with $R(X) = A_R \cos(\frac{2\pi}{\lambda_R} X)$ where A_R and λ_R denote the amplitude and the wavelength of the surface feature respectively.

A set of numerical simulations is performed considering different wavelengths (λ_R=0.1, 0.25, 0.5, 1.), varying the amplitude from the extremely low values to some high values representative of the real amplitude of roughness encountered in gears ($A_R = 0.0005 - 0.1$) and sweeping a wide range of operating conditions (M, L, A and T). Figure B.1 shows a snapshot of the pressure at one given time-step during the simulation for a given set of A_R and λ_R ($A_R = 0.05, \lambda_R = 0.5$). Some localized high pressure peaks are noticed that can exceed 1.5 times the maximum Hertzian pressure and can in some conditions go up to twice the Hertzian pressure. The pressure increase is normally proportional to the ratio A_R/λ_R. An equivalent damping coefficient C_{l_s} is computed following the same strategy used earlier for perfectly smooth surfaces.

Figure B.2 exposes a set of results obtained with amplitudes of roughness up to 0.025. The ratio of the rough damping with respect to smooth damping is plotted as a function of the Hertzian pressure. The level of amplitudes considered is considered sufficiently low to guarantee a linear behavior of the contact. A great dependence of the damping on the roughness is noticed in Figure B.2. Higher amplitudes generate a higher reduction of the damping coefficients leading

Cette thèse est accessible à l'adresse : http://theses.insa-lyon.fr/publication/2016LYSEI089/these.pdf
© [M. Ankouni], [2016], INSA Lyon, tous droits réservés

to some values up to 20 % of the smooth damping values (1 GPa). The effect is less noticeable for lightly or extremely high loaded contacts. For low loads, the lubricated gap between the contact bodies is relatively large and a higher roughness is needed to cause a local increase in the pressure, furthermore the amplitude of the roughness is largely smoothened under high loads and narrow effect is found on damping.

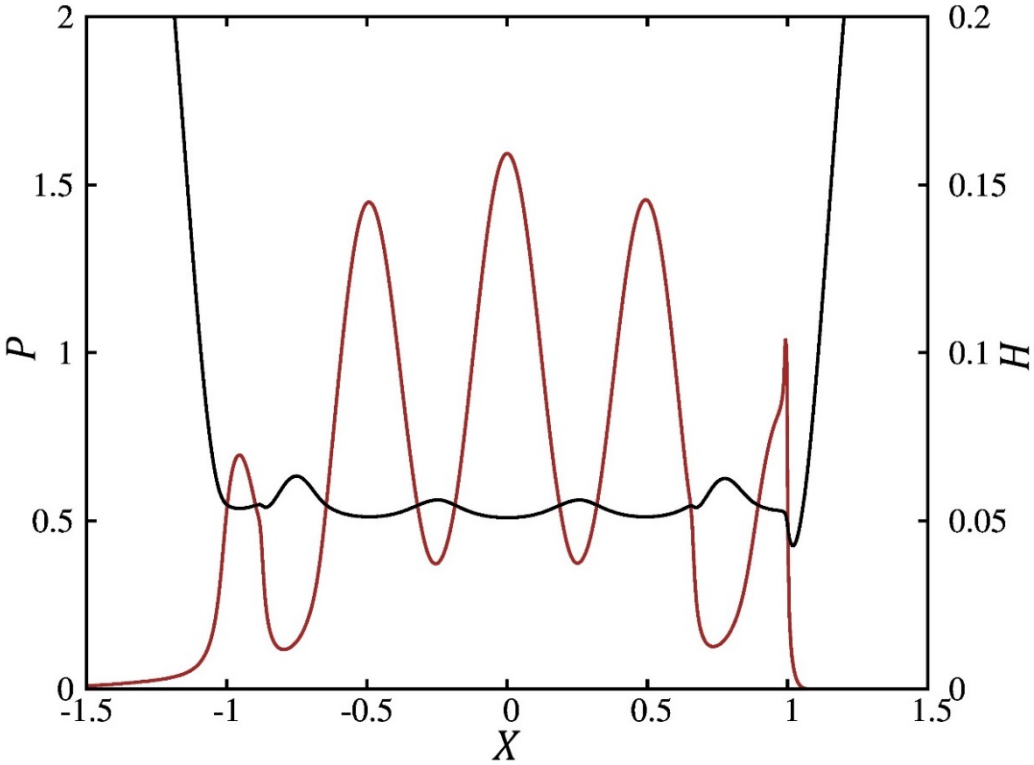

Figure B.1: Pressure distribution and film thickness in an EHL rough contact ($M = 25, L = 10, A_R = 0.05, \lambda_R = 0.5$).

The previous observations are unlikely be extended to rougher surfaces. An increasingly nonlinear behavior is induced by higher amplitudes. In this context, few simulations were performed considering some roughness values comparable or even higher from the average film thickness (of the order of gear teeth roughness). The obtained results showed that a further increase of the surface roughness can lead to a lower reduction and even a small increase of the damping values. This can be explained by the extremely low pressures that appear between the pressure peaks and that results in lowering the viscosity of the lubricant that can therefore flow again and thus dissipate further. The computing of damping in this case is not truly accurate since the behavior becomes hugely nonlinear and thus the assumption of linear damper is no more appropriate. Further investigation are indeed needed to properly quantify the influence of the roughness on the dynamic behavior of the contact.

Cette thèse est accessible à l'adresse : http://theses.insa-lyon.fr/publication/2016LYSEI089/these.pdf
© [M. Ankouni], [2016], INSA Lyon, tous droits réservés

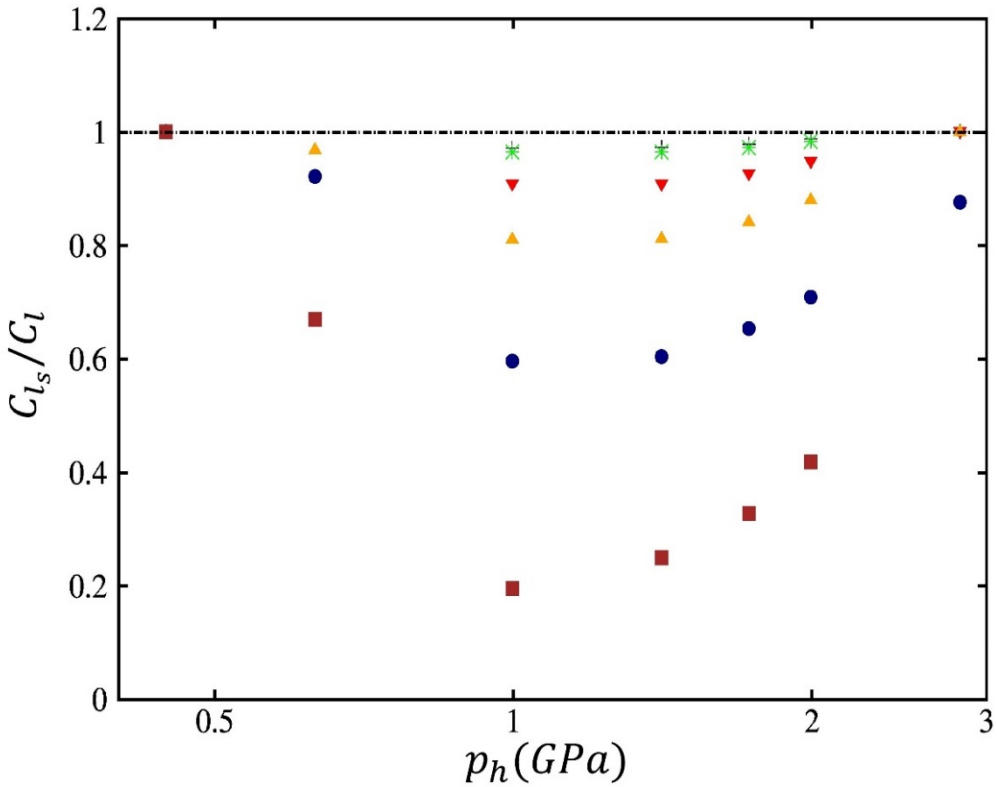

Figure B.2: Damping reduction for different amplitudes of roughness. From top to bottom: $A_R = 5e^{-4}, 1e^{-3}, 2.5e^{-3}, 5e^{-3}, 1e^{-2}, 2.5e^{-2}$. $\lambda_R = 0.5$.

Cette thèse est accessible à l'adresse : http://theses.insa-lyon.fr/publication/2016LYSEI089/these.pdf
© [M. Ankouni], [2016], INSA Lyon, tous droits réservés

Cette thèse est accessible à l'adresse : http://theses.insa-lyon.fr/publication/2016LYSEI089/these.pdf
© [M. Ankouni], [2016], INSA Lyon, tous droits réservés

FOLIO ADMINISTRATIF

THESE DE L'UNIVERSITE DE LYON OPEREE AU SEIN DE L'INSA LYON

NOM : ANKOUNI
(avec précision du nom de jeune fille, le cas échéant)

DATE de SOUTENANCE :

28 Septembre 2016

Prénoms : Mouhamad

TITRE : Modeling of damping in elastohydrodynamic lubricated contacts. Application to gear dynamics.

NATURE : Doctorat

Numéro d'ordre : 2016LYSEI089

Ecole doctorale : Mécanique, Energétique, Génie Civil, Acoustique

Spécialité : Génie Mécanique

RESUME :

Les principaux mécanismes d'amortissement présents dans les transmissions par engrenages sont étudiés, en se basant sur une analyse transitoire du problème de lubrification élasto-hydrodynamique dans les contacts linéiques. Plusieurs modèles linéaires sont proposés suite à de nombreuses simulations numériques, permettant de prédire l'amortissement du lubrifiant dans les différentes conditions de contact, y compris les situations des pertes de contact momentanées suivies d'impact. Un modèle dynamique d'engrenage à un seul degré de liberté est présenté qui combine les contributions diverses du lubrifiant à l'amortissement structurel représentatif de la dissipation interne des engrenages. Un certain nombre de comparaisons avec des résultats expérimentaux est présenté pour une gamme de conditions de fonctionnement et de géométries d'engrenages, qui prouve la capacité du modèle à reproduire proprement le comportement dynamique des engrenages droits. On montre que l'amortissement associé au lubrifiant contribue essentiellement lors des pertes de contact et des chocs entre dentures se produisant au voisinage des vitesses critiques. Le cas des engrenages hélicoïdaux est analysé différemment du fait de l'absence de perte de contact pour ce type d'engrenage. Un modèle tridimensionnel simple est ainsi développé qui prend en compte la dissipation des différents éléments de la transmission. Un nombre de résultats est présenté qui, d'abord, confirme la contribution majeure de l'engrènement à l'amortissement global des engrenages droits, et, dans un second lieu, montre que les paliers constituent la principale source d'amortissement dans les transmissions par engrenages hélicoïdaux.

MOTS-CLÉS : Amortissement, dynamique des engrenages, lubrification elasto-hydrodynamique, contacts linéiques, multigrilles, vibration et bruit, paliers.

Laboratoire (s) de recherche : Laboratoire de Mécanique des Contacts et des Structures (LaMCoS)
UMR CNRS 5259 – INSA de Lyon

Directeur de thèse: Philippe VELEX

Président de jury : Georges JACQUET-RICHARDET

Composition du jury : JACQUET-RICHARDET, Georges, EVANS, Pwt, THEODOSSIADES, Stephanos, LUBRECHT, Ton, VELEX, Philippe

Cette thèse est accessible à l'adresse : http://theses.insa-lyon.fr/publication/2016LYSEI089/these.pdf
© [M. Ankouni], [2016], INSA Lyon, tous droits réservés